Cocks, Daniel Graeme (2010) ***Photoassociation of ultracold metastable helium.*** **PhD Thesis, James Cook University.**

https://doi.org/10.25903/bgn3%2Dqa32

Photoassociation of Ultracold Metastable Helium

Thesis submitted by

Daniel Graeme Cocks
B.Sc Physics (Hons)
in August 2010

for the degree of Doctor of Philosophy
in the School of Engineering and Physical Sciences

James Cook University

Abstract

A theoretical analysis of photoassociation in ultracold metastable helium has been undertaken for the $2\,{}^3S_1 + 2\,{}^3S_1$ to $2\,{}^3S_1 + 2\,{}^3P$ transition. A full multichannel calculation is presented for two aspects of the system, a) the accurate calculation of energies for the bound vibrational levels of the dimer; and b) the non-perturbative calculation of the photoassociation line shapes allowing for abitrary laser intensity and detuning. A strong emphasis is placed on the accuracy of the calculations, and the elimination of approximations that have been used in previous investigations. The results indicate that full multichannel calculations are required rather than approximate single-channel calculations in some important situations, and are especially useful for making assignments between experiment and theory.

Bound levels have been previously measured from the photoassociation of cold metastable thermal gases to energies close to the three asymptotes $j = 0, 1, 2$ of the $2\,{}^3S_1 \rightarrow 2\,{}^3P_j$ atomic transition. Previous analysis of these measurements was made using either approximate accumulated phase techniques based on long-range single-channel potentials, or using multichannel calculations and long-range potentials. Because accurate short-range electronic potentials have been calculated only recently, this thesis presents the first multichannel calculation for the levels near the $j = 1, 2$ asymptotes. The new short-range potentials had previously been used in an approximate single-channel calculation, but this type of calculation ignores the effects of non-adiabatic and Coriolis couplings. Presented here are the binding energies calculated from a fully multichannel technique which includes these couplings, and some differences of up to 10% from the single-channel calculations are observed. The detailed knowledge of the bound wave functions is then exploited to determine a set of observability criteria that produce a near unique assignment of theoretical levels to experimental observations. From these unique assignments, a 1% correction to the short-range electronic potentials has been implemented that significantly improves the agreement between theory and experiment.

Experimental measurements have previously been made of line shifts in the photoassociation spectra of vibrational levels in the 0_u^+ long-range potential that asymptotes to $2\,{}^3S_1 + 2\,{}^3P_0$ and their variation with laser intensity. These results were previously analysed by performing an approximate second-order perturbative calculation of the line shift that is valid only for low laser intensities. In this thesis a completely non-perturbative calculation of the spectra and line shapes for abitrary laser intensity is presented for photoassociation to the levels probed in experiment. The techniques of dressed state formalism and a modified radiative coupling are employed to properly treat the laser coupling for large interatomic separations. These calculations produce resonance profiles superimposed on a very significant background, a feature that is not seen in photoassociation calculations of other atomic species. From the calculated line shapes, the line shifts and line widths were determined for varying intensity and a small nonlinear intensity-dependence of up to 2.5% was found for the line shift. The effects of invoking the dipole approximation for the laser coupling for the long-range molecular system are analysed by solving the equations using the complete laser coupling that does not assume the dipole approximation. Important differences are obtained between the profiles with and without the dipole approximation, and the photoassociation resonances are found to be more discernible at larger intensities when the complete laser coupling is used.

Acknowledgements

I would like to thank my supervisor, Ian Whittingham, for his unending patience, gentle guidance and deftness with a red pen throughout the course of this PhD. It has been a long journey and I am very lucky to have had a mentor of such enthusiasm, open-mindedness and modesty. Thank you Ian, for putting my fumbling footsteps on the road to the wonderful world of research in quantum physics. Thanks also to Annie Whittingham for her constant moral support and her ability to always put a smile on my face.

Thanks also go to the fantastic people who have supported me, motivational and academically, over my eight years as undergraduate and post-graduate at James Cook University. You have made me appreciate what a great place the world of science can be.

Of course, I would not have got to where I am now without the support of my family. They have always been happy to lend an ear when I had problems, were understanding when I needed my space and have always pushed me to make the most of the opportunities that have come my way. Thanks in particular to Malcolm for his amazingly fast proof-reading of this thesis.

The undertaking of this PhD would not have been as rewarding without the great group of fellow post-graduates who have shared the ups and downs of the research student experience. I wish you all the best for your careers and hope that you will all continue to perform excellent scientific research.

Contents

Abstract **i**

Acknowledgements **iii**

Chapter 1 Introduction **1**

1.1 Ultracold atoms 1

1.2 Photoassociation 4

1.3 Metastable Helium 5

1.4 Experimental studies of metastable helium 7

1.5 Theoretical studies of metastable helium 8

1.6 Aims and objectives of project 11

1.7 Structure of thesis 11

Chapter 2 Formulation of basis states and matrix elements **13**

2.1 Hamiltonian 13

2.1.1 Electronic Hamiltonian 14

2.1.2 Relativistic correction Hamiltonian 17

2.1.3 Kinetic term 17

2.1.4 Laser field Hamiltonian 18

2.1.5 Laser interaction term 18

2.2 Angular momentum basis states 19

2.2.1 Coupling of angular momenta 19

2.2.2 Molecular symmetries 21

2.3 Matrix elements of the Molecular Hamiltonian 22

2.4 Spontaneous loss from the $2s2p$ manifold 24

2.5 Summary 25

Chapter 3 Bound levels of the $2s2p$ manifold **27**

3.1 Introduction 27

3.2 Single-channel calculation 29

3.2.1 Potentials 29

3.2.2 Differential equations 31

3.2.3 Comparison with Deguilhem *et al* 32

3.3 Multichannel calculation 33

3.3.1 Differential equations 33

3.3.2 Non-adiabatic effects 36

3.3.3 Coriolis effects 36

3.3.4 Bound levels above the $j = 2$ asymptotic limit 40

3.4 Experimental assignments 45

3.4.1 Single-channel assignments 45

3.4.2 Observability Criteria 47

3.4.3 Spin-polarised experiments beneath the $j = 2$ asymptote 49

3.4.4 Unpolarised experiments beneath the $j = 2$ asymptote 52

3.4.5 Unpolarised experiments above the $j = 2$ asymptote 54

3.5 Short-range correction 57

3.6 Zhang *et al* coefficients 62

3.7 Summary 62

Chapter 4 Photoassociation dynamics of long-range levels **65**

4.1 Introduction 65

4.2 Laser coupling 67

4.3 Dipole approximation 73

4.4 Photoassociation profiles 74

4.5 Perturbative line shifts in the dipole approximation 75

4.5.1 Direct perturbative calculation 75

4.5.2 F-operator solution 77

4.6 Multichannel solution in the dipole approximation 81

4.6.1 Introduction 81

4.6.2 Multichannel equations 82

4.6.3 Dressed state formalism 86
4.6.4 Modified radiation coupling 88
4.6.5 Numerical implementation details 89
4.6.6 Detection of the resonance through spontaneous loss 90
4.6.7 Detection without spontaneous loss 99
4.7 Multichannel solutions with the complete coupling term 103
4.7.1 Differences between the approximate and exact coupling 103
4.7.2 Results 104
4.7.3 Couplings to $J > 3$ levels 108
4.8 Summary 109

Chapter 5 Conclusions and future work **111**
5.1 Conclusions 111
5.1.1 Calculations performed 111
5.1.2 Critical Appraisal 112
5.2 Future work 114

Publications and Conference Contributions **117**

Bibliography **119**

Appendix A Notation and Physical Constants **131**
A.1 Notation 131
A.2 Physical constants 132

Appendix B Coupling Schemes and Symmetrisation **133**
B.1 jj symmetrisation 133
B.2 LS coupling 136
B.3 Transformation between LS and jj bases 138
B.4 Electronic matrix element 140
B.5 Experimentally relevant basis states 142

Appendix C Renormalised Numerov method **143**
C.1 Bound states 143
C.2 Resonances 145
C.3 Application to regions of different step size 146

Appendix D Discrete Variable Representation (DVR) method 149

D.1 Introduction 149

D.2 Conversion of differential equations to matrix equations 151

D.3 Fourier sine DVR basis 152

D.4 Fourier cosine DVR basis 156

D.5 Scaled grid 158

Appendix E Tabulation of results 161

List of Figures

1.1 Born-Oppenheimer potentials of the $2s2s$ molecular level of helium. Units of THz (1 THz = 33.36 cm^{-1}) are used so as to conform with the majority of results presented in this thesis. 9

1.2 Born-Oppenheimer potentials of the $2s2p$ molecular level of helium. 10

3.1 Near degenerate single-channel potentials of the 0_u^+, $J = 1$ set. 34

3.2 Short-range scaling. 59

4.1 Relevant states of the helium atom. 67

4.2 The photoassociation process. 68

4.3 Diatomic coordinate system. 69

4.4 Continuum contributions of the perturbation equation. 76

4.5 Perturbative line shifts with varying kinetic energy. 77

4.6 Dressed PA profile at low intensity. 91

4.7 Modified coupling PA profiles at low intensity. 93

4.8 Reflection and mixing induced by the modified radiation coupling. 93

4.9 Averaged modified coupling PA profiles at low intensity. 94

4.10 Dressed PA profiles at high intensity. 96

4.11 Modified coupling PA profile at high intensity. 97

4.12 PA spectrum of a bound level within an artificially deepened potential well. 97

4.13 Line shifts with varying intensity. 98

4.14 Line widths with varying intensity. 98

4.15 Modified coupling PA profiles without loss. 100

4.16 Dressed PA profiles without loss at low intensity. 101

4.17 Dressed PA profiles without loss at high intensity. 102

4.18 Non-dipole PA profiles with only the $p = 0$ summation term. 105

4.19 Non-dipole PA profiles with all even terms of the p summation. 106

4.20 Non-dipole PA profiles with all terms included. 107

4.21 Non-dipole PA profiles with all terms included for separate channels. 107

4.22 Non-dipole PA profile that breaks the dipole approximation selection rules. 109

List of Tables

2.1 Long range interaction coefficients of Marinescu. 16

2.2 Long range interaction coefficients of Zhang *et al.* 16

2.3 Tabulated extrapolation coefficients of the BO potentials towards the origin. 17

3.1 Comparison of single-channel results with that of Deguilhem *et al.* 33

3.2 Comparison of single-channel smoothing methods. 34

3.3 Comparison of non-adiabatic couplings for the 2_u, $J = 2$ set. 37

3.4 Comparison of non-adiabatic couplings for the 0_u^+, $J = 1$ set. 38

3.5 Comparison of non-adiabatic couplings for the 1_g, $J = 1$ set. 39

3.6 Comparison of Coriolis couplings for the ungerade $J = 2$ set. 41

3.7 Comparison of Coriolis couplings for the gerade $J = 2$ set. 42

3.8 Resonances near the $j = 1$ asymptote. 46

3.9 Resonances near the $j = 0$ asymptote. 47

3.10 Assignments to the observations of Kim *et al.* 51

3.11 Predicted bound levels to be observed in spin-polarised experiments. 52

3.12 Assignments to the observations of van Rijnbach and Tol. 55

3.13 Bound levels Predicted to be observable in unpolarised experiments. 56

3.14 Assignments to resonances near the $j = 1$ asymptote that allow ion detection. 56

3.15 Resonances predicted to be observable in spin-polarised experiments using an optical detection mechanism. 57

3.16 Comparison of short-range variations for spin-polarised experiments. 60

3.17 Comparison of short-range variations for unpolarised experiments. 61

3.18 Comparison of calculated binding energies from Marinescu and Zhang *et al* coefficients. 62

4.1 Perturbative line shifts. 81

4.2 Line shifts and widths determined from loss mechanism. 99
4.3 Line shifts and widths determined without loss. 103

E.1 Comparison of single-channel results with Deguilhem *et al*. 162
E.2 Complete list of resonances near the $j = 1$ asymptote. 163
E.3 Complete list of resonances near the $j = 0$ asymptote. 164
E.4 Resonances predicted to be observable in experiments using an ion detection mechanism. 165

Chapter 1

Introduction

1.1 Ultracold atoms

Ultracold physics research has grown tremendously over recent decades to become a major force in the field of atomic physics. The successful cooling of gases to temperatures in the sub-mK regime has produced a wide range of unique diagnostic tools and unusual physical phenomena such as Bose-Einstein condensation, atom lasers, atom interferometry and atoms trapped in optical lattices. The success of ultracold physics research is due not only to the incredibly precise nature of experimental measurements and theoretical calculations but also to the controlled manipulations of atoms and their interactions that radiation and magnetic fields provide at these temperatures. Ultracold research has applications in condensed matter physics, as control over bulk behaviour in an ultracold system can be used as a highly configurable model of a more complicated and inflexible condensed matter system. Ultracold experiments also provide a pathway to study the possibilities of quantum computing, atom lithography and high precision atomic clocks. The topics of ultracold research discussed in this introduction provide a small sample of what research has been performed in ultracold experiments and by no means represents the breadth of current interest in the field. For a general review of ultracold physics, see in Weiner *et al* [1] and references therein.

Cooling techniques

The attainment of ultracold temperatures has been made possible by the development of advanced laser cooling techniques, for which Steven Chu, Claude Cohen-Tannoudji and William Phillips were awarded the 1997 Nobel Prize in Physics. The principle of laser cooling makes use of uni-directional photon absorption by an atom, followed by isotropic spontaneous emission. Averaged over many incident photons, the absorption/emission process creates a net momentum transfer directed along the incident laser beam. The Doppler shift experienced by an atom moving in the presence of a laser field can be exploited by red detuning the laser to orientate this momentum transfer to be in the opposite direction to the atom's motion, such that photon absorption will cause the atom to slow down and be cooled. The manipulation of the atom's energy levels by Zeeman shifts and the trapping of atoms using inhomogeneous magnetic fields are also vital to the cooling process. The most commonly used cooling and trapping techniques are Zeeman slowing, magneto-optical trapping, magnetic traps, optical molasses and evaporative cooling, see [1, 2, 3]. The methods used for the cooling of metastable helium will be described in more detail later in this chapter.

Manipulation of collisions

The accurate nature of ultracold physics allows the fine control of interaction properties for two-atom collisions, including those within many-body systems. Ultracold collisions are dominated by long interaction times and by the lowest order (s-wave) rotational collision terms which are characterised by the scattering length a. Knowledge of the value for a is essential for quantifying molecular physics in the low temperature limit. For example, if the scattering length is negative then the attractive forces between the atoms of a bosonic gas do not allow the production of a stable Bose-Einstein condensate. Alternatively, if the scattering length is large then the gas will have very large elastic cross sections, desirable for efficient cooling. The scattering length can be modified by applying external fields to invoke the magnetic tuning of Feshbach resonances [4], or the coupling to optical Feshbach resonances [5], otherwise known as photoassociation resonances. Feshbach resonances occur when a scattering state is energy shifted into resonance with a bound molecular level; see Chin *et al* [6] for a general review. The changes induced by these methods can reverse the sign of the scattering length and suppress inelastic loss rates, allowing condensation that would otherwise be prohibited, such as in cesium-133 [7], rubidium-85 [8] and potassium-39 [9]. Recently, an experiment in ytterbium by Yamazaki *et al* [10] applied a pulsed optical standing wave to spatially vary the scattering length by the use of an optical Feshbach resonance, providing a control of collisional properties on a sub-micron scale. A general review of ultracold collisions is presented by Julienne [11].

Quantum degenerate gases

The unique advantages of ultracold physics can be related to two important attributes of ultracold ensembles that promote the quantum aspects of the gas over the classical behaviour: extremely narrow thermal widths and very large de Broglie wavelengths. If the gas is dense and the thermal motion suppressed, the de Broglie wavelength becomes comparable to the distance between the atoms and a quantum degenerate gas is formed. For bosonic species the degenerate gas condenses into a macroscopic coherent quantum system known as a Bose-Einstein condensate (BEC). Much research has been undertaken to understand and exploit the coherence features of these condensates for a range of different atomic species. A BEC can be used to trap light [12], create atom lasers [13] and produce many other features that were previously thought to be restricted to the domain of electromagnetic waves.

Real-world materials are incredibly complicated systems that require significant effort to manipulate their behaviour in order that desirable behaviour such as semiconductivity or superconductivity can be generated. On the other hand, Bose condensates and quantum degenerate Fermi gases provide unique oppourtunities to study the physical properties of these many-body systems through the trapping of particles within optical lattices which then mimic the Hamiltonian of the more complicated system [14, 15]. The overwhelming benefit of these model condensed-matter systems, due to their highly configurable nature, is the ability to investigate the entire parameter space of the Hamiltonian. Details such as interaction strength, lattice spacing and hopping strength can be tuned by the use of resonances, trap geometry or laser-coupled quantum states with techniques that are far more precise, reliable and easier to implement than the manipulations required in solid-state experiments, such as doping of a crystal or compression at high pressure. These quantum degenerate gases demonstrate a rich variety of phases, that go well beyond standard textbook theory of analogous solid state systems. For example, due to the presence of local interactions between particles at the same site, strongly-correlated phases can be observed. In one case, this results in the Mott insulator phase transition [16] that arises from repulsive interactions between particles and does not rely on a filled valence band to provide insulating behaviour. Effects such as Anderson localisation that is caused by weak to strong disorder, a structure that is always present in real-world systems, can also be experimentally investigated through the use of random speckle potentials [17] or photonic lattices [18]. Recent advances in experimental technique have even provided the ability for single-site detection and preparation of bosonic condensates [19], and fermionic systems [20]. Furthermore, model systems in optical lattices can simulate gauge fields [21, 22] that are described by effective Hamiltonians with magnetic flux and spin-orbit coupling. These systems can produce exotic phases such as topological insulators [23] that allow for a quantum spin Hall effect in which the bulk of the material remains insulating yet the boundaries allow for charge or spin currents that are insensitive to impurities. See Bloch *et al* [24] for a general review of many-body physics in optical lattices.

Quantum degenerate Fermi gases have been investigated experimentally in a range of confinement geometries and theoretically with a large variety of different interactions. Due to their similarity to electron behaviour within real-world materials, there is a great deal of interest in the detailed understanding of degenerate Fermi gases. The fundamental difference between bosonic and fermionic systems lies with their symmetric and antisymmetric natures, respectively. This manifests itself in the Pauli exclusion principle for fermions, in which no two particles may be present in the same state. However, fermions may also join to form bosonic composites in a process termed Bardeen-Cooper-Schrieffer (BCS) pairing, which has shed much light upon the origin of superconductivity and even allows for a BEC-like state that can even be formed using fermionic atoms [25]. Furthermore, bosonic systems can be made to behave in a fermionic manner, by tuning their same-species interaction to become so large that an effective 'hard-core' constraint is effected that mimics the Pauli exclusion principle. This permits the differences due to exchange interactions between particles to be investigated in great detail. The combination of Bose-Fermi mixtures also provide a unique insight into exotic phases such as supersolid behaviour [26].

Rubidium was the first species successfully used to form a Bose-Einstein condensate in 1995 by Anderson *et al* [27]. Condensates have since been created in several alkali metals: lithium by Bradley *et al* [28], sodium by Davis *et al* [29] and potassium by Modugno *et al* [30] as well as hydrogen by Fried *et al* [31]. Condensates have also been observed in alkali earth metals such as calcium by Kraft [32] and strontium by Stellmer *et al* [33]. BECs have also been formed in ytterbium by Takasu *et al* [34], chromium by Griesmaier *et al* [35], cesium by Weber *et al* [7] and metastable helium, by two groups in close succession, Robert *et al* [36] and Pereira Dos Santos *et al* [37]. The 2001 Nobel Prize in Physics was awarded to Eric Cornell, Wolfgang Ketterle and Carl E. Wieman for their contributions that lead to the creation of atomic BECs.

1.2 PHOTOASSOCIATION

Photoassociation (PA) is the process of resonant excitation of a pair of colliding atoms in the presence of a radiation field to a molecular bound level via a free→bound transition that creates a molecule in the excited state. Because the laser field shifts the excited state into resonance with the scattering state, the process can be considered to be an optical Feshbach resonance. The PA process was first suggested by Thorsheim *et al* [38] and was first measured from an associative ionisation process by Gould *et al* [39] in a gas of sodium at approximately 1 K. In experiment, PA spectroscopy scans a probe laser across a range of detuning from the asymptotic excited state energy. This spectroscopy is very precise because the thermal distribution is negligible compared to the line width of the PA transition and measurements made from scattering collisions can reach even sub-kHz precision. The initial scattering state of the PA process also makes possible the excitation of purely long-range molecules [40] that may be described entirely by well known long-range interactions. A general review of photoassociation research is presented by Jones *et al* [41] and a review of the formation of cold molecules is presented by Dulieu and Gabbanini [42].

Experimental studies

Many different atomic species have been investigated using PA and other related processes. The majority of these are ground state species, dominated by the alkali-metal species [41] that possess a single active electron. Other species, such as the alkali-rare-earth series [43, 44] and combinations of mixed species such as RbCs [45] have also been experimentally investigated. PA is often used to perform precise measurements on atomic properties such as radiative lifetimes, see Bouloufa *et al* [46] and references therein. Ultra-fast dynamics of the photoassociation system at femtosecond [47, 48] or attosecond [49] timescales have also been investigated and detailed control of the photoassociation process has been made possible, including techniques to limit the loss rates of the process. Two-colour PA configurations allow even further manipulation of atomic ensembles and can access ground state molecules such as the association of Na_2, performed by Jones *et al* [50], or allow for high precision determination of the scattering length, as performed by Kitagawa *et al* [51].

Theoretical studies

Several theoretical formalisms have been developed for describing the dynamics of the photoassociation process. The generalised PA problem with many resonant lasers has been treated semi-analytically by Bohn and Julienne [52] by making use of the concepts of quantum defect theory. Line shapes and scattering properties can be calculated from their formulation, but a perturbative treatment was invoked for the laser coupling and this coupling was assumed to vanish at large interatomic distance. Simoni *et al* [53] calculated line shapes in rubidium for arbitrary laser intensity, but also assumed that the laser coupling was negligible at asymptotic separations so that their asymptotic equations became uncoupled. Napolitano [54] presented a theory for the semi-analytic calculation of S-matrix elements and PA profiles in a sodium system which made use of dressed states to correctly treat the asymptotic laser coupling. However, the detuning was assumed to be large compared to the laser intensity and fine structure was not included in the formalism. Montavão and Napolitano [55] then extended the formalism of [54] to allow for a fully three dimensional collision process and then calculated line shapes of strontium for high laser intensity.

The dynamics of PA has also been investigated in Bose-Einstein condensates where the many body interactions can be highly influenced by the laser coupling [56, 57]. Trapping effects also play a significant role in modifying PA spectra, as shown by the calculations of Deb and You [58] and Grishkevich *et al* [59]. Finally, theoretical studies of photoassociation involving mixed species, such as LiCs [60] and KRb [61], have been performed.

1.3 Metastable Helium

This thesis focuses on the metastable form of the atomic species of helium, often written as He*. Metastable helium is unique amongst all other atomic species that have been condensed as it is in an excited state, the $1s2s$ atomic state. The natural lifetime of He* is nearly two hours [62], which is the longest of any excited atomic state. The interactions of He* are similar to that of alkali species, as He* has only one valence electron, but there are many distinct features for which He* provides significant advantages. The ease of detection of the atom and its related processes is due to the large 19.82 eV internal electronic energy of the $2s$ electron. For example, an individual He* atom colliding with a surface will invariably release a high energy electron in the process which can be captured by a detector such as an electron multiplier with near 100% probability. As well, He* can autoionise via the processes of Penning and associative ionisation:

$$\begin{aligned} &\mathrm{He}^* + \mathrm{He}^* \to \mathrm{He} + \mathrm{He}^+ + e^- && \text{Penning ionisation} \\ &\mathrm{He}^* + \mathrm{He}^* \to \mathrm{He}_2^+ + e^- && \text{Associative ionisation} \qquad (1.1) \end{aligned}$$

These processes provide very useful mechanisms to probe the behaviour of the gas. On the negative side, these ionisation processes are inelastic processes that can be regarded as undesirable aspects that introduce loss from the system. Fortunately, the resultant high energy products of the ionisation are not trapped under the same conditions as the metastable helium atoms, so there is minimal contamination of the trapped gas. Of the two common isotopes of helium, this thesis analyses the behaviour of helium-4 which has no net nuclear spin. This is of enormous benefit when compared to other atomic species, as it means the complicated interactions arising from hyperfine structure are avoided. Unfortunately, fewer opportunities are available for magnetic tuning of Feshbach resonances. A detailed discussion of the advantages of studying metastable helium in ultracold physics is presented by Baldwin [63].

Metastable helium is cooled in a multi-step process. Initially, a gas of ground state helium is cooled to temperatures below 100 K by thermalisation with liquid nitrogen or a similar technique. An electric discharge is then used to impart energy to the atoms and those which undergo a transition to the metastable state are sent through a Zeeman slower. The Zeeman slower exploits the momentum of photons to slow the beam of atoms and does this optimally by using the magnetic Zeeman shift to counteract the Doppler shift of the photon that the helium atom sees from its rest frame of reference. After exiting the Zeeman slower, at a speed of approximately 40 m/s and temperature of < 1 K, the atoms are trapped in a magneto-optical trap (MOT) that makes use of three pairs of counter-propagating lasers detuned from an appropriate transition. The spatial variation of the magnetic field in the MOT then promotes absorption from one particular laser of each pair depending on the position of the atom in the trap. This trap not only contains the atoms, but further cools them to mK temperatures. MOT cooling below this temperature, however, is not possible because of the Doppler recoil limit. Further cooling takes place using an optical molasses [3], and then to reach the temperatures required for Bose-Einstein condensation requires the gas to be transferred into a purely magnetic trap. The atoms are cooled evaporatively in this trap by regularly lowering the trapping potential so that the most energetic atoms escape, thus decreasing the average temperature of the gas. High elastic collision rates are important in this process as the gas must quickly thermalise after the trap potential has been re-raised. To achieve a high density of atoms confined in the gas, inelastic loss rates must be small throughout the entire cooling process. The largest contributions to inelastic losses are the ionisation processes described above and these can be suppressed by five orders of magnitude [64] by spin-polarising the gas. The polarisation of the gas is performed by using a magnetic field gradient that only traps those atoms whose spin is aligned in a particular direction. Every atom in the gas will then have spins aligned and so can only collide in the ‘spin stretched’ state: the molecular state with maximal combined spin. For ionisation to occur in this stretched state, a spin flip is required due to the Pauli exclusion principle and so the process is heavily suppressed. Further details of cooling and slowing processes for metastable helium may be found in [65, 66, 67].

1.4 EXPERIMENTAL STUDIES OF METASTABLE HELIUM

Photoassociation

Photoassociation experiments of metastable helium-4 have observed a number of resonance peaks near the three asymptotes $j = 0, 1, 2$ of the excited state $2\,^3S_1 + 2\,^3P_j$. Herschbach *et al* [68] first found peaks near the $j = 2$ dissociation limit and, more recently, Kim *et al* [67] and van Rijnbach [66] have added to the observations such that over 40 peaks with binding energies ≤ 14 GHz are known near this limit. In addition, van Rijnbach observed six levels near the $j = 1$ dissociation limit and Kim *et al* observed five purely long-range levels near the $j = 0$ dissociation limit. These observations to the different dissociation limits were first analysed approximately by the experimental groups themselves using the accumulated phase method [69], in the absence of short-range electronic potentials. The accuracy of these approximate assignments requires further investigation and validation using detailed multichannel calculations. Kim *et al* [70] also studied the effect of laser intensity on the PA resonance line shapes of long-range levels near the $j = 0$ asymptote. From their theoretical analysis, bounds could be placed on the value of the scattering length by the linear dependence of the line shift on intensity.

Precision measurements

Many experiments in He* seek to accurately determine the value of the scattering length. Seidelin *et al* [71] were able to make an estimate based upon the variation of ionisation rates as a gas is condensed during evaporative cooling and Tol *et al* [72] performed a measurement using a similar technique. The most accurate determination to date is that of Moal *et al* [73] who used a two-photon experiment and calculated the scattering length to be $a = 7.512 \pm 0.005$ nm from the position of a dark resonance in their spectra. Of interest to photoassociation experiments are the decay rates of the excited states, and a series of precise measurements has been performed for the $2\,^3P_1$—$1\,^1S_0$ transition by Dall *et al* [74], the $2\,^3P_j$—$2\,^3S_1$ transitions by Hodgman *et al* [75] and the $2\,^3S_1$—$1\,^1S_0$ transition that governs the metastable lifetime by Hodgman *et al* [62].

Ionisation rates

Knowledge of ionisation rates is crucial to ultracold He* experiments because the ionisation processes (1.1) can dominate He* experiments. Stas *et al* [76] have made detailed measurements of the ionisation rates in both helium-3 and helium-4 gases. Koelemeij *et al* [77] observed the strength of ionisation in excited $2s2p$ and $2s3p$ levels of He*, which are used for optical manipulation. Ionisation also limits the lifetime of the weakly bound He_2^* molecules but the observations by Moal *et al* [78] are in disagreement with the theory of Beams *et al* [79]. The loss rates in helium-4 condensates can be almost totally attributed to the ionisation rates and Sirjean *et al* [80] have determined two- and three-body contributions to the loss rate.

Fermi-Bose combinations

The use of two-colour laser traps makes possible the containment of both fermionic helium-3 and bosonic helium-4 in a degenerate Bose-Fermi mixture, as performed by McNamara *et al* [81]. The group has measured ionisation rates resulting from hetero-nuclear collisions in the dual condensate system [82]. Goosen *et al* [83] have performed a theoretical calculation that predicts the existence of a large exploitable Feshbach resonance between the hetero-nuclear pairs which they aim to experimentally investigate in the coming years. The measurement of correlations between thermal fermionic helium-3 and bosonic helium-4 gases by Jeltes *et al* [84] has demonstrated the Hanbury Brown-Twiss effect that was originally observed in chaotic light sources for atomic ensembles. The experiment revealed a bunching and anti-bunching effect for bosonic and fermionic gases respectively due to the quantum statistics of the gases.

1.5 THEORETICAL STUDIES OF METASTABLE HELIUM

Photoassociation

Theoretical calculations of photoassociation of metastable helium have mostly been limited to approximate perturbative techniques. Dickinson *et al* [85] computed *ab initio* short-range potentials for the $2s2p$ system and were able to make initial assignments to three quarters of the peaks observed in experiment by [66, 67, 68]. Deguilhem *et al* [86] then revisited these potentials by optimising the basis set to achieve convergence at smaller interatomic regions and were able to improve upon the assignments to the observed peaks. However, their assignments were based on approximate single-channel methods that omitted the effects of non-adiabatic and Coriolis couplings in the system. The purely long-range levels that have been observed by Kim *et al* [67] have been analysed by Leonard *et al* [87] to determine the binding energies and experimental uncertainties, and their theoretical values were calculated using approximate adiabatic potentials. The measurements of line shifts at different laser intensities made by Kim *et al* [70] have been analysed using second-order perturbation theory by Portier *et al* [88] and, from these results, bounds were placed upon the scattering length of the metastable system. Koelemeij *et al* [89] have considered the use of photoassociation in manipulating scattering lengths by expanding upon the model described by Bohn and Julienne [52].

Only two multichannel calculations exist of PA in metastable helium. Venturi *et al* [90] performed a detailed multichannel theoretical calculation that showed that the adiabatic approximation is very good for the calculation of binding energies of purely long-range levels and van der Zwan *et al* [91] have modelled ionisation in the photoassociation process of metastable helium by calculating line shapes over a range of parameters in a simplified model system and have successfully compared their results to experimental measurements. Neither of these calculations describe the photoassociation dynamics under arbitrary laser intensity and both calculations were performed before the accurate short-range potentials

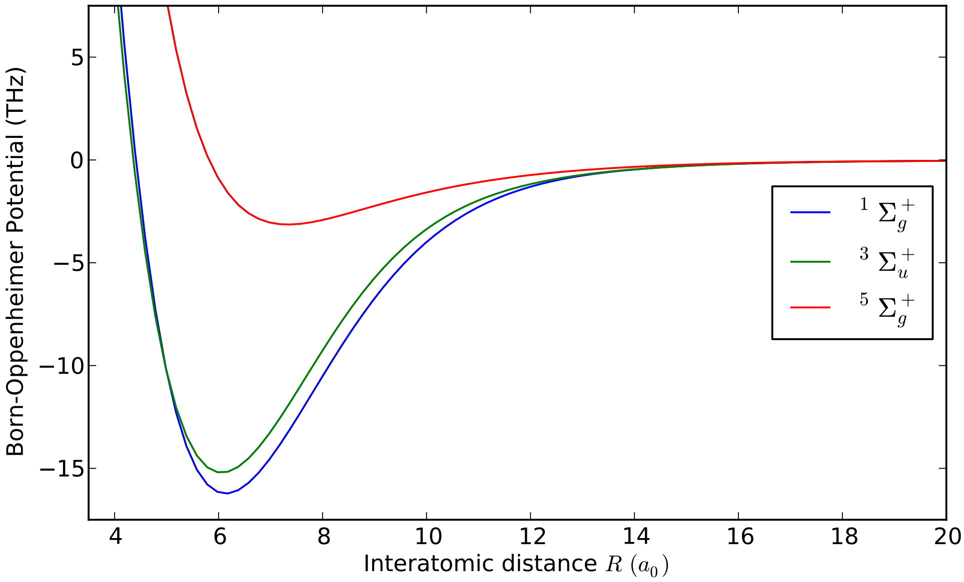

Figure 1.1: Born-Oppenheimer potentials of the $2s2s$ molecular level of helium. Units of THz (1 THz = 33.36 cm^{-1}) are used so as to conform with the majority of results presented in this thesis.

of [86] were available.

Although successful predictions have been made using the above approximate theories, a complete theoretical analysis of all the observed levels requires inclusion of all interaction terms in the system, the use of potentials accurate over the entire range of interatomic separation, and a full multichannel calculation which includes non-adiabatic and Coriolis couplings. This calculation forms a major part of this thesis.

Ab initio calculations

To perform calculations in metastable helium and its accessible excited states, several interaction potentials are required. For the He* interactions, the singlet and triplet potentials of Müeller [92] and the quintet potential of Przybytek and Jeziorski [93], which include relativistic and QED corrections, are available. These are shown in figure 1.1. The focus of this thesis is investigation of the levels belonging to the $2s2p$ system and the interaction potentials for this system have recently been calculated by Deguilhem *et al* [86]. The long-range interactions of the $2s2p$ system can be described by dipole-dipole and dispersion interactions that arise from well known atomic properties. In this thesis, the short-range potentials of [86] are matched to these long-range forms and are shown in figure 1.2.

Several theoretical studies have determined the scattering lengths of He* by purely *ab initio* processes. The works of Gadéa *et al* [94] and Dickinson *et al* [95] have calculated scattering lengths of spin-polarised He* in helium-3 and helium-4 combinations. The precise potentials calculated by Przybytek and Jeziorski [93] allowed them to make a very accurate determination of the least-bound quintet level and their potentials were used by

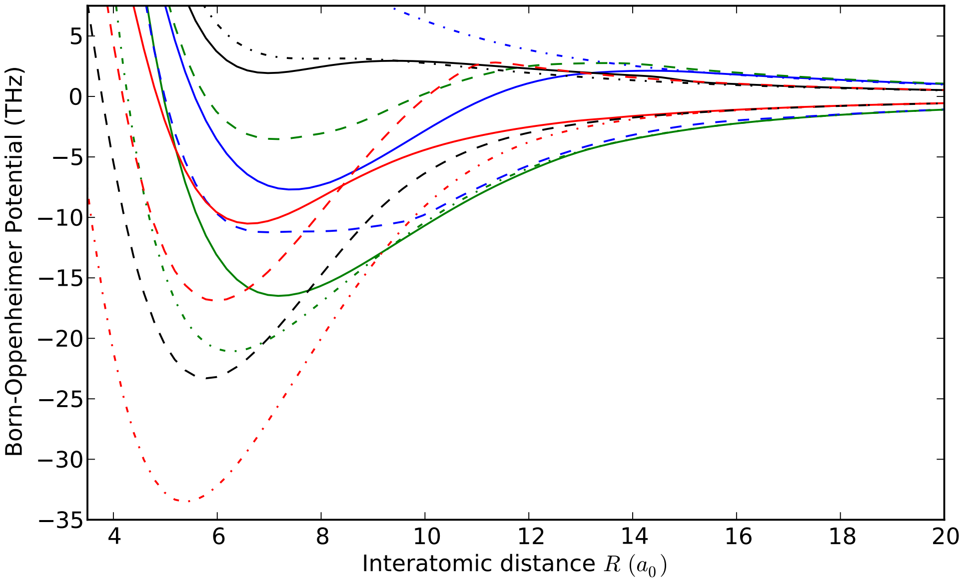

Figure 1.2: Potentials of the $2s2p$ molecular level of helium. The potentials consist of short-range *ab initio* potentials matched onto long-range dipole and dispersion potentials. The colour coding is as follows, blue: ${}^{2S+1}\Sigma_g^+$, green: ${}^{2S+1}\Sigma_u^+$, red: ${}^{2S+1}\Pi_g$, black: ${}^{2S+1}\Pi_u$. Lines marked with a solid line have $S = 0$, those with a dashed line $S = 1$ and those with a dash-dot line $S = 2$. Units of THz (1 THz = 33.36 cm^{-1}) are used so as to conform with the majority of results presented in this thesis.

Moal *et al* [73] to obtain the most accurate experimental value for the scattering length from their two-photon dark-resonance experiments.

Ionisation

Ionisation rates play a very important role in He* experiments and a large body of work has been devoted to calculating inelastic cross sections and methods to enhance or suppress these rates. Fedichev *et al* [96] used perturbation theory to calculate ionisation rates of spin-polarised helium for a range of temperatures and magnetic fields. Venturi *et al* calculated rates in field-free [97] and magnetostatically trapped [98] collisions using a multichannel calculation and varied the input potentials in order to place bounds on the ionisation rates. Beams *et al* [99] modelled very tightly trapped collisions to determine trap lifetimes due to ionisation losses using a perturbative theory [100] based upon their earlier quantum defect theory [101]. More recently Dickinson [102] used a quantum reflection model to determine ionisation rate coefficients for a range of temperatures and for different combinations of helium-3 and helium-4.

Combinations of spin states

The theoretical analysis of Leo *et al* [103] of metastable atoms colliding in different combinations of spin states predicted very different elastic and inelastic cross sections for particular spin combinations. These predictions have been confirmed by the experiments of Partridge *et al* [104] who observed characteristic combinations that persist in a thermal gas after a radio frequency sweep was made. The unequal scattering lengths for different spin combinations allowed Dall *et al* [105] to observe four-wave mixing in a He* condensate by paired atoms formed from collisions of the out-coupled atoms with the bulk condensate.

1.6 Aims and objectives of project

This thesis focuses on the calculation of the bound states and line shapes relevant to photoassociation of metastable helium to the $2\,^3S_1 + 2\,^3P_j$ level. As discussed above, a large body of work is available to assist with analysis of the system, but there exists no non-perturbative, non-approximate general treatment of PA resonance profiles for arbitrary laser intensity that may be applied to the helium system. As well, numerical calculations of bound states in metastable helium are mostly limited to single-channel perturbative approaches. The multichannel calculations that exist have not been performed using the recently calculated accurate short-range potentials of [86]. Hence, there is a need for a precise multichannel calculation to be performed for the metastable helium system.

The objectives of this thesis are:

- Perform a multichannel calculation which includes non-adiabatic and Coriolis couplings for photoassociation in metastable helium to the $2\,^3S_1 + 2\,^3P_j$ excited state.
- Undertake a comparison between these results and those of an approximate single-channel calculation to determine the accuracy of the various approximations.
- Use the detailed information available from the multichannel bound wave functions to make definite assignments to experimental data by developing unambiguous observability criteria.
- Perform a multichannel scattering calculation to determine the line shapes of the photoassociation resonances to purely long-range bound levels in the 0_u^+ potential near the $2\,^3S_1 + 2\,^3P_0$ asymptote. The formalism is to be valid for arbitrary laser intensities thus requiring a non-perturbative treatment of the laser coupling and its correct incorporation at asymptotic separation. Two procedures will be employed: a dressed-state formalism and a modified radiation coupling method.
- Test the validity of the dipole approximation to the laser coupling, especially for the case of long-range bound levels, by calculating photoassociation spectra using the full laser coupling without approximation.

1.7 Structure of thesis

This thesis comprises three major sections. Chapter 2 presents the formalism needed to describe metastable helium and the $2s2p$ system, and carefully considers the coupling schemes and Hamiltonian matrix elements that are required for the calculations reported in the remaining chapters of the thesis. The molecular basis to be used in the calculations must be chosen wisely, as a naive choice may lead to nearly intractable numerical problems further on in the calculations.

Chapter 3 discusses the calculation and identification of bound levels present in the $2\,^3S_1 + 2\,^3P_j$ system with focus upon those near the $j = 0, 1, 2$ asymptotes. Several calculations are presented, commencing with the most approximate and simplest method and layers of approximation are gradually removed until a complete multichannel calculation is achieved. This allows the evaluation of the effects from different interaction terms and tests the validity of the approximations. The results are then compared with experimental observations, and a set of criteria is formulated to allow a unique assignment of theoretical levels to those measured in experiment.

In chapter 4, the detailed dynamics of the photoassociation process is investigated for colliding metastable atoms to a particular set of purely long-range bound levels in the $2s2p$ state and the spectroscopic profiles for the configurations determined. An approximate calculation is first presented, followed by an accurate multichannel calculation valid for arbitrary laser intensities. The effects at high laser intensity are specifically investigated. Finally, the validity of the dipole approximation for the laser-matter coupling is analysed for shallow potentials, especially for photoassociation involving ultra-long range bound levels.

Several appendices present the more technical aspects of the symmetrisation of the molecular bases and the evaluation of matrix elements of the system Hamiltonian, detail some of the numerical methods and procedures used to perform the calculations, and provide a more complete tabulation of results.

Chapter 2

Formulation of basis states and matrix elements

2.1 HAMILTONIAN

A precise definition of the Hamiltonian is required to perform calculations on the quantum mechanical system of two atoms, whether they are in a scattering state or are bound to one another. The two-body system is described by the coordinates of the nuclei $\boldsymbol{r}_{A,B}^N$, where A and B label the nuclei, and the electronic coordinates $\boldsymbol{r}_i$. For the electronic configurations investigated in this thesis $i = 1, 2$ labels the outermost electrons (in either the $2s$ or $2p$ orbitals) and $i = 3, 4$ labels the innermost $1s$ electrons. For convenience, the origin of the coordinate system is placed at the centre of mass of the system which is also the centre of charge for the two helium-4 atoms. The equations of motion are reduced to an equivalent single body problem by separating the centre of mass motion, which is unaffected by molecular interactions, from the relative motion that describes the vibration of the nuclei. In the single body problem the reduced mass of the system $\mu = m_1 m_2/(m_1 + m_2)$ is $m/2$ for helium-4, where both bodies have identical mass $m_1 = m_2 = m = 4.002603$ amu. In this description, the radial variable, $R = |\boldsymbol{r}_B^N - \boldsymbol{r}_A^N|$, is the interatomic separation of the two atoms.

The Hamiltonian that describes the two atom helium-4 system is given by

$$\begin{aligned}\hat{H}_{\text{mol}} &= \hat{T}_{\text{n}} + \hat{H}_{\text{el}} + \hat{H}_{\text{fs}} \\ &= \hat{T}_R + \hat{H}_{\text{rot}} + \hat{H}_{\text{el}} + \hat{H}_{\text{fs}},\end{aligned} \tag{2.1}$$

where $\hat{T}_{\text{n}} = \hat{\boldsymbol{p}}^2(\boldsymbol{R})/2\mu$ is the kinetic energy associated with the nuclear vibrational and rotational motion of the reduced system, which can be further decomposed into a radial component $\hat{T}_R$ and a rotational component $\hat{H}_{\text{rot}} = -\hat{l}^2/2\mu R^2$ where $\hat{l}$ is the rotational angular momentum operator of the nuclei. The electronic Hamiltonian, $\hat{H}_{\text{el}} = \hat{H}_A + \hat{H}_B + \hat{H}_{AB}$ includes the atomic Hamiltonians $\hat{H}_k$, $k = A, B$, and the electrostatic interaction $\hat{H}_{AB}$ between the atoms. The relativistic corrections to the metastable helium system require the introduction of the fine-structure Hamiltonian $\hat{H}_{\text{fs}}$ which contains couplings between the orbital and spin angular momenta of the individual atoms. No hyperfine structure is present in helium-4 as there is no net nuclear spin.

When the molecular system is also coupled to a laser field, the inclusion of the radiation field Hamiltonian, $\hat{H}_{\text{rad}}$, and the interaction term, $\hat{H}_{\text{int}}$, are required. This enlarges the total Hamiltonian so that it becomes

$$\hat{H} = \hat{H}_{\text{mol}} + \hat{H}_{\text{rad}} + \hat{H}_{\text{int}}. \tag{2.2}$$

To apply the Hamiltonians $\hat{H}_{\text{mol}}$ or $\hat{H}$ in calculations, matrix elements must be formed from the inner product of $\hat{H}_{\text{mol}}$ between two molecular basis states. However, different bases cause matrix elements of different terms of the Hamiltonian to become diagonal, so the choice of which molecular basis to be used to describe the system must be made carefully. The molecular basis must also be able to accommodate the couplings introduced by the laser interaction term. Each term of the complete Hamiltonian of the system containing the two atoms and laser is described in more detail below.

2.1.1 Electronic Hamiltonian

The electronic Hamiltonian, $\hat{H}_{\text{el}} = \hat{H}_A + \hat{H}_B + \hat{H}_{AB}$, represents the electronic motion and all of the electrostatic interactions between the electrons and nuclei of each atom. Explicitly, the atomic Hamiltonians are given by

$$\hat{H}_k = \sum_{i\in k}\left[\frac{\hat{\boldsymbol{p}}^2(\boldsymbol{r}_i)}{2m_e} - \frac{Ze^2}{4\pi\epsilon_0|\boldsymbol{r}_i - \boldsymbol{r}_k^N|} + \sum_{j>i}\frac{e^2}{4\pi\epsilon_0|\boldsymbol{r}_i - \boldsymbol{r}_j|}\right] \tag{2.3}$$

where the notation $i \in k$ indicates the sum is over the two electrons that are orbiting nucleus k, and the electrostatic interaction is

$$\hat{H}_{AB} = \frac{Z^2e^2}{4\pi\epsilon_0|\boldsymbol{r}_A^N - \boldsymbol{r}_B^N|} + \sum_{\substack{k=\{A,B\}\\ i\notin k}}\frac{-Ze^2}{4\pi\epsilon_0|\boldsymbol{r}_i - \boldsymbol{r}_k^N|} + \sum_{\substack{i\in A\\ j\in B}}\frac{e^2}{4\pi\epsilon_0|\boldsymbol{r}_i - \boldsymbol{r}_j|} \tag{2.4}$$

where $i \notin k$ ensures the sum is over the two electrons that are not orbiting nucleus k and $Z = 2$ is the proton number of the helium nucleus. The action of $\hat{H}_{\text{el}}$ is difficult to deal with exactly, so the Born-Oppenheimer (BO) approximation [106] is imposed which decouples the nuclear motion from the electronic motion. In the BO approximation, the electrostatic interactions of the dimer are calculated by considering the nuclei to be fixed at an interatomic distance R and the electronic wave function determined without consideration of the nuclear motion. The interatomic separation is then varied as a parameter of the electronic interaction to build up the electronic potential as a function of R. This allows the basis states of the molecular system to be represented in the form $F(R)|a\rangle$ where $F(R)$ is the vibrational wave function and $|a\rangle$ is the electronic and rotational state which may be treated as independent of R (but may still depend upon the orientation of $\hat{\boldsymbol{R}}$).

The BO approximation is only valid if the nuclear motion is much slower than the motion of the electrons such that the electronic distribution can be considered able to instantaneously adapt to the varying interatomic distance. At room temperatures, this validity criterion is normally expressed using the mass ratio between the electron and the nucleus, which is small even for the light-weight nucleus of helium-4. Furthermore, the ultracold temperatures of the system under investigation in this thesis suggest that the nuclear motion is many magnitudes smaller than the electronic motion. In the BO approximation, $\hat{H}_{\mathrm{el}}$ satisfies an eigenvalue equation of the form

$$\hat{H}_{\mathrm{el}}|\Lambda^{\sigma} S w\rangle = \left[E^{\infty} + {}^{2S+1}\Lambda_{w}^{\sigma}(R)\right]|\Lambda^{\sigma} S w\rangle \tag{2.5}$$

where ${}^{2S+1}\Lambda_{w}^{\sigma}(R)$ are known as the BO potentials and E^{∞} is the asymptotic energy of the state. The states $|\Lambda^{\sigma} S w\rangle$, also known as Hund's case (a) states [106], are labelled by the absolute value of the projection of the total orbital angular momentum along the intermolecular axis Λ, the total spin S, the symmetry w under electronic inversion through the centre of charge, and the symmetry σ under reflection of the electronic wave function through a plane containing the intermolecular axis which only exists for $\Lambda = 0$. The basis states best used to describe $\hat{H}_{\mathrm{el}}$ must then combine the atomic orbital angular momenta $\boldsymbol{L}_1$, $\boldsymbol{L}_2$ and spin angular momenta $\boldsymbol{S}_1$, $\boldsymbol{S}_2$ to form $\boldsymbol{L} = \boldsymbol{L}_1 + \boldsymbol{L}_2$ and $\boldsymbol{S} = \boldsymbol{S}_1 + \boldsymbol{S}_2$ respectively.

In this thesis, the BO equations that result from the action of operators (2.3) and (2.4) are not solved. Instead, input data for the BO potentials is obtained from several sources. The three metastable $2s2s$ potentials are taken from Müeller *et al* [92] for the ${}^{1}\Sigma_{g}^{+}(R)$ and ${}^{3}\Sigma_{u}^{+}(R)$ potentials and the ${}^{5}\Sigma_{g}^{+}(R)$ potential is taken from the calculation of Przybytek and Jeziorski [93] which includes adiabatic, relativistic, and QED corrections. The $2s2p$ manifold is described by the recently available short range multi-configuration self-consistent field (MCSCF) ${}^{1,3}\Sigma_{g,u}^{+}$ and ${}^{1,3}\Pi_{g,u}$ potentials and short-range multi-reference configuration interaction (MRCI) ${}^{5}\Sigma_{g,u}^{+}$ and ${}^{5}\Pi_{g,u}$ potentials of Deguilhem *et al* [86], matched onto long-range retarded dipole-dipole and dispersion potentials using parameters supplied by either Marinescu [90] or Zhang *et al* [107]. These long-range potentials have the form

$$-f\left(\frac{R}{\lambdabar}\right)\frac{C_3}{R^3} - \frac{C_6}{R^6} - \frac{C_8}{R^8} \tag{2.6}$$

for the parameters of Marinescu, and

$$-f\left(\frac{R}{\lambdabar}\right)\frac{C_3}{R^3} - \frac{C_6}{R^6} - \frac{C_8}{R^8} - \frac{C_9}{R^9} - \frac{C_{10}}{R^{10}} \tag{2.7}$$

for the parameters of Zhang *et al*, where

$$f(x) = \begin{cases} \cos x + x\sin x & \text{for} \quad \Lambda = \Sigma \\ \cos x + x\sin x - x^2\cos x & \text{for} \quad \Lambda = \Pi \end{cases} \tag{2.8}$$

is a retardation correction factor [108] and $\lambdabar = \lambda/(2\pi) = 3258.17\,a_0$ where λ is the $2s \to 2p$ transition wavelength [109]. Because long-range molecules are investigated in this thesis,

Table 2.1: The parameters for the $2s2p$ long-range retarded dipole and dispersion interactions taken from Marinescu [110], where $C_{3\Pi} = 6.41022\ E_h a_0^3$. S is the total spin and $w = 0, 1$ is the even or odd inversion symmetry of the dimer.

Λ	C_6 ($E_h a_0^6$)	$(-1)^{S+w}$	C_3	C_8 ($E_h a_0^8$)
Σ	2620.76	$+1$	$-2C_{3\Pi}$	1.515383×10^6
		-1	$2C_{3\Pi}$	2.972159×10^5
Π	1846.60	$+1$	$C_{3\Pi}$	9.724475×10^4
		-1	$-C_{3\Pi}$	1.627638×10^5

Table 2.2: The parameters for the $2s2p$ long-range retarded dipole and dispersion interactions taken from Zhang *et al* [107] where $C_{3\Pi} = 6.4090875603\ E_h a_0^3$. S is the total spin and $w = g, u = 0, 1$ is the even or odd inversion symmetry of the dimer.

Λ	C_6 ($E_h a_0^6$)	w	C_8 ($E_h a_0^8$)	C_9 ($E_h a_0^9$)	C_{10} ($E_h a_0^{10}$)
Σ	2641.5083	g	311955.4	512572.343	2.922304×10^7
		u	1542352	-512572.343	1.8574503×10^8
Π	1863.4726	g	168921.6	-117199.211	1.611325×10^7
		u	103039.5	117199.211	2.40608×10^6

Λ	$(-1)^{S+w}$	C_3
Σ	$+1$	$-2C_{3\Pi}$
	-1	$2C_{3\Pi}$
Π	$+1$	$C_{3\Pi}$
	-1	$-C_{3\Pi}$

the effects of retardation can be significant. The Marinescu parameters for C_n are listed in table 2.1 and the Zhang *et al* coefficients in table 2.2. Although the Zhang *et al* coefficients represent the latest and most accurate calculations, the coefficients of Marinescu will be used in most of the calculations undertaken in this thesis so that the results can be validated against existing values that have been calculated using the Marinescu coefficients.

The short-range $2s2p$ ${}^{1,3}\Sigma^+_{g,u}$ and ${}^{1,3}\Pi_{g,u}$ potentials are tabulated out to an interatomic distance of $30\,a_0$ and the ${}^5\Sigma^+_{g,u}$ and ${}^5\Pi_{g,u}$ potentials to $100\,a_0$. The matching to the long-range potentials occurs at this outer tabulated point, R_m, by vertically shifting the short-range potentials so that they equal the long-range potential energy. Although the derivatives are well connected between the short-range and long-range forms at this point, a spline fit to the shifted short-range potentials was performed for $R \leq R_\mathrm{m} + 3\,a_0$ using additional points $R_\mathrm{m} + n\,a_0$, where $n = 1, 2, 3$, from the long-range potentials to obtain a smoother matching. The long-range analytical form (2.6) was used for $R > R_\mathrm{m} + 3\,a_0$.

The short-range potentials are tabulated into the classically forbidden region for small interatomic distances but some variation of binding energies is observed with different forms of extrapolation to $R = 0$. An extrapolation of the form

$$\frac{1}{R} + A + BR^2 \tag{2.9}$$

is used [111], to emulate the expected behaviour for small interatomic distances [112]. The constants A and B are determined by matching to the first two tabulated values of the MCSCF and MRCI potentials and are shown in table 2.3.

Table 2.3: Values for A and B coefficients of the extrapolation of the BO potentials for the $2s2p$ manifold towards the origin using equation (2.9).

Case (a) Label	A (E_h)	B ($\times 10^{-3}$ E_h/a_0^2)
$^1\Sigma_g^+$	-0.227	1.51
$^1\Sigma_u^+$	-0.210	25.2
$^1\Pi_g$	-0.339	8.14
$^1\Pi_u$	-0.350	0.116
$^3\Sigma_g^+$	-0.207	64.2
$^3\Sigma_u^+$	-0.323	8.40
$^3\Pi_g$	-0.334	6.63
$^3\Pi_u$	-0.397	0.108
$^5\Sigma_g^+$	-0.194	92.9
$^5\Sigma_u^+$	-0.174	-5.00
$^5\Pi_g$	-0.373	6.29
$^5\Pi_u$	-0.305	7.09

2.1.2 Relativistic correction Hamiltonian

The only relativistic corrections relevant to helium-4 are the fine-structure terms; no hyperfine structure is present as helium-4 has no net nuclear spin. The atomic fine-structure Hamiltonian can be calculated to a very high degree of accuracy by using explicit QED forms, however here it shall be represented simply by the operator $\hat{H}_{\mathrm{fs},\alpha}$ and its action by the observed splittings from experiment. The fine-structure corrections are dependent upon the orbital (L_α), spin (S_α) and total (j_α) angular momenta of each atom, where $\alpha = 1, 2$. Provided these momenta remain approximately good quantum numbers (i.e. they are conserved for all intermolecular distances R between the atoms) then the operator may simply be considered the sum of the fine-structure terms for the individual atoms, $\hat{H}_{\mathrm{fs}} = \hat{H}_{\mathrm{fs},1} + \hat{H}_{\mathrm{fs},2}$. The eigenvalues of $\hat{H}_{\mathrm{fs}}$ are therefore $\Delta E^{\mathrm{fs}}_{\gamma_1 j_1} + \Delta E^{\mathrm{fs}}_{\gamma_2 j_2}$where the atomic fine-structure splittings are given by $\Delta E^{\mathrm{fs}}_{\gamma_\alpha j_\alpha}$.

For the metastable state, which has orbital angular momenta of zero, there is no fine-structure splitting and this term vanishes. For the excited $1s2p$ triplet level under investigation in this thesis however, the splittings are present and inverted with the $j_\alpha = 1$ level lying 29.6169 GHz below the $j_\alpha = 0$ level and the $j_\alpha = 2$ level lying 31.9081 GHz below the $j_\alpha = 0$ level [109].

2.1.3 Kinetic term

The kinetic term represents the vibrational and rotational motion of the nuclei and is $\hat{T}_{\mathrm{n}} = \hat{\boldsymbol{p}}^2(\boldsymbol{R})/2\mu$, where $\hat{\boldsymbol{p}}(\boldsymbol{R}) = -i\hbar\nabla(\boldsymbol{R})$. This term can be separated into a radial part

$$\hat{T}_R = -\frac{\hbar^2}{2\mu R}\frac{\partial^2}{\partial R^2}R \tag{2.10}$$

and a rotational part $\hat{H}_{\mathrm{rot}} = \hat{l}^2/2\mu R^2$, where $\hat{l}$ is the rotational angular momentum of the molecule. In order to simplify the action of $\hat{T}_R$ upon the basis $F(R)|a\rangle$ described in section

2.1.1, the radial function will be written $F(R) = R^{-1}G(R)$. The radial kinetic term has the action

$$\hat{T}_R \frac{1}{R} G_a(R)|a\rangle = -\frac{\hbar^2}{2\mu R}\left(\frac{d^2G_a}{dR^2}|a\rangle + 2\frac{dG_a}{dR}\frac{d|a\rangle}{dR} + G_a\frac{d^2|a\rangle}{dR^2}\right). \tag{2.11}$$

If the angular momentum basis states are assumed to have negligible variation with respect to R, a valid assumption for the large interatomic distances considered in this thesis, then this expression simplifies to

$$\hat{T}_R \frac{1}{R} G_a(R)|a\rangle = -\frac{\hbar^2}{2\mu R}\frac{d^2G_a}{dR^2}|a\rangle, \tag{2.12}$$

and the matrix element $\langle a'|\hat{T}_R R^{-1} G_a|a\rangle$ is diagonal. The use of approximate single-channel basis states, however, does not permit the reduction to (2.12), due to the R-dependence of the adiabatic behaviour. The action of $\hat{T}_R$ upon these states will be discussed later in section 3.2.2.

The rotational part of the kinetic term contains $\hat{l}$ and so forms diagonal matrix elements in bases with the quantum number l. Only small values of l are relevant in ultracold collisions because atoms with small kinetic energies cannot overcome the relatively large centrifugal barriers. Hence, most of the dynamics occurs in the s- and p-wave collisional channels.

2.1.4 Laser field Hamiltonian

The energy of the radiation field is represented by the Hamiltonian $\hat{H}_{\text{rad}} = \sum_\xi \hbar\omega_\xi \hat{a}_\xi^\dagger \hat{a}_\xi$ where $\hat{a}_\xi^\dagger$ and $\hat{a}_\xi$ are the creation and annihilation operators for a photon of frequency ω_ξ and polarisation $\boldsymbol{\epsilon}_\xi$. The basis states for a polarised laser field of n_ξ photons are

$$|n_\xi, \omega_\xi, \boldsymbol{\epsilon}_\xi\rangle = \frac{1}{n!}(a_\xi^\dagger)^{n_\xi}|\text{vac}\rangle \tag{2.13}$$

and so the action of $\hat{H}_{\text{rad}}$ upon these states is

$$\hat{H}_{\text{rad}}|n_\xi, \omega_\xi, \boldsymbol{\epsilon}_\xi\rangle = n_\xi \hbar\omega_\xi |n_\xi, \omega_\xi, \boldsymbol{\epsilon}_\xi\rangle. \tag{2.14}$$

2.1.5 Laser interaction term

The coupling between the molecular states and the laser field is given by

$$\hat{H}_{\text{int}} = -\left(\frac{e}{m}\right)\sum_{i=1,2} \hat{\boldsymbol{p}}_i \cdot \hat{\boldsymbol{A}}(\boldsymbol{r}_i) \tag{2.15}$$

where $\hat{\boldsymbol{p}}_i = -i\hbar\boldsymbol{\nabla}(\boldsymbol{r}_i)$ and the vector potential $\hat{\boldsymbol{A}}(\boldsymbol{r}_i)$ is

$$\hat{\boldsymbol{A}}(\boldsymbol{r}_i) = \sum_\xi \left[\mathcal{E}_\xi(\boldsymbol{r}_i)\hat{a}_\xi + \mathcal{E}_\xi^*(\boldsymbol{r}_i)\hat{a}_\xi^\dagger\right]. \tag{2.16}$$

Here,

$$\mathcal{E}_\xi(\boldsymbol{r}_i) = \sqrt{\frac{\hbar}{2\omega_\xi \epsilon_0 \mathcal{V}}} e^{i\boldsymbol{k}\cdot\boldsymbol{r}_i} \boldsymbol{\epsilon}_\xi, \tag{2.17}$$

where the wave vector $\boldsymbol{k}$ of the laser field has magnitude ω_ξ/c and $\mathcal{V}$ is the normalisation volume. Note that only the outer electrons, $i = 1, 2$ are considered in the interaction and it is assumed that the inner electrons, $i = 3, 4$ remain unaffected by transitions of the outer electrons to excited states.

The dipole approximation, $\exp(i\boldsymbol{k} \cdot \boldsymbol{r}_i) \approx 1$, allows the action of $\hat{H}_{\text{int}}$ to be expressed more simply. The validity of the dipole approximation is discussed in depth in chapter 4. In section 4.3 it will be shown that in this approximation the angular momenta of the molecular system must satisfy the selection rules $|J - 1| \leq J' \leq |J + 1|$ and $m_{J'} - m_J = q$ where the dashed quantities represent the state of highest excitation and $q = 0, \pm 1$ for π and $\sigma^\pm$ polarisation respectively. This suggests that the total angular momentum J and its projection along the space-fixed axis m_J are required in the basis set to most effectively describe the laser interaction.

2.2 ANGULAR MOMENTUM BASIS STATES

2.2.1 Coupling of angular momenta

Based on the discussion of the components of the molecular Hamiltonian and the coupling of the molecular system to the radiation field, an informed choice can be made for the molecular basis states to be used in the calculations of the system. The two well known coupling schemes of the jj basis and the LS basis provide the initial coupling description of the molecular system. The jj basis couples each atom's individual orbital and spin angular momenta together to form its total angular momentum $\boldsymbol{j}_\alpha = \boldsymbol{L}_\alpha + \boldsymbol{S}_\alpha$ where $\alpha = 1, 2$. These are then coupled together to form the total electronic angular momenta $\boldsymbol{j} = \boldsymbol{j}_1 + \boldsymbol{j}_2$. The alternative LS basis couples each atom's orbital angular momenta and each atom's spin angular momenta separately to form $\boldsymbol{L} = \boldsymbol{L}_1 + \boldsymbol{L}_2$ and $\boldsymbol{S} = \boldsymbol{S}_1 + \boldsymbol{S}_2$, so that $\boldsymbol{j} = \boldsymbol{L} + \boldsymbol{S}$. The jj basis diagonalises the matrix elements of the fine-structure Hamiltonian and hence is best suited for large interatomic distances where the fine-structure is much larger than the electronic splittings. On the other hand, the LS basis diagonalises the matrix elements of the electronic interactions and is best suited for small interatomic distances. Because the investigations throughout this thesis look at long-range molecules and make use of entrance channels that must be, by definition, uncoupled in the asymptotic interatomic region, the jj basis is chosen for the calculations and is described in further detail below. The LS basis is required for the evaluation of the electronic matrix elements and is described in detail in appendix B.2.

In the space-fixed frame, the atomic states of the separated atom basis are given by

$$|\bar{\gamma}_\alpha L_\alpha m_{L_\alpha} S_\alpha m_{S_\alpha}\rangle_{A,B} \tag{2.18}$$

where $\alpha = 1, 2$ indicates the atomic state which is centred on either nuclei A or B, and $\bar{\gamma}_\alpha$ denotes the quantum numbers necessary to specify the $1s2s$ metastable state or the $1s2p$ excited state. For convenience, the label A or B will be dropped when it is not required. Labels m_x indicate quantities projected along the space-fixed axis Oz. The states of total angular momentum of the atom are

$$|\gamma_\alpha j_\alpha m_{j_\alpha}\rangle = \sum_{m_{L_\alpha} m_{S_\alpha}} C^{L_\alpha S_\alpha j_\alpha}_{m_{L_\alpha} m_{S_\alpha} m_{j_\alpha}} |\bar{\gamma}_\alpha L_\alpha m_{L_\alpha} S_\alpha m_{S_\alpha}\rangle \tag{2.19}$$

where $C^{j_1 j_2 j}_{m_{j1} m_{j_2} m_j}$ is a Clebsch-Gordan coefficient and $\gamma_\alpha = \{\bar{\gamma}_\alpha, L_\alpha, S_\alpha\}$. The two atomic states are coupled together by $\boldsymbol{j}_1 + \boldsymbol{j}_2 = \boldsymbol{j}$ to form the total electronic angular momentum of the dimer:

$$|\gamma j_1 j_2 j m_j\rangle \quad = \sum_{m_{j_1} m_{j_2}} C^{j_1 j_2 j}_{m_{j_1} m_{j_2} m_j} |\gamma_1 j_1 m_{j_1}\rangle |\gamma_2 j_2 m_{j_2}\rangle \tag{2.20}$$

where $\gamma = \{\gamma_1, \gamma_2\}$.

For molecular interactions it is preferable to express the bases in the molecular-fixed frame. Equations (2.18), (2.19) and (2.20) have the same form in the molecular frame, with all labels m_x replaced with Ω_x, the projection of quantity x along the intermolecular axis OZ. The transformation between the two frames of reference is found by applying Wigner rotation matrices, $D^j_{m_j \Omega_j}(\alpha, \beta, \gamma)$, such that

$$|\gamma j_1 j_2 j \Omega_j\rangle = \sum_{m_j} D^j_{m_j \Omega_j}(\phi, \theta, 0) |\gamma j_1 j_2 j m_j\rangle, \tag{2.21}$$

where $(\alpha, \beta, \gamma) = (\phi, \theta, 0)$ are the Euler angles, given by the Z-Y-Z convention of rotation, required to rotate the space-fixed Oz axis onto the intermolecular axis. Here the convention of Brink and Satchler [113] is used.

The electronic state (2.21) does not include nuclear spin or rotation. Helium-4 has no nuclear spin but the nuclear rotation, represented by states of the relative angular momentum $\boldsymbol{l}$ of the nuclei, is required:

$$|l m_l\rangle \equiv Y_{l, m_l}(\theta, \phi) = \sqrt{\frac{2l+1}{4\pi}} D^{l*}_{m_l 0}(\phi, \theta, 0), \tag{2.22}$$

where θ and ϕ specify the rotation of the intermolecular axis relative to the space-fixed Oz-axis. These states can be combined with the electronic basis states in the space-fixed frame by forming $\boldsymbol{J} = \boldsymbol{j} + \boldsymbol{l}$, the total angular momentum of the dimer:

$$|\gamma j_1 j_2 j l J m_J\rangle = \sum_{m_j m_l} C^{j l J}_{m_j m_l m_J} |\gamma j_1 j_2 j m_j\rangle |l m_l\rangle. \tag{2.23}$$

The states (2.23), despite generating a matrix of $\hat{H}_{\text{rot}}$ which is diagonal, do not describe the molecular dynamics very well as they do not incorporate any projections along the intermolecular axis. As the nature of ultracold collisions allows colliding atoms to only approach one another for small values of l, there is no great benefit in diagonalising the rotational part of the Hamiltonian. It is desirable however, to keep the quantity m_J in the basis because of the laser coupling selection rules described in section 2.1.5.

In light of these considerations, the coupling (2.23) is rewritten by making use of the inversion of (2.21), so that

$$|\gamma j_1 j_2 j l J m_J\rangle = \sum_{m_j m_l} C^{jlJ}_{m_j m_l m_J} \sqrt{\frac{2l+1}{4\pi}} D^{l*}_{m_l 0}(\phi,\theta,0) \sum_{\Omega_j} D^{j*}_{m_j \Omega_j}(\phi,\theta,0)|\gamma j_1 j_2 j \Omega_j\rangle. \quad (2.24)$$

After combining the Wigner rotation matrices and summing over the resultant Clebsch-Gordan coefficients [113], equation (2.24) becomes

$$|\gamma j_1 j_2 j l J m_J\rangle = \sum_{\Omega_j} (-1)^{j-\Omega_j} C^{jJl}_{\Omega_j -\Omega_j 0} N^J_{m_J \Omega_j}(\theta,\phi)|\gamma j_1 j_2 j \Omega_j\rangle, \quad (2.25)$$

where $\Omega_l = 0$ by definition and $N^J_{m_J\Omega_j}$ is the symmetric top function defined as

$$N^J_{m_J\Omega_j}(\theta,\phi) \equiv \sqrt{\frac{2J+1}{4\pi}} D^{J*}_{m_J\Omega_j}(\phi,\theta,0). \quad (2.26)$$

Equation (2.25) can be interpreted as a coupling of $\boldsymbol{j} = \boldsymbol{j}_1 + \boldsymbol{j}_2$ and $\boldsymbol{J}$ to form $\boldsymbol{l}$ and hence naturally introduces the basis states

$$|\gamma j_1 j_2 j \Omega_j J m_J\rangle \equiv N^J_{m_J\Omega_j}(\theta,\phi)|\gamma j_1 j_2 \Omega_j\rangle. \quad (2.27)$$

This basis generates a diagonal set of matrix elements of $\hat{H}_{\text{fs}}$ and is well suited to the dynamics introduced by the laser interaction $\hat{H}_{\text{int}}$. It will be used throughout the remainder of this thesis and be referred to as the hybrid jj basis, or simply as the jj basis when the context is unambiguous. It separates manifolds of differing values of Ω_j which are coupled by the rotational Hamiltonian but are often negligible in molecular calculations. Of the Hund's cases [106], this basis represents Hund's case (c) where the fine-structure is larger than the electronic interactions, which are in turn larger than the rotational terms.

2.2.2 Molecular symmetries

The hybrid jj basis (2.27) includes all the quantum numbers of the molecular system in the coupling scheme, yet it does not incorporate the symmetries of the molecular Hamiltonian. These symmetries for a homonuclear dimer without nuclear spin include [114, 115]:

- $\hat{\imath}$; the inversion symmetry of the total wave function through the centre of charge of the diatom, with eigenvalue $(-1)^w$, where $w = 0$ and $w = 1$ for gerade (even) and ungerade (odd) symmetry respectively.
- $\hat{X}_n$; the permutation of the nuclei. For helium-4 the nuclei are bosons and so the eigenstates of this operator are required to be symmetric.

- $\hat{P}_T$; the total parity of the wave function acting in the space-fixed frame. This can be factored into the nuclear parity $\hat{P}_n$ and the electronic parity $\hat{\imath}$. Because the nuclei are bosonic and have no net nuclear spin, $\hat{P}_n = \hat{X}_n$ and $\hat{P}_T = \hat{P}_n \hat{\imath} = \hat{\imath}$ when acting on states of bosonic nuclear symmetry.

- $\hat{\sigma}_e$; the operator that reflects the electronic wave function through a plane containing the intermolecular axis, with eigenvalue $(-1)^\sigma$. This symmetry only exists if $\Omega = |\Omega_j| = 0$. This operator can easily be confused with the reflection of the total system, $\hat{\sigma}_v$, including the electronic, nuclear spin and nuclear rotation wave functions in the molecule-fixed frame. The operator $\hat{\sigma}_v$ can be shown [106] to have an identical symmetry to $\hat{P}_T$ and must be considered when heteronuclear systems or systems with nuclear spin are considered.

These symmetries are often designated by the Hund's case (c) notation Ω_w when $\Omega > 0$ and 0^σ_w when $\Omega = 0$.

The details of these symmetries applied to the jj basis states and the LS basis states are presented in appendix 2. The resultant jj states that are eigenvectors of $\hat{\imath}$ are

$$|\gamma j_1 j_2 j \Omega_j w J m_J\rangle \equiv N_{jj,w} \Big[|(\gamma_1 j_1)_A (\gamma_2 j_2)_B j \Omega_j J m_J\rangle + (-1)^{w+L_1+L_2+j_1+j_2-j} |(\gamma_2 j_2)_A (\gamma_1 j_1)_B j \Omega_j J m_J\rangle \Big], \quad (2.28)$$

where the normalisation constant $N_{jj,w} = 1/2$ for $\gamma_1 j_1 = \gamma_2 j_2$ and $N_{jj,w} = 1/\sqrt{2}$ otherwise. For metastable states that have $\gamma_1 j_1 = \gamma_2 j_2$, this places a restriction of $(-1)^{w-j} = 1$ on the allowed states.

Once the nuclear permutation is included, the jj states that transform correctly under $\hat{X}_n$ and $\hat{\imath}$ are

$$|\gamma j_1 j_2 j J m_J; \Omega w\rangle \equiv N_{jj,\Omega} \Big[|\gamma j_1 j_2 j \Omega w J m_J\rangle + (-1)^{w+L_1+L_2-j+J} |\gamma j_1 j_2 j, -\Omega, w J m_J\rangle \Big], \quad (2.29)$$

where $\Omega = |\Omega_j| \geq 0$ and the normalisation constant $N_{jj,\Omega} = 1/2$ for $\Omega = 0$ and $N_{jj,\Omega} = 1/\sqrt{2}$ otherwise. The states (2.29) are also eigenvectors of the reflection operator $\hat{\sigma}_e$ with the eigenvalue of $(-1)^{L_1+L_2-j}$.

2.3 MATRIX ELEMENTS OF THE MOLECULAR HAMILTONIAN

The matrix elements of the full molecular Hamiltonian, $\hat{H}_{\text{mol}} = \hat{T}_{\text{n}} + \hat{H}_{\text{el}} + \hat{H}_{\text{fs}}$, can be calculated in the extended hybrid jj basis $R^{-1} G_a(R) |a\rangle$ where $G_a(R)$ are the radial functions describing the vibrational states and $|a\rangle \equiv |\gamma j_1 j_2 j J m_J; \Omega w\rangle$.

The action of the radial kinetic term $\hat{T}_R$ is described in section 2.1.3 and the relevant inner products are

$$\begin{aligned} T^G_{aa'} &\equiv \langle a'|\hat{T}_R \frac{1}{R} G_a(R)|a\rangle \\ &= -\frac{\hbar^2}{2\mu R}\frac{d^2 G_a}{dR^2}\delta_{aa'}, \end{aligned} \tag{2.30}$$

where the superscript G in the notation $T^G_{aa'}$ implies that the pseudo matrix element only includes the radial function $R^{-1}G(R)$ associated with the ket $|a\rangle$.

The matrix elements of the relativistic Hamiltonian $V^{\text{fs}}_{aa'} = \langle a'|\hat{H}_{\text{fs}}|a\rangle$, described in section 2.1.2, are

$$V^{\text{fs}}_{aa'} = \Delta E^{\text{fs}}_{\gamma_1 j_1} + \Delta E^{\text{fs}}_{\gamma_2 j_2}. \tag{2.31}$$

For the $1s2p$ atomic configuration, the reference energy is taken to be zero at the energy of the $j_\alpha = 0$ asymptote which gives the explicit values $\Delta E^{\text{fs}}_{\gamma_\alpha 1} = -29.6169$ GHz and $\Delta E^{\text{fs}}_{\gamma_\alpha 2} = -31.9081$ GHz. The metastable levels have no fine-structure, i.e. $V^{\text{fs}}_{aa'} = 0$.

The matrix elements of the electronic Hamiltonian $\hat{H}_{\text{el}}$ require the transformation of the eigenvalue equation (2.5) in the LS basis to the jj basis, as described in appendix B.4, and are given by

$$\begin{aligned} V^{\text{el}}_{aa'} &= \langle a'|\hat{H}_{\text{el}}|a\rangle \\ &= E^\infty_a \delta_{a'a} + \delta_{\eta\eta'} \sum_{L\Omega_L S\Omega_S} {}^{2S+1}\Lambda^\sigma_w(R)\, F^{j_1 j_2 j\Omega}_{LS\Omega_L\Omega_S} F^{j_1' j_2' j'\Omega}_{LS\Omega_L\Omega_S}, \end{aligned} \tag{2.32}$$

where E^∞_a is the sum of the asymptotic energies of the separated atoms, $\Lambda = |\Omega_L|$ and the BO potential ${}^{2S+1}\Lambda^\sigma_w(R) \to 0$ for $R \to \infty$. The details of the BO potentials are presented in section 2.1.1 and the label η represents the set of quantum numbers $\{\gamma, \Omega, w, J, m_J\}$. The $F^{j_1 j_2 j\Omega}_{LS\Omega_L\Omega_S}$ coefficients are given by

$$F^{j_1 j_2 j\Omega_j}_{LS\Omega_L\Omega_S} = \sqrt{(2S+1)(2L+1)(2j_1+1)(2j_2+1)} \begin{Bmatrix} L_1 & L_2 & L \\ S_1 & S_2 & S \\ j_1 & j_2 & j \end{Bmatrix} C^{LSj}_{\Omega_L\Omega_S\Omega_j}, \tag{2.33}$$

where the term $\{\cdots\}$ is a Wigner 9-j symbol and the implicit set of quantum numbers $\{\gamma_1, \gamma_2\}$ has been suppressed in the labelling of $F^{j_1 j_2 j\Omega_j}_{LS\Omega_L\Omega_S}$.

The matrix elements of the rotational Hamiltonian, $\hat{H}_{\text{rot}}$, require the evaluation of $\hat{l}^2$. This operator is expanded in terms of the ladder operators, $\hat{j}_\pm = \hat{j}_X \pm i\hat{j}_Y$ and $\hat{J}_\pm = \hat{J}_X \pm i\hat{J}_Y$:

$$\hat{l}^2 = (\hat{\boldsymbol{J}} - \hat{\boldsymbol{j}})^2 = \hat{J}^2 + \hat{j}^2 - (2\hat{J}_Z\hat{j}_Z + \hat{J}_+\hat{j}_- + \hat{J}_-\hat{j}_+) \tag{2.34}$$

where the subscripts X, Y, Z refer to the molecule-fixed axes. The action of the ladder operators on the jj basis components is

$$\hat{j}_\pm |j\Omega_j\rangle = \hbar\sqrt{j(j+1) - \Omega_j(\Omega_j \pm 1)}\,|j\Omega_j \pm 1\rangle \tag{2.35}$$

$$\hat{J}_\pm N^J_{m_J\Omega_j} = \hbar\sqrt{J(J+1) - \Omega_j(\Omega_j \mp 1)}\,N^J_{m_J\Omega_j\mp 1}. \tag{2.36}$$

The irregular action of $\hat{J}_\pm$ arises from the rotation of the intermolecular axis with respect to $\boldsymbol{J}$ [116]. The matrix elements in the hybrid jj basis without symmetrisation (2.27) are therefore

$$\begin{aligned}
&\langle \gamma' j_1' j_2' j' \Omega_j' J' m_J' | \frac{\hat{l}^2}{2\mu R^2} | \gamma j_1 j_2 j \Omega_j J m_J \rangle \\
&= \frac{\hbar^2}{2\mu R^2}\delta_{\rho\rho'} \Bigg[\left[J(J+1) + j(j+1) - 2\Omega_j^2 \right] \delta_{\Omega_j\Omega_j'} \\
&\quad - (\delta_{\Omega_j-1,\Omega_j'} + \delta_{\Omega_j+1,\Omega_j'}) \sqrt{\left[J(J+1) - \Omega_j\Omega_j' \right] \left[j(j+1) - \Omega_j\Omega_j' \right]} \Bigg]
\end{aligned} \tag{2.37}$$

where ρ represents the quantum numbers $\{\gamma, j_1 j_2, j, J, m_j\}$. The second term represents the off-diagonal Coriolis couplings between states of differing Ω. In the symmetrised basis, the normalisation constants must be considered and the resultant matrix elements are

$$\begin{aligned}
V^{\mathrm{rot}}_{aa'} &= \langle a' | \frac{\hat{l}^2}{2\mu R^2} | a \rangle \\
&= \frac{\hbar^2}{2\mu R^2}\delta_{\rho\rho'}\delta_{ww'} \Bigg[\left[J(J+1) + j(j+1) - 2\Omega^2 \right] \delta_{\Omega\Omega'} \\
&\quad - N^{\mathrm{rot}}_{\Omega\Omega'} (\delta_{\Omega-1,\Omega'} + \delta_{\Omega+1,\Omega'}) \sqrt{\left[J(J+1) - \Omega\Omega' \right] \left[j(j+1) - \Omega\Omega' \right]} \Bigg]
\end{aligned} \tag{2.38}$$

where $N^{\mathrm{rot}}_{\Omega\Omega'} = N^{\mathrm{rot}}_{\Omega'\Omega} = \sqrt{2}$ if $\Omega = 0$ and $\Omega' > 0$, and $N^{\mathrm{rot}}_{\Omega\Omega'} = 1$ otherwise.

2.4 SPONTANEOUS LOSS FROM THE $2s2p$ MANIFOLD

In the multi-channel photoassociation calculations of chapter 4, spontaneous emission from the excited state provides one mechanism for observing the resonances of excited bound levels. This can be included in the Hamiltonian by introducing a loss term $i\Gamma/2$ where Γ is the emission width. It is common to take a constant width for Γ but, for the large distances involved in the photoassociation processes studied in this thesis, a more complete description of spontaneous emission is required. The constant atomic spontaneous emission width, derived from fundamental properties of the excited state and transition line involved is $\Gamma_a = 4d_{\mathrm{at}}^2/3\lambda\!\!\!^{-3}$ [117] where d_{at} is the atomic dipole moment and $\lambda\!\!\!^{-} = \lambda/2\pi$, where λ is the wavelength of the atomic transition. The molecular emission width [108] for a basis state $|a\rangle$ in the LS basis is

$$\Gamma(x) = \Gamma_a - (-1)^w 3\Gamma_a \begin{cases} -(x\cos x - \sin x)/x^3 & \text{for} \quad \Lambda = \Sigma \\ (x^2 \sin x + x\cos x - \sin x)/2x^3 & \text{for} \quad \Lambda = \Pi, \end{cases} \tag{2.39}$$

where $x = R/\lambda\!\!\!^{-}$. When $R \ll \lambda\!\!\!^{-}$ the molecule is much smaller than the wavelength of the light and $\Gamma(R/\lambda\!\!\!^{-}) \approx 2\Gamma_a$ for ungerade states and $\Gamma(R/\lambda\!\!\!^{-}) \approx 0$ for gerade states. Spontaneous emission from the atomic triplet $2p$ state is dominated by the $2s \to 2p$ transition, for which the atomic width is $\Gamma_a = 1.6246$ MHz.

This R-dependent emission width can be written as the action of an operator, $\hat{H}_{\text{spon}}$, such that

$$\hat{H}_{\text{spon}}|a\rangle = \frac{i}{2}\Gamma\left(\frac{R}{\lambda\!\!\!^{-}}\right)|a\rangle. \tag{2.40}$$

This enables $\hat{H}_{\text{mol}}$ to be written as

$$\hat{H}_{\text{mol}} = \hat{T}_R + \hat{H}_{\text{rot}} + \hat{H}_{\text{el}} + \hat{H}_{\text{fs}} + \hat{H}_{\text{spon}} \tag{2.41}$$

to completely describe the helium system including loss.

2.5 SUMMARY

This chapter has described the determination of the essential properties of the helium system required for the investigations in the following chapters. The Hamiltonian for the metastable and $2s2p$ systems have been analysed, and the individual contributions to the molecular interactions for the radial kinetic term $\hat{T}_R$, the rotational term $\hat{H}_{\text{rot}}$, the electronic term $\hat{H}_{\text{el}}$ and the relativistic term $\hat{H}_{\text{fs}}$ described in detail. The laser field and its coupling to the molecular system has been described and the process of spontaneous loss from the excited state included through the operator $\hat{H}_{\text{spon}}$. Various properties of relevant basis states have been discussed, including the incorporation of all symmetry requirements. Finally, matrix elements of all the contributions to the total Hamiltonian have been obtained using these basis states.

In the following chapters these results will be used to investigate the bound states and photoassociation resonances in the helium-4 system.

Chapter 3

Bound levels of the $2s2p$ manifold

3.1 INTRODUCTION

Interatomic interactions play a significant role in ultracold gases and condensates, creating a rich diversity of features to be explored. However, these interatomic forces can induce inelastic loss processes and, to be able to exploit the interactions to make useful measurements or to provide fine control over scattering properties, a detailed understanding of these interactions is required. One method to examine these interactions is to investigate the scattering collisions or the molecular bound states of the two-body systems of interest.

The investigations in this chapter examine the bound levels of the $2s\,^3S_1 + 2p\,^3P_j$ helium system to determine their properties that are relevant to experiment and to predict which levels are accessible in the laboratory. For short interatomic distances, bound levels are formed because of the competing electronic interactions between the atoms and these types of molecules have been substantially investigated in chemical physics research. Ultracold photoassociation experiments can also create bound levels that exist only at long range separations, and arise from asymptotic couplings between the different electronic states.

A number of experimental investigations in ultracold gases have taken place using photoassociation as the diagnostic tool. A large body of work has been performed using alkali metal species of which a comprehensive review is given by Jones *et al* [41]. Of particular interest to the present study are the observations of transitions from metastable helium levels to levels near the $2s\,^3S_1 + 2p\,^3P_j$, $j = 0, 1, 2$ asymptotes which have been performed by several groups [65, 66, 67], who have recorded over 40 peaks near the $j = 0, 1, 2$ asymptotes. The measurements of van Rijnbach [66] were obtained using ion detection from a metastable gas in a magneto-optical trap (MOT) at approximately 2 mK. Due to a large background in the ion signal present in the trapped gas, the measurements were obtained in brief 'trap-off' periods. Near the $j = 2$ asymptote 36 peaks were detected and of these 15 were classified as 'weak'. The weak levels were observed at a very low intensity but were recorded in multiple trials on different days. Near the $j = 1$ asymptote, six additional levels were observed, but no levels were observed near the $j = 0$ asymptote.

The measurements of Tol [65] were performed in a similar manner to the van Rijnbach experiments. Two sets of observations consisting of 25 peaks were made of levels near the $j = 2$ asymptote by experimental groups in both Amsterdam and Utrecht, of which the former focused upon smaller laser detunings of less than 2 GHz and observed only 9 peaks. The Utrecht values of [65] unfortunately suffered from a calibration error that was corrected post-experiment by comparison with other experimental results and therefore will not be considered in this thesis.

Kim *et al* [67] performed PA measurements near the asymptotes $j = 2$ and $j = 0$ using a different technique to detect trap loss. In their experiment the metastable atoms were cooled to temperatures in the range $2 - 30$ μK in a magnetic trap, placing the gas just outside of the typical conditions for Bose-Einstein condensation. The atoms were also spin-polarised so that a large density could be achieved. The PA profile was observed after pulsing the PA laser using three different mechanisms: the number of atoms, the optical density and the final temperature of the gas after deactivating the trap following a brief period of thermalisation. Because a reduction of atom number and optical density and an increase in temperature will occur for any decay process from the excited $2s2p$ state, all decay channels were detected, including spontaneous emission. Near the $j = 2$ asymptote detunings of up to 6 GHz were methodically scanned and 23 peaks were observed. From initial analysis of these peaks, a further four levels were predicted to exist with detunings larger than 6 GHz and these were found in narrow scans in those regions. Near the $j = 0$ asymptote five peaks were observed that correspond to levels which exist entirely at large interatomic ranges, $R > 100$ a_0. Known as purely long-range levels, their interaction may be described completely by retarded dipole and dispersion potentials, which are well understood and depend only upon accurately known atomic parameters, allowing calculation of their properties to a very high degree of accuracy.

The experimental groups associated the observed peaks to particular Hund's case (c) configurations by using the accumulated phase (AP) method (first described by [118]) that makes use of long-range forms of the interaction potentials and does not require the detailed short-range forms of the potentials. The AP method groups observations into series belonging to separate adiabatic potentials such that each level in a particular series possesses a very similar accumulated phase in its associated potential at some inner distance which is deemed to be the short-range limit of the long-range potentials. The method is very successful in assigning observations to potentials, as will be shown in later sections.

Theoretical analyses of the ultra-long range levels that asymptote to $j = 0$ have been completed using single-channel adiabatic calculations [87] and full multichannel calculations [90] using long-range potentials, and give excellent agreement with measured binding energies. For the short-range levels of all asymptotes, Dickinson *et al* [85] were able to calculate the first *ab initio* hybrid short-range potentials for the quintet potentials in the $2s2p$ configuration by performing multi-reference configuration interaction (MRCI) and multi-configuration self-consistent field (MCSCF) calculations. From these, single-channel adiabatic binding energies were determined that were assigned to many observations from experiments performed using spin-polarised atoms. Recently, Deguilhem *et al* revisited these calculations [86], optimising the atomic basis set and were able to achieve convergence for separations shorter than 6.25 a_0 in a multi-reference configuration interaction (MRCI) calculation for the ${}^5\Sigma^+_{g,u}$ and ${}^5\Pi_{g,u}$ potentials. They also calculated multi-configuration self-consistent field (MCSCF) ${}^{1,3}\Sigma^+_{g,u}$ and ${}^{1,3}\Pi_{g,u}$ potentials and were able to determine adiabatic binding energies that could be matched to all of the experimental results. The nature of the single-channel calculation however, meant that non-adiabatic and Coriolis couplings (off-diagonal rotational terms in the Hund's case (c) coupling scheme) were neglected.

This chapter investigates the influence of non-adiabatic and Coriolis effects upon the binding energies and seeks to improve the agreement between experimental measurement and theoretical prediction by using a fully multichannel method. Although earlier multichannel calculations for purely long-range bound levels indicate that the Coriolis couplings are of negligible influence, there is no guarantee that they can be neglected for levels that exist entirely in the short-range region or that partially extend into this region, especially if significant coupling between the adiabatic potentials is present.

In order to assess the benefits of the multichannel calculation, a single-channel calculation will also be performed so that results may be compared and the validity of using the more easily calculable single-channel results determined. The single-channel calculation is also useful in associating Hund's case (c) labels to the multichannel results.

3.2 SINGLE-CHANNEL CALCULATION

3.2.1 Potentials

The bound levels of a molecular system exist at discrete energies that are beneath the dissociation limit of the atoms and are solutions of the eigenvalue equation of the Hamiltonian:

$$\hat{H}_{\mathrm{mol}}|\Psi\rangle = E|\Psi\rangle. \tag{3.1}$$

To solve this equation exactly, a multichannel calculation is required that includes all of the couplings of the molecular system. This is often difficult to perform and requires a sophisticated set of numerical tools to calculate and analyse the results. Although a complete multichannel calculation will be presented later in this chapter, a simpler single-channel calculation is first performed to aid in the comparison of results. The calculation isolates parts of the molecular system such that only uncoupled differential equations of the form

$$\left[\frac{1}{2\mu}\frac{d^2}{dR^2} + V(R) - E\right]\psi(R) = 0 \tag{3.2}$$

need be solved. One possible choice for the single-channel potentials $V(R)$ are the adiabatic potentials, $V_i^{\mathrm{adi}}(R)$. These are formed by diagonalising at each value of R the extended Movre-Pichler model matrix that includes rotation [119]

$$V^{\Omega}_{a'a} = V^{\mathrm{el}}_{a'a} + V^{\mathrm{fs}}_{a'a} + V^{\mathrm{rot}}_{a'a}\delta_{\Omega'\Omega} \tag{3.3}$$

where the terms $V^x_{a'a}$ are the matrix elements of x in the basis $|a\rangle$ and are described in chapter 2. It is assumed that $|a\rangle$ is the hybrid jj basis $|\gamma j_1 j_2 j J m_J;\Omega w\rangle$ given by (2.29). Only the diagonal terms of $V^{\mathrm{rot}}_{a'a}$ are kept and the neglected off-diagonal terms are referred to as the Coriolis couplings. The adiabatic eigenstates are R-dependent and are designated by

$$|i\rangle \equiv |i, R, \mathrm{adi}\rangle = \sum_a C_{ai}(R)|a\rangle \tag{3.4}$$

where $C_{ai}(R)$ are the eigenvectors of the $V^{\Omega}_{a'a}$ matrix and the adiabatic potentials $V^{\mathrm{adi}}_i(R) = \sum_{a'a} C^{-1}_{a'i} V^{\Omega}_{a'a} C_{ai}$ are the eigenvalues. Each adiabatic state $|i\rangle$ can be uniquely specified by a Hund's case (c) label $\{J, \Omega^{\sigma}_w\}$, the electronic angular momentum $j = 0, 1, 2$ of the asymptotic $2s\,{}^3S_1 + 2p\,{}^3P_j$ limit and, to distinguish any remaining multiplicity, the minima of the potentials.

For an allowed crossing to occur between two adiabatic potentials, the associated basis states must be uncoupled from one another. If a coupling is present or introduced via an interaction, the allowed crossing will become an avoided crossing in the adiabatic potentials regardless of the strength of the coupling. Hence, assuming that all the basis states $|a\rangle$ are somewhat coupled, the adiabatic potentials cannot cross one another and only possess avoided crossings. The most accurate single-channel approximation however, must allow crossings to occur in regions of significant diabatic behaviour to more closely emulate the dynamics of the interacting system. These hybrid adiabatic/diabatic potentials may be formed by following the smoothest connections between potentials when crossings do occur. That is, sharply crossing potential curves which are only weakly interacting should exhibit diabatic behaviour, whereas near degenerate potential curves which are strongly interacting should exhibit avoided crossings.

To programmatically perform the smoothing, two similar methods were developed. The first method diagonalises the adiabatic potentials on a coarse mesh grid ΔR and reorders the potentials at each value of R_n to minimise

$$\left| \left(\frac{dV^{\mathrm{adi}}_{k_{n+1}}}{dR}\right)_{R_{n+1}} - \left(\frac{dV^{\mathrm{adi}}_{k_n}}{dR}\right)_{R_n} \right| \tag{3.5}$$

where k_n enumerates the potentials analogously to i, except that the order of the enumeration may differ at adjacent distances R_n and R_{n+1}. The resultant potentials, $V^{\mathrm{SC}}_k(R_n) \equiv V^{\mathrm{adi}}_{k_n}(R_n)$ are then the result of the action of $\hat{H}_{\mathrm{el}} + \hat{H}_{\mathrm{fs}} + \hat{H}_{\mathrm{rot}}$ on the R-dependent basis

$$|k\rangle \equiv |k, R_n, \mathrm{SC}\rangle = |k_n, R, \mathrm{adi}\rangle = \sum_a D_{ak}(R_n)|a\rangle, \tag{3.6}$$

where $D_{ak}(R)$ is the unitary transformation from the hybrid jj basis to the single-channel basis. The choice of mesh grid ΔR significantly influences the behaviour of the potentials and as $\Delta R \to 0$ the potentials V^{SC}_k become identical to V^{adi}_i.

The second method [120], isolates each crossing between two potentials and computes the ratio between the minimum spacing of the potentials and the spacing of the adjacent grid points, again on a finite mesh grid ΔR. To do this, the function

$$Y(R_n) = \frac{2X(R_n)}{X(R_{n-1}) + X(R_{n+1})}, \tag{3.7}$$

where $X(R_n) = |V_a^{\text{adi}}(R_n) - V_b^{\text{adi}}(R_n)|$, is applied to each pair of adiabatic potentials $\{a, b\}$ and the condition $Y(R_n) \leq 1$ is used to isolate all of the crossings. Each crossing is then treated as an avoided crossing for $Y(R_n) > \alpha$ and a true crossing for $Y(R_n) \leq \alpha$, where the parameter α can be adapted to produce the best behaviour in each set of potentials. This method again produces an index k_n that is applied in the same manner of equation (3.6).

It was found that the second smoothing method more closely matches the results of the multichannel calculation and as such will be used in the following single-channel calculations.

3.2.2 Differential equations

For each single-channel basis state, solutions to the equation

$$\langle k| \left[\hat{T}_R + V_k^{\text{SC}}(R) - E_v\right] \frac{G_{k,v}(R)}{R} |k\rangle = 0 \tag{3.8}$$

are found, where E_v enumerates the binding energies of valid bound levels and $G_{k,v}(R)$ is the vibrational wave function for level v of state $|k\rangle$. Because the basis $|k\rangle$ is R-dependent, equation (2.12) is only an approximation to the complete radial kinetic term (2.11). The second term of (2.11), utilised to evaluate the inner product $\langle k|\hat{T}_R R^{-1} G_{k,v}(R)|k\rangle$ is

$$2\frac{dG_{k,v}}{dR}\langle k|\frac{d|k\rangle}{dR} = 2\frac{dG_{k,v}}{dR}\sum_a D_{ak}^* \frac{dD_{ak}}{dR}. \tag{3.9}$$

This term is real because D_{ak} is real as it is comprised of the eigenvectors of $V_{a'a}^{\Omega}$, which is a real symmetric matrix in the hybrid jj basis. Thus,

$$2\frac{dG_{k,v}}{dR}\langle k|\frac{d|k\rangle}{dR} = \frac{dG_{k,v}}{dR}\frac{d\langle k|k\rangle}{dR} = 0 \tag{3.10}$$

because $\langle k|k\rangle = 1$ by definition. The third term of (2.11) is nonzero and is often called the kinetic correction term, $V_k^{\text{KC}}(R)$. It can easily be calculated because

$$\begin{aligned} V_k^{\text{KC}}(R) = \langle k|\frac{d^2|k\rangle}{dR^2} &= \sum_{aa'} D_{a'k}(R)\frac{d^2 D_{ak}(R)}{dR^2}\langle a'|a\rangle \\ &= \sum_a D_{ak}(R)\frac{d^2 D_{ak}(R)}{dR^2}. \end{aligned} \tag{3.11}$$

Note that the radial kinetic term also couples different single-channel potentials to one another, however these non-adiabatic couplings are ignored in the single-channel approximation. For most single channel potentials the kinetic correction is problematic as the derivative d^2D_{ak}/dR^2 can be significantly affected near sharp adiabatic crossings by the choice of the smoothing. To avoid any arbitrariness in the single-channel results the kinetic correction term is ignored in this chapter and the simple form of (2.12) is used to generate the differential equation

$$\left[-\frac{\hbar^2}{2\mu}\frac{d^2}{dR^2}+V_k^{\mathrm{SC}}(R)-E_v\right]G_{k,v}(R)=0. \tag{3.12}$$

The differential equations (3.12) have been solved using two numerical methods. The first, the renormalised Numerov method [121], is used to count nodes of the wave function as it is integrated outwards from the origin and is described in more depth in appendix C. The second, the discrete variable representation (DVR) method, is a boundary value matrix method that is more efficient because it is able to generate all eigenvalues for the potential simultaneously and is described in appendix D. Although the DVR method is the quickest to run due to its parallel nature (it need not be run for each individual eigenvalue) it also requires a large amount of computer memory to perform its calculations. On the other hand, the memory usage of the Numerov method scales linearly with mesh grid size but can require significantly more time to calculate as it must iteratively place upper and lower bounds on each individual eigenvalue. As such, the Numerov method was chosen to calculate to the precision required and the DVR method used to validate the Numerov method results. For the results presented in this chapter, the calculations of the Numerov method used a set of regions with different step sizes, as described in C.3, of

$$\Delta R=\begin{cases}10^{-4}\,a_0 & \text{for } 1\,a_0<R<5\,a_0\\ 10^{-3}\,a_0 & \text{for } 5\,a_0<R<50\,a_0\\ 10^{-2}\,a_0 & \text{for } 50\,a_0<R<500\,a_0\\ 0.1\,a_0 & \text{for } 500\,a_0<R<1000\,a_0\\ 0.2\,a_0 & \text{for } 1000\,a_0<R<2000\,a_0.\end{cases} \tag{3.13}$$

3.2.3 Comparison with Deguilhem *et al*

The single-channel results calculated in this thesis have been compared with the single-channel results of Deguilhem *et al* [86] that were calculated in a similar manner. Good agreement (to within 0.2%) is obtained for the majority of levels shown in tables 2, 3 and 4 in [86]. A maximum absolute difference of 20 MHz is observed which is comparable to experimental accuracy. Sample comparisons of some series are presented in table 3.1 and a comparison of all of the values is shown in table E.1. Note that the only data of [86] that has not been compared is that for 0_u^+, $J=0$ in table 4 of [86], as symmetry considerations do not allow even values of J in the 0_u^+ electronic configuration.

The only significant differences found in this comparison are for the series 0_u^+, $J=1,3$ of table 2 in [86]. It was found that the origin of these differences was in the creation of the smoothed single-channel potentials from the diagonalised adiabatic potentials as described

Table 3.1: Comparison of single-channel results with that of Deguilhem *et al* [86] for the 1_u, $J = 1$ and 2_u, $J = 2$ sets. Excellent agreement is obtained, and similar agreement is obtained for most other series tabulated in [86]. Binding energies are in GHz from the $j = 2$ asymptote.

1_u, $J = 1$			2_u, $J = 2$		
v	This work	Deguilhem *et al*	v	This work	Deguilhem *et al*
70	11.319	11.301	70	13.666	13.647
71	7.167	7.154	71	9.020	9.006
72	4.316	4.307	72	5.703	5.692
73	2.432	2.426	73	3.414	3.407
74	1.250	1.246	74	1.913	1.908
75	0.566	0.564	75	0.996	0.992
76	0.216	0.215	76	0.478	0.476
			77	0.208	0.207
			78	0.079	0.079
			79	0.025	0.025

in section 3.2.1. In fact, three different methods of smoothing yielded different numbers of levels in the two 0_u^+ adiabatic potentials that asymptote to $j = 2$. These differences are due to the near degeneracies of the potentials in the region $17\,a_0 < R < 17.5\,a_0$ as shown in figure 3.1. These results are listed in table 3.2. The three smoothing methods were: (a) the smoothing method of equation (3.5) applied to a $\Delta R = 0.1\ a_0$ mesh grid; (b) the smoothing method of (3.5) applied to a $\Delta R = 0.01\ a_0$ mesh grid; and (c) the method of (3.7) applied to a mesh grid of $\Delta R = 0.01\ a_0$ with $\alpha = 0.5$. From the results it is apparent that the Deguilhem *et al* values most closely match the smoothing method of (3.5) with $\Delta R = 0.1\ a_0$ but do not match very well with the multichannel results.

It is important to note that the extrapolation of the Born-Oppenheimer potentials into the classically forbidden region towards the origin can subtly but noticeably modify the binding energies of even very-long bound states [111]. This occurs because the data of the BO potentials is tabulated only to distances of 3 a_0 or 4.75 a_0, which lie just within the classically forbidden region. Modification of the potentials inwards of these innermost tabulated points can cause up to 0.25% variation in the binding energies.

3.3 MULTICHANNEL CALCULATION

3.3.1 Differential equations

In order to investigate the approximations introduced by ignoring the non-adiabatic and Coriolis couplings, respectively the off-diagonal kinetic and rotational terms, a complete multichannel calculation must be performed which includes all interactions. Although this makes both the numerical integration and interpretation of the results more difficult, the advantages gained from the increased accuracy and the detailed knowledge of the vibrational wave functions makes the multichannel approach more than worthwhile.

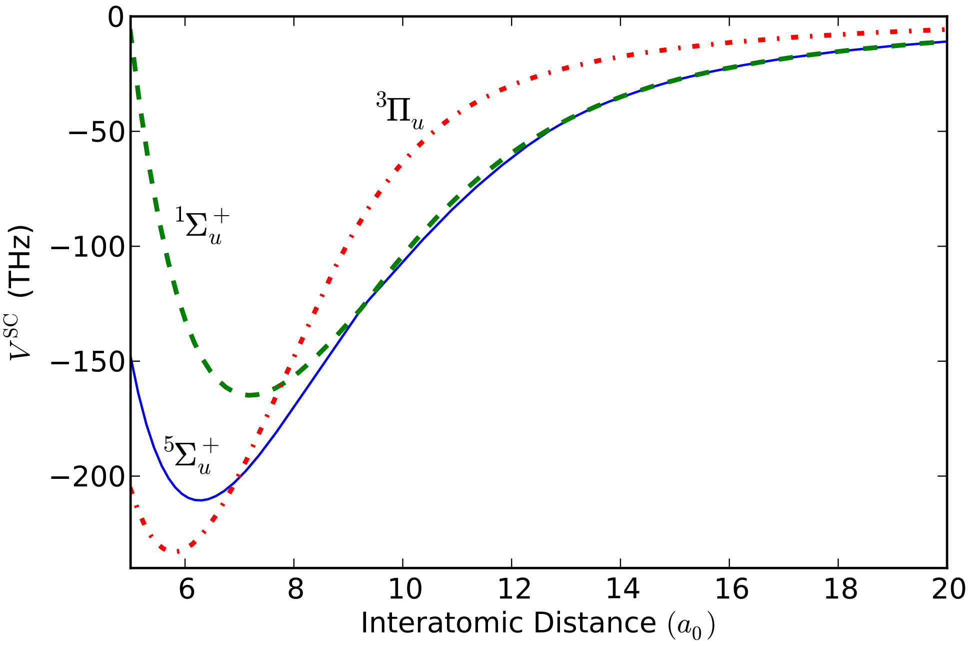

Figure 3.1: Single-channel potentials of the 0_u^+, $J = 1$ set. The short-range case (a) assignments are indicated on the plot. The near degeneracies in the $^{1,5}\Sigma_u^+$ potentials over the region $17\,a_0 < R < 17.5\,a_0$ cause difficulties in forming accurate single-channel potentials.

Table 3.2: Comparison of the binding energies, in GHz from the $j = 2$ asymptote, predicted from the hybrid adiabatic/diabatic single channel potentials. I and II denote smoothing using equations (3.5) and (3.7) respectively. The two potentials are of the 0_u^+, $J = 1$ set, asymptoting to $j = 2$ and the double degeneracy of this specification is indicated by the labels A and B. The results of Deguilhem *et al* [86] are included in the final column and most closely resemble the values calculated using smoothing I with a grid spacing of $\Delta R = 0.1\ a_0$.

	I ($\Delta R = 0.1\ a_0$)		I ($\Delta R = 0.01\ a_0$)		II ($\Delta R = 0.01\ a_0$)		
v	A	B	A	B	A	B	Deguilhem *et al* [86]
70	13.600	0.456	9.979	1.316	14.583	0.380	13.658
71	8.987	0.137	6.227	0.693	9.699	0.109	9.029
72	5.706	0.029	3.668	0.338	6.205	0.021	5.735
73	3.462		1.970	0.150	3.796		3.481
74	2.003		0.909	0.059	2.215		2.015
75	1.101		0.335	0.019	1.229		1.108
76	0.568		0.092		0.642		0.572
77	0.271		0.017		0.311		0.273
78	0.116				0.136		0.117
79	0.044				0.052		0.044
80	0.013				0.016		

Additionally, situations involving resonances, as opposed to purely bound levels, arise in the multichannel calculation for energies above the $j = 2$ asymptote since these levels are able to predissociate via the presence of open channels.

The multichannel calculation solves differential equations that are generated from the inner product

$$\langle a'| \sum_a \left[\hat{H}_{\text{mol}} - E_v\right] \frac{1}{R} G_{a,v}(R)|a\rangle = 0 \tag{3.14}$$

which, in the hybrid jj basis (2.29), becomes

$$\frac{d^2 G_{a',v}(R)}{dR^2}\delta_{a'a} + \sum_a \left[V^{\text{el}}_{a'a} + V^{\text{fs}}_{a'a} + V^{\text{rot}}_{a'a} - E_v \delta_{a'a}\right] G_{a,v}(R) = 0. \tag{3.15}$$

To investigate the Coriolis couplings, the non-diagonal terms of $V^{\text{rot}}_{a'a}$ may be turned off, which causes the Hund's case (c) subsets of differing Ω to decouple. These calculations without Coriolis couplings will be referred to as the MC1 calculations and are identified by the quantum numbers $\{J, \Omega^\sigma_w, v\}$. The calculations that involve the complete Hamiltonian, and include the Coriolis couplings, are referred to as the MC2 calculations and are identified by the quantum numbers $\{J, w, v\}$.

The association of levels from the single-channel and the multichannel calculations is possible by minimising the difference of their binding energies. A better association may be obtained from the multichannel results by analysing the resultant bound vibrational wave functions. Using the transformation matrix, $D_{ka}(R)$ of (3.6), the amount that the single-channel basis $|k\rangle$ contributes to each multichannel bound level can be calculated from

$$C^{\text{SC}}_{k,v} = \sum_a \int D_{ka}(R) G_{a,v}(R)\, dR \tag{3.16}$$

where it is assumed that the vibrational wave functions of the bound level, $G_{a,v}(R)$, are normalised. For states that are not very much different to their single-channel counterparts, the contribution for the corresponding value of k will be nearly 100%. When comparing the results between the MC1 and MC2 calculations, it is of more interest to analyse the contributions from an entire Ω^σ_w manifold which may be calculated by

$$C^{\text{MC1}}_{\Omega,v} = \sum_{k\in\Omega} C^{\text{SC}}_{k,v} \tag{3.17}$$

where $k \in \Omega$ indicates the sum should take place over single-channels $|k\rangle$ that have that value of Ω.

To determine bound levels of the multichannel system, the allowed energies E_v of equations (3.15) must be found. This may be performed numerically by using the same procedures as for the single-channel calculations. For levels beneath the $j = 2$ asymptote, all channels of the multichannel problem are closed and the allowed energies correspond to binding energies of the system. Above the $j = 2$ asymptote, yet below the $j = 1$ or $j = 0$

asymptotes, the multichannel problem consists of coupled closed and open channels and the allowed energies of the system will often correspond to continuum scattering states which have been discretised by the enforcement of the zero value boundary conditions at the outer numerical limit of integration. These continuum solutions are not of interest here and careful analysis and selection procedures must be used to discard them from the set of solutions. The considerations of bound levels and resonances that exist above the $j = 2$ asymptote will be discussed in further detail in section 3.3.4.

3.3.2 Non-adiabatic effects

The single-channel results and the MC1 results differ only through the inclusion of non-adiabatic couplings in MC1. The results show that the majority of sets of levels agree to better than 0.1% for all but the least bound levels where, although the relative differences can be up to $\sim$ 1%, the absolute differences are relatively small ($<$ 10 MHz). These differences are comparable to the uncertainty in the potentials and are smaller than the uncertainties of experimental measurements. The 2_u sets shown in table 3.3 are also in good agreement, except that they differ by up to 5% for the least bound levels. The agreement between the SC and MC1 results can also be seen in the dominance of the contribution from one particular SC potential for each MC1 level, shown in the final columns of table 3.3.

The only results that do differ markedly between the single-channel and MC1 methods are those of the 0_u^+ and 1_g sets as shown in tables 3.4 and 3.5 respectively. In section 3.2.3, it was mentioned that there can be a large variation in the formation of the SC potentials and so the differences for this set are presumably due to the arbitrary choice in forming the single-channel potentials, resulting from near degeneracies in the Born-Oppenheimer potentials. The difference is even more apparent when comparing the contributions of the single-channel states as the largest contribution can be as low as 50%, as opposed to the near 100% contribution from one basis state that is observed in table 3.3.

3.3.3 Coriolis effects

The complete coupling scheme includes the Coriolis couplings between states of differing Ω. Within this scheme, the set of basis states may be broken into several uncoupled manifolds that are designated by the quantum numbers $\{J, w\}$. These are referred to as the MC2 manifolds. Although the Coriolis couplings vary as R^{-2} and may be expected to play a major role for small R, the results indicate that it is the levels which span both short and large interatomic ranges that are most influenced by the Coriolis couplings.

The majority of levels that belong to the $J = 1, 2$ ungerade ($w = 1$) MC2 manifolds show small differences of less than 0.1% between the MC1 and MC2 results. A sample of the ungerade $J = 2$ set is given in table 3.6. For deeply bound levels with binding energies greater than 7 GHz, almost all the $J = 1, 2$ ungerade levels agree between the MC1 and MC2 calculations to within 0.5%. Similar behaviour is observed in the $J = 3$

Table 3.3: Comparison of the multichannel results MC1, that include non-adiabatic couplings but ignore Coriolis couplings, and the single-channel results for the 2_u, $J = 2$ set. The sixth column indicates the percentage difference between the results and shows that near perfect agreement is obtained for deeply bound levels. Weakly bound levels show some larger differences but remain within reasonably good agreement. The final columns list the fractions of the MC1 vibrational wave function from each single-channel basis as described by equation (3.16).

		Single-channel Binding Energies			Single-channel Contribution	
v	MC1	$j = 2$, A	$j = 2$, B	Diff. (%)	$j = 2$, A	$j = 2$, B
8	179.4 THz	179.4 THz		0.0	1.0	
9	175.2 THz		175.2 THz	0.0		1.0
10	170.9 THz	170.9 THz		0.0	1.0	
11	165.2 THz		165.2 THz	0.0		1.0
12	162.7 THz	162.67 THz		0.0	1.0	
115	125.5 GHz	125.5 GHz		0.0	1.0	
116	96.14 GHz	96.14 GHz		0.0	1.0	
117	95.86 GHz		95.86 GHz	0.0		1.0
118	72.68 GHz	72.68 GHz		0.0	1.0	
119	67.30 GHz		67.30 GHz	0.0		1.0
120	54.15 GHz	54.15 GHz		0.0	1.0	
134	1.925 GHz	1.913 GHz		0.6	0.97	0.03
135	1.807 GHz		1.823 GHz	0.9	0.02	0.98
136	1.005 GHz	0.996 GHz		0.9	0.99	0.01
137	0.5395 GHz		0.5566 GHz	3.1	0.05	0.95
138	0.4824 GHz	0.4776 GHz		1.0	0.96	0.04
139	0.2113 GHz	0.2076 GHz		1.8	1.0	
140	0.0809 GHz	0.0791 GHz		2.3	1.0	

Table 3.4: As per table 3.3 but for the 0_u^+, $J = 1$ set. Larger differences are present between the results which can be isolated to the two $j = 2$ single-channel potentials. The separation into the single-channel basis calculated from (3.16) highlights this as most levels possess contributions from both single-channel bases.

		Single-channel Binding Energies				Single-channel Contribution		
v	MC1	$j = 2$, A	$j = 2$, B	$j = 1$	Diff. (%)	$j = 2$, A	$j = 2$, B	$j = 1$
10	170.9 THz	170.9 THz			0.0	1.0		
11	165.2 THz			165.2 THz	0.0			1.0
12	162.6 THz	162.6 THz			0.0	1.0		
13	161.0 THz		161.0 THz		0.0		1.0	
40	93.31 THz			93.31 THz	0.0			1.0
41	91.34 THz	92.49 THz			1.3	0.56	0.44	
42	87.80 THz	86.69 THz			1.3	0.46	0.54	
43	85.44 THz		85.43 THz		0.0			1.0
44	85.37 THz		86.50 THz		1.3	0.55	0.45	
45	82.13 THz	81.08 THz			1.3	0.51	0.49	
46	79.63 THz		80.70 THz		1.3	0.50	0.50	
47	77.88 THz			77.88 THz	0.0			1.0
180	57.51 GHz	56.86 GHz			1.1	0.85	0.15	
181	56.19 GHz			56.21 GHz	0.0			1.0
182	48.10 GHz		48.60 GHz		1.0	0.17	0.83	
183	42.15 GHz	41.77 GHz			0.9	0.84	0.16	
184	34.93 GHz			34.97 GHz	0.1			1.0
200	2.086 GHz		2.125 GHz		1.9	0.16	0.84	
201	1.813 GHz			1.862 GHz	2.7			1.0
202	1.262 GHz	1.229 GHz			2.6	0.91	0.09	
203	0.9663 GHz		1.001 GHz		3.5	0.09	0.91	
204	0.6638 GHz	0.6420 GHz			3.3	0.95	0.05	

Table 3.5: As per table 3.3 but for the 1_g, $J = 1$ set. Larger differences are present between the results which can be isolated to two of the $j = 2$ single-channel potentials and one of the $j = 1$ potentials. The separation into the single-channel basis calculated from (3.16) highlights this as most levels possess contributions from these single-channel bases.

		Single-channel Binding Energies					Single-channel Contribution			
v	MC1	$j = 2$, A	$j = 2$, B	$j = 2$, C	$j = 1$	Diff. (%)	$j = 2$, A	$j = 2$, B	$j = 2$, C	$j = 1$
10	269.8 THz			269.8 THz		0.0			1.0	
11	269.7 THz		269.7THz			0.0		1.0		
12	258.6 THz			258.6 THz		0.0			1.0	
13	258.4 THz		258.4 THz			0.0		1.0		
159	7.083 THz				6.717 THz	5.3	0.04	0.14	0.02	0.80
160	6.705 THz	6.987 THz				4.1	0.98			0.02
161	6.533 THz		6.532 THz			0.0		0.60	0.31	0.09
162	6.516 THz			6.528 THz		0.2		0.12	0.65	0.22
163	6.007 THz				5.668 THz	5.8	0.03	0.40	0.02	0.55
164	5.877 THz	6.133 THz				4.3	0.99			0.01
165	5.438 THz		5.454 THz			0.3		0.41	0.54	0.05
166	5.422 THz			5.434 THz		0.2		0.07	0.51	0.42
234	119.9 GHz	131.5 GHz				2.5	1.0			
235	113.5 GHz			113.76 GHz		2.4		0.09	0.91	
236	113.1 GHz		116.29 GHz			0.6		0.90	0.07	0.02
237	99.59 GHz				83.85 GHz	0.8		0.03	0.01	0.96
238	91.13 GHz	100.41 GHz				8.3	1.0			
265	2.916 GHz	3.495 GHz				18.1	1.0			
266	2.170 GHz		2.353 GHz			8.1		0.84	0.16	
267	2.121 GHz			2.084 GHz		1.7		0.15	0.72	0.12
268	1.838 GHz	2.029 GHz				9.9		0.03	0.11	0.86
269	1.663 GHz	1.114 GHz				39.6	1.0			

ungerade manifold, except that the agreement to within 0.5% occurs only for binding energies greater than 5000 GHz. Larger differences in the $J = 3$ ungerade manifold of up to 2% occur for the smaller binding energies greater than 15 GHz. Manifolds with $J > 3$ were not investigated because selection rules forbid excitation to these states from the s-wave metastable collisions that dominate the entrance channels in ultracold experiments.

The greatest variation caused by the Coriolis couplings can be observed in the more weakly bound levels in the ungerade sets and most of the experimental observations lie within this range. For the $J = 1, 2$ manifolds, approximately a third of the levels with detunings less than 7 GHz show differences ranging from $1 - 5\%$, and are larger than the experimental uncertainties. The $J = 3$ differences are even larger, with up to 10% difference noticeable for some levels with binding energies less than 15 GHz. Obviously these differences are quite significant and of much greater importance than the difference caused by the introduction of the non-adiabatic couplings.

The gerade ($w = 0$) manifolds exhibit similar behaviour albeit with slightly larger variation between the MC1 and MC2 methods. In summary, the $J = 1, 2, 3$ gerade manifolds differ between their MC1 and MC2 values by less than 0.5% for detunings larger than 800, 3600 and 5000 GHz respectively. For smaller detunings, differences of up to 10% do occur, although most levels agree to within 0.5%. A sample comparison of the gerade MC1 and MC2 results is given in table 3.7.

An additional comparison between the MC1 and MC2 results can be performed by calculating the contribution of each MC1 set to the MC2 states, using equation (3.17). These contributions are listed in the final columns of tables 3.6 and 3.7. When the contributions from each MC1 set are compared, there does not appear to be a correlation between large differences in the binding energies and significant contributions from separate MC1 sets. In fact, the more deeply bound states which occupy purely short interatomic distances have very large contributions from two or more manifolds but with minimal modification of binding energy. Conversely, the bound levels that exist at large interatomic distances possess dominant contributions of greater than 90% from one MC1 set but can have large percentage differences in binding energies.

The results reported in [120] were based upon the use of the basis states (2.28) rather than the correct states (2.29) which include symmetry with respect to nuclear permutation. However, this does not affect the values for the binding energies. The only difference between the results here and the results in [120], is that each level which corresponds to $\Omega > 0$ was given as a doublet in [120]. One member of each doublet does not obey the nuclear statistics of helium-4 and corresponds to an artificial fermionic helium-4 system. If these levels are ignored, the calculations are identical.

3.3.4 Bound levels above the $j = 2$ asymptotic limit

Levels that lie above the $j = 2$ asymptote include basis states that asymptote to scattering solutions, thus requiring open channel solutions to the differential equations (3.15). These levels introduce two important aspects into the calculation:

Table 3.6: Comparison of the multichannel results including (MC2) and excluding (MC1) Coriolis couplings for the ungerade, $J = 2$ manifold. Larger differences are observed than those that result from the inclusion of non-adiabatic couplings as shown in table 3.3. Significant mixing of the contributions from each MC1 set, calculated using equation (3.17), is apparent for the more deeply bound levels, despite the small difference in binding energies. Conversely, the weakly bound levels that possess large differences in binding energies are mostly comprised of a single MC1 set.

		MC1 Binding Energies				MC1 Contribution		
v	MC2	0_u^-	1_u	2_u	Diff. (%)	0_u^-	1_u	2_u
15	195.31 THz		195.41 THz		0.1	0.39	0.54	0.07
16	188.13 THz			188.08 THz	0.0		0.19	0.81
17	187.91 THz		187.95 THz		0.0		0.81	0.19
18	185.29 THz			185.24 THz	0.0	0.10	0.29	0.62
19	185.19 THz	185.14 THz			0.0	0.51	0.17	0.32
114	45.506 THz	45.472 THz			0.1	0.52	0.17	0.31
115	45.401 THz		45.468 THz		0.1	0.39	0.55	0.07
116	41.836 THz			41.813 THz	0.1		0.19	0.81
117	41.716 THz		41.739 THz		0.1		0.81	0.19
118	40.292 THz			40.261 THz	0.1	0.09	0.28	0.62
119	40.227 THz	40.195 THz			0.1	0.52	0.17	0.31
286	183.98 GHz			183.49 GHz	0.3	0.02	0.06	0.92
287	180.58 GHz	179.75 GHz			0.5	0.84	0.12	0.05
288	174.35 GHz		175.64 GHz		0.7	0.14	0.82	0.03
289	162.24 GHz			161.88 GHz	0.2		0.06	0.94
290	154.82 GHz		155.17 GHz		0.2		0.95	0.05
344	0.741 GHz	0.727 GHz			2.0	0.96	0.04	
345	0.543 GHz			0.539 GHz	0.6		0.02	0.98
346	0.508 GHz		0.515 GHz		1.1		0.92	0.08
347	0.487 GHz			0.482 GHz	1.0		0.07	0.93
348	0.215 GHz			0.211 GHz	1.6		0.01	0.99

Table 3.7: As per table 3.6 but for the gerade, $J = 2$ set. While most results are reasonably close in binding energy, some are significantly (and measurably) different. This does not appear to be reflected in the contribution of the constituent MC1 subsets.

		MC1 Binding Energies				MC1 Contribution		
v	MC2	0_g^+	1_g	2_g	Diff. (%)	0_g^+	1_g	2_g
10	304.50 THz	304.49 THz			0.0	0.19	0.51	0.30
11	304.25 THz			292.80 THz	0.1	0.44	0.49	0.07
12	292.98 THz		292.79 THz		0.1	0.29	0.49	0.23
13	292.86 THz		292.68 THz		0.0	0.09	0.51	0.40
14	292.68 THz	292.67 THz			0.0	0.19	0.51	0.30
131	88.371 THz	88.546 THz			0.2	0.44	0.49	0.06
132	87.716 THz		87.716 THz		0.0		1.0	
133	85.234 THz		85.234 THz		0.0		1.0	
134	83.991 THz			83.947 THz	0.1	0.08	0.28	0.63
135	83.895 THz		83.850 THz		0.1	0.50	0.19	0.31
363	789.29 GHz			753.01 GHz	4.7	0.08	0.28	0.64
364	726.58 GHz		726.57 GHz		0.0		1.0	
365	707.99 GHz		670.14 GHz		5.5	0.49	0.20	0.30
366	648.98 GHz	664.81 GHz			2.4	0.05	0.67	0.29
367	639.13 GHz			643.66 GHz	0.7	0.19	0.80	0.01
450	2.789 GHz		2.788 GHz		0.0		1.0	
451	2.552 GHz	2.426 GHz			5.0	0.85	0.13	
452	1.933 GHz		1.971 GHz		2.0	0.04	0.90	0.06
453	1.893 GHz		1.905 GHz		0.6	0.01	0.98	0.01
454	1.575 GHz		1.574 GHz		0.0		1.0	

a) Utilising a numerical boundary value method which imposes zero value boundary conditions does not only find solutions that are bound levels of the system, but also finds solutions that include incoming and outgoing waves in the open channels having a node at the outer boundary. These artificial levels, often called box states, may be recognised and separated from the true bound levels by observing a shift of their eigenvalues with a variation of the position of the outer boundary, or by the proportion of the wave function that exists in the asymptotic region. The asymptotic region is defined as a region of large interatomic spacing where no bound levels are expected to be found, for example $R > 1500\ a_0$.

b) Pure bound levels are unlikely to exist when couplings to open channels are present because of the possibility of predissociation. In their place exist resonance states that have finite lifetimes. Resonances which possess very large lifetimes are most likely to produce the observed peaks in experimental measurements as short lifetimes lead to broad and weak resonances. To find resonances numerically, the binding energies must be allowed to become complex, $E_v^{\mathrm{res}} = E_v - i\Gamma_v^{\mathrm{pre}}/2$, where the imaginary part represents the lifetime of the resonance $\tau_v = \hbar/\Gamma_v^{\mathrm{pre}}$ due to predissociation. The asymptotic boundary conditions placed on the open channels differ from those for the closed channels in that they represent outgoing solutions, that is

$$G_{a,v}(R) \underset{R\to\infty}{\sim} e^{ik_a^r R} e^{k_a^i R} \tag{3.18}$$

where $k_a = k_a^r - ik_a^i = \sqrt{2\mu E_v^{\mathrm{res}}}$ and k_a^r and k_a^i are real. Note that this boundary condition produces wave functions whose magnitude increases in the positive R direction. This is to be expected in a time-independent calculation because (a) the asymptotic region represents only the predissociated part of the wave function and (b) larger values of R represent predissociation that has occurred further in the past. Because the resonance population decreases with time, the time-independent wave function must increase as $R \to \infty$. The outgoing boundary conditions were unable to be modelled using the DVR method so only the renormalised Numerov method was used to determine the resonance energies. However, the node counting method mentioned in section 3.2.2 that is used for levels beneath the $j = 2$ asymptote cannot be applied because the energies lie in the complex plane and not along the real axis.

Several alternative techniques to replace the node counting procedure were formulated to isolate the complex resonance energies. The first, a search for the complex energies using a gradient descent method as described in appendix C, was trialled by using each real energy that corresponded to artificial box states from the node counting method as a starting point for the descent procedure. This method proved unsatisfactory, however, as several known observations of resonances near the $j = 1$ and $j = 0$ asymptotes were not obtained in the calculations. To remedy the deficiency, an intermediate stage was introduced in which Cauchy's argument principle was applied to isolate all possible resonances throughout the energy domain under investigation. This can be successfully done because Cauchy's argument principle states that

$$\frac{1}{2\pi i}\oint_C \frac{f'(z)}{f(z)}dz = N - P \tag{3.19}$$

where $f(z)$ is a meromorphic function, that is, $f(z)$ is analytic for all z except for a set of points that are poles. Here C is a bounded contour which contains N zeros and P poles. By assuming that the matching condition for the outward and inward integrations of the renormalised Numerov method, $D(E) = 0$ (see appendix C), is a meromorphic function, the argument principle may be applied. However, if the integration region contains both zeros and poles then the poles will 'mask' the presence of the zeros, whereas if the poles and zeros are well separated, a series of small contours will each find either a single pole, a single zero or nothing. Hence, the calculation makes use of an adjacent series of box contours of real width 5 MHz and imaginary dimension ranging from 1 MHz to −100 MHz. The series of contours spanned two ranges of real energies from −600 MHz to −5 MHz detuning from the $j = 1$ asymptote and −1500 MHz to −5 MHz detuning from the $j = 0$ asymptote. The imaginary boundaries of the regions were chosen so that (a) pure bound states with no imaginary component could be identified and (b) the maximum predissociation width is less than 100 MHz. The integration around each of these contours indicates whether a resonance is present in each range and, if present, the contour is narrowed in a manner similar to the bisection method. Unfortunately, the integral of the argument principle is numerically costly to evaluate so the narrowing of the contours occurs only until a energy tolerance is achieved, which was set to be 0.1 MHz. At this point, the gradient descent search is used to determine the resonance energy exactly. Note that no 'artificial' resonances, which are analogous to artificial box states, were observed because these cannot exist when outgoing boundary conditions are specified.

By scanning the range of binding energies with matching points placed at distances from 100 a_0 up to 600 a_0, a total of 18 gerade and 16 ungerade levels were found near the $j = 1$ asymptote (shown in table 3.8) and a total of 6 gerade and 9 ungerade levels were found near the $j = 0$ asymptote (shown in table 3.9). All of the resonances near the $j = 0$ asymptote and some ungerade resonances near the $j = 1$ asymptote can be classified as purely long-range by calculating the proportion of wave function that is present at a short interatomic distance of $R < 20\,a_0$. This is shown in tables 3.8 and 3.9 as the parameter $f_{R<20}$, which is defined as

$$f_{R<20} = \frac{\sum_a \int_0^{20\,a_0} |G_{a,v}(R)|^2\,dR}{\sum_a \int_0^{\infty} |G_{a,v}(R)|^2\,dR}. \tag{3.20}$$

Equation (3.20) includes any part of the wave function associated with the predissociated pair of atoms and so may not accurately represent the proportion of the resonance at short interatomic range. However, only the relative magnitude of $f_{R<20}$ is important: resonances with a proportion less than 10^{-8} are purely long-range (for example the entire $j = 0$ manifold) whereas resonances with proportions greater than 10^{-5} possess significant short-range character. The values in between these bounds are difficult to classify and could fall into either category. For example, a purely long-range resonance could be strongly predissociating and hence possess a large $f_{R<20}$, or a resonance could be weakly present at short interatomic distances with no predissociation.

The purely long-range resonances have been previously analysed by Venturi *et al* [90] using only long-range potentials and their results are also shown in the final column of tables 3.8 and 3.9 for comparison. The agreement between the results is very good as can be expected because the long-range levels are not affected by the choice of short-range potential. Also mentioned in [90] are several resonances of the $J = 1$, g configuration near the $j = 1$ asymptote that were believed to possess significant predissociation, although precise calculations could not be made without the detail of the short-range interactions. These are the resonances that are observed here at -164.426, -62.573 and -27.739 MHz and it can be seen that they do not significantly predissociate as they have widths of 0.259, 1.156 and 0.057 MHz respectively, which are smaller than the radiative width of ~ 3.2 MHz.

3.4 EXPERIMENTAL ASSIGNMENTS

3.4.1 Single-channel assignments

Before the first calculation of *ab initio* short-range potentials by Dickinson *et al* [85], assignments of experimental observations were made by using only the long-range dispersion and resonant dipole-dipole interaction potentials. To be able to accommodate the unknown details of the short range part of the potential the accumulated phase (AP) method was used (see [69] and references therein), which makes use of the observed binding energy to predict the phase at some inner cut-off point of the long-range potentials. Each observation can be assigned an accumulated phase for every potential so it is not possible to make an assignment to a single isolated level. However, when a group of observations all possess a similar phase in one particular potential, it is highly likely that the measurements form a series corresponding to that potential's molecular configuration. While the AP method does not guarantee the correct assignment of levels, it has shown great success despite the lack of information available about the short-range form of the interaction.

With the calculation of precise *ab initio* potentials [86], it is possible to theoretically calculate the binding energies as has been shown in the previous sections. The simplest method of assignment using a single-channel calculation is to compare the observed energies to the theoretical levels in each single-channel potential and to associate levels based upon the closeness of their binding energies. Further details, such as the likelihood of Penning ionisation, may be used to aid the selection process and discard unlikely sets of theoretical levels. Penning ionisation acts as both a level broadening mechanism and a detection method for many experiments and occurs in metastable $2s2s$ helium and $2s2p$ helium systems when the bound level possesses singlet or triplet character in its Hund's case (a) basis for $R < 20\ a_0$ [92]. Deguilhem *et al* [86] have made assignments to many experimental observations in this manner.

Table 3.8: Resonances that are present within 600 MHz of detuning from the $j = 1$ asymptote. The detuning and predissociation width Γ_v^{pre} are given in MHz. The fifth column lists the proportion of the wave function at short range and the final column lists the calculations of Venturi *et al* [90].

$j = 1$ asymptote					
J, w	Detuning	Γ_v^{pre}	Case (c)	$f_{R<20}$	Venturi *et al*
$J = 1,\ g$	-282.55	6.51	0_g^-	1×10^{-4}	
	-164.43	0.26	1_g	6×10^{-5}	
	-116.70	3.28	0_g^-	6×10^{-5}	
	-62.57	1.16	1_g	2×10^{-4}	
	-40.46	1.31	0_g^-	3×10^{-5}	
	-27.74	0.06	1_g	1×10^{-5}	
	-15.90	0.68	1_g	1×10^{-4}	
	-9.98	0.47	0_g^-	1×10^{-5}	
$J = 2,\ g$	-130.22	0.36	1_g	7×10^{-6}	
	-30.23	0.37	1_g	9×10^{-6}	
	-19.07	0.04	1_g	1×10^{-6}	
$J = 3,\ g$	-427.21	70.19	0_g^-	2×10^{-5}	
	-181.80	35.99	0_g^-	5×10^{-5}	
	-87.66	0.22	1_g	1×10^{-6}	
	-64.68	16.15	0_g^-	5×10^{-5}	
	-17.34	5.85	0_g^-	3×10^{-5}	
	-11.69	0.05	1_g	5×10^{-7}	
	-5.66	0.03	1_g	4×10^{-7}	
$J = 0,\ u$	-18.28	0.00	0_u^-	1×10^{-9}	-18.27
$J = 1,\ u$	-418.24	0.42	0_u^+	1×10^{-4}	
	-204.73	0.28	0_u^+	8×10^{-5}	
	-82.01	0.15	0_u^+	4×10^{-5}	
	-25.65	0.06	0_u^+	2×10^{-5}	
$J = 2,\ u$	-191.50	0.02	2_u	4×10^{-8}	-191
	-72.25	0.02	2_u	4×10^{-8}	-72
	-21.43	0.01	2_u	2×10^{-8}	-21.5
$J = 3,\ u$	-478.14	5.30	0_u^+	3×10^{-4}	
	-282.48	3.21	0_u^+	2×10^{-4}	
	-166.78	0.06	2_u	4×10^{-8}	-167
	-121.64	1.61	0_u^+	8×10^{-5}	
	-57.56	0.04	2_u	3×10^{-8}	-57
	-38.41	0.67	0_u^+	3×10^{-5}	
	-14.29	0.02	2_u	1×10^{-8}	-14.4
	-7.02	0.22	0_u^+	2×10^{-5}	

Table 3.9: Resonances present within 1500 MHz of detuning from the $j = 0$ asymptote. The detuning and predissociation width Γ_v^{pre} are given in MHz. The fifth column lists the proportion of the wave function at short range and the final column lists the calculations of Venturi *et al* [90].

$j = 0$ asymptote					
J, w	Detuning	Γ_v^{pre}	Case (c)	$f_{R<20}$	Venturi *et al*
$J = 1,\ g$	-207.68	0.002	1_g	4×10^{-13}	-207.66
	-43.80	0.002	1_g	1×10^{-13}	-43.80
$J = 2,\ g$	-170.93	0.002	1_g	1×10^{-10}	-170.92
	-28.52	0.002	1_g	7×10^{-11}	-28.52
$J = 3,\ g$	-115.74	0.000	1_g	3×10^{-11}	-115.73
	-7.96	0.002	1_g	4×10^{-14}	-7.97
$J = 1,\ u$	-1418.05	0.008	0_u^+	1×10^{-9}	-1418.1
	-648.49	0.008	0_u^+	3×10^{-10}	-649
	-253.12	0.008	0_u^+	1×10^{-11}	-253.12
	-79.65	0.002	0_u^+	6×10^{-11}	-79.65
	-18.29	0.002	0_u^+	2×10^{-11}	-18.30
$J = 3,\ u$	-1212.67	0.045	0_u^+	9×10^{-10}	-1212.7
	-513.07	0.045	0_u^+	4×10^{-10}	-513
	-174.56	0.026	0_u^+	3×10^{-9}	-174.5
	-41.64	0.008	0_u^+	2×10^{-9}	-41.6

The absence of measurements to associate with theoretically predicted levels can also be used as a means to predict the coupling between differing manifolds. Léonard *et al* [122] have used the absence or presence of levels between two experimental setups that differ by their detection mechanism and the use of spin-polarisation (Paris experiment) or lack of polarisation (Utrecht experiment) to infer the rotational coupling between different case (c) sets. Levels that are predicted to become purely quintet at short-range in the single channel approximation should be observable in the Paris experiment (which uses an optical detection mechanism) but unobservable in the Utrecht experiment (which relies on an ion detection mechanism). However, if the actual experimental data does show the level, then it must be that coupling to other single-channel potentials with non-quintet character at short-range is present. Levels that are strongly coupled by Coriolis couplings to potentials that are significantly non-quintet will decay very quickly via Penning ionisation.

3.4.2 Observability Criteria

The multichannel calculations in this chapter allow further characterisation of each level and make possible rejection on an individual level-by-level basis. This is because the complete vibrational wave function is available for analysis and level specific information can be easily generated. For each level, the short-range spin-S fraction $f_{2S+1,v}$ and an approximate coupling factor $\mathcal{A}_v$ between the excited bound level and metastable colliding states of an experimental setup can be calculated. The spin fraction $f_{2S+1,v}$ is defined by

$$f_{2S+1,v} = \frac{Q_{S,v}}{\sum_{S'} Q_{S',v}}. \tag{3.21}$$

Here, the spin probability $Q_{S,v}$ is calculated in the LS basis (see appendix B.3)

$$Q_{S,v} = \sum_{L'S'\Omega'_L\Omega'_S} \delta_{S,S'} \sum_a F^{j_1 j_2 j \Omega_j}_{L'S'\Omega'_L\Omega'_S} \int_0^{20\,a_0} G_{a,v}(R)\, dR \tag{3.22}$$

where the quantity $F^{j_1 j_2 j \Omega_j}_{L'S'\Omega'_L\Omega'_S}$ is given by equation (B.22) and $G_{a,v}(R)$ are the vibrational wave functions calculated from the differential equations (3.15). This spin fraction is useful in estimating the likelihood of Penning ionisation in collisions of non-quintet character. It is assumed that Penning ionisation occurs with nearly 100% probability for states with non-quintet character for $R < 20\,a_0$. Therefore larger values of $f_{1,v} + f_{3,v}$ (or, equivalently, smaller values of $f_{5,v}$) will result in smaller lifetimes for those bound levels.

The coupling factor $\mathcal{A}_v$, defined by

$$\mathcal{A}_v = \frac{1}{N_g} \sum_{a,g} \langle S m_s l m_l | \hat{H}_{\text{int}} | a \rangle \int G_g(R) G_{a,v}(R)\, dR, \tag{3.23}$$

is essentially a Franck-Condon integral between the excited state $\sum_a G_{a,v}(R)|a\rangle$ and a set of N_g metastable states $G_g(R)|S m_S l m_l\rangle$ where the particular value of g determines the quantum numbers $\{S, m_S, l, m_l\}$ that are most relevant in specifying experimental conditions. As the temperature of the colliding metastable system is unknown and can range from μK to mK, the metastable wave function, $G_g(R)$, is replaced with unity. The coupling between the metastable and excited states, $\langle a' | \hat{H}_{\text{int}} | a \rangle$, is evaluated in the dipole approximation and is given by equation (4.32). The transformation from the hybrid jj basis $|a\rangle$ to the experimentally relevant basis $|S m_S, l m_l\rangle$ is given by (B.38).

The calculation of the short-range spin character is motivated by the expectation that experiments will not observe levels that possess too short a lifetime and hence have too broad a resonance to be detectable. A direct measure of this lifetime can be calculated by also considering the oscillation time of the wave function and a semi-classical model for the loss of population in the state as a particle oscillates back and forth. The process with most effect on the lifetime is that of Penning ionisation, so other loss processes such as spontaneous emission are ignored in the calculation. It is assumed that the ensemble of particles will decrease by a percentage of $f_{1,v} + f_{3,v}$ for every oscillation. To determine the speed of the particles, an approximate potential $V_a(R)$ is calculated for each channel from (3.12) using

$$E - V_a(R) = -\frac{\hbar^2}{2\mu} \frac{G''_{a,v}(R)}{G_{a,v}(R)}. \tag{3.24}$$

The speed, v, at each point is $v_a = \sqrt{2(E - V_a)/\mu}$ and the time for oscillation $t_{a,\text{osc}} = 2 \int v_a^{-1} dR$ where the integral is over values of R for which v_a is real and positive. These values lie between the classical turning points of the potential. If a double-well structure is evident in the potential then that level is ignored and no lifetime is calculated. By approximating the semi-classical oscillation by a continuous decay equation

$$N(t) = N_0 e^{-t/\tau_a}, \tag{3.25}$$

the lifetime of the state τ_a may be found. After substitution of $N(t_{a,\mathrm{osc}}) = f_{5,v} N_0$ into (3.25), $\tau_a = -t_{a,\mathrm{osc}} / \ln f_{5,v}$ is found, from which the decay width can be calculated from $\Gamma_a = \hbar/\tau_a$. As there is a value Γ_a for each channel $|a\rangle$, a single value for the width is determined from an average oscillation time weighted by the probability of wave function in each channel:

$$\Gamma_v = \sum_a \Gamma_a \int_0^\infty |G_{a,v}(R)|^2 \, dR. \tag{3.26}$$

These values are included in the tables in the following sections, and it appears that the decay widths are small for the majority of assigned levels. However, other unassigned levels that are not shown in the tables also possess decay widths that can be negligible and so there appears to be limited usefulness in considering the decay width as an observability criterion. The final observability criteria for assignment of theoretical levels with experimental levels do not make use of Γ_v.

The results reported in [120] were performed using the incorrect symmetrised basis (2.28). This has an influence on the averaging processes used for the calculation of the observability criteria and biases the values towards channels with $\Omega > 0$ by a factor of two. However, these criteria are not rigorously defined quantities and are used only as estimates to classify levels.

3.4.3 Spin-polarised experiments beneath the $j = 2$ asymptote

The first experimental observations to be considered are those of Kim *et al* [67], who confined spin-polarised atoms in a magnetic trap at approximately 10 μK. Colliding spin-polarised metastable helium atoms have spin projections that are aligned in the same direction, represented here by the quantum numbers $S_1 = S_2 = 1$, $m_{S_1} = m_{S_2} = 1$, $S = 2$ and $m_S = 2$. The experiment used an optical detection method and was able to detect all decay paths from the excited state, including spontaneous emission. As the spin-polarised state has a gerade symmetry, only ungerade excited levels are accessible by the laser coupling, due to the selection rules of the dipole approximation. In the colliding atoms, partial waves greater than s-waves will contribute little to the photoassociation process as the very low temperatures are highly unlikely to permit d-wave or higher partial waves reaching the interatomic distances of the excited resonances. Quantitatively, based on the average collisional energy of $E_k = (3/2)kT$, atoms at 10 μK in a d-wave channel will be classically repelled by the centrifugal barrier at 1600 a_0.

The experiment systematically scanned the range $0 - 6$ GHz of detuning from the $j = 2$ asymptote. After initial analysis of the observed levels in this region, more-deeply bound levels were predicted to be observed and additional narrow scans were made that validated these predictions. To perform a sensible analysis in this present study, only the observations belonging to the systematically scanned region will initially be compared to theoretical predictions. In this region, constraints may be placed upon the calculated theoretical quantities $f_{5,v}$ and $\mathcal{A}_v$ in an attempt to reproduce the exact number and position of the observed levels. This can only be done because it is certain there are no missing potentially observable levels that lie between the reported levels in this region. Theoretical levels that are to match observations from narrow scans should also obey these constraints, but nearby theoretical levels that do not match to experimental observations cannot be rejected without verified observability criteria as there is no experimental evidence to suggest their invalidity.

In the range of detunings $0.08 - 6$ GHz, a possible 71 theoretical levels are predicted to exist in the ungerade excited manifold. To reduce this large number of levels to the 23 observations made in this region, different combinations of constraints – referred to as the observability criteria – are placed upon the quantities $f_{5,v}$ and $\mathcal{A}_v$. Theoretical levels that possess too small a value of $f_{5,v}$ will consist of significant singlet and triplet contributions, have a short lifetime, and therefore a weak and broad resonance, and hence be unlikely to be observed in experiment. Additionally, theoretical levels that are likely to be coupled by the laser interaction from the metastable collisional state will possess large values of $\mathcal{A}_v$. With these concepts in mind, two observability criteria were found empirically by iteratively choosing values that included appropriate matches to the experimental observations while excluding those that do not match well. The final criteria were found to be a 87.5% quintet short-range character and a minimum coupling of 0.9 E_h. These conditions isolate 19 levels, shown in table 3.10, that match consistently and almost uniquely with the experimental measurements. Two of these theoretical levels lie very close to one another (-0.185 and -0.184 GHz) and are likely to be indistinguishable due to overlap of their resonance peaks and therefore belong to the observed level of -0.200 GHz.

Also included in table 3.10 are four theoretical levels that do not satisfy both of the observability criteria, yet can be assigned to experimental observations in the knowledge that the one criterion that is satisfied is unusually strong. For example, the theoretical level -0.928 GHz has a reduced short-range quintet character f_5 but is very strongly coupled to the metastable manifold by a coupling which is approximately twice as strong as that for the other levels.

From the assignments, it is evident that there is a trend for the theoretical levels to be consistently lower than the observed experimental levels by approximately $3 - 5\%$. Because of this discrepancy, the assignments that are made here differ from that of [86] quite often. It is worth noting that the majority of assignments agree with those of the accumulated phase method calculated by the experimental group [122], confirming the versatility of the AP method and suggesting that comparison of binding energies as used by [86] is not the best method to associate theoretical results with experimental observation.

In some entries of table 3.10, assignments are made to more than one Hund's case (c) set. Each case (c) set that has a contribution greater than 20% as calculated from equation (3.16) has been included in the table. It should be noted that this contribution is averaged

Table 3.10: Theoretical bound levels, with energies in GHz from the $j = 2$ asymptote, that have been calculated to be observable in spin-polarised experiments and their assignments to the observations of Kim *et al* [67]. The observability criteria used are $\mathcal{A}_v > 0.9\ E_h$ and $f_{5,v} > 87.5\%$. Some levels do not completely satisfy the observability criteria, but can be considered assignable due to the strength of one of the criteria. The fifth column lists the contributions from case (c) sets that are larger than 20%.

Exp	Theor	$\mathcal{A}_v$ (E_h)	$f_{5,v}$ (%)	Case (c)	[86] assignment	Γ_v (MHz)
-5.90	-5.729	1.306	99.9	2_u, $J = 2$	2_u, $J = 2$	0.3
-5.64	-5.463	1.775	98.9	2_u, $J = 3$	0_u^+, $J = 1$	2.0
-4.53	-4.394	1.157	96.8	$1_u, 0_u^+$, $J = 1$	0_u^+, $J = 3$	11.9
-4.25	-4.141	1.954	91.7	$0_u^+, 1_u$, $J = 3$	1_u, $J = 2$	28.5
-3.57	-3.438	1.388	99.2	2_u, $J = 2$	0_u^+, $J = 1$	2.6
-3.37	-3.251	2.077	99.2	2_u, $J = 3$	2_u, $J = 2$	2.6
-2.59	-2.499	1.155	99.0	$1_u, 0_u^+$, $J = 1$	1_u, $J = 3$	2.6
-2.42	-2.337	2.214	96.3	$0_u^+, 1_u$, $J = 3$	1_u, $J = 1$	8.2
-2.00	-1.937	1.420	98.5	2_u, $J = 2$	0_u^+, $J = 1$	3.1
-1.88	-1.807	2.418	99.7	2_u, $J = 3$	2_u, $J = 2$	0.5
-1.37	-1.326	1.058	98.7	$0_u^+, 1_u$, $J = 1$	1_u, $J = 3$	2.0
-1.275	-1.223	2.552	99.8	$0_u^+, 1_u$, $J = 3$	–	0.3
-1.22	-1.160[a]	0.574	100.0	1_u, $J = 2$	1_u, $J = 2$	0.0
-1.07	-1.013	1.539	98.2	2_u, $J = 2$	0_u^+, $J = 1$	2.0
-0.98	-0.928[a]	3.196	84.6	2_u, $J = 3$	2_u, $J = 2$	20.9
-0.62	-0.589	2.733	99.3	$0_u^+, 2_u$, $J = 3$	1_u, $J = 1$	0.5
-0.51	-0.487[a]	1.673	86.8	2_u, $J = 2$	2_u, $J = 2$	8.7
-0.455	–	–	–	–	0_u^+, $J = 3$	–
-0.280	-0.263[a]	3.483	73.6	$0_u^+, 2_u$, $J = 3$	0_u^+, $J = 1$	9.7
-0.235	-0.215	1.861	99.1	2_u, $J = 2$	1_u, $J = 1$	1.8
-0.200	-0.185	0.989	99.9	1_u, $J = 2$	2_u, $J = 2$	0.0
–	-0.184	3.012	95.6	2_u, $J = 3$	–	1.3
-0.185	-0.167	5.059	92.7	$0_u^+, 1_u$, $J = 3$	1_u, $J = 2$	1.1
-0.09	-0.083	2.328	99.7	2_u, $J = 2$	0_u^+, $J = 3$	0.0

[a] Observability criteria relaxed.

Table 3.11: Theoretical bound levels, with energies in GHz from the $j = 2$ asymptote, that are expected to be observed in experiments such as that of Kim *et al* that use spin-polarised atoms and an optical detection mechanism. Some narrow scans of measurements were performed by Kim *et al* and these assignments have been included. However, the majority of energies have not been scanned in experiment.

Exp	Theor	$\mathcal{A}_v$ (E_h)	$f_{5,v}$ (%)	Case (c)	[86] assignment	Γ_v (MHz)
–	-124.26	0.963	99.0	2_u, $J = 3$	–	68.8
–	-95.030	1.009	98.8	2_u, $J = 3$	–	55.0
–	-71.694	1.033	98.7	2_u, $J = 3$	–	39.7
–	-68.734	0.912	96.4	$1_u, 0_u^+$, $J = 1$	–	131.9
–	-67.246	0.903	89.9	$1_u, 0_u^+$, $J = 3$	–	357.4
–	-53.287	1.060	98.5	2_u, $J = 3$	–	36.9
–	-50.408	0.953	96.1	$1_u, 0_u^+$, $J = 1$	–	109.2
–	-49.151	1.011	88.6	$1_u, 0_u^+$, $J = 3$	–	334.2
–	-38.927	1.230	99.1	2_u, $J = 3$	–	20.9
–	-36.204	0.981	95.9	1_u, $J = 1$	–	79.5
–	-35.158	1.118	87.7	$1_u, 0_u^+$, $J = 3$	–	278.9
–	-28.566	0.947	100.0	2_u, $J = 2$	–	0.0
–	-27.876	1.257	98.9	2_u, $J = 3$	–	17.9
–	-25.388	1.019	95.7	1_u, $J = 1$	–	66.8
–	-20.061	1.022	99.5	2_u, $J = 2$	–	7.0
–	-19.500	1.344	98.8	2_u, $J = 3$	–	14.6
–	-17.316	1.053	95.5	1_u, $J = 1$	–	50.3
–	-13.705	1.111	99.8	2_u, $J = 2$	–	0.1
-13.67	-13.259	1.472	99.0	2_u, $J = 3$	2_u, $J = 2$	10.2
-11.70	-11.434	1.094	95.3	1_u, $J = 1$	1_u, $J = 1$	36.6
–	-9.051	1.208	100.0	2_u, $J = 2$	–	0.1
-8.95	-8.705	1.655	99.0	2_u, $J = 3$	2_u, $J = 2$	7.2
-7.45	-7.262	1.131	95.6	1_u, $J = 1$	1_u, $J = 1$	15.4

across the entire range of the bound level and may not well represent the detailed behaviour of the level. For example, a level can be composed of 100% of one particular basis state in a narrow region of interatomic distance, yet may not be listed as a case (c) contribution. Furthermore, case (c) sets that have contributions as large as 15% have been omitted in the table and could possible play an important role in properties associated with the levels.

The observability criteria established to account for levels with binding energies less than 6 GHz can be used to make assignments to the experimental observations of binding energies greater than 6 GHz. All levels that are predicted to occur are shown in table 3.11 along with assignments to observed levels if possible. The lack of assignment for theoretical level -9.051 GHz is not due to a problem in the observability criteria, but because the experiment did not scan this region of detuning.

3.4.4 Unpolarised experiments beneath the $j = 2$ asymptote

The second set of experimental observations to be considered are those of van Rijnbach [66] and Tol [65]. Like the majority of photoassociation experiments involving metastable helium, these experiments use unpolarised gases which allow for many more collisional channels and can excite gerade and ungerade $2s2p$ combinations. As the Utrecht measurements of Tol suffered from a calibration error which was corrected post-measurement by comparison to other experimental data, only the Amsterdam measurements of Tol will be considered. The measurements of van Rijnbach and Tol for binding energies less than 1.5 GHz mostly overlap, except for three values that are not recorded by van Rijnbach and one that is not observed by Tol. In both experiments ion detection was used as a signal of the excited state, which requires some singlet or triplet character of the excited bound levels. Hence, it is not expected that all of the levels observed in the spin-polarised experiments will also be observed in these ion-detection experiments.

For these experiments a metastable helium gas at approximately $1 - 2$ mK was used. It is likely that the lowest order partial wave will dominate the collisions of metastable atoms, but for ungerade metastable collisions this corresponds to p-wave collisions. The p-wave centrifugal barrier is significant for the low temperatures used, as the region $R < 200\ a_0$ becomes classically forbidden for colliding metastable atoms at a temperature of 1 mK. Hence it is far more likely that ungerade $2s2p$ states will be excited by metastable collisions than gerade $2s2p$ states. Additionally, excited gerade levels will only be strongly coupled if they possess significant triplet character for a region of interatomic distance, yet this will likely cause high rates of decay due to significant triplet character at short range.

The experiments systematically scanned a range of $0.045 - 13.57$ GHz detuning and observed 37 levels. Within this range, a total of 205 theoretical levels exist, and a subset of levels is again determined based on similar observability criteria as for the spin-polarised experiments. The exact empirical criteria were a minimum coupling to the metastable manifold of $0.7\ E_h$ and a quintet short-range character that must lie within $87.5\% < f_{5,v} < 99.8\%$. The maximum imposed upon the quintet short-range character is necessary, as the ion-detection mechanism of the experiment rules out purely quintet levels. Under these constraints, 21 levels are found that match reasonably well with experimental observations and three more levels can be assigned with a slight relaxation of one of their observability criteria (see table 3.12). Within the van Rijnbach observations, 15 were noted to be weakly observed and only four of these have been assigned to theoretical levels. To attempt to make further assignments to these levels would require a significant relaxation of the observability criteria and introduce many more theoretical levels that would not be assignable to any experimental measurement. Of the remaining 'strong' experimental levels, three were not assigned. Three theoretical levels (-1.013, -0.215 and -0.167 GHz) cannot be assigned to any experimental level. Note that the three observations of Tol that do not overlap with van Rijnbach, -0.045, -0.105 and -0.622 GHz, are required to complete assignments to the predicted theoretical levels, as is the observation of van Rijnbach at -0.08 GHz that does not overlap with that of Tol.

Again the assigned theoretical levels have binding energies consistently lower than the experimentally observed binding energies and this brings about a disagreement between the assignments reported here and those of Deguilhem *et al.* While the majority of the levels again agree with the assignments predicted by the accumulated phase method used in the initial predictions by the experimental groups, special mention must be made regarding the observed levels assigned to 2_u, $J = 2$, that is -3.49, -2.01 and -0.52 GHz. Despite the assignment by Léonard *et al* [122] to these sets, they believed that neighbouring levels or possibly gerade levels were the reason for these observations [123] as the 2_u, $J = 2$ adiabatic levels were predicted to possess purely quintet behaviour at short-range and not produce ionisation. The results here show that this is not the case: these levels possess properties that firmly place them in the ion detection regime. It is evident that the non-adiabatic and Coriolis couplings reduce the strong quintet behaviour of these levels at short interatomic distances.

It is worth noting that the gerade excited levels are almost completely unrepresented, except for one corresponding to -0.109 GHz. This is not due to the $l = 1$ centrifugal barrier, as the barrier is not included in the coupling strength calculation (3.23). Instead, it is because excited gerade levels can only be coupled to metastable ungerade levels and these are in triplet configurations. The spin-conserving nature of the coupling therefore means that coupled excited gerade levels must have a strong triplet nature. In fact, almost all of the 38 strongly coupled gerade levels (that is, those with $\mathcal{A}_v > 0.7\ E_h$) in the range $0.045 - 13.57$ GHz have a value of $f_{5,v} < 0.2$.

To characterise the nature of the gerade coupling the single-channel gerade potentials can be analysed. If a gerade level is to be effectively coupled to the metastable manifold it must possess triplet character at large interatomic distances yet become mostly quintet at short interatomic distance to avoid loss by ionisation. Only three potentials that asymptote to $j = 2$ satisfy this criteria in the gerade manifold, one from each of the 0_g^+, 1_g and 2_g sets. The first two potentials, 0_g^+ and 1_g, possess less than 10% triplet character at 300 a_0 and for the wave function to extend out to this interatomic distance the binding energy must be less than 350 MHz. Similarly, the remaining 2_g potential does not possess 10% triplet character until distances $R > 500\ a_0$ and permits the wave function to extend out to this distance only for binding energies less than 140 MHz. The wave functions of these levels must also extend out past the centrifugal barrier of the metastable collisions which also places a limit upon the maximum binding energy of approximately 400 MHz. Crucially, each of the three potentials is purely quintet at short-range and hence requires some coupling to other manifolds to permit ion detection in experiment. The low probability of photoassociation due to the combination of each of these properties and the lack of many gerade levels in the observations should therefore be unsurprising.

Using the formulated observability criteria, predictions of observable levels may be made for binding energies greater than the 14 GHz of detuning from the $j = 2$ asymptote that was performed in the experiments. These levels are given in table 3.13.

3.4.5 Unpolarised experiments above the $j = 2$ asymptote

The experiments of van Rijnbach also studied resonances near the $j = 1$ asymptote. By applying the observability criteria of the previous section to the levels calculated in section 3.3.3 and shown in tables 3.8 and 3.9, a direct one-to-one assignment can be made to all

Table 3.12: Theoretical bound levels, with energies in GHz from the $j = 2$ asymptote, that are calculated to be observable in ion detection experiments and their assignment to the observations of van Rijnbach [66] and Tol [65]. The Utrecht values of Tol suffered from a calibration error and so are included in the table only for completeness. The last column represents the approximate decay width calculated from modelling the states as a semi-classical oscillation, see equation (3.26), and its values are unhelpful in making assignments to the observations.

Exp [66]	Exp [65]	Theor	$\mathcal{A}_v$ (E_h)	$f_{5,v}$ (%)	Case (c)	[86] assignment	Γ_v (MHz)
−13.57	–	−13.259	1.045	98.8	2_u, $J = 3$	2_u, $J = 2$	9.0
-11.70^{b}	-11.69^{bc}	−11.433	0.711	95.5	1_u, $J = 1$	1_u, $J = 1$	42.3
-11.10^{b}	-10.93^{bc}	−10.930	1.087	87.5	$1_u, 0_u^+$, $J = 3$	1_u, $J = 2$	111.4
−8.94	-8.96^{c}	−8.705	1.169	98.9	2_u, $J = 3$	2_u, $J = 2$	6.0
−7.44	-7.44^{c}	−7.262	0.741	95.8	1_u, $J = 1$	1_u, $J = 1$	16.8
−7.01	-7.03^{c}	-6.895^{a}	1.148	79.6	$1_u, 0_u^+$, $J = 3$	1_u, $J = 2$	68.9
−5.64	-5.65^{c}	−5.463	1.262	98.9	2_u, $J = 3$	0_u^+, $J = 1$	2.0
−4.53	-4.51^{c}	−4.393	0.784	96.8	$1_u, 0_u^+$, $J = 1$	0_u^+, $J = 3$	11.9
−4.26	-4.26^{c}	−4.141	1.389	91.7	$0_u^+, 1_u$, $J = 3$	1_u, $J = 2$	28.5
-3.49^{b}	–	−3.438	1.209	99.2	2_u, $J = 2$	3_g, $J = 3$	2.6
−3.38	-3.37^{c}	−3.251	1.477	99.2	2_u, $J = 3$	2_u, $J = 2$	2.6
−2.87	–	–	–	–	–	2_u, $J = 4$	–
−2.60	-2.57^{c}	−2.499	0.855	99.0	$1_u, 0_u^+$, $J = 1$	1_u, $J = 3$	2.6
−2.42	-2.40^{c}	−2.338	1.574	96.3	$0_u^+, 1_u$, $J = 3$	1_u, $J = 1$	8.2
−2.01	-2.02^{c}	−1.937	1.236	98.5	2_u, $J = 2$	0_u^+, $J = 1$	3.1
−1.88	-1.88^{c}	−1.807	1.719	99.7	2_u, $J = 3$	2_u, $J = 2$	0.5
−1.54	–	−1.326	0.997	98.7	$0_u^+, 1_u$, $J = 1$	2_u, $J = 4$	2.0
−1.28	−1.287	−1.223	1.814	99.7	$0_u^+, 1_u$, $J = 3$	1_u, $J = 1$	0.3
–	–	−1.013	1.340	98.2	2_u, $J = 2$	–	2.0
−0.98	−0.996	-0.928^{a}	2.272	84.6	2_u, $J = 3$	2_u, $J = 2$	17.8
–	−0.622	−0.589	1.943	99.3	$0_u^+, 2_u$, $J = 3$	1_u, $J = 1$	0.5
−0.52	−0.533	-0.487^{a}	1.457	86.8	2_u, $J = 2$	2_u, $J = 2$	8.7
−0.46	−0.465	–	–	–	$2_u, 0_u^+$, $J = 3$	0_u^+, $J = 3$	–
−0.27	−0.275	–	–	–	$0_u^+, 2_u$, $J = 3$	0_u^+, $J = 1$	–
–	–	−0.215	1.620	99.1	2_u, $J = 2$	–	0.3
−0.19	−0.182	−0.184	2.141	95.6	2_u, $J = 3$	2_u, $J = 2$	1.3
–	–	−0.167	3.597	92.7	$0_u^+, 1_u$, $J = 3$	–	1.1
–	−0.105	−0.109	1.693	99.5	2_g, $J = 2$	0_u^+, $J = 1$	0.1
-0.08^{b}	–	−0.066	3.094	99.4	2_u, $J = 3$	0_u^+, $J = 3$	0.1
–	−0.045	−0.050	4.138	97.6	$0_u^+, 1_u$, $J = 3$	0_u^+, $J = 1$	0.2

[a] Observability criteria relaxed.

[b] Measurement that was recorded as a weakly observed level.

[c] Value from the Amsterdam measurements of Tol corrected for calibration error.

Table 3.13: Theoretical bound levels, with energies in GHz from the $j = 2$ asymptote, that are expected to be observed for binding energies greater than 14 GHz in experiments that use unpolarised atoms and an ion detection mechanism.

Theor	$\mathcal{A}_v$ (E_h)	$f_{5,v}$ (%)	Case (c)	Γ_v (MHz)
−95.030	0.717	98.8	2_u, $J = 3$	55.0
−71.694	0.734	98.7	2_u, $J = 3$	39.7
−53.287	0.753	98.5	2_u, $J = 3$	36.9
−49.151	0.719	88.6	$1_u, 0_u^+$, $J = 3$	334.2
−38.927	0.875	99.1	2_u, $J = 3$	20.9
−35.158	0.795	87.7	$1_u, 0_u^+$, $J = 3$	278.9
−27.876	0.894	98.9	2_u, $J = 3$	17.9
−20.061	0.890	99.5	2_u, $J = 2$	7.3
−19.500	0.955	98.8	2_u, $J = 3$	14.6

Table 3.14: Theoretical resonances, with energies in MHz from the $j = 1$ asymptote that satisfy the observability criteria for ion detection experiments. Note that these criteria exclude all purely long-range levels. The assignments are calculated from only the closed channels of the resonance wave function.

Exp	Theor	Γ_v^{pre}(MHz)	$\mathcal{A}_v$ (E_h)	$f_{5,v}$ (%)	Case (c)	[86] assignment
−452	−427	70.2	1.331	98.9	0_g^-, $J = 3$	0_g^-, $J = 3$
−343	−283	6.5	1.827	99.6	0_g^-, $J = 1$	0_g^-, $J = 1$
−238	−182	36.0	1.708	98.7	0_g^-, $J = 3$	0_g^-, $J = 3$
−159	−117	3.3	2.418	99.2	0_g^-, $J = 1$	0_g^-, $J = 1$
−89	−65	16.1	2.154	98.8	0_g^-, $J = 3$	0_g^-, $J = 3$
−43	−40	1.3	3.273	99.5	0_g^-, $J = 1$	0_g^-, $J = 1$

of the experimental observations. These are presented in table 3.14. Note that effectively a third observability criterion is active, as each of these theoretical levels possesses a predissociation width of less than 100 MHz, determined by the search process described in section 3.3.4. This is a reasonable criterion to place upon the system as levels with large widths are very weak and difficult to observe experimentally.

The assignments agree exactly with those of Deguilhem *et al.* It is interesting to see that the only observable levels near this asymptote are those of the gerade excited manifold, despite the indications and conclusions of the previous sections regarding gerade coupling and triplet behaviour. This may be explained by again analysing the nature of the single-channel potentials. In contrast to the $j = 2$ asymptotic potentials, the 0_g^- adiabatic potential asymptoting to $j = 1$ that is mostly quintet at short range reaches 20% triplet character for interatomic distances larger than 300 a_0 and, more importantly, allows wave functions to extend outwards to this distance for binding energies less than 1.8 GHz. Hence, levels near the $j = 1$ asymptote have a greater opportunity to be coupled to the metastable manifold.

All of the resonances that have been calculated near the $j = 0$ asymptote, listed in table E.2, cannot be observed in ion-detection experiments because they are purely long-range

Table 3.15: Theoretical resonances, with energies in MHz from the $j = 0$ asymptote, that are observable in spin-polarised experiments using an optical detection mechanism and their assignments to Kim *et al* [67]. The observability criteria for $\mathcal{A}_v$, $f_{5,v}$ and Γ_v^{pre} have been applied in a similar manner to table 3.14. An additional criterion, $f_{R<20}$, is present which indicates whether or not the resonance has a purely long-range nature. For purely long-range resonances, the criterion upon $f_{5,v}$ may be ignored, as ionisation cannot occur.

Exp	Theor	Γ_v^{pre}(MHz)	$\mathcal{A}_v$ (E_h)	$f_{R<20}$	Case (c)
−1418.1	−1418.05	0.008	3.472	1×10^{-9}	0_u^+, $J = 1$
−648.5	−648.49	0.008	2.095	3×10^{-10}	0_u^+, $J = 1$
−253.3	−253.12	0.008	3.812	1×10^{-11}	0_u^+, $J = 1$
−79.6	−79.65	0.002	4.399	6×10^{-11}	0_u^+, $J = 1$
−18.2	−18.29	0.002	6.858	2×10^{-11}	0_u^+, $J = 1$

and hence cannot ionise. Experiments that use an optical detection method, however, can observe these states. For the Kim *et al* experiments, only spin-polarised atoms are used and so only ungerade excited resonances may be observed. The list of resonances that can be assigned to the Kim *et al* measurements are presented in table 3.15. The very good agreement between theory and experiment is due to the purely long-range nature of the resonances, as the long-range electronic potentials are well understood in terms of their precise atomic properties. Note that purely long-range resonances are not affected by the short-range quintet fraction $f_{5,v}$ as they cannot extend into the short-range distances required for ionisation.

The search for resonances was also performed for up to 2 GHz of detuning from the $j = 0$ and $j = 1$ asymptotes and some additional resonances were found near the $j = 1$ asymptote that fit the observability criteria for ion detection experiments. These are listed in table E.4. A large number of the resonances appear to overlap one another and almost all of the resonances possess a short-range proportion $f_{R<20}$ between 10^{-6} and 10^{-8}. As mentioned in section 3.3.4, this does not distinguish the purely long-range resonances from others. As all of the predictions are gerade levels, only unpolarised ion detection experiments would be able to observe the peaks, which in turn requires the resonances to not be purely long-range so that they can produce ions for detection. The dynamics of these resonances should therefore be analysed in more detail in future calculations.

3.5 SHORT-RANGE CORRECTION

As the theoretical binding energies for ungerade levels are consistently lower than the experimental observations, a correction to the input potentials of the theoretical calculation is suggested. Because the only gerade level that satisfies the observability criteria is reasonably close to its assigned observation, only the ungerade potentials are considered for variation. Motivated by the observation that many ultracold molecular properties are very sensitive to the slope of the potential at the inner classical turning point [103], the MCSCF $^{1,3}\Sigma_u^+$ and $^{1,3}\Pi_u$ and the MRCI $^5\Sigma_{g,u}^+$ and $^5\Pi_{g,u}$ input potentials are modified in this region by introducing a multiplicative factor c through a smoothing function of the form

$$V'(R) = V(R) \begin{cases} (1+2c) & R < R_1 \\ [1 + c(1+\cos[a(R-R_1)])] & R_1 < R < R_2 \; , \\ 1 & R_2 < R \end{cases} \tag{3.27}$$

where $a = \pi/(R_2 - R_1)$, which represents a fractional increase of $2c$ inwards of R_1 that is smoothly activated over the region $R_1 < R < R_2$. Because the bound levels are strongly quintet in character at short range (due to the observability criterion $f_{5,v} > 87.5\%$) the largest influence from variation of the potentials is expected to come from the quintet potentials. In fact, because the ${}^5\Pi_u$ potential is purely repulsive, the ${}^5\Sigma_u^+$ potential will have the largest influence. This need to vary the quintet potentials, however, contradicts the expectation [124] that the MRCI potentials are the most accurate and that the MCSCF potentials are more likely to require adjustment.

Many different combinations of variations can be performed that cause both beneficial and detrimental changes to occur. Five such variations were performed in total and the results and their assignments are presented in tables 3.16 and 3.17 for the polarised and unpolarised results respectively. Variation A applies a 1% increase ($c = 0.005$) turned on over the region $5 < R < 10$ a_0 to all of the ungerade potentials. The results from A are promising and show much improvement in both binding energy and observability criteria. Variation B applies the scaling to only the MCSCF ${}^{1,3}\Sigma_u^+$ and ${}^{1,3}\Pi_u$ potentials and has only a modest effect on the results. A larger range for variation is applied in C, turned on over the region $20 < R < 30$ a_0 and applied to only the MCSCF potentials but this produces many detrimental effects in the assignments. Variation D, which applies the variation of A to only the MRCI ${}^5\Sigma_u^+$ and ${}^5\Pi_u$ potentials, produces results with a large improvement, although not as much as variation A. Variation E applies the combined variations of C and D, but is not successful in producing desirable changes.

Although the variation A (the effect of which is shown in figure 3.2) produces the best results, variation D ranks a close second. The results of A are now discussed in more detail. In the spin polarised results, the variation improves the situation for the levels -0.928 and -0.487 GHz, such that they no longer require a relaxation of the criteria for assignment. For most of the levels, the differences between the experimental observations and the theoretical binding energies have been significantly reduced and are within the experimental uncertainty of 20 MHz.

The situation for the unpolarised experiment results is improved even more by the use of the variation. A new theoretical assignment to the observation -0.27 GHz is now possible, albeit with a relaxed criterion, and the spurious theoretical level at -1.013 GHz has been removed. The levels at -6.895, -0.928 and -0.487 GHz that previously required relaxation of one criterion are now firmly placed as assignments to observations. The agreement between the theoretical and experimental binding energies is also greatly improved.

In total, between the polarised and unpolarised experiments, only three observed levels

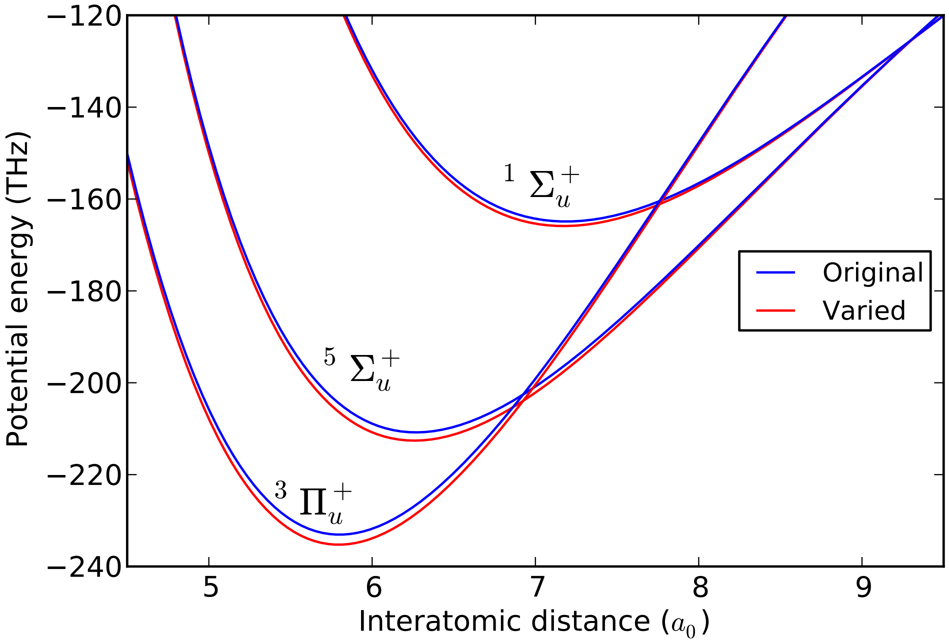

Figure 3.2: A plot of the scaled ungerade potentials that are not purely repulsive, before and after application of equation (3.27) for variation A, which scales the potentials by 1% turned on from $10\,a_0$ to $5\,a_0$.

are unable to be associated with the theoretical levels after application of the variation if weakly observed levels are excepted. Only two spurious levels were found that could not be assigned to any experimental observation. This is deemed to be a great success of the short-range correction that has been made possible due to the multichannel calculations.

The resonance levels above the $j = 2$ asymptote do not greatly benefit from the short-range correction to the ungerade potentials as applied in variations A–E. This is because all levels near the $j = 0$ asymptote are purely long-range and the ungerade levels that are near the $j = 1$ asymptote have very large ionisation rates as can be seen in tables E.2 and E.3.

During the review of this thesis, it was brought to the attention of the author that previous work relevant to corrections of potentials has been published [125, 126]. The authors of the articles found that, for a set of potentials carefully constructed from detailed physically motivated adjustments to standard forms of diabatic potentials, there was a consistent difference from *ab initio* potentials from MRCI and MCSCF calculations involving a slight increase of well depth by $< 3\%$ and a slight shift to smaller R by < 5 mÅ. While the adjustment in this thesis has a minor, unintended, effect of shifting the well position to smaller R, in hindsight it would be valuable to consider a translation of the *ab initio* potentials as a separate parameter. However, this consideration does not reduce the validity of the correction considered in this thesis, and the agreement between experiment and theory gained from the correction confirms its usefulness.

Table 3.16: The experimental observations of Kim *et al* and the effectiveness of theoretical assignments from the use of different variations of the short-range potentials. Missing assignments for an observation are highlighted in red, and levels that require a relaxation of the observability criteria are highlighted in yellow. The results from unvaried potentials are presented in the second column and the forms of the variations are described in the text. From the total missing assignments and relaxations required, it is obvious that variation A produces the best match. All energies are in GHz.

		Variation				
Exp	Theor	A	B	C	D	E
−13.67	−13.259	−13.626	−13.261	−13.266	−13.621	−13.634
−11.70	−11.434	−11.772	−11.447	–	−11.764	−11.840
–	–	−11.246	–	–	−11.220	–
–	−9.051	−9.324	−9.051	−9.052	−9.324	−9.324
−8.95	−8.705	−8.970	−8.706	−8.710	−8.967	−8.975
−7.45	−7.262	−7.498	−7.270	–	−7.493	−7.547
–	–	−7.112	–	–	−7.101	–
−5.90	−5.729	−5.920	−5.729	−5.729	−5.920	−5.921
−5.64	−5.463	−5.650	−5.464	−5.467	−5.648	−5.654
−4.53	−4.394	−4.554	−4.398	–	−4.551	−4.580
−4.25	−4.142	−4.293	−4.152	−4.129	−4.285	−4.338
−3.57	−3.438	−3.567	−3.438	−3.438	−3.566	−3.567
−3.37	−3.251	−3.376	−3.252	−3.252	−3.375	−3.377
−2.59	−2.499	−2.603	−2.500	−2.515	−2.603	−2.609
−2.42	−2.338	−2.435	−2.340	−2.358	−2.433	−2.449
−2.00	−1.937	−2.020	–	−1.936	−2.019	−2.017
−1.88	−1.807	−1.886	−1.808	−1.806	−1.886	−1.883
−1.37	−1.326	−1.387	−1.327	−1.334	−1.387	−1.389
−1.275	−1.223	−1.282	−1.224	−1.224	−1.282	−1.283
−1.22	−1.160	−1.220	–	−1.160	−1.220	−1.220
−1.07	−1.013	−1.062	−1.014	−1.014	−1.062	−1.062
−0.98	−0.928	−0.974	−0.928	−0.928	−0.973	−0.974
−0.62	−0.589	−0.621	−0.589	−0.590	–	−0.622
−0.51	−0.487	−0.515	−0.489	−0.489	−0.511	−0.516
−0.455	–	–	−0.432	−0.435	−0.458	−0.459
−0.280	−0.263	−0.278	−0.267	–	−0.276	–
−0.235	−0.215	−0.228	−0.215	−0.215	−0.228	−0.228
−0.200	−0.185	−0.199	−0.185	−0.185	−0.199	−0.199
–	−0.184	−0.196	−0.184	–	−0.196	−0.197
−0.185	−0.167	−0.179	−0.167	−0.168	−0.178	−0.181
−0.09	−0.083	−0.089	−0.083	−0.083	−0.089	−0.089
Total Missing	1	1	2	4	1	1
Total Relaxations	4	2	2	5	4	6

Table 3.17: The experimental observations of Rijnbach and Tol and the effectiveness of theoretical assignments from the use of different variations of the short-range potentials. Missing assignments for an observation are highlighted in red along with spurious theoretical levels that cannot be assigned to any experimental observation. Levels that require a relaxation of the observability criteria are highlighted in yellow. The results from unvaried potentials are presented in the second column and the forms of the variations are described in the text. From the total missing assignments, it is obvious that variation A produces the best match. The level at −0.105 GHz that is assigned to 2_g, $J = 2$ in table 3.12 has been omitted as the gerade potentials are not varied. All energies are in GHz.

		Variation				
Exp	Theor	A	B	C	D	E
−13.57	−13.259	−13.626	−13.261	−13.266	−13.621	−13.634
-11.70^b	−11.434	−11.772	−11.447	–	−11.764	−11.845
-11.10^b	−10.930	−11.246	−10.957	–	−11.224	−11.392
−8.94	−8.705	−8.970	−8.706	−8.710	−8.966	−8.975
−7.44	−7.262	−7.498	−7.270	–	−7.493	−7.547
−7.01	−6.895	−7.119	−6.912	–	−7.103	–
−5.64	−5.463	−5.650	−5.464	−5.466	−5.647	−5.654
−4.53	−4.394	−4.554	−4.398	–	−4.551	−4.580
−4.26	−4.145	−4.293	−4.152	–	−4.285	−4.338
-3.49^b	−3.438	−3.567	−3.438	–	−3.566	−3.567
−3.38	−3.251	−3.376	−3.252	–	−3.375	−3.377
−2.87	–	–	–	–	–	–
−2.60	−2.499	−2.603	−2.500	−2.515	−2.603	−2.609
−2.42	−2.338	−2.435	−2.340	−2.358	−2.433	−2.449
−2.01	−1.937	−2.020	-	−1.936	−2.019	−2.017
−1.88	−1.807	−1.886	−1.808	−1.806	−1.866	−1.883
−1.54	−1.326	−1.387	−1.327	−1.333	−1.338	−1.390
−1.28	−1.223	−1.282	−1.224	−1.224	−1.282	−1.283
–	−1.013	–	–	−1.014	−1.062	−1.062
−0.98	−0.928	−0.974	0.928	−0.928	−0.973	−0.974
-0.622^c	−0.589	−0.621	−0.589	−0.590	–	−0.622
−0.52	−0.487	−0.515	−0.489	−0.489	–	−0.516
−0.46	–	–	−0.432	−0.435	−0.458	−0.459
−0.27	–	−0.278	–	–	−0.276	−0.348
–	−0.215	−0.228	−0.215	−0.215	−0.228	−0.228
–	–	–	–	–	–	−0.199
−0.19	−0.184	−0.196	−0.185	−0.185	−0.196	−0.197
–	−0.167	−0.179	−0.167	−0.168	–	−0.181
–	–	–	–	−0.083	–	−0.089
-0.08^b	−0.066	−0.072	−0.066	–	−0.071	−0.072
-0.045^c	−0.050	−0.055	−0.050	−0.052	−0.055	−0.057
Total Missing or Spurious	6	4	5	14	5	6
Total Relaxations	3	1	3	2	1	5

[b] Measurement that was recorded as a weakly observed level.

[c] Value of Tol that was not observed by van Rijnbach.

Table 3.18: Comparison of the energies, in GHz, of theoretical levels that have been assigned to experimental observations near the $j = 2$ asymptote, calculated using either the long-range coefficients of Marinescu [110] or Zhang *et al* [107]. The short-range potentials have been corrected by applying variation A, as described in section 3.5.

Marinescu	Zhang *et al*	Marinescu	Zhang *et al*	Marinescu	Zhang *et al*
−13.626	−13.622	−3.567	−3.564	−0.974	−0.973
−11.772	−11.771	−3.376	−3.374	−0.621	−0.621
−11.246	−11.254	−2.603	−2.602	−0.515	−0.514
−9.324	−9.319	−2.435	−2.434	−0.278	−0.279
−8.970	−8.966	−2.020	−2.019	−0.228	−0.228
−7.498	−7.497	−1.886	−1.885	−0.199	−0.199
−7.119	−7.121	−1.387	−1.386	−0.196	−0.196
−5.920	−5.917	−1.282	−1.281	−0.179	−0.179
−5.650	−5.648	−1.220	−1.219	−0.072	−0.071
−4.554	−4.552	−1.062	−1.061	−0.055	−0.055
−4.293	−4.293				

3.6 ZHANG *et al* COEFFICIENTS

The calculations undertaken in the previous sections of this chapter have used the coefficients of Marinescu [110] for the long-range Born-Oppenhemier potentials, that are shown in table 2.1. Calculations have also been performed using the more recent coefficients of Zhang *et al* [107]. The calculated binding energies do not significantly differ between the different sets of coefficients. The only difference of note is that the Zhang *et al* coefficients predict an additional experimental assignment at −0.434 GHz when using the unvaried potentials. However, once variation A (described in section 3.5) is applied to the short-range potentials, the assignments predicted by the different coefficients are identical. Table 3.18 shows the difference between the binding energies for the two sets of coefficients after the short-range correction is applied.

3.7 SUMMARY

In this chapter the $2s2p$ manifold of excited states has been investigated using calculations with varying degrees of approximation, together with an exact calculation. It has been shown that the non-adiabatic and Coriolis couplings that are ignored in approximate calculations can significantly alter the results and these differences are measurable in experiment. Furthermore, although the input short-range potentials of Deguilhem *et al* [86] are very accurate, a 1% modification to the slope of the inner classical turning point of the ungerade quintet potentials is required to produce agreement between theory and experiment. This agreement has been obtained by formulating observability criteria that quantify the likelihood for the metastable gas to make a transition to the probed state and to also quantify the likelihood for observing such a state in terms of the probability of ionisation.

Several levels were observed in the $2s2p$ manifold that are classified as purely long-range states. These states exist entirely at large interatomic distances, $R > 100\,a_0$ and are determined completely by well known atomic parameters. In the next chapter, a particular set of levels in the 0_u^+, $J = 1$ set that asymptotes to $j = 0$ is investigated in terms of the precise nature of the line shapes that occur in the photoassociation process. Although any level may be investigated in such detail, the 0_u^+ levels have been chosen because there are existing measurements of their line shifts [70] and because they do not depend on any uncertainties in the short-range character of the potentials. They may also be accurately represented by the single-channel approximation as the non-adiabatic and Coriolis couplings for the purely long-range levels are not significant [90].

Chapter 4

Photoassociation dynamics of long-range levels

4.1 INTRODUCTION

Photoassociation (PA) of ultracold atoms provides a powerful technique to study the dynamics of ultracold collisions. The technique involves the resonant excitation of two atoms into a molecular state by the use of a carefully tuned laser. A very high resolution spectrum (< 1 MHz) can be observed in experiment due to the narrow thermal distribution of energies in the initial scattering state. In fact, the resolution of the spectra is often much narrower than the natural line width of the transition. For example, the helium $2s \to 2p$ transition has a width of 1.626 MHz which is much larger than the 42 kHz thermal width of colliding helium atoms at 2 μK. This means that the free→bound transition may be considered as well defined as an equivalent bound→bound transition of more traditional spectroscopy. Furthermore the free→bound spectroscopy allows for measurements to be made relative to well known reference energies which makes absolute level detection possible, a feat that is difficult in other types of spectroscopy.

For normal temperatures of the colliding atoms, calculations of the photoassocation process must consider a vast number of entrance channels corresponding to many different partial waves. This makes PA very difficult to analyse and observe at room temperature. However, the advent of cooling techniques to attain ultracold temperatures produces conditions where only a very few partial waves contribute and may even restrict collisions to the lowest order s-wave rotation. This has important consequences for the allowed configurations of excited molecules that may be formed, as selection rules limit the coupling of the total angular momentum. One advantage of using ultracold temperatures is that studying slowly rotating molecules is not only possible but relatively easy.

Many species other than metastable helium have been used in PA experiments, of which a selection of experiments and calculations may be found in [46] and [41]. Combinations of mixed species [60, 127] have also been investigated through the use of PA. The dynamics of PA has been studied in Bose-Einstein condensates where the many-body interactions can be highly influenced by the laser coupling [56, 128, 129]. The ultra-fast domain of femtosecond [47, 48] or even attosecond [49] light pulses to photoassociate molecules has also been investigated. These techniques allow detailed control of the photoassociation process, including the possibility of limiting the loss rates of the process.

One very important aspect of photoassociation spectroscopy that cannot be observed in most other types of spectroscopy is the ability to excite purely long-range molecules. These molecules possess inner classical turning points that exist far beyond the region of bound levels commonly associated with molecules, ranging from 100 a_0 up to 500 a_0. The properties for these levels can be studied in a very precise manner because their interactions are completely described by their long-range components only, such as the dispersion and dipole-dipole forces. These interactions are specified entirely in terms of atomic properties which are often known to much greater accuracy than the equivalent molecular properties. The photoassociation of these purely long-range states may also be used to precisely determine properties of the ground state system. This is because the interactions of the excited state system are highly sensitive to the coupling from the ground level and so small perturbations in the ground level will have a significant effect upon the photoassociation spectra. Molecular and collisional properties, such as the scattering length or radiative lifetime [46], may be calculated from observations of these long-range levels. Furthermore, processes that may occur at short interatomic distances such as ionisation are heavily suppressed in these cases. A general review of ultracold photoassociation is given in [41].

Advanced techniques such as two-photon PA have been used by Moal *et al* [73] to accurately measure the least bound vibrational level of the $^5\Sigma_g^+$ metastable state by analysing a dark resonance in the spectra. From this binding energy, combined with the *ab initio* potential of Przybytek and Jeziorski [93], a high precision value of the scattering length $a = 7.512 \pm 0.005$ nm was obtained. A related two-photon experiment was also performed with ytterbium by Kitagawa *et al* [51].

Photoassociation in metastable rare gases is of particular interest as the large internal energy of $\sim$ 20 eV can be released during collisions and provides useful experimental strategies to study these quantum gases. Two accessible transitions are of experimental interest, the triplet $2s \to 2p$ (1083 nm) and $2s \to 3p$ (389 nm) transitions. These are illustrated in figure 4.1. In this chapter, the system of colliding metastable helium atoms being photoassociated to the $2s2p$, 0_u^+, $J = 1$ molecular state belonging to the $j = 0$ asymptote will be modelled. This molecular state fits entirely within the purely long-range description of the photoassociation process, as the inner classical turning points of levels in the potential lie at large interatomic distances of approximately 150 a_0. A diagram of this process is presented in figure 4.2, showing the notation used for each energy pertaining to the system and the transition between them.

A theoretical description for a generalised PA problem has been formulated by Bohn and Julienne [52] by making use of quantum defect theory and treating the laser coupling as a perturbation. In this way, analytical derivation of the PA line shapes was possible. Simoni *et al* [53] calculated line shapes in rubidium for arbitrary laser intensity, but assumed

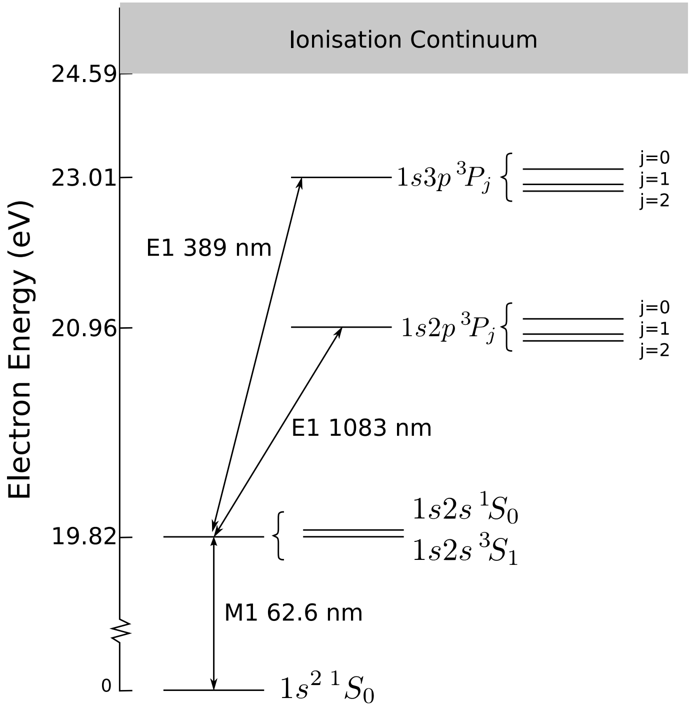

Figure 4.1: Atomic states of helium relevant to photoassociation of metastable helium.

that the laser coupling was negligible at asymptotic separation. Napolitano [54] presented a theory for the semi-analytic calculation of S-matrix elements in a sodium system which made use of dressed states to correctly treat the asymptotic laser coupling. Napolitano, however, assumed that the detuning was large compared with the intensity and did not include fine structure into the formalism. Montavão and Napolitano [55] then extended the formalism of [54] to calculate line shapes of strontium.

Theoretical calculations of PA dynamics in metastable helium are limited to the calculation of Portier *et al* [88], which was based upon second-order perturbation theory and was therefore restricted to the low laser intensity limit. The need exists to determine the behaviour of metastable helium under high intensity photoassociation and this is the subject of the study presented in chapter. A series of progressively more accurate calculations will be performed, starting from a perturbative calculation and finishing with a complete multichannel calculation. The multichannel equations will be solved without invoking approximations regarding the laser detunings and coupling strengths. To do this, the dressed state formalism of Napolitano will be applied in order to correctly treat the asymptotic laser coupling. However, numerical calculations will be employed so that arbitrary laser intensity and detunings can be investigated without treating the laser coupling as a perturbation.

4.2 Laser coupling

The exact form of the laser coupling is required to be able to carefully investigate the properties of the matter and laser system. The definition of the laser coupling from section

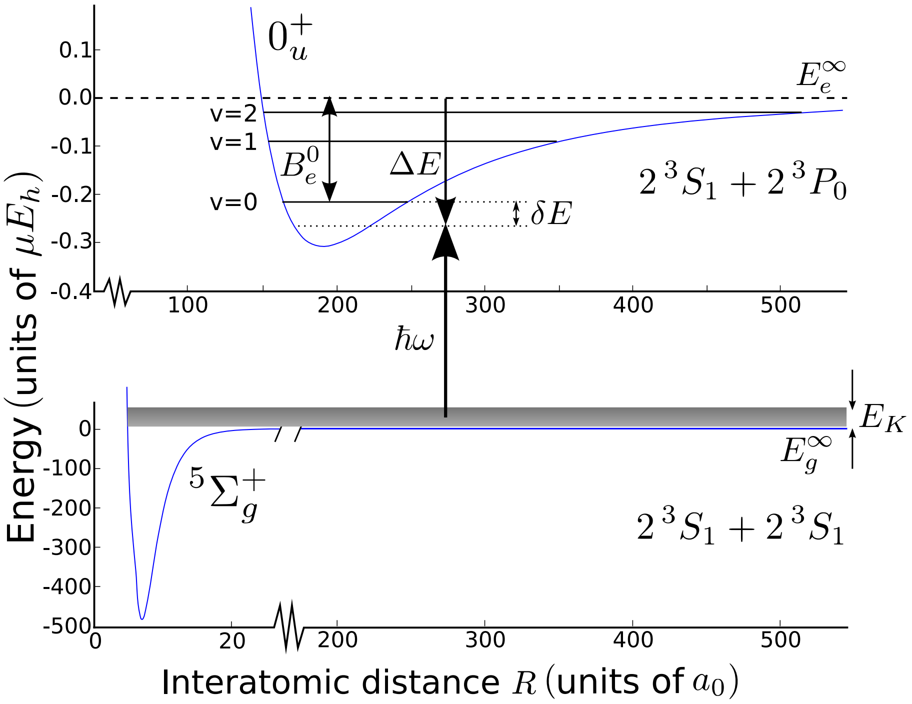

Figure 4.2: Photoassociation of metastable helium to the $2s2p$, 0_u^+, $J = 1$ molecular state asymptoting to $j = 0$. $E_{g,e}^\infty$ are the asymptotic energies for the metastable (ground) and $2s2p$ (excited) state potentials respectively and B_e^0 is the binding energy of the unperturbed $v = 0$ level. ΔE is the detuning from asymptotic resonance and δE is the line shift of the bound level due to the laser coupling. Note the disparate scales along the interatomic axis.

2.1.5 is:

$$\hat{H}_{\text{int}} = -\left(\frac{e}{m}\right) \sum_{i=1,2} \hat{\boldsymbol{p}}_i \cdot \hat{\boldsymbol{A}}(\boldsymbol{r}_i), \tag{4.1}$$

where the vector potential of the laser field is

$$\hat{\boldsymbol{A}}(\boldsymbol{r}_i) = \sum_{\xi} \left[\boldsymbol{\mathcal{E}}_\xi(\boldsymbol{r}_i)\hat{a}_\xi + \boldsymbol{\mathcal{E}}_\xi^*(\boldsymbol{r}_i)\hat{a}_\xi^\dagger\right] \tag{4.2}$$

and $\boldsymbol{\mathcal{E}}_\xi$ is given by

$$\boldsymbol{\mathcal{E}}_\xi(\boldsymbol{r}_i) = \sqrt{\frac{\hbar}{2\omega_\xi \epsilon_0 \mathcal{V}}}\, e^{i\boldsymbol{k}\cdot\boldsymbol{r}_i} \boldsymbol{\epsilon}_\xi. \tag{4.3}$$

Normally, the dipole approximation (DA) is invoked because it is known that the atomic $2s \rightarrow 2p$ transition is dominated by the electric dipole term, see figure 4.1. However, the DA requires $\boldsymbol{k} \cdot \boldsymbol{r_i} \ll 1$. Consequently the approximation is not necessarily valid for long range molecules where the interatomic distance, R, is an appreciable fraction of k. In this section, the complete laser coupling term will be derived without making the DA. A detailed comparison of results obtained with and without the DA will be performed for the non-perturbative, multichannel calculation. The DA will be made in the perturbative calculations as they are already approximate and all previous calculations make this

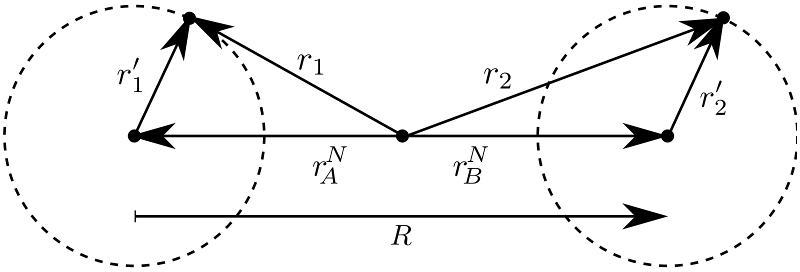

Figure 4.3: The coordinate system chosen to represent the nuclear and electron coordinates where the origin of the coordinate frame is located at the centre of the dimer. In this particular representation, the electron around atom A has been given the label 1 and that around B the label 2.

approximation.

In order that the derivation may be more easily generalised to other systems, the basis states of the system will not be assumed to be the hybrid jj basis (2.29) but will instead take the more general form

$$|a\rangle \equiv |\psi_a^{\text{rot}}\rangle|\psi_a^{\text{el}}\rangle, \tag{4.4}$$

where $a = (g, e)$. In this factored form, all of the nuclear rotation of the molecule that depends upon the orientation angles (θ, ϕ) is contained in $|\psi_a^{\text{rot}}\rangle$ and no $\boldsymbol{R}$-dependence is present in the electronic states $|\psi_a^{\text{el}}\rangle$.

The required matrix elements are

$$V_{eg}^{\text{int}} \equiv \langle e|\langle n-1, \omega, \boldsymbol{\epsilon}_\lambda|\hat{H}_{\text{int}}|g\rangle|n, \omega, \boldsymbol{\epsilon}_\lambda\rangle. \tag{4.5}$$

In equation (4.5), only the $\hat{a}_\xi$ terms of $\hat{H}_{\text{int}}$ contribute, which leads to

$$V_{eg}^{\text{int}} = -\frac{e}{m}\sqrt{\frac{n\hbar}{2\omega\epsilon_0\mathcal{V}}}\langle e|\sum_i \left[\hat{\boldsymbol{p}}(\boldsymbol{r}_i)\cdot\boldsymbol{\epsilon}_\lambda\right] e^{i\boldsymbol{k}\cdot\boldsymbol{r}_i}|g\rangle \tag{4.6}$$

where $\langle n-1, \omega, \boldsymbol{\epsilon}_\lambda|\hat{a}_\xi|n, \omega, \boldsymbol{\epsilon}_\lambda\rangle = \delta_{\lambda\xi}\sqrt{n}$ has been used. In order to simplify this equation, a coordinate system must be specified. If the origin of this system is taken to be the centre of mass of the dimer, then

$$\boldsymbol{r}_i = \hat{\eta}_i\frac{1}{2}\boldsymbol{R} + \boldsymbol{r}_i' \tag{4.7}$$

$$\boldsymbol{R} = \boldsymbol{r}_B^N - \boldsymbol{r}_A^N \tag{4.8}$$

where $\boldsymbol{r}_A^N$ and $\boldsymbol{r}_B^N$ are the coordinates for the nucleus of atom A and B respectively (see figure 4.3). As the basis states are to be symmetrised with respect to electron exchange, it is not known which electron label (1 or 2) is associated with which atom and so an operator $\hat{\eta}_i$ is defined that takes the values of ∓ 1 if electron i orbits nucleus A or B respectively. This operator facilitates the evaluation of the matrix element in (4.6). Similarly the momentum operators are given by

$$\hat{\boldsymbol{p}}(\boldsymbol{r}_i) = \hat{\eta}_i\frac{1}{2}\hat{\boldsymbol{p}}(\boldsymbol{R}) + \hat{\boldsymbol{p}}(\boldsymbol{r}_i'). \tag{4.9}$$

With this representation of the coordinate system, equation (4.6) becomes

$$V_{eg}^{\mathrm{int}} = -\frac{e}{m}\sqrt{\frac{n\hbar}{2\omega\epsilon_0\mathcal{V}}}\sum_i \langle e| \left[\hat{\eta}_i \frac{1}{2}\hat{\boldsymbol{p}}(\boldsymbol{R}) + \hat{\boldsymbol{p}}(\boldsymbol{r}_i')\right] \cdot \boldsymbol{\epsilon}_\lambda e^{\hat{\eta}_i i\boldsymbol{k}\cdot\boldsymbol{R}/2} e^{i\boldsymbol{k}\cdot\boldsymbol{r}_i'}|g\rangle. \tag{4.10}$$

If the states are expanded in the product form (4.4), the action of the momentum operators within the inner product $\langle e|\ldots|g\rangle$ produces the following terms

$$\begin{aligned}
&\langle\psi_e^{\mathrm{rot}}|\frac{i\boldsymbol{k}\cdot\boldsymbol{\epsilon}_\lambda}{4}\langle\psi_e^{\mathrm{el}}|\hat{\eta}_i^2 e^{\hat{\eta}_i i\boldsymbol{k}\cdot\boldsymbol{R}/2} e^{i\boldsymbol{k}\cdot\boldsymbol{r}_i'}|\psi_g^{\mathrm{el}}\rangle|\psi_g^{\mathrm{rot}}\rangle \\
&+ \langle\psi_e^{\mathrm{rot}}|\frac{1}{2}\langle\psi_e^{\mathrm{el}}|\hat{\eta}_i e^{\hat{\eta}_i i\boldsymbol{k}\cdot\boldsymbol{R}/2} e^{i\boldsymbol{k}\cdot\boldsymbol{r}_i'}|\psi_g^{\mathrm{el}}\rangle\hat{\boldsymbol{p}}(\boldsymbol{R})\cdot\boldsymbol{\epsilon}_\lambda|\psi_g^{\mathrm{rot}}\rangle \\
&+ \langle\psi_e^{\mathrm{rot}}|i(\boldsymbol{k}\cdot\boldsymbol{\epsilon}_\lambda)\langle\psi_e^{\mathrm{el}}|e^{\hat{\eta}_i i\boldsymbol{k}\cdot\boldsymbol{R}/2} e^{i\boldsymbol{k}\cdot\boldsymbol{r}_i'}|\psi_g^{\mathrm{el}}\rangle|\psi_g^{\mathrm{rot}}\rangle \\
&+ \langle\psi_e^{\mathrm{rot}}|\langle\psi_e^{\mathrm{el}}|e^{\hat{\eta}_i i\boldsymbol{k}\cdot\boldsymbol{R}/2} e^{i\boldsymbol{k}\cdot\boldsymbol{r}_i'}\hat{\boldsymbol{p}}(\boldsymbol{r}_i')|\psi_g^{\mathrm{el}}\rangle\cdot\boldsymbol{\epsilon}_\lambda|\psi_g^{\mathrm{rot}}\rangle.
\end{aligned} \tag{4.11}$$

Although $\hat{\eta}_i$ by necessity must be evaluated inside the electronic inner product, its action is only to replace the operator by ±1 and does not otherwise affect the evaluation of the inner product $\langle\psi_e^{\mathrm{el}}|\ldots|\psi_g^{\mathrm{el}}\rangle$. Of the four terms in (4.11), the first and third are zero because $\boldsymbol{k}\cdot\boldsymbol{\epsilon}_\lambda = 0$ for the transversely polarised laser field. Furthermore, as the electronic states are assumed to be independent of interatomic distance, the inner products $\langle\psi_e^{\mathrm{el}}|\ldots|\psi_g^{\mathrm{el}}\rangle$ will only be non-zero if $\boldsymbol{r}_i'$ is within the extent of its respective atomic orbital. Hence, it can be assumed that $\exp(i\boldsymbol{k}\cdot\boldsymbol{r}_i') \approx 1$ because the wavelength is much greater than the radial extent of the atomic orbital. Note that this does not invoke the dipole approximation as only an assumption is being made about the extent of the atomic orbitals and not the entire molecule. With this assumption the second term is zero as the excited and metastable basis states are orthogonal, leaving only the remaining non-zero fourth term.

To proceed further, the term $e^{\hat{\eta}_i i\boldsymbol{k}\cdot\boldsymbol{R}/2}$ must be manipulated into a usable form. By expanding it in terms of Legendre polynomials [113],

$$\begin{aligned}
e^{\hat{\eta}_i i\boldsymbol{k}\cdot\boldsymbol{R}/2} &= \sum_p i^p(2p+1)j_p(kR/2)P_p(\hat{\eta}_i\cos\theta) \\
&= \sum_p i^p(2p+1)j_p(kR/2)(\hat{\eta}_i)^p D_{00}^{p*}(\theta,\phi,0),
\end{aligned} \tag{4.12}$$

the matrix element (4.10) may be written as

$$V_{eg}^{\mathrm{int}} = -\frac{e}{m}\sqrt{\frac{n\hbar}{2\omega\epsilon_0\mathcal{V}}}\sum_{i,p} i^p(2p+1)j_p(kR/2)\langle\psi_e^{\mathrm{rot}}|D_{00}^{p*}\langle\psi_e^{\mathrm{el}}|(\hat{\eta}_i)^p\hat{\boldsymbol{p}}(\boldsymbol{r}_i')|\psi_g^{\mathrm{el}}\rangle\cdot\boldsymbol{\epsilon}_\lambda|\psi_g^{\mathrm{rot}}\rangle \tag{4.13}$$

where, for convenience, the angular variables of the rotation matrix are suppressed. Because all terms except the kinetic term of $\hat{H}_{\mathrm{mol}}$, given by (2.1) and (2.10), commute with the coordinates $\boldsymbol{r}_i$, the following relationship can be derived:

$$\frac{e}{m}\hat{\boldsymbol{p}}(\boldsymbol{r}_i') = \frac{i}{\hbar}\left[\hat{H}_{\mathrm{mol}}, \hat{\boldsymbol{d}}^i\right], \tag{4.14}$$

where $\hat{\boldsymbol{d}}^i = e\boldsymbol{r}'_i$. Noting that

$$\langle\psi_e^{\mathrm{el}}|(\hat{\eta}_i)^p[\hat{H}_{\mathrm{mol}}, \hat{\boldsymbol{d}}^i]|\psi_g^{\mathrm{el}}\rangle = (E_e - E_g)\langle\psi_e^{\mathrm{el}}|(\hat{\eta}_i)^p\hat{\boldsymbol{d}}^i|\psi_g^{\mathrm{el}}\rangle \tag{4.15}$$

then the coupling becomes

$$V_{eg}^{\mathrm{int}} = -\sqrt{\frac{n\hbar\omega}{2\epsilon_0\mathcal{V}}}\sum_{i,p} i^{p+1}(2p+1)j_p(kR/2)\langle\psi_e^{\mathrm{rot}}|D_{00}^{p*}\langle\psi_e^{\mathrm{el}}|(\hat{\eta}_i)^p\hat{\boldsymbol{d}}^i|\psi_g^{\mathrm{el}}\rangle\cdot\boldsymbol{\epsilon}_\lambda|\psi_g^{\mathrm{rot}}\rangle, \tag{4.16}$$

where the difference of electronic energies $E_e - E_g$ has been set equal to the laser energy $\hbar\omega$ in (4.16). The matrix element of $\hat{\boldsymbol{d}}^i$ is most easily evaluated in the molecular frame using spherical tensors, which requires the expansion:

$$\begin{aligned}\hat{\boldsymbol{d}}^i\cdot\boldsymbol{\epsilon}_\lambda &= \sum_\mu(-1)^\mu(\boldsymbol{\epsilon}_\lambda)_{-\mu}\hat{d}^i_\mu = (-1)^\lambda\hat{d}^i_\lambda \\ &= (-1)^\lambda\sum_\beta D^{1*}_{\lambda\beta}\hat{d}^i_\beta,\end{aligned} \tag{4.17}$$

where the subscripts μ and β denote the spherical tensor components in the space- and molecular-fixed frames respectively and $(\boldsymbol{\epsilon}_\lambda)_{-\mu} = \delta_{\lambda,\mu}$. This allows the complete separation of the rotational and electronic parts of the matrix element

$$\begin{aligned}V_{eg}^{\mathrm{int}} &= -(-1)^\lambda\sqrt{\frac{n\hbar\omega}{2\epsilon_0\mathcal{V}}} \\ &\quad\times\sum_{i,p,\beta} i^{p+1}(2p+1)j_p(kR/2)\langle\psi_e^{\mathrm{rot}}|D_{00}^{p*}D^{1*}_{\lambda\beta}|\psi_g^{\mathrm{rot}}\rangle\langle\psi_e^{\mathrm{el}}|(\hat{\eta}_i)^p\hat{d}^i_\beta|\psi_g^{\mathrm{el}}\rangle.\end{aligned} \tag{4.18}$$

Combining the two rotation matrices [113] yields the general form of the coupling

$$\begin{aligned}V_{eg}^{\mathrm{int}} &= -(-1)^\lambda\sqrt{\frac{n\hbar\omega}{2\epsilon_0\mathcal{V}}} \\ &\quad\times\sum_p i^{p+1}(2p+1)j_p(kR/2)\sum_{i,\beta,F}C^{1pF}_{\lambda0\lambda}C^{1pF}_{\beta0\beta}\langle\psi_e^{\mathrm{rot}}|D^{F*}_{\lambda\beta}|\psi_g^{\mathrm{rot}}\rangle\langle\psi_e^{\mathrm{el}}|(\hat{\eta}_i)^p\hat{d}^i_\beta|\psi_g^{\mathrm{el}}\rangle.\end{aligned} \tag{4.19}$$

At this point a distinct choice of basis must be made. For the jj basis in the helium system symmetrised with respect to electronic inversion (w-symmetrised jj basis) (B.3) is used, which is equivalent to setting $|\psi_a^{\mathrm{el}}\rangle \equiv |\gamma j_1 j_2 j\Omega_j w\rangle$ and $|\psi_a^{\mathrm{rot}}\rangle \equiv N^J_{m_J\Omega_j} = \sqrt{(2J+1)/4\pi}D^{J*}_{m_J\Omega_j}$. This is possible because the electronic inversion symmetry does not involve the rotational part of the system and so allows the definition

$$\begin{aligned}|\gamma j_1 j_2 j\Omega_j w\rangle \equiv N_{jj,w}\Big[&|(\gamma_1 j_1)_A(\gamma_2 j_2)_B j\Omega_j\rangle \\ &+ (-1)^{w+L_1+L_2+j_1+j_2-j}|(\gamma_1 j_1)_B(\gamma_2 j_2)_A j\Omega_j\rangle\Big]\end{aligned} \tag{4.20}$$

where $N_{jj,w} = 1/2$ for $\gamma_1 j_1 = \gamma_2 j_2$ and $N_{jj,w} = 1/\sqrt{2}$ otherwise, as has been previously defined. Under these substitutions, the electronic matrix element becomes

$$\langle \psi_e^{\mathrm{el}} | (\hat{\eta}_i)^p \hat{d}_\beta^i | \psi_g^{\mathrm{el}} \rangle = \langle \gamma' j_1' j_2' j' \Omega_j' w' | (\hat{\eta}_i)^p \hat{d}_\beta^i | \gamma j_1 j_2 j \Omega_j w \rangle \tag{4.21}$$

and must be evaluated in the w-symmetrised LS basis (B.17). For the metastable $(2s2s)$ and $2s2p$ systems, this symmetrisation reduces to

$$|2s2s\rangle = \frac{1}{\sqrt{2}} \left[|(2s)^A (2s)^B 0S0\Omega_S; \boldsymbol{r}_1, \boldsymbol{r}_2\rangle - |(2s)^A (2s)^B 0S0\Omega_S; \boldsymbol{r}_2, \boldsymbol{r}_1\rangle \right] \tag{4.22}$$

$$\begin{aligned} |2s2p\rangle = \frac{1}{2} \Big(& \left[|(2s)^A (2p)^B 1S\Omega_L\Omega_S; \boldsymbol{r}_1, \boldsymbol{r}_2\rangle - |(2s)^A (2p)^B 1S\Omega_L\Omega_S; \boldsymbol{r}_2, \boldsymbol{r}_1\rangle \right] \\ & + (-1)^{1-S+w} \left[|(2p)^A (2s)^B 1S\Omega_L\Omega_S; \boldsymbol{r}_1, \boldsymbol{r}_2\rangle - |(2p)^A (2s)^B 1S\Omega_L\Omega_S; \boldsymbol{r}_2, \boldsymbol{r}_1\rangle \right] \Big) \end{aligned} \tag{4.23}$$

where the electron permutation has been included as described by (B.1). The electronic matrix element is therefore

$$\langle 2s2p | (\hat{\eta}_i)^p \hat{d}_\beta^i | 2s2s \rangle = \frac{d_{at}}{2\sqrt{2}} \left[1 + (-1)^{w'+1+S+p} \right] \delta_{\beta\Omega_L'}, \tag{4.24}$$

where $d_{\mathrm{at}} = \langle L' = 1, \Omega_L' || \hat{d}_\beta^i || L = 0, \Omega_L = 0 \rangle$ is the reduced matrix element of the atomic dipole moment and all dashed quantities refer to the excited state. Note that the p index is a result of the inclusion of $\hat{\eta}_i$. Equation (4.23) is similar to the LS symmetrisation of Burke [130], except that the spin states are included in the symmetrisation presented here. To complete the evaluation of the electronic matrix element this result must be transformed into the jj basis by using (B.25), yielding the matrix element

$$\langle \gamma' j_1' j_2' j' \Omega_j' w' | (\hat{\eta}_i)^p \hat{d}_\beta^i | \gamma j_1 j_2 j \Omega_j w \rangle = \sum_{LS\Omega_L\Omega_S} \frac{1}{2\sqrt{2}} d_{\mathrm{at}} F_{LS\Omega_L\Omega_S}^{j_1' j_2' j' \Omega_j'} F_{LS\Omega_L\Omega_S}^{j_1 j_2 j \Omega_j} \left[1 + (-1)^{w'+1+S+p} \right], \tag{4.25}$$

that simplifies on applying the quantum numbers of the metastable basis, $L_1 = L_2 = 0$ and $S_1 = S_2 = j_1 = j_2 = 1$, to become

$$\langle \gamma' j_1' j_2' j' \Omega_j' w' | (\hat{\eta}_i)^p \hat{d}_\beta^i | \gamma j_1 j_2 j \Omega_j w \rangle = \frac{1}{2\sqrt{2}} d_{\mathrm{at}} F_{1j\beta\Omega_j}^{j_1' j_2' j' \Omega_j'} \left[1 + (-1)^{w'+1+w+p} \right]. \tag{4.26}$$

Note that $(-1)^S = (-1)^j = (-1)^w$ has been used, since $(-1)^{w-S} = (-1)^{w-j} = 1$ for the $2s2s$ state.

The rotational matrix element is

$$\langle \psi_e^{\mathrm{rot}} | D_{\lambda\beta}^{F*} | \psi_g^{\mathrm{rot}} \rangle = \iint d\Omega \frac{\sqrt{(2J+1)(2J'+1)}}{4\pi} D_{m_J'\Omega_j'}^{J'} D_{\lambda\beta}^{F*} D_{m_J\Omega_j}^{J*} \tag{4.27}$$

which, after integration over the rotation matrices [113], becomes

$$\langle \psi_e^{\mathrm{rot}} | D_{\lambda\beta}^{F*} | \psi_g^{\mathrm{rot}} \rangle = \sqrt{\frac{2J+1}{2J'+1}} C_{m_J\lambda m_J'}^{JFJ'} C_{\Omega_j\beta\Omega_j'}^{JFJ'}. \tag{4.28}$$

The complete matrix element for the w-symmetrised basis is therefore

$$\begin{aligned} V_{eg}^{\mathrm{int},w} &= -(-1)^{\lambda}\sqrt{\frac{I}{\epsilon_0 c}}\sqrt{\frac{2J+1}{2J'+1}}\sum_p i^{p+1}(2p+1)j_p(kR/2) \\ &\times \sum_{\beta,F} C^{1pF}_{\lambda 0\lambda} C^{1pF}_{\beta 0\beta} C^{JFJ'}_{m_J\lambda m'_J} C^{JFJ'}_{\Omega_j\beta\Omega'_j} d_{\mathrm{at}} F^{j'_1 j'_2 j'\Omega'_j}_{1j\beta\Omega_j} \frac{\left[1+(-1)^{w'+1+w+p}\right]}{2} \end{aligned} \tag{4.29}$$

where the laser intensity is given by $I = n\hbar\omega c/\mathcal{V}$.

For the $2s \rightarrow 2p$ transition in metastable helium, $d_{\mathrm{at}}^{sp} = 2.146 \times 10^{-29}$ C m which can be determined from knowledge of the spontaneous decay width $\Gamma_a = 1.6246$ MHz [109] and the relationship [117]:

$$\Gamma = \frac{d_{at}^2\omega^3}{3\pi\epsilon_0 c^3} \tag{4.30}$$

where ω is the angular frequency of the transition.

The matrix element in the complete symmetrised jj basis (2.29) follows from (4.29) with careful consideration of the normalisation coefficients:

$$\begin{aligned} V_{eg}^{\mathrm{int}} &= -(-1)^{\lambda}\sqrt{\frac{I}{\epsilon_0 c}}\sqrt{\frac{2J+1}{2J'+1}} N_{jj}^{\mathrm{int}} \sum_p i^{p+1}(2p+1)j_p(kR/2) \\ &\times \sum_{\beta,F} C^{1pF}_{\lambda 0\lambda} C^{1pF}_{\beta 0\beta} C^{JFJ'}_{m_J\lambda m'_J} C^{JFJ'}_{\Omega\beta\Omega'} d_{\mathrm{at}} F^{j'_1 j'_2 j'\Omega'}_{1j\beta\Omega} \frac{\left[1+(-1)^{w'+1+w+p}\right]}{2} \end{aligned} \tag{4.31}$$

where $N_{jj}^{\mathrm{int}} = \sqrt{2}$ if either $\Omega = 0$ and $\Omega' > 0$ or vice versa and $N_{jj}^{\mathrm{int}} = 1$ otherwise.

4.3 DIPOLE APPROXIMATION

In the dipole approximation (DA) the assumption $\boldsymbol{k} \cdot \boldsymbol{R} \ll 1$ is made which is satisfied when the laser wavelength is much larger than the molecule under consideration. Under this assumption, $j_p(kR/2) \rightarrow j_p(0) = \delta_{p0}$ and the laser coupling matrix element reduces to

$$V_{eg}^{\mathrm{int}} = -i(-1)^{\lambda}\sqrt{\frac{I}{\epsilon_0 c}}\sqrt{\frac{2J+1}{2J'+1}} N_{jj}^{\mathrm{int}} \sum_{\beta} C^{J1J'}_{m_J\lambda m'_J} C^{J1J'}_{\Omega\beta\Omega'} d_{\mathrm{at}} F^{j'_1 j'_2 j'\Omega'}_{1j\beta\Omega} \frac{\left[1+(-1)^{w'+1+w}\right]}{2}. \tag{4.32}$$

There are two major differences between (4.31) and (4.32). First, the DA enforces the selection rules $|J-1| \leq J' \leq |J+1|$ and $w' = 1-w$ (gerade ↔ ungerade), whereas the full matrix element allows couplings from J to any J' with even values of p coupled to opposite w parity and odd values to the same w parity. Second, the presence of the spherical Bessel functions in the full matrix element (4.31) modifies the effective momentum of the coupled vibrational wave function. This is because the coupling from a scattering wave function $\psi_g(R)$, with wave number $k_g = \sqrt{2\mu E_k}$ and kinetic energy E_k in the asymptotic limit

$R \to \infty$ becomes:

$$\begin{aligned} V_{eg}^{\mathrm{int}}\psi_g(R) \propto j_p(kR/2)e^{ik_gR} &\propto e^{i(k_g+k/2)R-ip\pi/2} - e^{i(k_g-k/2)R+ip\pi/2} \\ &= e^{ik_+R-ip\pi/2} - e^{ik_-R+ip\pi/2} \end{aligned} \tag{4.33}$$

where $k_\pm = k_g \pm k/2$. This can be recognised in physical terms as a momentum transfer from the photon to the vibrational motion of the dimer which either dampens the vibration (k_-) or enhances it (k_+). Because of the form of (4.33), it is expected that atoms colliding at temperatures with values of k_g much greater than the value k of the laser field (e.g. room temperature physics) will not be noticeably influenced by the use of the dipole approximation ($p = 0$). However, ultracold gases are commonly cooled below the photon recoil limit of a suitable transition and this transition is often one that is exploited in the photoassociation process. These gases are therefore highly likely to have $k_g \lesssim k$. For example, ultracold metastable helium can be condensed to a Bose-Einstein condensate at approximately $2\,\mu$K for which the colliding atoms have $k_g = 2.6 \times 10^{-3} a_0^{-1}$, whereas the photons of the laser field for the 1083 nm $2s \to 2p$ transition have $k = 3.1 \times 10^{-3} a_0^{-1}$. In this case, there is a significant difference between the $\exp(ik_\pm R)$ terms of the complete coupling and the $\exp(ik_g R)$ term of the approximate coupling. Therefore, significant effects can be anticipated from the introduction of the dipole approximation.

4.4 PHOTOASSOCIATION PROFILES

With the complete laser coupling formulated, the photoassociation process may now be investigated. The goal of the following sections is to calculate the properties of the PA profiles for arbitrary laser frequency and intensity. These profiles can be described in terms of their line widths and positions or, alternatively, their line shifts from the unperturbed energy level. The calculations will investigate the purely long-range rovibrational levels in the 0_u^+, $J = 1$ potential which asymptotes to $j = 0$, and will determine the properties of the profiles through a series of progressively more complete calculations. These long-range levels are investigated because their binding energies have been analysed to a high degree of accuracy both theoretically [90] and experimentally [67]. Furthermore, experimental measurements exist of line shifts at varying intensities [70]. Initially perturbative calculations of the line shifts will be performed, followed by a multichannel calculation in the dipole approximation and finally a complete multichannel calculation that includes the complete laser coupling term.

As has been mentioned in chapter 3, the influence of the non-adiabatic and Coriolis couplings upon these ultra-long range bound levels is very small and highly unlikely to cause noticeable secondary effects in the line shapes of the levels. Consequently the single-channel treatment will be used for the excited state in order to simplify the calculations. This R-dependent single-channel molecular state is of the form (3.6) and will be denoted $|e_0\rangle$. For the metastable molecular basis states, $|g\rangle$ will be used to represent the hybrid jj basis states of (2.29). This notation indicates the molecular properties only; the complete states including the vibrational wave functions $G_e^0(R)$ and $G_g(R)$ will be denoted $|e_0, R\rangle \equiv R^{-1}G_e^0(R)|e_0\rangle$ and $|g, R\rangle \equiv R^{-1}G_g(R)|g\rangle$.

4.5 PERTURBATIVE LINE SHIFTS IN THE DIPOLE APPROXIMATION

4.5.1 Direct perturbative calculation

For small laser intensities, the coupling may be considered a perturbation to the molecular system. The unperturbed Hamiltonian is then $\hat{H}_0 = \hat{H}_{\rm mol} + \hat{H}_{\rm rad}$. In this limit, the line shifts and widths are given by second order perturbation theory. The shift in the energy of the state $|e_0, R\rangle$ is

$$\delta E^{(2)} = \sum_v \frac{|\langle e_0, R|\hat{H}_{\rm int}|g_v, R\rangle|^2}{E_0 - E_v} + \int \frac{|\langle e_0, R|\hat{H}_{\rm int}|g(E'), R\rangle|^2}{E_0 - E'} dE', \tag{4.34}$$

where the explicit notations $|g_v, R\rangle$ and $|g(E'), R\rangle$ are used to refer to a normalised bound level v and an energy normalised scattering state of energy E' respectively of the basis states $|g, R\rangle$. The term E_0 is the unperturbed energy of the excited state including that of the laser field, i.e. $E_0 = E_e^\infty - B_e^v + (n-1)\hbar\omega$. Here E_a^∞ is the energy of the asymptotically separated atoms of state a and B_a^v is the binding energy of the bound level v of the state a. The metastable energies are $E_v = E_g^\infty - B_g^v + n\hbar\omega$ and $E' = E_g^\infty + E'' + n\hbar\omega$ where $E'' \geq 0$.

To use these relations, one must carefully identify the different laser frequencies that are used during an experiment. Usually an experiment involves excitation of the dimers to the state $|e_0, R\rangle$ from many colliding pairs of metastable atoms which have a small kinetic energy E_k. To maximise the coupling to the excited level, the laser detuning should accommodate this kinetic energy by setting $\hbar\omega = \hbar\omega_0 - B_v^e - E_k$, where $\hbar\omega_0 = E_e^\infty - E_g^\infty$ is the asymptotic energy difference. In this situation, the denominators of (4.34) become

$$E_0 - E_v = E_k + B_g^v, \tag{4.35}$$

$$E_0 - E' = E_k - E''. \tag{4.36}$$

Unfortunately, the direct calculation of the line shift using equation (4.34) requires the matrix elements of the molecular Hamiltonian $\hat{H}_{\rm mol}$ to be diagonal in the basis $|g\rangle$, which is not true for the hybrid jj basis. To make use of a diagonal basis, a much larger basis set is required (see for example, Portier *et al* [88] who required 24 basis states as opposed to the nine directly coupled states of the hybrid jj basis). However, some useful conclusions may be drawn from the form of the perturbation. In the ultracold limit of $E_k \to 0$ the first term of (4.34) shows that couplings from the excited state to bound levels of the metastable states produce blue shifts because B_g^v is positive whereas the second term shows that the scattering continuum produces red shifts in the excited levels. When finite temperatures

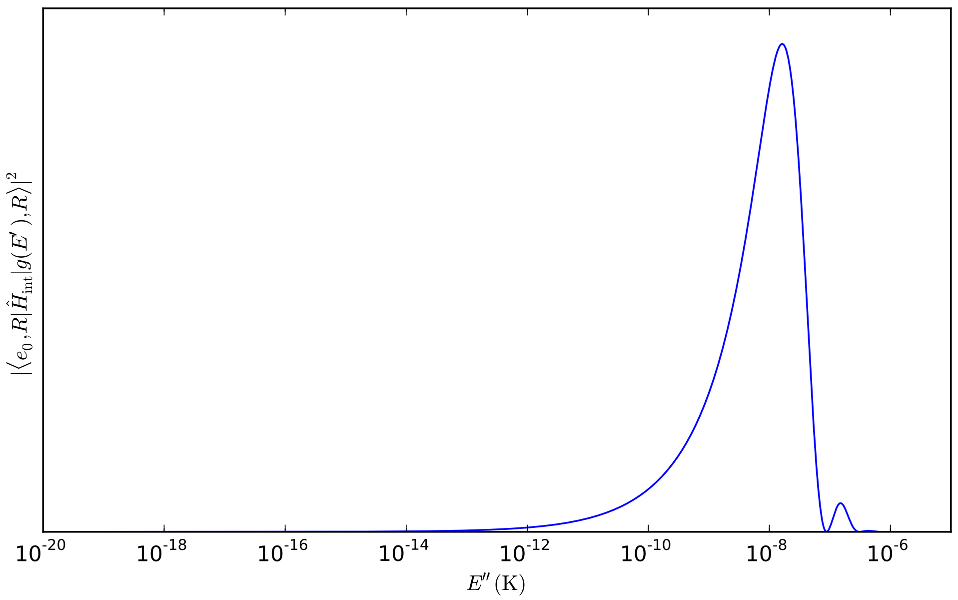

Figure 4.4: Energy dependence of the numerator of the continuum contributions to the second order perturbative energy shift given by equation (4.34).

are considered, there is a crossover temperature at which the continuum term will cease to produce red shifts and begin to effect blue shifts. Additionally, since $\hat{H}_{\rm int} \propto \sqrt{I}$, it is clear from the perturbative formula (4.34) that the line shift is linearly proportional to laser intensity.

To demonstrate the method of direct calculation using equation (4.34), the use of the hybrid jj basis is temporarily set aside and the basis states $|g\rangle$ are chosen to include the rotation l as a quantum number and make the matrix elements of the molecular Hamiltonian diagonal. In this case, the LS basis $|\gamma LSm_Lm_Slm_l\rangle \equiv |\gamma LSm_Lm_S\rangle|lm_l\rangle$ for the spin-polarised metastable state will be used, see appendix B.2. In this basis, the numerator of the continuum term in (4.34) has the energy dependence shown in figure 4.4. These values are calculated using energy normalised metastable scattering functions

$$G_g(R) = \sqrt{\frac{2\mu}{\hbar^2\pi k}}\sin(kR-\phi) \tag{4.37}$$

where $k = \sqrt{2\mu(E'-E_g^\infty)}$ and $\phi = \phi(E')$ is a phase shift. The line shift $\delta E^{(2)}$ calculated from equation (4.34) is shown in figure 4.5. It can be seen that the crossover from red to blue detunings occurs at approximately 5 mK.

Direct calculation of line shifts using equation (4.34) provides a simple procedure, made unattractive by the inherent requirements of a basis $|g\rangle$ with diagonal matrix elements, which leads to a considerably larger basis set, and the required calculation of the wave function $|g(E'),R\rangle$ at each value of E'. Problems with convergence are also possible if a sufficiently fine grid for E'' is not used. Despite these drawbacks, it is still a viable approach for calculating the line shift of the excited level. This has been done for the $v=0$ level coupled by σ^- laser light to the spin-polarised metastable state, $|Sm_S,lm_l\rangle =$

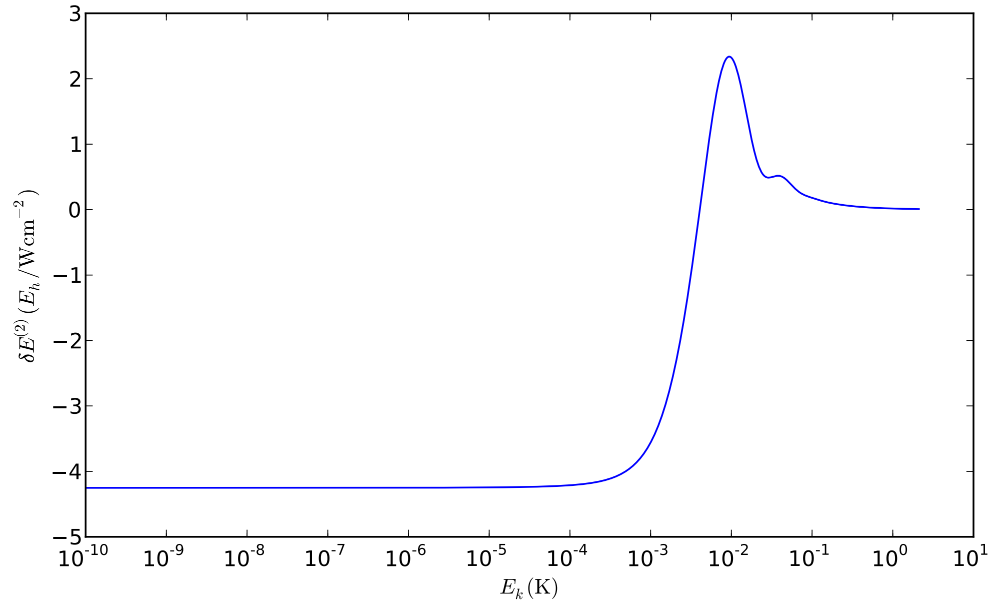

Figure 4.5: Perturbative line shifts per laser intensity calculated from equation (4.34) for varying kinetic energy E_k. The laser is assumed to be tuned so that it is resonant with the unperturbed energy of the bound level.

$|22, 00\rangle$, for which the result $\delta E^{(2)} = cI$ is obtained where the proportionality constant is $c = -4.25$ MHz/W.cm^{-2}. This value agrees well with -4.42 MHz/W.cm^{-2}, the partial s-wave contribution obtained by Portier *et al* [88].

4.5.2 F-operator solution

To overcome the limitations of the direct evaluation of the second order perturbation equation, (4.34), various techniques have been developed that allow the equation to be represented in a different form. One technique called the propagator method has been used by Portier *et al* [88] to calculate the perturbative line shifts of metastable helium. In this section an alternative technique, that is due to Dalgarno and Lewis [131] and referred to here as the $\hat{F}$-operator method, will be used to calculate the perturbative line shift $\delta E^{(2)}$. This method converts the summation and integration over bound levels and scattering energies to a set of coupled differential equations, the number of which equals the number of coupled metastable basis states.

The method introduces an operator $\hat{F}$ which is required to satisfy

$$[\hat{F}, \hat{H}_0]|e_0, R, n-1\rangle = \hat{H}_{\mathrm{int}}|e_0, R, n-1\rangle \tag{4.38}$$

where $\hat{H}_0 = \hat{H}_{\mathrm{mol}} + \hat{H}_{\mathrm{rad}}$ must include the laser field Hamiltonian so that energy conservation is satisfied. Equation (4.34) is then reduced to the form

$$\begin{aligned}\delta E^{(2)} &= \langle e_0, R, n-1|\hat{H}_{\text{int}}\hat{F}|e_0, R, n-1\rangle \\ &\quad - \langle e_0, R, n-1|\hat{F}|e_0, R, n-1\rangle\langle e_0, R, n-1|\hat{H}_{\text{int}}|e_0, R, n-1\rangle \\ &= \langle e_0, R, n-1|\hat{H}_{\text{int}}\hat{F}|e_0, R, n-1\rangle \end{aligned} \tag{4.39}$$

where $|e_0, R, n-1\rangle \equiv |e_0, R\rangle \otimes |n-1, \omega, \epsilon\rangle$ and the second term is zero because there is no direct coupling by the laser interaction from the excited state to itself.

To solve equation (4.38) for the operator $\hat{F}$, the inner products with the metastable and excited basis states must be formed. The inner product with the excited basis state $|e_0, n-1\rangle \equiv |e_0\rangle \otimes |n-1, \omega, \epsilon\rangle$ gives

$$\langle e_0, n-1| \left(E_0 - \hat{H}_{\text{mol}} - \hat{H}_{\text{rad}}\right) \hat{F}|e_0, R, n-1\rangle = 0 \tag{4.40}$$

where $\hat{H}_0|e_0, R, n-1\rangle = E_0|e_0, R, n-1\rangle$. The term $\hat{F}|e, R, n-1\rangle$ is then expanded in terms of the metastable and excited bases

$$\hat{F}|e_0, R, n-1\rangle = \frac{1}{R}\left[\sum_{g'} f_{g'}(R)|g, n\rangle + f_e(R)|e_0, n-1\rangle\right], \tag{4.41}$$

where $|g, n\rangle \equiv |g\rangle \otimes |n, \omega, \epsilon\rangle$, such that (4.40) becomes

$$\left(E_0 - \langle e_0|\hat{H}_{\text{mol}}|e_0\rangle - \langle n-1, \omega, \epsilon|\hat{H}_{\text{rad}}|n-1, \omega, \epsilon\rangle\right) \frac{1}{R} f_e(R) = 0. \tag{4.42}$$

In the hybrid jj basis, this becomes

$$\left(\frac{\hbar^2}{2\mu}\frac{d^2}{dR^2} - V_e^{\text{KC}}(R) - V_e^{\text{SC}}(R) - (n-1)\hbar\omega + E_0\right) f_e(R) = 0 \tag{4.43}$$

where $V_e^{\text{SC}}(R) = \langle e_0|\hat{H}_{\text{el}} + \hat{H}_{\text{rot}}|e_0\rangle$ is the excited state single-channel potential as described in section 3.2.1. $V_e^{\text{KC}}(R)$ is the kinetic correction term for the single-channel potential, see equation (3.11), which was excluded in chapter 3 because it caused problems in its evaluation due to the sharply varying nature of the single-channel potentials at diabatic crossings. It is included here as it remains smooth and unambiguous throughout the region of the long-range 0_u^+ potentials and gives rise to noticeable variations in the results obtained.

The inner product of equation (4.38) with a metastable basis state gives

$$\langle g, n| \left(E_0 - \hat{H}_{\text{mol}} - \hat{H}_{\text{rad}}\right) \hat{F}|e_0, R, n-1\rangle = \langle g, n|\hat{H}_{\text{int}}\frac{1}{R}G_e(R)|e_0, n-1\rangle \tag{4.44}$$

where $G_e(R)$ is the vibrational wave function of the excited state. After applying the expansion (4.41), the equation becomes

$$\sum_{g'} \left[E_0 \delta_{g'g} - \langle g|\hat{H}_{\mathrm{mol}}|g'\rangle - \langle n,\omega,\epsilon|\hat{H}_{\mathrm{rad}}|n,\omega,\epsilon\rangle \delta_{g'g} \right] \frac{1}{R} f_{g'}(R) = V^{\mathrm{int}}_{ge_0}(R). \tag{4.45}$$

In the hybrid jj basis, this becomes

$$\left[\frac{\hbar^2}{2\mu} \frac{d^2}{dR^2} + (E_0 - n\hbar\omega) \right] f_g(R) - \sum_{g'} \left[V^{\mathrm{rot}}_{gg'} + V^{\mathrm{el}}_{gg'} \right] f_{g'}(R) = V^{\mathrm{int}}_{ge_0}(R), \tag{4.46}$$

where the matrix elements $V^{\mathrm{rot}}_{gg'}$ and $V^{\mathrm{el}}_{gg'}$ are given by (2.38) and (2.32) respectively and the laser coupling matrix element between the single-channel excited state and a metastable basis state is

$$\begin{aligned} V^{\mathrm{int}}_{ge_0}(R) &= \langle g, n|\hat{H}_{\mathrm{int}}|e_0, n-1\rangle \\ &= \sum_a D_{ae}(R) V^{\mathrm{int}}_{ga} \end{aligned} \tag{4.47}$$

where the single-channel coefficients $D_{ae}(R)$ in the hybrid basis are given by (3.6) and a enumerates the hybrid basis states that comprise the single-channel excited state.

The substitution of expansion (4.41) into (4.39) produces the desired solution for the line shift:

$$\delta E^{(2)} = \sum_g \int G^0_e(R) V^{\mathrm{int}}_{ge_0}(R) f_g(R)\, dR. \tag{4.48}$$

From this equation, and the fact that differential equation (4.43) is uncoupled from the differential equations (4.46), it is clear that $f_e(R)$ is not required in order to determine the line shift. Hence, only the differential equations (4.46) need be solved.

The boundary conditions for equations (4.46) require special mention. The action of $\hat{F}$ must be finite for all R, hence the asymptotic form of $f_g(R)$ is required to not increase faster than R. The influence of the laser field coupling from the excited state is also expected to be negligible at large R, hence the requirement $f_g(R)/R \to 0$ as $R \to \infty$ must be imposed. From the form of equations (4.46), it can be seen that they asymptotically uncouple and simplify in the limit $R \to \infty$ to the form

$$\left[\frac{\hbar^2}{2\mu} \frac{d^2}{dR^2} + E_0 - n\hbar\omega - E^{\infty}_g \right] f_g(R) = 0. \tag{4.49}$$

This equation has three general solutions depending upon the sign of $E_0 - n\hbar\omega - E^{\infty}_g = -B^e_v - \hbar\Delta\omega$ where $\Delta\omega = \omega - \omega_0$. If the laser is red detuned to the bound level then this quantity is positive and oscillatory solutions are obtained whereas for blue detunings the quantity is negative and exponentially increasing and decaying solutions are obtained. In the special case of detuning precisely to the bound level, $f_g(R)$ is linear in R.

As mentioned in the previous section, an experiment involving the excitation of colliding metastable atoms will attempt to tune the laser frequency as closely as possible to the transition so that $\hbar\Delta\omega = -B^e_v - E_k$. In the ultracold limit $E_k \to 0$ the solutions of (4.49) become linear, $f_g(R) = C + mR$ and to produce finite solutions such that $f_g(R)/R \to 0$ as $R \to \infty$, the condition $m = 0$ must be imposed. This can be enforced by applying zero-derivative boundary conditions upon the differential equations, in contrast to the more commonly applied boundary conditions that the function values are zero.

To solve these equations, the discrete variable representation (DVR) method is used, which is fully described in appendix D. The cosine basis is required in order to impose the zero-derivative boundary conditions upon the equations and $N = 10^4$ grid points are used in the range of $R_{\min} = 3\,a_0$ to $R_{\max} = 2000\,a_0$. The equi-spacing of the cosine basis across the region is not optimal as rapidly oscillating wave functions over the ranges of the ground state potentials require a dense spacing of grid points at smaller R, whereas few grid points are required in the asymptotic region of the solutions due to the large wavelengths for scattering at ultracold temperatures. Hence, a quartic scaling function $R = \zeta(t)$ is used to redistribute the grid points across the region without modifying the boundary conditions. This quartic, of the form $\zeta(t) = c_0 + c_1 t + c_2 t^2 + c_3 t^3 + c_4 t^4$, must satisfy the requirements, see appendix section D.5,

$$\begin{aligned} c_0 &= a, \\ c_1 &> 0, \\ c_2 &= 0, \\ c_3 &= 2(b - a - c_1), \\ c_4 &= -c_3/2. \end{aligned} \tag{4.50}$$

Larger values of c_1 straighten the scaling function and in the limit $c_1 \to \infty$, $R \propto t$. A value of $c_1 = 10$ was chosen. This placed 53% of points within the first quartile and 22% within the second quartile and produced acceptable results. When compared to an equi-spaced grid, this choice of scaling decreased the total number of grid points required for calculation to the necessary precision by an order of magnitude.

The excited single-channel state of the form (3.6) is a linear combination of four particular hybrid basis functions that share the quantum numbers $\gamma_1 = (L_1, S_1) = (0, 1)$, $\gamma_2 = (L_2, S_2) = (1, 1)$, $j_1 = 1$, $\Omega = 0$, $J = m_J = 1$ and $w = 1$ and these will be suppressed in the labels of the basis states. The four states can then be written with the reduced notation $|j_2, j\rangle$ and are explicitly,

$$|j_2, j\rangle = \Big\{ |0,1\rangle, \quad |1,1\rangle, \quad |2,1\rangle, \quad |2,3\rangle \Big\}. \tag{4.51}$$

The metastable basis states, denoted by the shorthand $|j\Omega, Jm_J\rangle$, that are directly coupled to this set of hybrid excited states by σ^- polarised laser light are

$$|j\Omega, Jm_J\rangle = \Big\{ |00,22\rangle, \quad |20,22\rangle, \quad |21,22\rangle \Big\} \tag{4.52}$$

where the quantum numbers $\gamma_1 = \gamma_2 = (L_\alpha, S_\alpha) = (0, 1)$, $j_1 = j_2 = 1$ and $w = 0$ are implied. Additionally, the metastable state $|22, 22\rangle$ is indirectly coupled to the excited

Table 4.1: Perturbative line shifts per laser intensity in MHz/(W cm^{-2}) calculated from equation (4.48) for the long-range bound levels of the single-channel potential asymptoting to He($2s\,{}^3S_1$) + He($2p\,{}^3P_0$) in the 0_u^+ configuration. Results are shown for the inclusion and exclusion of the kinetic correction term V_e^{KC}. The results are also compared to those of Portier *et al* [88] who used a propagator method to solve the second order perturbation equations without inclusion of the kinetic correction term.

Levels	Polarisation	No V_e^{KC}	With V_e^{KC}	Ref. [88]
$v=0$	σ^-	-6.439	-6.507	-6.37
	σ^+	-7.724	-7.784	-7.36
$v=1$	σ^-	-11.662	-11.748	-11.70
	σ^+	-10.205	-10.270	-10.25
$v=2$	σ^-	-29.442	-29.692	-29.57
	σ^+	-24.675	-24.877	-24.11

state because of Coriolis couplings to the states listed in (4.52). Similarly the states directly coupled by σ^+ polarised laser light are

$$|j\Omega, Jm_J\rangle = \Big\{|00,00\rangle, \quad |00,20\rangle, \quad |20,00\rangle, \quad |21,10\rangle, \quad |20,20\rangle, \quad |21,20\rangle\Big\} \tag{4.53}$$

and those that are indirectly coupled via the Coriolis couplings are

$$|j\Omega, Jm_J\rangle = \Big\{|20,10\rangle, \quad |22,20\rangle\Big\}. \tag{4.54}$$

The results for the shifts of the three lowest bound levels calculated by solving for $f_g(R)$ in equation (4.46) and substituting into equation (4.48) are presented in table 4.1. Results are shown with and without the inclusion of the kinetic correction term V_e^{KC}. There is good agreement between the results and those of Portier *et al* who did not include the kinetic correction term. The small differences in this case are likely due to the input potentials and parameters used in the calculation. The effect of including V_e^{KC} is also small but noticeable, which suggests that non-adiabatic effects may be of more importance to line shape calculations than to the binding energies of the bound levels. For example, inclusion of the kinetic correction term yields a 0.7% variation in the $v=0$ binding energy, yet the line shift that results from the presence of a laser field of intensity 1 W.cm^{-2} varies by 1.1% for the same conditions.

4.6 MULTICHANNEL SOLUTION IN THE DIPOLE APPROXIMATION

4.6.1 Introduction

The perturbative calculation of the line-shift requires the laser coupling to be small and predicts a linear dependence upon laser intensity. To investigate higher laser intensities and to determine whether deviations from linearity occur requires a complete multichannel non-perturbative solution. In the calculation the linearly independent scattering solutions are found as a function of laser detuning and the scattering ($\boldsymbol{S}$) matrix is determined by matching to the asymptotic forms of the solutions. Profiles of cross sections calculated from the $\boldsymbol{S}$-matrix can then be plotted and the resonance peaks analysed.

However, to be able to define the $\boldsymbol{S}$-matrix, asymptotic matching of the wave functions must be possible, requiring the scattering channels to be asymptotically uncoupled. In the dipole approximation the laser interaction does not vanish asymptotically, which has necessitated the development of several different methods to facilitate the decoupling of the scattering channels. Simoni *et al* [53] have performed calculations assuming that the laser coupling is small and negligible at large R and were able to use an analytical method to calculate the $\boldsymbol{S}$-matrix. Napolitano [54] resolves the issue by using 'dressed' states, which are specific combinations of the basis states that become asymptotically decoupled. In Napolitano's calculation, semi-analytical solutions to the $\boldsymbol{S}$-matrix were produced, although this required the assumption that the laser detuning was much greater than the laser coupling. Additionally, fine-structure was not included in Napolitano's calculations.

In this section, the $\boldsymbol{S}$-matrix elements will be calculated in the dipole approximation using two alternative methods that treat the helium system non-perturbatively. The first uses dressed states to asymptotically uncouple the basis states following Napolitano's procedure but without making any assumptions. The second applies an artificial dampening to the laser coupling at very large interatomic distances to asymptotically uncouple the basis states in a different manner. The two methods behave differently under variation of the laser frequency and intensity for the helium system under investigation but give nearly identical results for the widths and shifts of the resonance peaks.

4.6.2 Multichannel equations

The non-perturbative calculation requires the solution of the complete differential equations

$$\left(\hat{H}_{\text{mol}} + \hat{H}_{\text{rad}} + \hat{H}_{\text{int}} + \hat{H}_{\text{spon}}\right)|\Psi\rangle = E|\Psi\rangle \tag{4.55}$$

where the state of the total system, $|\Psi\rangle$, is expanded in terms of the metastable hybrid basis $|g\rangle$ and the excited single-channel state $|e_0\rangle$ in the form

$$|\Psi\rangle = \sum_{g'} \frac{1}{R} G_{g'}(R)|g', n\rangle + \frac{1}{R} G_e^0(R)|e_0, n-1\rangle. \tag{4.56}$$

To solve equation (4.55) for the radial wave functions $G_g(R)$ and $G_e^0(R)$, scalar products must be formed with the metastable and excited basis states. This results in a set of coupled differential equations of the form

$$\sum_{g'}\left[\langle g|\hat{H}_{\mathrm{mol}}\frac{1}{R}G_{g'}(R)|g'\rangle+\langle n,\omega,\epsilon|\hat{H}_{\mathrm{rad}}|n,\omega,\epsilon\rangle\right] \\ +\langle g,n|\hat{H}_{\mathrm{int}}\frac{1}{R}G_e^0(R)|e_0,n-1\rangle=E\frac{1}{R}G_g(R) \quad (4.57)$$

and

$$\langle e_0|\hat{H}_{\mathrm{mol}}\frac{1}{R}G_e^0(R)|e_0\rangle+\langle n-1,\omega,\epsilon|\hat{H}_{\mathrm{rad}}|n-1,\omega,\epsilon\rangle \\ +\sum_{g'}\langle e_0,n-1|\hat{H}_{\mathrm{int}}\frac{1}{R}G_{g'}(R)|g',n\rangle=E\frac{1}{R}G_e^0(R). \quad (4.58)$$

In the hybrid jj basis, these equations become

$$\left[-\frac{\hbar^2}{2\mu}\frac{d^2}{dR^2}+n\hbar\omega-E\right]G_g(R)+\sum_{g'}V_{gg'}G_{g'}(R)+V_{ge_0}^{\mathrm{int}}G_e^0(R)=0 \quad (4.59)$$

and

$$\left[-\frac{\hbar^2}{2\mu}\frac{d^2}{dR^2}+V_e^{\mathrm{SC}}(R)+V_e^{\mathrm{KC}}(R)+\frac{i}{2}\Gamma_{e_0}(R)+(n-1)\hbar\omega-E\right]G_e^0(R) \\ +\sum_{g'}V_{g'e_0}^{\mathrm{int}}G_{g'}(R)=0. \quad (4.60)$$

Here the laser coupling matrix element $V_{ge_0}^{\mathrm{int}}$ is given by equation (4.47), $V_{gg'}=\langle g|\hat{H}_{\mathrm{rot}}+\hat{H}_{\mathrm{el}}+\hat{H}_{\mathrm{fs}}|g'\rangle$, the single-channel excited state potential is $V_e^{\mathrm{SC}}(R)$ as described in section 3.2.1 and the kinetic correction term is $V_e^{\mathrm{KC}}(R)$ as described by equation (3.11). The term

$$\frac{i}{2}\Gamma_{e_0}(R)=\langle e_0|\hat{H}_{\mathrm{spon}}|e_0\rangle \quad (4.61)$$

represents the spontaneous loss as described in section 2.4. This loss term may be enabled or disabled as desired.

Once the radial wave functions $G_g(R)$ and $G_e^0(R)$ have been determined, the $\boldsymbol{S}$ matrix elements may be calculated [132] by asymptotically matching

$$\boldsymbol{G}\underset{R\to\infty}{=}\boldsymbol{H}_-^0\boldsymbol{A}+\boldsymbol{H}_+^0\boldsymbol{B}=(\boldsymbol{H}_-^0-\boldsymbol{H}_+^0\boldsymbol{S})\boldsymbol{A} \quad (4.62)$$

where the matrix $\boldsymbol{G}$ is formed from the radial wave functions so that $G_{\gamma\gamma'}$ represents a vector of solutions $G_\gamma=\{G_g,G_e^0\}$ and the second subscript γ' labels the linearly independent solutions found by applying linearly independent boundary conditions to (4.55). Henceforth, the states $|\gamma\rangle$ will be used to represent both $|g,n\rangle$ and $|e_0,n-1\rangle$. The diagonal matrices $\boldsymbol{H}_\pm^0=\delta_{\gamma\gamma'}h_\gamma^\pm$ take the form of incoming and outgoing waves for the open channels (real k_γ) and exponentially decaying and increasing functions for the closed channels (imaginary k_γ):

$$h_\gamma^\mp = \frac{1}{\sqrt{2|k_\gamma|}} e^{i\phi_\gamma} e^{\mp i k_\gamma R}, \tag{4.63}$$

where $k_\gamma = \sqrt{2\mu(E - E_\gamma^\infty)}$, E_γ^∞ is the asymptotic energy of state $|\gamma\rangle$ and the phase factor $\exp(i\phi_\gamma)$ is unity for open channels. The matrices $\boldsymbol{A}$, $\boldsymbol{B}$ and $\boldsymbol{S} = -\boldsymbol{B}\boldsymbol{A}^{-1}$ have the block structure

$$\boldsymbol{A} = \begin{bmatrix} \boldsymbol{A}_{oo} & \boldsymbol{A}_{oc} \\ \boldsymbol{A}_{co} & \boldsymbol{A}_{cc} \end{bmatrix}, \qquad \boldsymbol{B} = \begin{bmatrix} \boldsymbol{B}_{oo} & \boldsymbol{B}_{oc} \\ \boldsymbol{B}_{co} & \boldsymbol{B}_{cc} \end{bmatrix}, \qquad \boldsymbol{S} = \begin{bmatrix} \boldsymbol{S}_{oo} & \boldsymbol{S}_{oc} \\ \boldsymbol{S}_{co} & \boldsymbol{S}_{cc} \end{bmatrix} \tag{4.64}$$

where o refers to the open channels and c to the closed channels. It is desirable to avoid matching to the asymptotic closed channel solutions, as it is difficult to accurately separate the exponentially increasing and decreasing components. However, if $\boldsymbol{A}_{co} = \boldsymbol{0}$ then $\boldsymbol{S}_{oo} = -\boldsymbol{B}_{oo}\boldsymbol{A}_{oo}^{-1}$. To enforce $\boldsymbol{A}_{co} = \boldsymbol{0}$ it is enough to ensure that the closed channel solutions decay as $R \to \infty$; that is, the solutions must remain physical. This makes the calculations easier to perform and is possible because only $\boldsymbol{S}_{oo}$ is required to extract the photoassociation profiles.

The differential equations (4.59) and (4.60) can be written in the matrix form

$$\left[-\frac{\hbar^2}{2\mu}\frac{d^2}{dR^2}\delta_{\gamma\gamma'} + \sum_{\gamma'} W_{\gamma\gamma'}(R) \right] G_{\gamma'}(R) = 0 \tag{4.65}$$

where $W_{\gamma\gamma'} = \langle\gamma'| \left(\hat{H}_{\text{rot}} + \hat{H}_{\text{el}} + \hat{H}_{\text{fs}} + \hat{H}_{\text{rad}} + \hat{H}_{\text{int}} + \hat{H}_{\text{spon}} - E \right) |\gamma\rangle$ is the potential matrix. In the hybrid jj basis coupled by σ^- laser light, the potential matrix is

$$\boldsymbol{W} = \begin{bmatrix} D_1^0 & 0 & 0 & 0 & \hbar\Omega_1^0 \\ 0 & D_5^0 & L^{01} & 0 & \hbar\Omega_5^0 \\ 0 & L^{10} & D_5^1 & L^{12} & \hbar\Omega_5^1 \\ 0 & 0 & L^{21} & D_5^2 & 0 \\ \hbar\Omega_1^0 & \hbar\Omega_5^0 & \hbar\Omega_5^1 & 0 & V_e - \Delta E \end{bmatrix}. \tag{4.66}$$

Here, $D_{2S+1}^\Omega = {}^{2S+1}\Sigma_g^+ + L^{\Omega\Omega} - E_k$ and $L^{\Omega\Omega'} = V_{gg'}^{\text{rot}}$. The incident kinetic energy is $E_k = E - E_g^\infty$ and the Rabi couplings are $\hbar\Omega_{2S+1}^\Omega = V_{ge_0}^{\text{int}}$. The excited state potential is $V_e = V_e^{SC} + V_e^{KC} + i\Gamma_{e0}/2$ and the laser detuning from dissociation is ΔE. In reaching (4.66) from equations (4.59) and (4.60), the energy relations

$$E - E_g^\infty - n\hbar\omega = E_k \tag{4.67}$$

and

$$E - E_e^\infty - (n-1)\hbar\omega = \Delta E \tag{4.68}$$

were used, see figure 4.2. Finally, the basis states $|\gamma\rangle$ are ordered according to

$$\begin{aligned}
|1\rangle &= |j=0,\Omega=0\rangle \otimes |n,\omega_\lambda,\boldsymbol{\epsilon}_\lambda\rangle,\\
|2\rangle &= |j=2,\Omega=0\rangle \otimes |n,\omega_\lambda,\boldsymbol{\epsilon}_\lambda\rangle,\\
|3\rangle &= |j=2,\Omega=1\rangle \otimes |n,\omega_\lambda,\boldsymbol{\epsilon}_\lambda\rangle,\\
|4\rangle &= |j=2,\Omega=2\rangle \otimes |n,\omega_\lambda,\boldsymbol{\epsilon}_\lambda\rangle,\\
|5\rangle &= |e_0\rangle \otimes |n-1,\omega_\lambda,\boldsymbol{\epsilon}_\lambda\rangle,
\end{aligned} \tag{4.69}$$

where the states $|1\rangle \to |4\rangle$ have the implicit quantum numbers of the metastable manifold coupled by σ^- laser light: $L_1 = L_2 = 0$, $S_1 = S_2 = j_1 = j_2 = 1$, $J = 2$, $m_J = 2$ and $w = 0$.

Two mechanisms may be used to probe the population of the excited state and hence the strength of the photoassociation resonance. If the loss term is omitted from (4.66) then the elastic and total cross sections of the entrance channels can be calculated and a sharp variation of the cross sections will be observed in the neighbourhood of the resonance. However, if the loss term for the excited state is included within (4.66) then the $\boldsymbol{S}$-matrix will no longer be unitary and the PA line shape of the spontaneously emitted photons will be proportional to this loss of unitarity. Although the spontaneous loss produces a $2p$ to $2s$ atomic transition, the decayed $2s$ (metastable) atoms are not considered to repopulate the initial entrance channel. This is because the decayed atoms have a thermal distribution that is much greater than that for the bulk of the ultracold gas and so will not be confined by the trapping potentials used in the experiment. The higher thermal energy of the decayed atoms also heats the ultracold gas which may then be detected as an increased temperature or a reduced optical density of the gas [67].

The asymptotic form of the radial wave functions must be completely uncoupled in order to properly define the $\boldsymbol{S}$ matrix using (4.62). However, the asymptotic coupling matrix

$$\boldsymbol{W}_\infty = \begin{bmatrix} -E_k & 0 & 0 & 0 & \hbar\Omega_1^0 \\ 0 & -E_k & 0 & 0 & \hbar\Omega_5^0 \\ 0 & 0 & -E_k & 0 & \hbar\Omega_5^1 \\ 0 & 0 & 0 & -E_k & 0 \\ \hbar\Omega_1^0 & \hbar\Omega_5^0 & \hbar\Omega_5^1 & 0 & -\Delta E + i\Gamma/2 \end{bmatrix} \tag{4.70}$$

is clearly not diagonal. To resolve this problem either the correct basis under which this matrix does become diagonal must be determined (the dressed state formalism, see section 4.6.3), or the off-diagonal elements must be artificially dampened to zero in the asymptotic region (the modified radiation coupling method, see section 4.6.4).

The treatment of σ^+ polarisation is identical to that for σ^- polarisation except that its basis set is larger:

$$\begin{aligned}
|1\rangle &= |j=0,\Omega=0,J=0,m_J=0\rangle \otimes |n,\omega_\lambda,\boldsymbol{\epsilon}_\lambda\rangle, \\
|2\rangle &= |j=0,\Omega=0,J=2,m_J=0\rangle \otimes |n,\omega_\lambda,\boldsymbol{\epsilon}_\lambda\rangle, \\
|3\rangle &= |j=2,\Omega=0,J=0,m_J=0\rangle \otimes |n,\omega_\lambda,\boldsymbol{\epsilon}_\lambda\rangle, \\
|4\rangle &= |j=2,\Omega=1,J=1,m_J=0\rangle \otimes |n,\omega_\lambda,\boldsymbol{\epsilon}_\lambda\rangle, \\
|5\rangle &= |j=2,\Omega=0,J=2,m_J=0\rangle \otimes |n,\omega_\lambda,\boldsymbol{\epsilon}_\lambda\rangle, \\
|6\rangle &= |j=2,\Omega=1,J=2,m_J=0\rangle \otimes |n,\omega_\lambda,\boldsymbol{\epsilon}_\lambda\rangle, \\
|7\rangle &= |j=2,\Omega=2,J=2,m_J=0\rangle \otimes |n,\omega_\lambda,\boldsymbol{\epsilon}_\lambda\rangle, \\
|8\rangle &= |e_0\rangle \otimes |n-1,\omega_\lambda,\boldsymbol{\epsilon}_\lambda\rangle. \qquad (4.71)
\end{aligned}$$

In the following sections, only the σ^- polarisation case will be discussed, as the σ^+ polarisation calculation is almost identical in all respects.

4.6.3 Dressed state formalism

To determine the correct states that will uncouple at large R, the asymptotic potential matrix (4.70) can be diagonalised,

$$\boldsymbol{W}^D_\infty = \boldsymbol{U}^{-1}\boldsymbol{W}_\infty\boldsymbol{U} \qquad (4.72)$$

so that $\boldsymbol{W}^D(R) = \boldsymbol{U}^{-1}\boldsymbol{W}(R)\boldsymbol{U}$ becomes diagonal for $R \to \infty$. The eigenvectors of the diagonalisation, $\boldsymbol{U}$, define the transformation from the hybrid jj basis to the new 'dressed' basis by $|\beta\rangle = \sum_a (\boldsymbol{U}^{-1})_{a\beta}|a\rangle$. In the dressed basis the differential equations (4.65) become

$$\sum_{\beta'} \left[-\frac{\hbar^2}{2\mu}\frac{d^2}{dR^2}\delta_{\beta\beta'} + W^D_{\beta\beta'}(R) \right] \tilde{G}_{\beta'}(R) = 0 \qquad (4.73)$$

where the radial wave functions $\tilde{G}_\beta(R)$ possess the asymptotic form (4.62). The energies are then $E_\beta = -W^D_{\beta\beta}(R \to \infty)$ and can be complex.

Napolitano [54] used the dressed state formalism to analyse a sodium system and was able to diagonalise this basis by a completely analytical method, because the effect of the laser term was restricted to the coupling of two separate pairs of states within the six total basis states. Napolitano then invoked the approximations $\Delta E \gg \Gamma$ and $\Delta E \gg \hbar\Omega$, where Ω was the Rabi frequency of the states under consideration, to reduce the diagonalisation to an analytically manageable form. However, in the present calculations, analytical diagonalisation is not used because a larger number of asymptotically coupled states exist in the helium system and also because these approximations on ΔE need to be avoided for this system. Instead, direct numerical diagonalisation is utilised, with the eigenvalues and eigenvectors of $\boldsymbol{W}$ found using a standard numerical package.

Because numerical diagonalisation is utilised however, some important issues become apparent. Firstly, it is not guaranteed that there will be the same number of open and closed channels before and after the diagonalisation, although in practice this is not a problem for the chosen energies of the helium system. Secondly, the imaginary component of the undressed closed excited channel may taint the other channels, thereby introducing 'closed-like' behaviour in them. Thirdly, the diagonalisation procedure results in a set of degenerate eigenvalues for which numerical techniques do not produce a unique ordering or unique orthogonal representation of the eigenvectors.

The first issue regarding the number of open and closed channels for a particular energy E is of no consequence in the current investigation as the asymptotic energies of the metastable and the excited levels 'repel' each other as they are coupled. Hence the dressed scattering states have increased scattering energy relative to the undressed metastable scattering states. Similarly an energy that is bound in the excited state potential will always remain bound after the dressing.

The second issue – the tainting of the open channels by the imaginary component of the excited state – is a subtle, but important, modification of the system. In the original undressed states (4.69), four are open and one is closed. This can be shown by determining the asymptotic behaviour of the wave functions for each of these channels when the laser intensity is zero so that the Rabi couplings vanish. The undressed states have two distinct energies, E_k (which is four-fold degenerate) and $\Delta E - i\Gamma/2$, see (4.70). The channels that have oscillatory wave functions at long range, corresponding to $E_k > 0$ and k_γ real, persist to $R \to \infty$ and so are called open channels, whereas those with exponentially increasing and decreasing wave functions, corresponding to $\Delta E < 0$ and k_γ imaginary, cannot exist physically at $R \to \infty$ and are termed closed channels. The five dressed states cannot be classified so easily. After the diagonalisation there are three distinct asymptotic energies E_γ^∞. One represents a set of three open channels as it is purely real with $E_\gamma^\infty > 0$ and has a three-fold degeneracy. Of the channels associated with the other two energies, one must be classified as closed because E_γ^∞ is comprised of a large negative real component and a small imaginary component and will be dominated by exponentially increasing and decreasing solutions at long range. The final channel, however, is not so easily classified; its energy has a positive real component so that it would normally be considered an open channel except that its energy also possesses a small imaginary component. This means that its asymptotic wave function is of the form (4.62) where the incoming and outgoing solutions are represented by (4.63), which can be written in the alternative form

$$h_\gamma^\mp \sim e^{\mp i k_\gamma^r R} e^{\pm k_\gamma^i R}, \tag{4.74}$$

where $k_\gamma = k_\gamma^r + i k_\gamma^i$ and both k_γ^r and k_γ^i are real and positive. If these asymptotic solutions are continued to $R \to \infty$, the solution h_γ^- increases nonphysically and $h_\gamma^+ \to 0$, indicating that this energy must logically correspond to a closed channel. The practicalities of the situation however, make the use of such a definition unfeasible. Firstly, other systems such as the sodium system investigated by Napolitano or systems with no undressed degenerate entrance energies, would consist entirely of closed channels if the solutions are treated in this way. Secondly, k_γ is predominantly real with $k_\gamma^i \ll k_\gamma^r$, so that the numerical integration would have to be performed over a huge number of oscillations of the wave function before it substantially decays. Additionally, k^r_γ and k^i_γ vary with laser detuning and intensity, further complicating the issue. Therefore, for the analysis of the dressed states, this ambiguous channel is treated as a 'pseudo-open' channel by enforcing a maximum interatomic separation R_{max} at an interatomic range where the separate channels are completely decoupled, the usual procedure for multichannel calculations, and where the exponential factors $e^{\pm k^i_\gamma R}$ may be considered approximately constant in the matching to the asymptotic wave function of the pseudo-open channel. The matrix element $S_{\gamma\gamma'}$, normally used to represent the outgoing flux in channel γ as $R \to \infty$ that results from the incoming flux in channel γ' from $R \to \infty$, is redefined by this choice of R_{max}. Hereafter, the matrix element $S_{\gamma\gamma'}$ will be defined as the outgoing flux at R_{max} resulting from the incoming flux at R_{max}.

The third issue presented by use of numerical diagonalisation concerns the ordering of the eigenvectors corresponding to the degenerate energies of the dressed channels. No eigenvalue decomposition routine that the author is aware of has enough robustness in its ordering of eigenvectors to ensure that a small perturbation of the potential matrix $\boldsymbol{W}$ is guaranteed to produce a small and smooth perturbation of its eigenvectors. In fact, the standard method of QR decomposition without pivoting converges to one of two neighbourhoods. Attempts have been made to alleviate this problem so that a specific ordering can be imposed upon the result of the diagonalisation as the laser frequency is varied, but no successful method was found. Fortunately, any observable quantity generated from the S matrix must not rely on the ordering of the individual degenerate channels over the range of different laser frequencies. Hence, neither the overall loss of unitarity nor an average formed over all the degenerate channels will vary, as a unitary transformation that reorders the degenerate eigenvectors cannot affect the observables of the system.

4.6.4 Modified radiation coupling

The alternative to using the dressed state formalism is to artificially force the existing basis to become diagonal by imposing a R-dependent decay upon the laser coupling. This requirement is simple to implement through the replacement $V^{\text{int}}_{eg} \to \tilde{V}^{\text{int}}_{eg}$ where

$$\tilde{V}^{\text{int}}_{eg} = \begin{cases} V^{\text{int}}_{eg}(R) & \text{for } R \leq R_z \\ V^{\text{int}}_{eg}(R)\exp\left[-\rho(R-R_z)^2\right] & \text{for } R > R_z. \end{cases} \tag{4.75}$$

Here ρ is a decay constant that should be chosen so that the dampening does not introduce any artifacts into the numerical calculation. These artifacts can be the result of back reflections of the incoming part of a channel off the Gaussian profile of the modified laser coupling or sudden mixing between the channels in the dampening region. As will be shown later (see figure 4.8), the form of dampening (4.75) does cause artifacts in the results but these may also be avoided by judicious choice in the types of profiles formed from the S-matrix elements. A value for ρ in this thesis is chosen such that the coupling decay takes place over many wavelengths of oscillation. The constant R_z bears some resemblance to the $R_{\max}$ parameter of the dressed state formalism and indeed the two should be made equal so that the results can be more easily compared between the two methods.

The modified radiation coupling avoids the diagonalisation of $\boldsymbol{W}_\infty$and hence also avoids the issues presented in the previous section. It is a much more attractive scheme to implement, although the possibility of reflections from, and mixing through, the activation of the laser coupling can causes some problems which will be discussed in the following sections.

4.6.5 Numerical implementation details

The equations for the dressed state formalism, (4.73), and the equations for the modified radiation coupling, (4.65) with the substitution (4.75), were solved using two different techniques. The first was based on the relaxation method [133] which employs a matrix boundary value method. The differential equations are converted to matrix form by replacing the derivatives with their numerical approximation on adjacent grid points and the values of the wave function by a trial solution. The matrix equations, which are of a sparse block structure that is predominantly tri-diagonal, are iteratively solved for the wave function which is then substituted back into the equations as a new trial solution. By careful application of intermediate boundary conditions in the method, a series of regions with different step sizes were created that allowed the mesh grid to best represent the solution in each region. To reach the desired accuracies, very few (less than five) iterations were required. However, to calculate the complete set of linearly independent solutions that are needed to construct the scattering matrix, the relaxation method must be run many times with differing boundary conditions. Although the matrices involved in the calculation are sparse, they must span the entire interatomic range of interest at a fine enough spacing to maintain numerical accuracy and hence are computationally intensive.

The second technique, the renormalised Numerov method, was used in order to decrease the calculation time of the PA profiles. The method, which is described in further detail in appendix C, is a shooting method that is well suited to differential equations of the form of Schrödinger's equation. It has the advantage of being able to calculate simultaneously all the linearly independent solutions and can be used with arbitrary granularity without memory limitations. Although the retained solution may be produced on a relatively coarse grid, it will have been calculated using a very finely spaced grid. Furthermore, the renormalised Numerov method can also split the calculation into separate regions so that different step sizes may be used to best represent the dynamics of the solution.

For either method, the outer boundary of the calculation was placed at $10^6\ a_0$. At this distance the maximum coupling between different channels, even for the dressed state formalism at high intensity, is less than $2 \times 10^{-16}\ E_h$. For the modified radiation coupling, the dampening of the coupling began at $R_z = 2 \times 10^5\ a_0$ with a dampening factor of $\rho = 1.6 \times 10^{-4}\ a_0^{-2}$. This allowed the dampening to take place over many wavelengths of the incident flux so as to not affect the results adversely. The wavelength of the open channels is $\lambda \approx 2300\, a_0$ for a kinetic energy $E_k = 10^{-11}\, E_h$ ($T = 2.1\,\mu\mathrm{K}$) so the coupling will gradually dampen to 99% of its original value after 250 wavelengths. The regions of differing step size for the renormalised Numerov method were determined empirically and the following values were used for the step size ΔR:

$$\Delta R = \begin{cases} 0.001\, a_0 & 3\, a_0 < R < 40\, a_0, \\ 0.01\, a_0 & 40\, a_0 < R < 500\, a_0, \\ 0.1\, a_0 & 500\, a_0 < R < 10^4\, a_0, \\ 5.0\, a_0 & 10^4\, a_0 < R < 10^6\, a_0. \end{cases} \tag{4.76}$$

4.6.6 Detection of the resonance through spontaneous loss

Away from resonance, the $\boldsymbol{S}$-matrix is expected to slowly vary with laser detuning and laser intensity. However, at the location of a resonance corresponding to a bound level in the excited state potential, the S-matrix is expected to pass through a region of sharp and sudden variation. This can be observed in the spectroscopic profiles with and without the presence of the spontaneous loss term. The elastic and total collision cross sections are the only profiles that can be calculated without the presence of loss. These are often very dynamic away from resonance and can mask the sharp variation of the resonance itself. In contrast, the cross section for spontaneous photon emission is often negligible away from resonance, causing the resonance peaks to be more prominent. The cross section for photon emission from a single entrance channel γ is represented by the loss term $i\Gamma/2$ in the excited state and so can be related to the loss of unitarity of the S-matrix. The cross section is given by

$$\sigma_\gamma^{\text{photon}} = \frac{\pi}{k_\gamma^2}\left(1 - \sum_{\gamma'} |S_{\gamma'\gamma}|^2\right). \tag{4.77}$$

The loss rate is then $\mathcal{L}_\gamma = \langle v_\gamma \sigma_\gamma^{\text{photon}} \rangle$ where $\langle \ldots \rangle$ denotes a thermal average over a distribution of the asymptotic relative velocities $v_\gamma = \hbar k_\gamma/\mu$ of the two colliding atoms. Because ultracold temperatures are considered here, the thermal distribution is very narrow and the thermal averaging can be ignored, giving $\mathcal{L}_\gamma \approx v_\gamma \sigma_\gamma^{\text{photon}}$.

As previously mentioned in section 4.6.3, the degenerate dressed state channels are not guaranteed to be a smooth function of laser frequency and/or intensity due to the arbitrary ordering produced in the numerical diagonalisation. Consequently $\sigma_\gamma^{\text{photon}}$ will not vary smoothly with respect to laser detuning. In order to overcome this problem and to produce a smoothly varying profile, the cross sections $\sigma_\gamma^{\text{photon}}$ are averaged over degenerate channels. This combination must be smooth as the average is invariant with respect to the ordering of the degenerate channels and so is an observable of the system. Further combinations

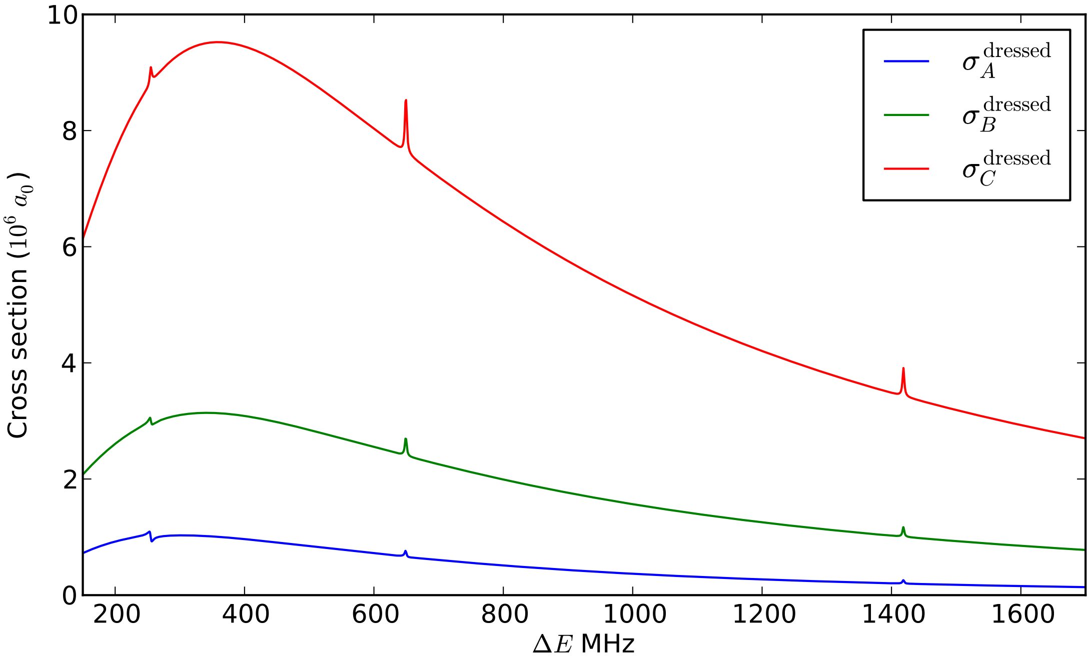

Figure 4.6: Photoassociation profiles at low laser intensity of 64 mW/cm^2 in the dressed state formalism using spontaneous loss from the excited state as the spectroscopic signal. The loss is calculated from three different averages A, B and C of the entrance channels, see (4.78), (4.79) and (4.80). The PA resonances are overlaid on a pronounced background profile.

---

may be formed by including the pseudo-open channel. Three particular possibilities are:

$$\sigma_A^{\text{dressed}} = \frac{1}{n_d} \sum_{\beta_d} \sigma_{\beta_d}^{\text{photon}}, \tag{4.78}$$

$$\sigma_B^{\text{dressed}} = \frac{1}{1+n_d} \sum_{\beta} \sigma_{\beta}^{\text{photon}} \tag{4.79}$$

and

$$\sigma_C^{\text{dressed}} = \sigma_{\beta_p}^{\text{photon}}, \tag{4.80}$$

where β_d enumerates the degenerate channels, n_d is the total number of degenerate channels, β_p represents the pseudo-open channel and $\beta = \{\beta_d, \beta_p\}$ enumerates all open and pseudo-open channels. Although separate contributions from the colliding channels are present in each profile, the resonance position and width will not differ between the profiles.

A sample plot of the three dressed profiles for a low intensity of 64 mW is presented in figure 4.6. It can be seen that the resonance occurs in exactly the same position for all three profiles, although the relative magnitudes of the profiles are vastly different. Much of the loss and strength of the resonance originates in the pseudo-open channel. This is expected as the pseudo-open channel is most strongly coupled to the excited state.

The profiles of $\sigma_\gamma^{\text{photon}}$ for the modified radiation coupling do not suffer from the problem of degeneracies as in the case of the dressed profiles and each profile varies smoothly with laser detuning. However, in order to compare the results of the dressed states procedure with those for the modified radiative coupling procedure, the profile

$$\sigma^{\text{modified}} = \frac{1}{n_o} \sum_{\beta} \sigma_{\beta}^{\text{photon}} \tag{4.81}$$

is also generated, where n_o is the number of open channels. This cross section is closely related to $\sigma_B^{\text{dressed}}$. Sample plots of the modified radiation coupling profiles $\sigma_\gamma^{\text{photon}}$ are presented in figure 4.7. All of the channels exhibit oscillatory background behaviour in the profiles, apart from the suppression in the channel $\Omega = 2$ that is not directly coupled to the excited state. This oscillatory background can be significantly varied by changing the smoothing constant ρ in the R-dependent coupling $\tilde{V}_{eg}^{\text{int}}$.

This behaviour can be understood by undertaking a calculation limited to the asymptotic region around R_z which emulates a single incoming channel by enforcing travelling wave boundary conditions. The solutions resulting from this isolated calculation consist of a back reflection produced by the activation of the laser coupling, and an inwards admixture of channels, as illustrated in figure 4.8. This mixing and reflection is heavily dependent upon the laser coupling and gives rise to the significant oscillatory behaviour in the profiles. The formation of the averaged profile σ^{modified} suppresses this behaviour, as can be seen in figure 4.9. A conclusion that can be drawn from the oscillatory behaviour of the $\sigma_\gamma^{\text{photon}}$ profiles is that the form of the laser activation is very important to the physics of the system. As will be shown in the next section, the use of the complete laser coupling term rather than that based upon the dipole approximation introduces the correct R-dependence of the coupling for large R and removes this oscillatory behaviour.

Dressed profiles and the σ^{modified} profile of the modified radiation coupling for high laser intensities are shown in figures 4.10 and 4.11 respectively. All the low and high intensity profiles show prominent backgrounds. These backgrounds do not occur in theoretical spectra calculated for other systems such as the spectra of Montalvão and Napolitano [55] calculated for photoassociation of strontium.

For the modified radiation coupling profiles, it is quite straight forward to determine the origin of the background. Firstly, the profiles asymptote to zero as $\Delta E \to \infty$ and become Lorenztian-like as $\Delta E \to 0$. Secondly, if the excited state potential well is artificially deepened by a several orders of magnitude, the background becomes much smaller in magnitude. A similar reduction in background is observed when E_k is increased by several orders of magnitude. Because the laser can populate scattering states of the excited manifold if it is not significantly detuned from atomic resonance, these observations suggest that the shallow nature of the excited potential well is the reason for the significant background. This shallow nature can be quantified by the relative magnitude of the asymptotic matrix elements in the potential (4.70). Because the kinetic energies E_k are very small (< 1 MHz) and the only other diagonal term $\Delta E \leq 1500$ MHz is not overly large when compared to the spontaneous width of the excited state (3 MHz FWHM) or the off-diagonal coupling terms (which can be as large as 50 MHz), the matrix is not strongly diagonal and deviates

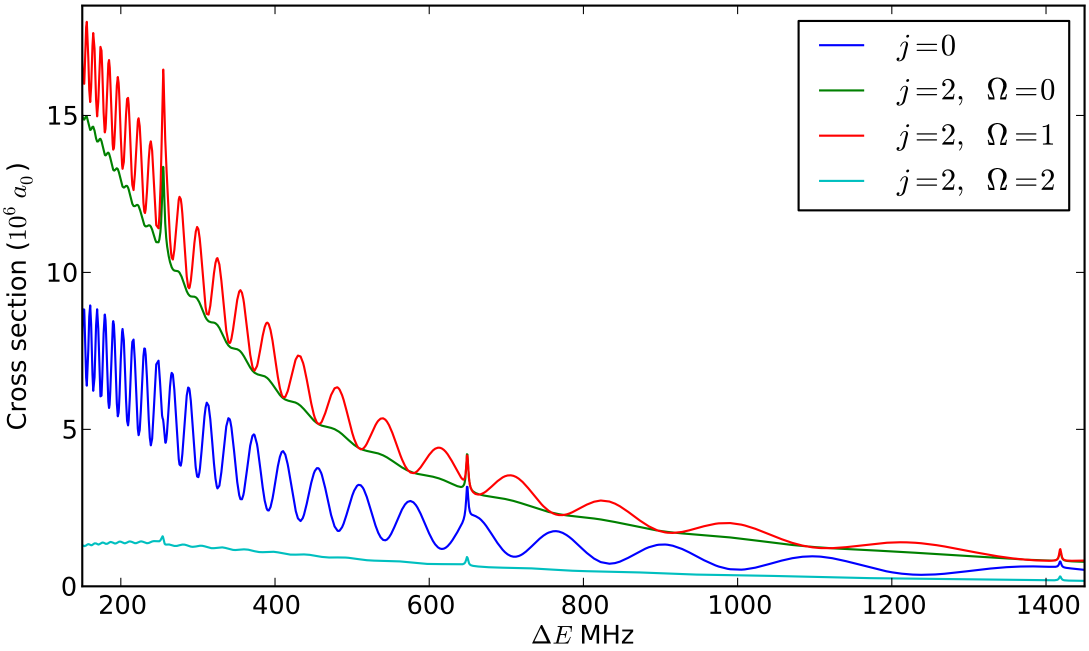

Figure 4.7: Photoassociation profiles, $\sigma_\gamma^{\text{photon}}$ at low laser intensity of 64 mW in the modified radiation coupling formalism using spontaneous loss from the excited state as the spectroscopic signal. The background to the profiles has significant oscillatory behaviour and partially obscures the resonance peaks. The legend indicates the metastable basis state that corresponds to the value of γ.

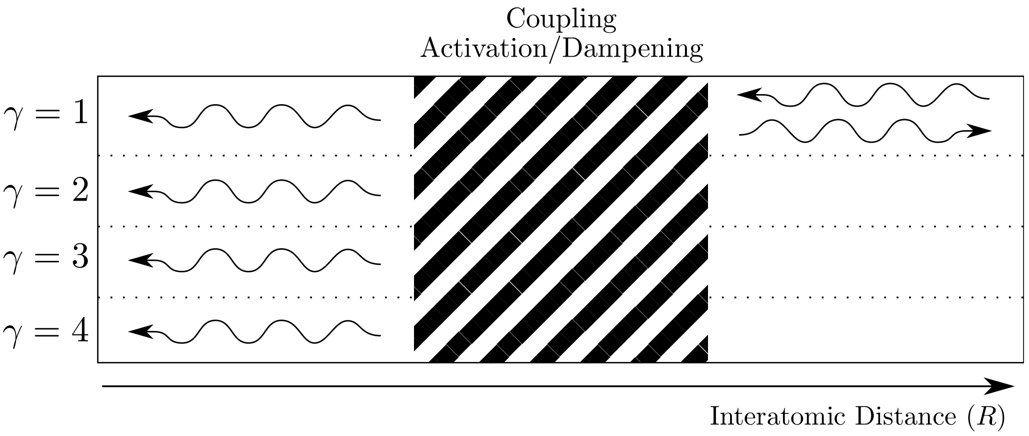

Figure 4.8: An illustration demonstrating the mixing and reflection from the dampening of the modified radiation coupling, represented here by the shaded region.

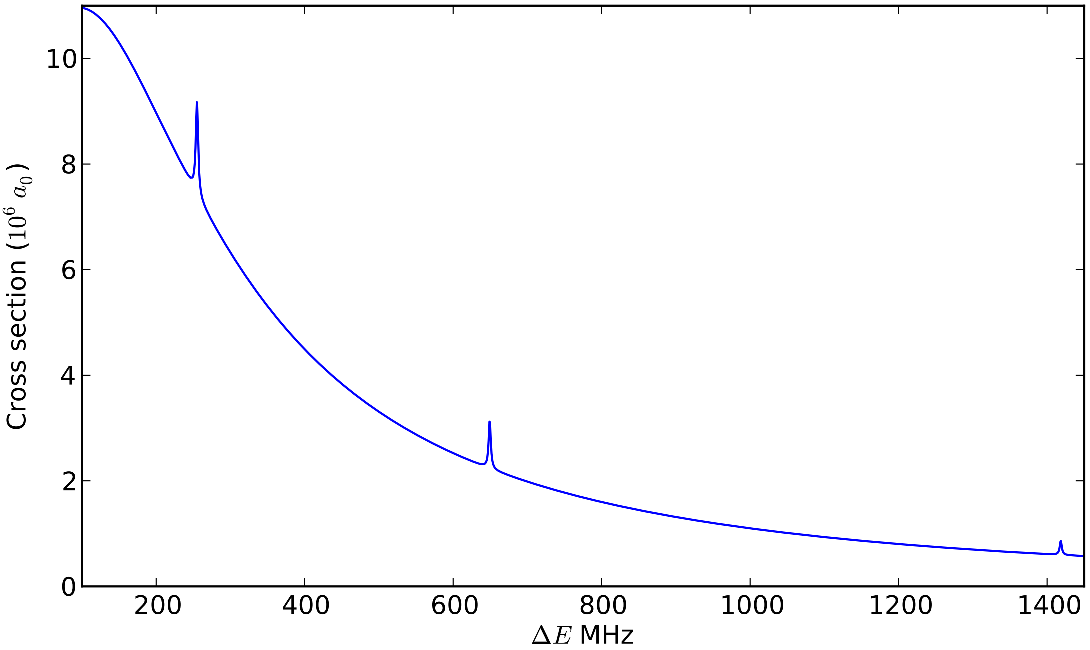

Figure 4.9: The average of the photoassociation profiles in figure 4.7, given by equation (4.81), demonstrating the smoothing of the oscillatory background.

significantly from Hermiticity. To demonstrate this nature, an additional calculation was performed that artificially deepened the excited state potential $V_e^{\mathrm{SC}}(R)$ of the potential matrix (4.66) by a factor of 100. In this toy model, the PA spectrum, shown in figure 4.12, has a much reduced background.

The backgrounds of the dressed state profiles require a more complicated explanation because they must be considered from the laser coupled picture which is difficult to consider semi-classically. As the undressed potential matrix becomes more and more off-diagonal, by either increasing the laser intensity or by probing smaller laser detunings, the dressed pseudo-open channel takes on more of the excited state character and becomes more strongly coupled to the dressed closed channel. In contrast, the degenerate open channels become *less* coupled to either of the excited or pseudo-open channels. In this situation the pseudo-open profile, $\sigma_C^{\mathrm{dressed}}$, will approach nearly complete loss as the pseudo-open channel becomes more like a closed channel and the degenerate profile, $\sigma_A^{\mathrm{dressed}}$, will reduce in magnitude until only negligible loss is present in the open channels. This may seem counter-intuitive but an important process is missing in the description of the system that has been used to calculate the profiles: the turning on of the laser. If a system is to be prepared in the dressed basis then a conversion from a well defined undressed system by the introduction of a laser will result in a certain proportion of the undressed open channels transforming to the pseudo-open and closed dressed states. These contributions will decay very quickly, leaving only the remaining portion of the initial system in the degenerate open channels which are effectively decoupled from the excited state for high laser intensity. Because a small fraction will always transform to the dressed open channels, even in the limit of infinite intensity, a constraint upon the maximum loss from the system is enforced which can be termed the saturation of the laser. For finite intensities the loss from the conversion process is not as great but the degenerate open channels are somewhat coupled to the closed channel, allowing loss to occur in the resonance region and giving rise to visible resonance peaks.

The dressed state profiles also exhibit an unusual shape for the resonances in the regime of high laser intensity due to an interference between the background and the resonance itself. These resonances cannot be described by a simple Lorentzian profile but a Fano profile [134, 135] can accurately match the form of the resonance. The Fano profile is of the form

$$f(\epsilon) = A_{\mathrm{bg}}(\epsilon) + A_{\mathrm{res}} \frac{(\epsilon + q)^2}{1 + \epsilon^2}, \tag{4.82}$$

where $A_{\mathrm{bg}}(\epsilon)$ describes the background that is approximately linear in the neighbourhood of the resonance, A_{res} is the strength of resonance, $\epsilon = (E - E_{\mathrm{res}})/(\Gamma_{\mathrm{res}}/2)$ is a dimensionless variable representing the energy and E_{res} and Γ_{res} are the position and full width of the resonance. The parameter q is the Fano parameter that is a measure of the ratio of direct (background) scattering to resonant scattering. As the resonances reduce to Lorentzian profiles in the low intensity limit, which occurs for $q \to \infty$ and $A_{\mathrm{res}} \to 0$, it is simpler numerically to match to the alternate form

$$f(\epsilon) = A_{\mathrm{bg}}(\epsilon) + A'_{\mathrm{res}} \frac{(1 + p\epsilon)^2}{1 + \epsilon^2} \tag{4.83}$$

where $p = 1/q$ and $A'_{\mathrm{res}} = qA_{\mathrm{res}}$. The Lorentzian-like behaviour of the modified radiative coupling resonances and the low intensity dressed state resonances is indicated by their small value of $p \leq 10^{-2}$. However, the high intensity dressed state resonances are significantly non-Lorentzian, represented by values of up to $p \sim 0.5$, which indicate significant interference in the scattering solutions.

From the calculation of the profiles for a range of laser intensities, it is possible to obtain the resonance position and width as a function of laser intensity and to determine the dependence of line shift and width upon intensity. This is shown in figures 4.13 and 4.14 which illustrate the near-linear dependence of the line shift and quadratic dependence of the line width. A least squares fit to the data highlights this, as can be seen in table 4.2. One higher polynomial order has been calculated in the fits to quantify the deviation from linear and quadratic behaviour for the shift and width respectively. The last column of the table indicates the maximum intensity above which the resonance profile either (a) has too little magnitude to be detectable; or (b) overlaps other nearby resonances. The relative magnitudes of the coefficients indicate that at maximum intensity the quadratic contribution to the shift is approximately 2.5% and the cubic contribution to the width is approximately 15%. Note that these are the maximum deviations from linear and quadratic behaviour and the derivations are generally much smaller for more common laboratory laser intensities on the order of mW.cm^{-2}.

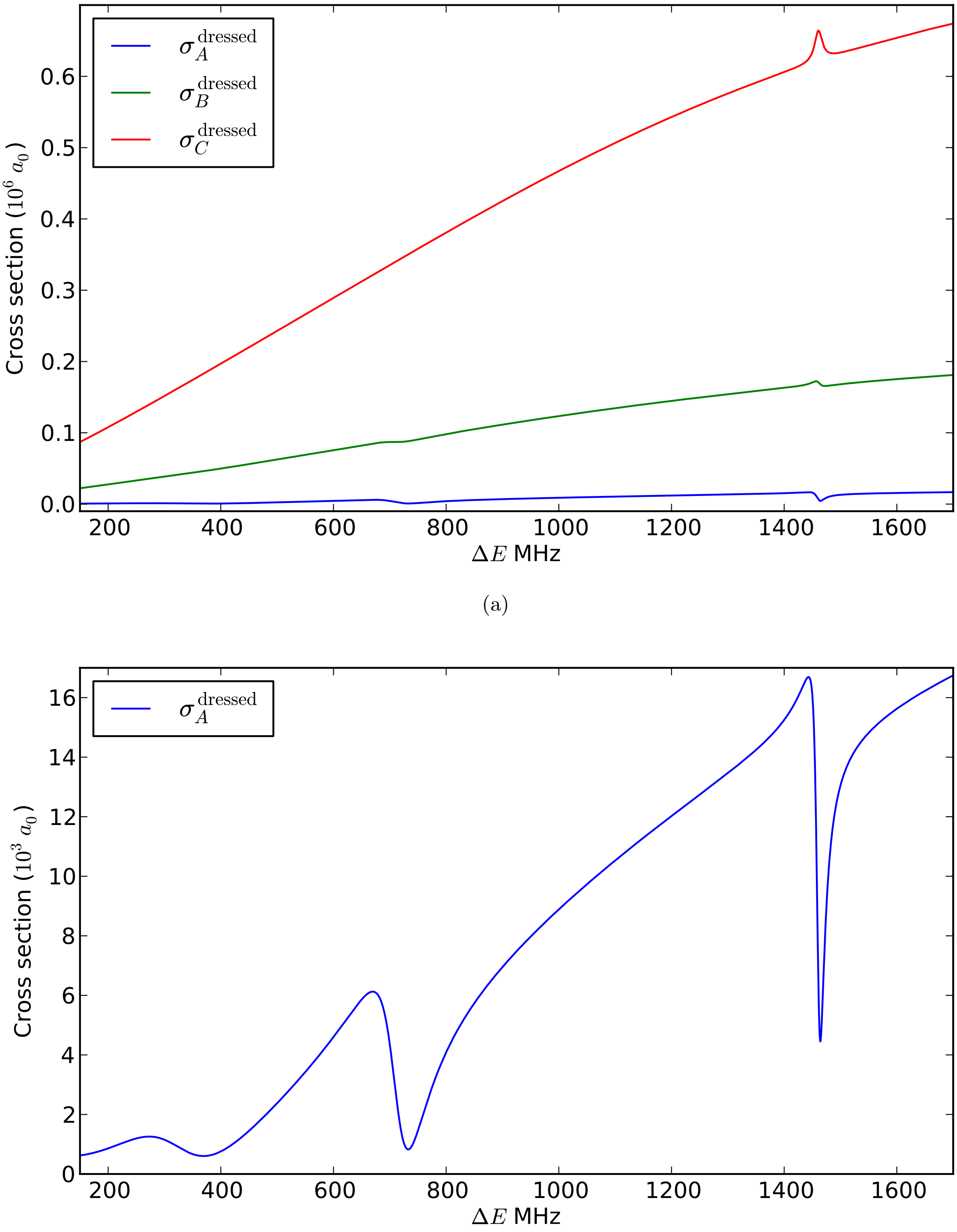

(a)

(b)

Figure 4.10: Photoassociation profiles at high laser intensity of 6.4 W in the dressed state formalism using spontaneous loss from the excited state as the spectroscopic signal. The profile for $\sigma_A^{\rm dressed}$ has been enlarged in (b) to highlight the unusual resonance shapes. Note the different y-axis scales between (a) and (b) and that in figure 4.6. Also note that the strength of the resonance and background diminishes as the laser detuning $\Delta E \to 0$.

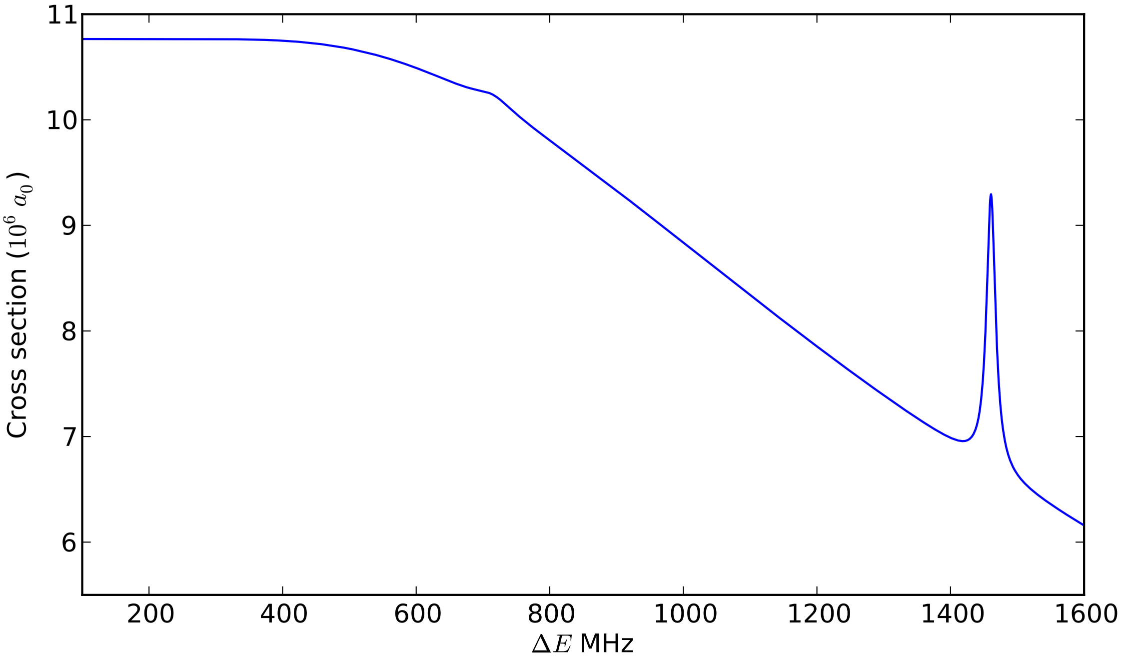

Figure 4.11: Photoassociation profile σ^{modified} at a high laser intensity of 6.4 W in the modified radiation coupling formalism using spontaneous loss from the excited state as the spectroscopic signal. Note the reduction in strength of resonance and the saturation of the background as laser detuning $\Delta E \to 0$.

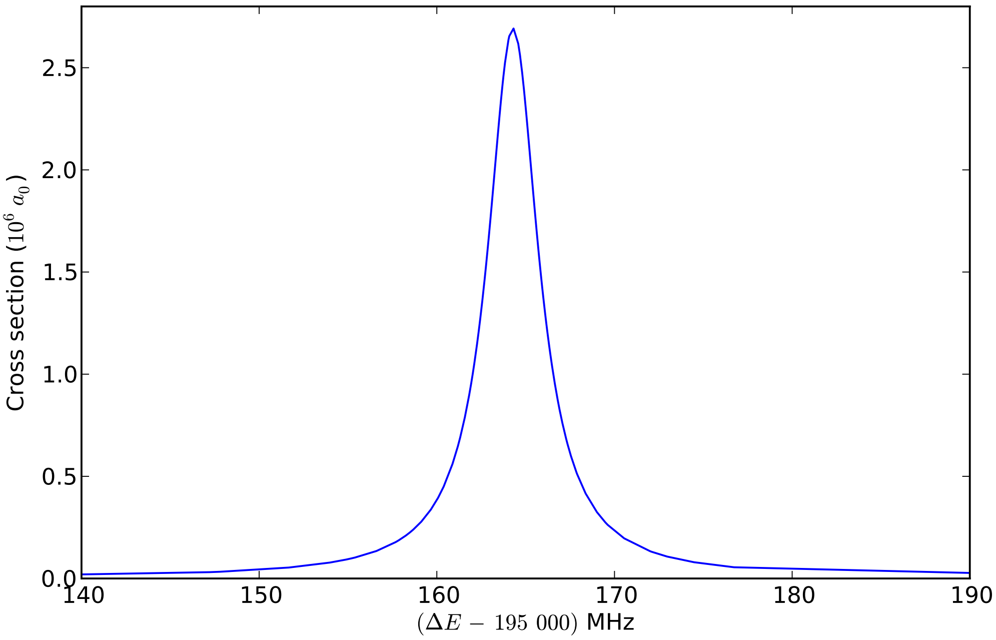

Figure 4.12: Photoassociation spectrum for the 0_u^+, $J = 1$ system at a laser intensity of 6.4 W/cm^{-2} with the excited state potential $V_e^{\text{SC}}(R)$ of the potential matrix (4.66) artificially deepened by a factor of 100. The detuning of the spectrum is localised around the most bound level of the potential. The background that was prominent in figures 4.6 and 4.9 has completely disappeared in this profile, indicating that it is the shallow nature of the potentials that is the cause for the non-zero background.

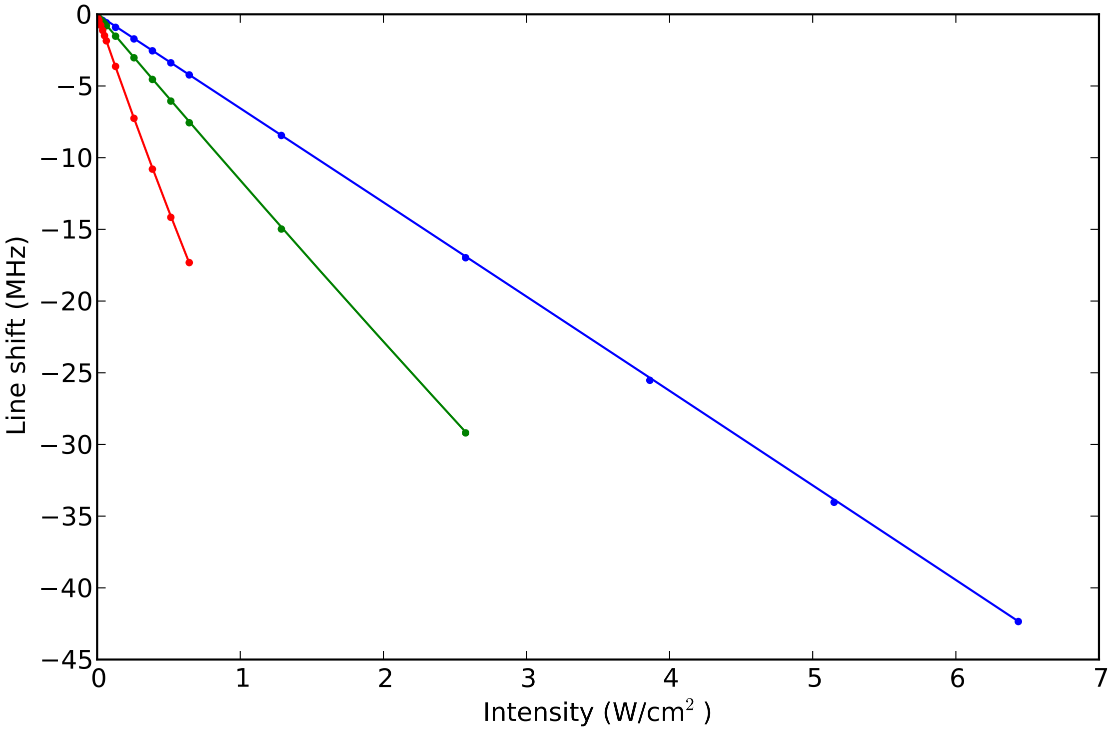

Figure 4.13: Laser intensity dependence of the line shift for the three lowest bound levels of the excited state when coupled to the metastable manifold by σ^-polarised light. The dependence is very close to linear.

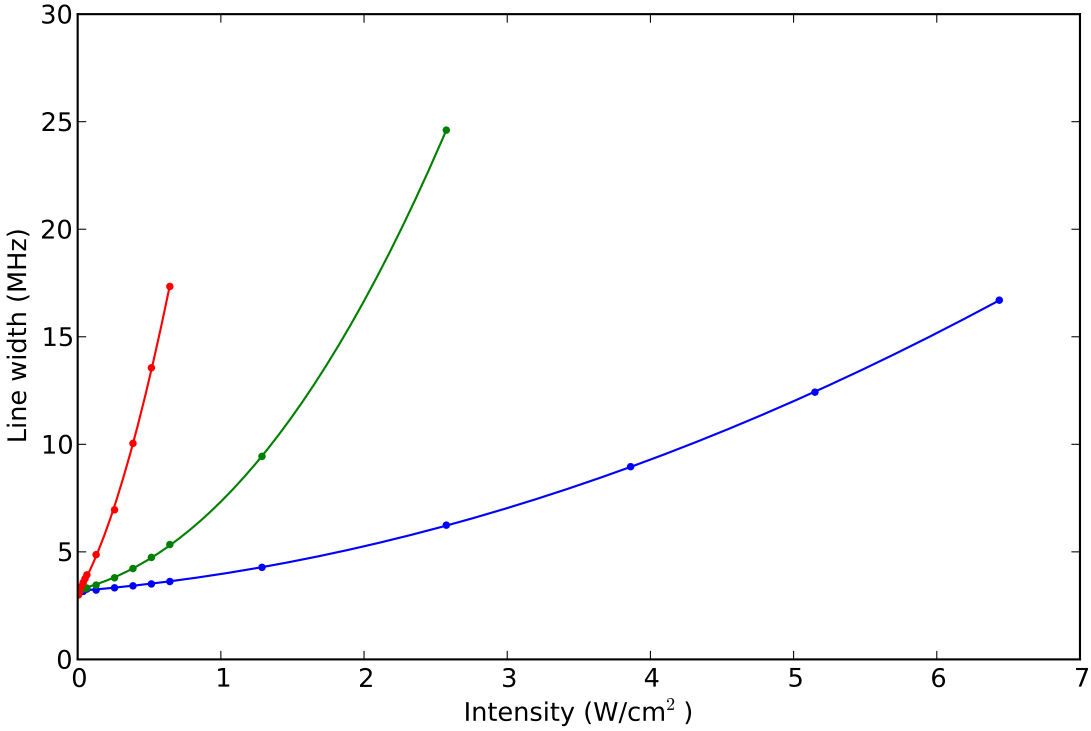

Figure 4.14: Laser intensity dependence of the resonance width for the three lowest bound levels of the excited state when coupled to the metastable manifold by σ^- polarised light. The dependence is close to quadratic, see table 4.2.

Table 4.2: Quadratic, $s_1 I + s_2 I^2$ and cubic, $w_0 + w_1 I + w_2 I^2 + w_3 I^3$ fits to the line shift and widths respectively of the resonances for the lowest three bound levels of the excited state. The final column indicates the intensity below which the resonances can be discerned. The shifts and widths are in MHz, the intensity in W/cm^2 and the coefficients (s_n, w_n) in MHz (W/cm^2)$^{-n}$.

		Shift		Width				
Level	Polarisation	s_1	s_2	w_0	w_1	w_2	w_3	$I_{\max}$
$v = 0$	σ^-	-6.514	-0.023	3.233	0.441	0.304	-0.0093	7.0
	σ^+	-7.781	-0.021	3.226	0.730	0.329	-0.0091	7.0
$v = 1$	σ^-	-11.77	0.074	3.231	1.51	2.87	-0.34	3.2
	σ^+	-10.30	-0.018	3.219	1.47	1.70	-0.10	3.2
$v = 2$	σ^-	-29.79	3.90	3.216	6.25	36.9	-21.9	0.4
	σ^+	-24.95	1.13	3.197	5.44	18.2	-4.20	0.6

4.6.7 Detection without spontaneous loss

When the spontaneous loss term $i\Gamma/2$ of the excited state is omitted, the diagonalisation procedure produces an asymptotic matrix that is Hermitian and has purely real diagonalised energies. Hence the dressed state formalism does not introduce a 'pseudo-open' channel as was found in section 4.6.3. Because the matrix is now Hermitian, however, no loss of unitarity can be observed and alternative profiles must be used to reveal the dynamical aspects of the resonances. Two such profiles are the total and elastic cross sections. The total cross section represents the likelihood for atoms in the entrance channel to make any kind of collision whereas the elastic cross section represents the likelihood that the system exits the collision in the same channel that it entered. These cross sections are given by

$$\sigma_\gamma^{\text{elastic}} = \frac{\pi}{k_\gamma^2}|T_{\gamma\gamma}|^2 = \frac{\pi}{k_\gamma^2}(|1 - S_{\gamma\gamma}|^2) \tag{4.84}$$

and

$$\begin{aligned} \sigma_\gamma^{\text{total}} &= \frac{\pi}{k_\gamma^2}|\sum_{\gamma'} T_{\gamma'\gamma}|^2 \\ &= \frac{\pi}{k_\gamma^2}|\sum_{\gamma'} S_{\gamma'\gamma} - \delta_{\gamma'\gamma}|^2 \end{aligned} \tag{4.85}$$

where $\boldsymbol{S} \equiv \boldsymbol{I} + i\boldsymbol{T}$. These cross sections are difficult to analyse because of the need to theoretically predict their behaviour for a multichannel system away from resonance. Indeed, calculating some sample profiles shows that the modified radiation coupling profiles possess a very rapidly oscillating background that completely overwhelms the resonance, see figure 4.15. The profiles presented in figure 4.15 are the averages $\sigma^{\text{elastic}} = \sum_\gamma \sigma_\gamma^{\text{elastic}}$ and $\sigma^{\text{total}} = \sum_\gamma \sigma_\gamma^{\text{total}}$. In contrast to the loss profiles presented in figures 4.7 and 4.9, the averaging process here does not remove the oscillatory behaviour.

The profiles that result from the dressed state formalism shown in figures 4.16 and 4.17

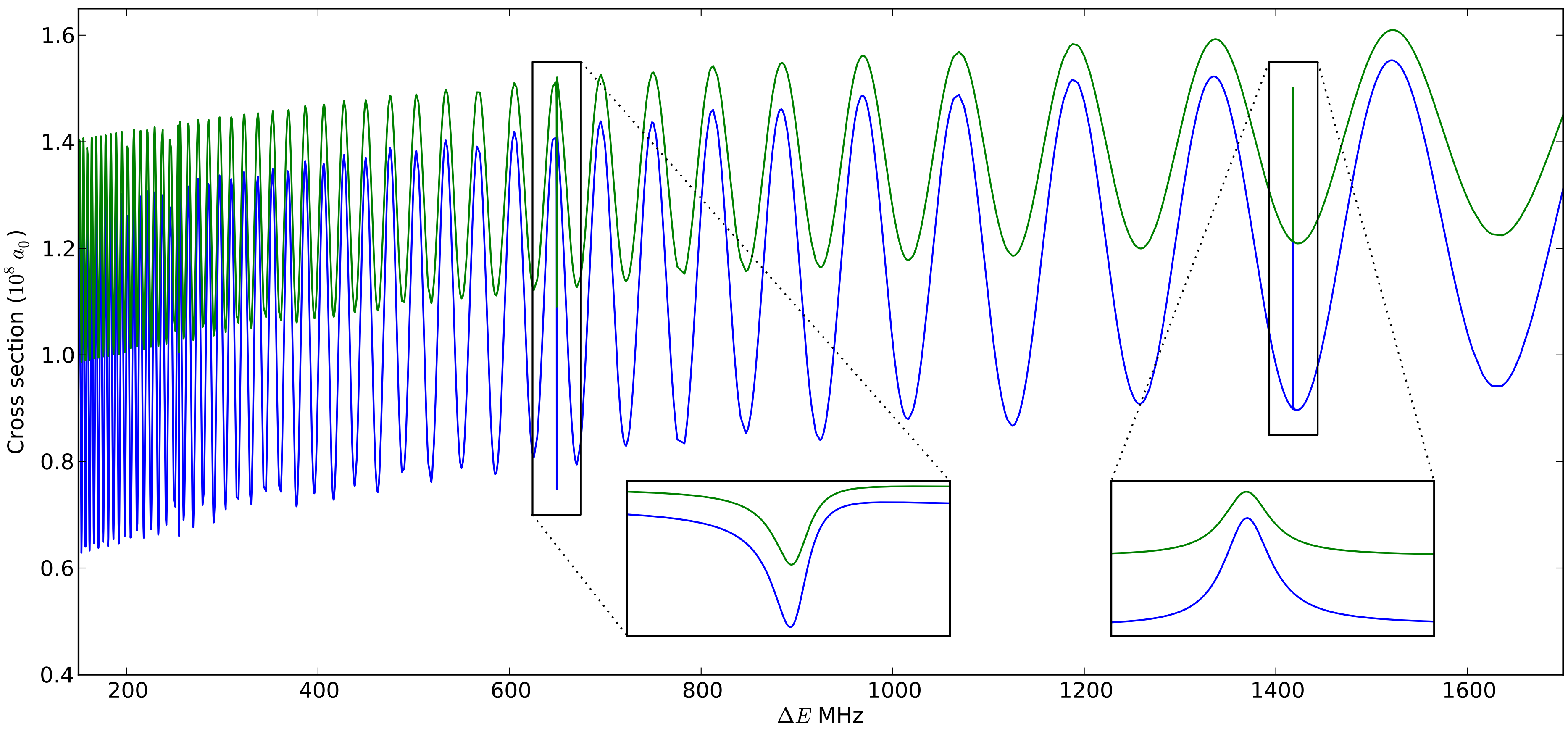

Figure 4.15: Profiles of the elastic and total cross sections of the modified radiation coupling method at low laser intensity of 64 mW/cm^2. The severe oscillatory behaviour completely overwhelms the resonances (shown in the inserts). The total cross section is the larger of the two cross sections.

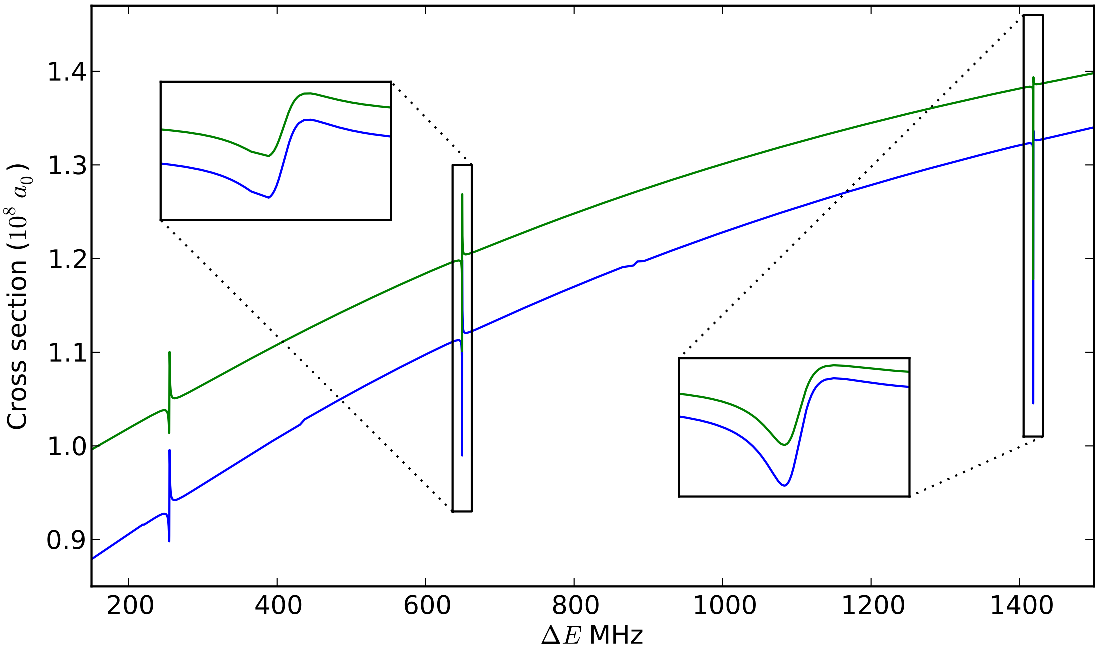

Figure 4.16: Profiles of the averaged elastic and total cross sections of the dressed state formalism at a low laser intensity of 64 mW/cm^2. The total cross section is the larger of the two cross sections.

do, however, possess a much smoother background that does not exhibit the significant oscillations that are present in the modified radiation coupling profiles. The resonances in these profiles fit very well to Fano profiles and the position and width parameters can be found for a range of laser intensities in a similar fashion to that described in section 4.6.6 for the profiles that included the loss term. The line shifts and widths calculated in this manner are very similar to the shifts and widths from the loss calculation and are shown in table 4.3. The small differences between the fits of the shifts from resonance detection with and without loss can be considered as the combined uncertainty of the numerical techniques. The values indicate that the line shifts are accurate to 0.1 MHz/W.cm^{-2}. Because the resonances of the profiles without loss are very narrow in the low intensity limit, these are more precise in determining the line shift when compared to the loss profiles that have a width ~ 3.2 MHz 'built in' to the Hamiltonian. As well, because of this 'built in' loss, the fit parameters for the width are necessarily different between the methods. Because the width of the profiles without loss must approach zero in the zero intensity limit, the form of fit $w = w_1 I + w_2 I^2 + w_3 I^3$ is used for the non-loss profiles.

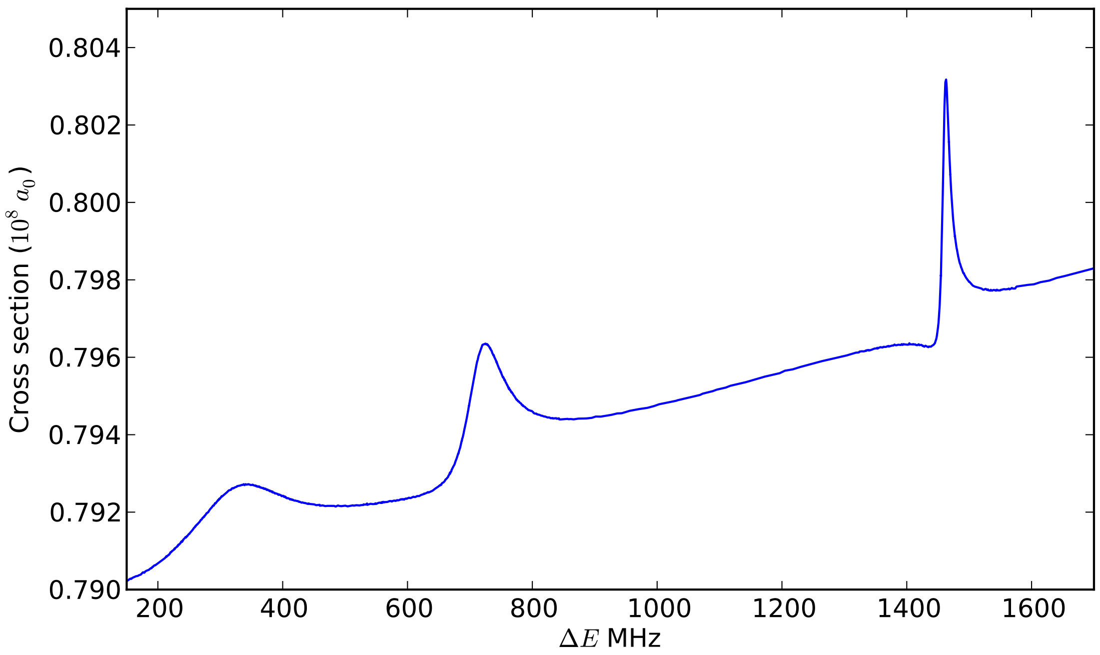

(a)

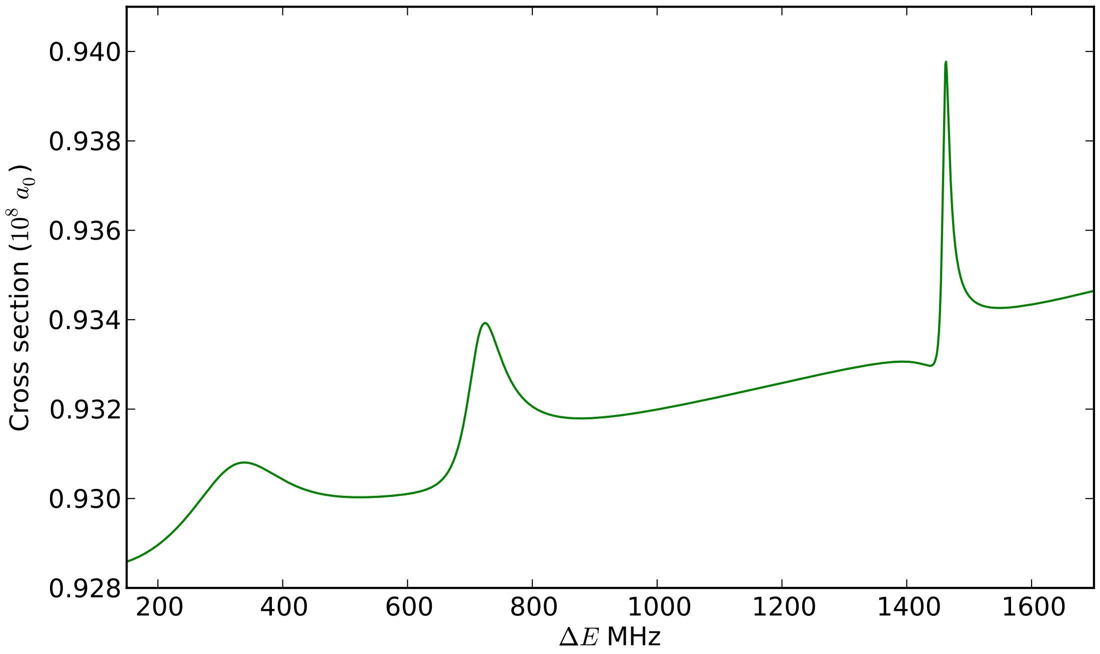

(b)

Figure 4.17: Profiles of the averaged elastic cross section (a) and total cross section (b) of the dressed state formalism at a high laser intensity of 6.4 W/cm^2.

Table 4.3: The quadratic, $s_1 I + s_2 I^2$ and cubic, $w_1 I + w_2 I^2 + w_3 I^3$ fits to the line shift and widths respectively of resonances for the lowest three bound levels of the excited state calculated without inclusion of loss. The final column indicates the intensity below which the resonances can be discerned. The shifts and widths are in MHz, the intensity in W/cm^2 and the coefficients (s_n, w_n) in MHz (W/cm^2)$^{-n}$.

		Shift		Width				
Level	Polarisation	s_1	s_2	w_0	w_1	w_2	w_3	$I_{\max}$
$v = 0$	σ^-	-6.535	-0.016	0	0.316	0.379	-0.018	7.0
	σ^+	-7.799	-0.015	0	0.601	0.402	-0.018	7.0
$v = 1$	σ^-	-11.791	0.120	0	1.178	3.433	-0.490	3.2
	σ^+	-10.282	-0.005	0	1.193	2.124	-0.232	3.2
$v = 2$	σ^-	-29.692	3.621	0	5.136	43.254	-28.597	0.4
	σ^+	-24.809	0.745	0	4.397	23.636	-11.836	0.6

4.7 MULTICHANNEL SOLUTIONS WITH THE COMPLETE COUPLING TERM

4.7.1 Differences between the approximate and exact coupling

Calculation of the PA profiles without making use of the dipole approximation for the laser coupling introduces two important differences. First, the dipole selection rules, $|J-1| \leq J' \leq |J+1|$ and gerade→ungerade parity are broken such that states with $J > 3$ are now accessible from s-wave metastable scattering channels. However, it will be shown in section 4.7.3 that these couplings are negligible in the resonance region. Second, as gerade→gerade transitions are allowed, a larger basis is required when calculating the profiles to the 0_u^+ manifold. The enlarged basis for σ^- polarisation consists of the gerade singlet and quintet states $|1\rangle, \ldots, |4\rangle$ described in (4.71), together with the following ungerade triplet states and the original excited state:

$$\begin{aligned}
|5\rangle &= |j = 1, \Omega = 0\rangle \otimes |n, \omega_\lambda, \boldsymbol{\epsilon}_\lambda\rangle, \\
|6\rangle &= |j = 1, \Omega = 1\rangle \otimes |n, \omega_\lambda, \boldsymbol{\epsilon}_\lambda\rangle, \\
|7\rangle &= |e_0\rangle \otimes |n-1, \omega_\lambda, \boldsymbol{\epsilon}_\lambda\rangle. \qquad (4.86)
\end{aligned}$$

The p summation of the complete coupling equation (4.31) can be separated into even values of p that couple gerade and ungerade states, and odd values of p which couple ungerade to ungerade states. The potential matrix $\boldsymbol{W}$ does not change its form and is given by (4.66) with the upper 4×4 submatrix expanded to a 6×6 matrix. Finally, because only colliding metastable states coupled to the 0_u^+, $J = 1$ manifold are considered here, only the terms $0 \leq p \leq 4$ will contribute due to the restrictions imposed by the Clebsch-Gordan coefficients in the coupling term (4.31). The σ^+ polarisation also requires the introduction of additional ungerade triplet states along with the existing states $|1\rangle, \ldots, |7\rangle$ described in

(4.71). These additional states, along with the original excited state, are:

$$\begin{aligned}
|8\rangle &= |j=1,\Omega=0,J=0,m_J=0\rangle \otimes |n,\omega_\lambda,\boldsymbol{\epsilon}_\lambda\rangle \\
|9\rangle &= |j=1,\Omega=1,J=1,m_J=0\rangle \otimes |n,\omega_\lambda,\boldsymbol{\epsilon}_\lambda\rangle \\
|10\rangle &= |j=1,\Omega=0,J=2,m_J=0\rangle \otimes |n,\omega_\lambda,\boldsymbol{\epsilon}_\lambda\rangle \\
|11\rangle &= |j=1,\Omega=1,J=2,m_J=0\rangle \otimes |n,\omega_\lambda,\boldsymbol{\epsilon}_\lambda\rangle \\
|12\rangle &= |e_0\rangle \otimes |n-1,\omega_\lambda,\boldsymbol{\epsilon}_\lambda\rangle .
\end{aligned} \tag{4.87}$$

The second major difference that the full coupling introduces is due to the presence of the spherical Bessel functions, $j_p(kR/2)$. Because the p-summation is finite, and the functions $j_p(x) \to x^{-1}\sin(x-p\pi/2)$ for $x \to \infty$, the full coupling term asymptotically disappears and the expanded set of basis states completely decouple at large R, removing the need for the dressed state formalism or artificial R-dependent dampening terms. As will also be shown, the presence of the oscillatory Bessel functions requires the complete gerade and ungerade metastable manifolds to be present otherwise severe background oscillations occur in the profiles. This also indicates that an initial gerade spin-polarised quintet entrance channel can scatter into a triplet ungerade exit channel. However, in the small R resonance region only the $p=0$ term strongly contributes because $j_p(kR/2) \approx 0$ for $kR \ll p$ and $p \neq 0$.

4.7.2 Results

The method of calculation proceeds identically to that of the modified radiation coupling calculation presented in section 4.6 except that the complete coupling is used for V_{eg}^{int} and either the additional states (4.86) or (4.87) are included as appropriate. The results in this section will be presented as a sequence of progressive corrections to the dipole-approximation arising from the inclusion of particular values of p within the summation over p in the complete coupling (4.31).

The first of these corrections is to allow only the $p=0$ term of the summation to contribute. This term is identical to the dipole approximation except for the presence of the $j_0(kR/2)$ factor and allows couplings only to the gerade metastable states. Sample plots for the averaged profile

$$\sigma^{\text{nondipole}} = \frac{1}{n}\sum_{\gamma}\sigma_{\gamma}^{\text{photon}}, \tag{4.88}$$

where n is the total number of channels, are presented in figure 4.18. It is evident that severe unphysical oscillations exist in the profile for high intensities. Inclusion of the remaining even p terms ($p=2,4$) results in the profiles shown in figure 4.19, which show that the oscillatory background has been significantly reduced but not completely removed.

Inclusions of all terms of the p-summation into the laser coupling gives profiles, see figure 4.20, which are much smoother and resemble the form of the dipole approximation profiles, except for a very small oscillatory background present at small detuning. Additionally, each individual $\sigma_{\gamma}^{\text{photon}}$ profile is smooth, see figure 4.21, in contrast to the oscillatory behaviour

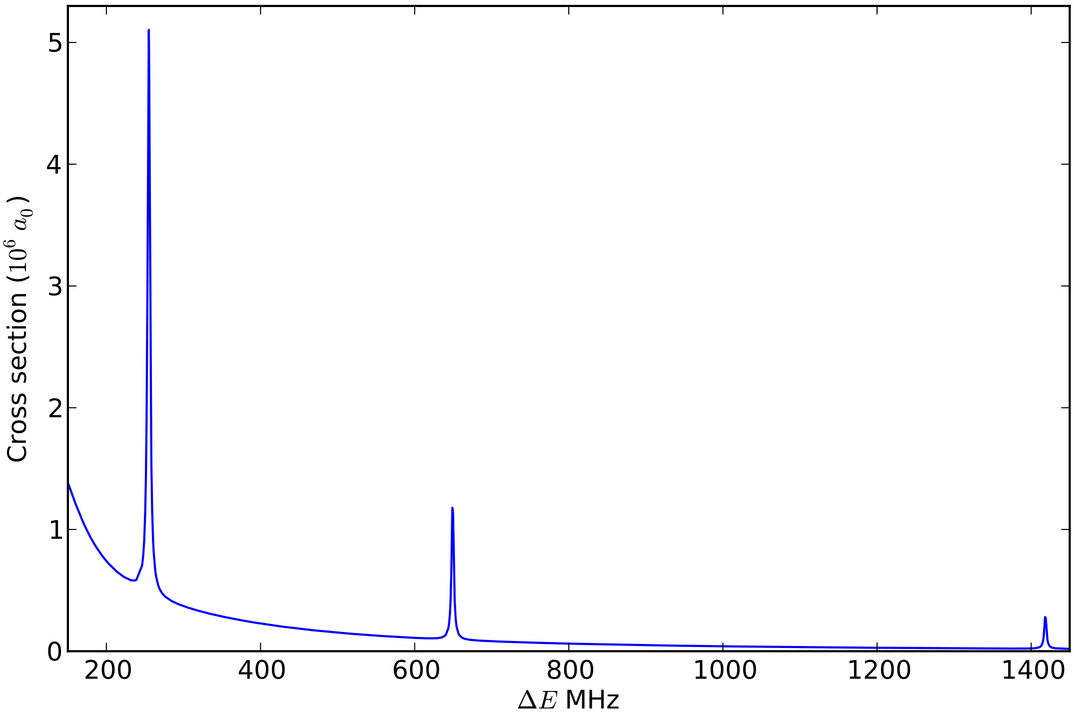

(a)

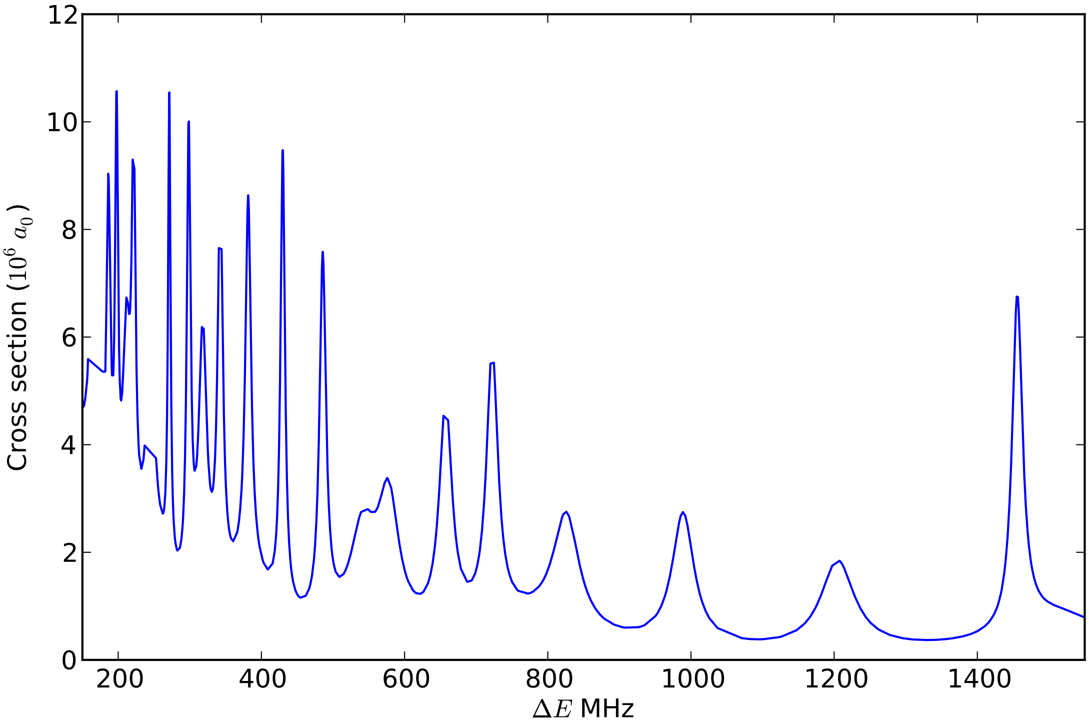

(b)

Figure 4.18: Photoassociation profiles from the $p = 0$ term of the complete coupling term using loss as the spectroscopic signal. Figure (a) uses a low laser intensity of 64 mW/cm^2 and figure (b) a high laser intensity of 6.4 W/cm^2. Large unphysical oscillations are present and increase dramatically as the laser intensity is increased.

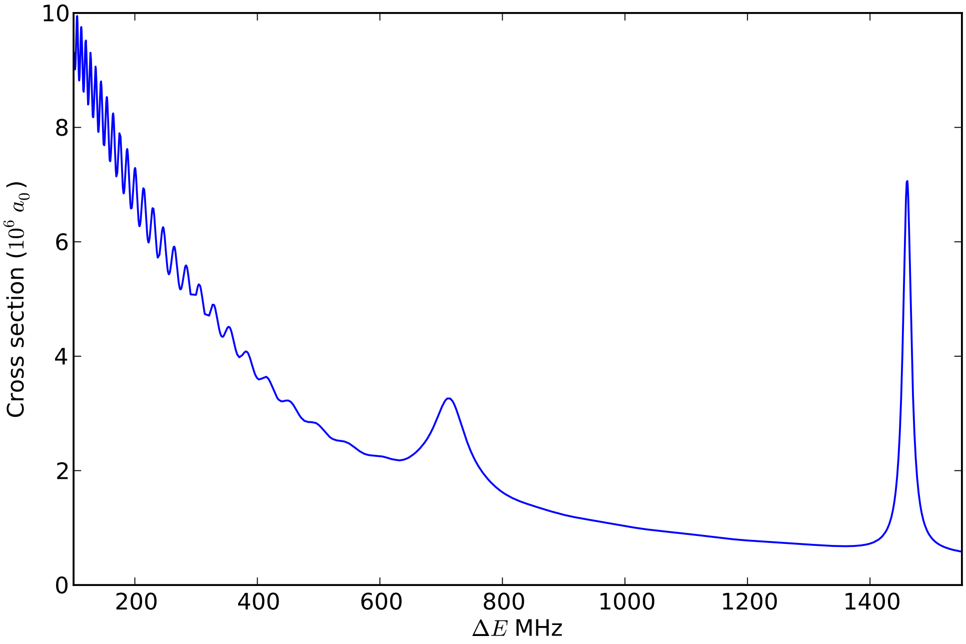

Figure 4.19: Photoassociation profiles identical to that of figure 4.18 (b) except that all even p summation terms are included. A severe reduction in the background oscillations is observed but the profiles are still not as smooth as desired.

observed for the modified radiation coupling, shown in figure 4.7. This indicates that the functions $j_p(kR/2)$ act as the true, physical R-dependent dampening of the coupling, and do not cause unphysical reflections or mixing of the channels as seen for the artificial dampening $\tilde{V}_{eg}^{\mathrm{int}}$ used previously in the modified radiation coupling.

Calculation of profiles from the elastic and total cross sections (4.84) and (4.85) respectively using the full coupling term, produces profiles with the background oscillatory behaviour similar to that for the modified radiation coupling and hence makes the profiles difficult to analyse. This means that the dressed state formalism in the dipole approximation is the only method by which the resonance shifts and widths may be easily calculated without introducing loss. The presumed reason for the inability of the modified radiation coupling and the full coupling methods to successfully do this is due to the activation of the laser since a strong variation of behaviour with respect to the laser detuning occurs as it is slowly ‘turned on’. The dressed state formalism, however, builds in the activated laser as part of the basis and so does not exhibit this variation with laser detuning.

Although the profile $\sigma^{\mathrm{nondipole}}$ in figure 4.20, calculated from the complete coupling is similar to the profile $\sigma^{\mathrm{modified}}$ in figures 4.9 and 4.11, some subtle but significant differences can be observed. At low intensities a reduction in the background loss for $\sigma^{\mathrm{nondipole}}$ is apparent which can easily be explained by the functions $j_p(kR/2)$ which asymptote to zero much faster than in the modified radiation coupling in the dipole-approximation profiles. The strength of the resonance, as determined by the parameter A'_{res} in equation (4.83) is larger by an order of magnitude. For higher laser intensities, similar behaviour is observed but the saturation behaviour also changes significantly. In the dipole approximation, saturation

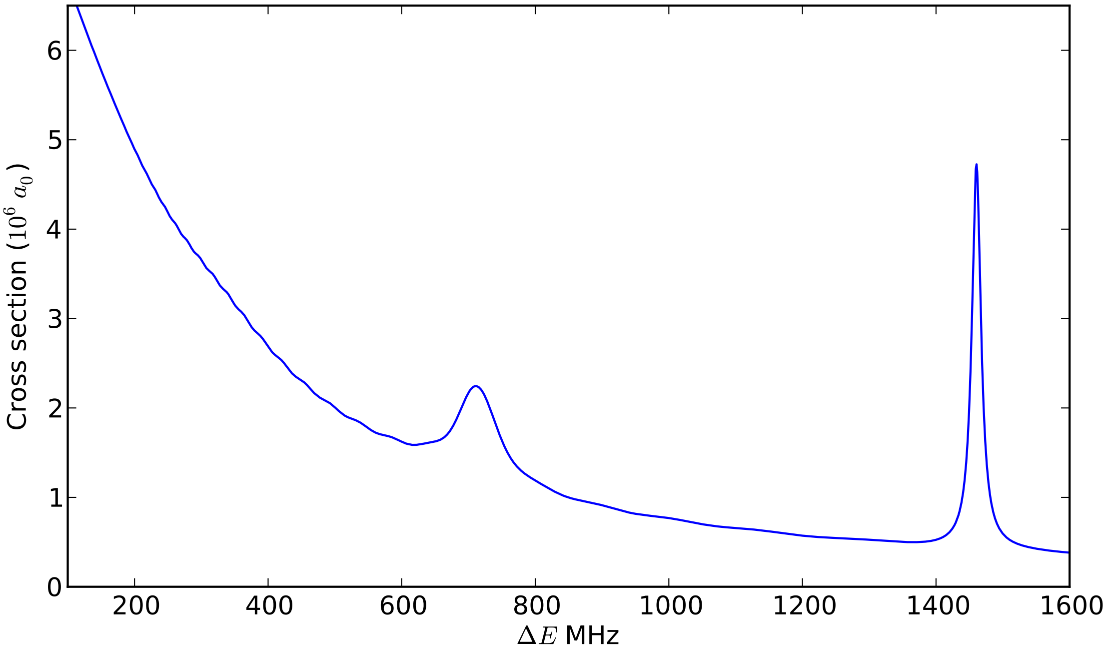

Figure 4.20: Photoassociation profile $\sigma^{\text{nondipole}}$ based on the complete coupling term including all terms of the p summation using loss as the spectroscopic signal and with a high laser intensity of 6.4 W/cm^2. A smooth background is observed in contrast to those of figures 4.18 and 4.19.

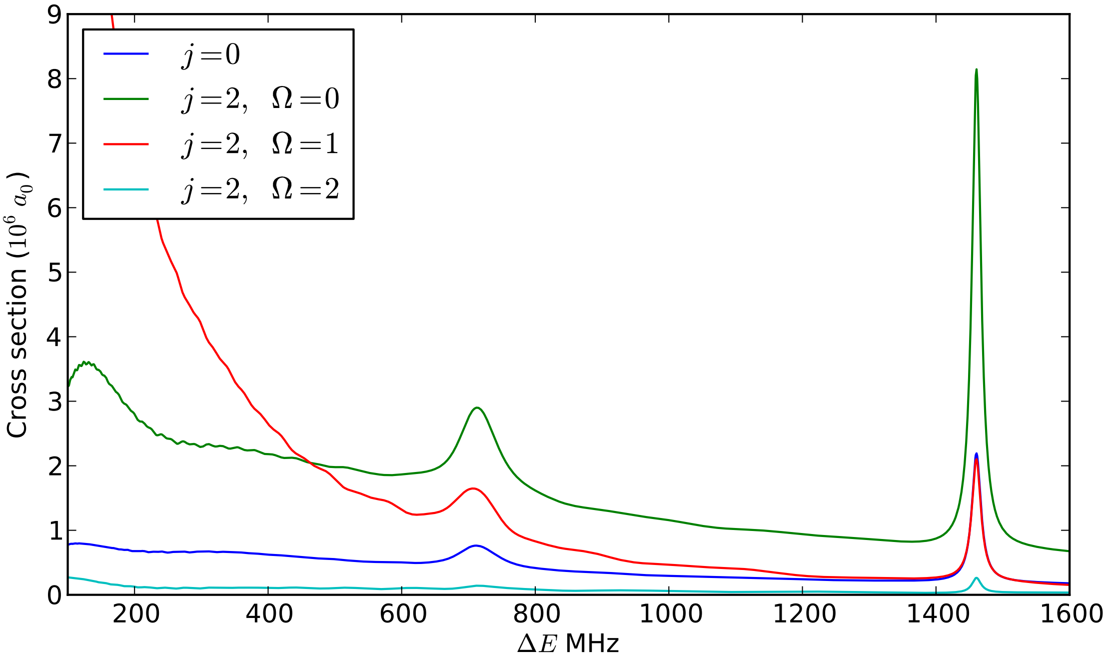

Figure 4.21: Photoassociation profiles $\sigma_{\gamma}^{\text{photon}}$ based on the complete coupling term including all terms in the p summation using loss as the spectroscopic signal. The smoothness of these profiles compared with the separate $\sigma_{\gamma}^{\text{photon}}$ profiles calculated in the modified radiation coupling of the dipole approximation, figure 4.7, indicate that the dampening introduced by the complete coupling does not introduce artifacts into the model.

was observed as the background of the profile plateaued, whereas the full coupling profiles evidently maintain a smoothly increasing structure. Additionally, the discernability of the resonance is maintained to larger intensities in the full coupling profiles, beyond intensities for which the resonance is no longer discernible in the dipole approximation profiles. For example, the $v = 0$ resonance can be visually identified up to an intensity of ~ 50 W.cm^{-2} in the $\sigma^{\text{nondipole}}$ profiles, as opposed to ~ 6.4 W.cm^{-2} in the σ^{dressed} profiles.

No noticeable differences are observed in the fits to the line shifts and widths as a function of intensity. This has been the consistent trend observed throughout the investigation of the photoassociation profiles: only the background of the profiles and the strength of the resonance vary between the methods used. For the dressed state and modified radiation coupling methods within the dipole approximation, and for the method based on the full coupling term, all of the resonance position and width parameters remained identical to within the accuracy of the calculation. However, it is important to highlight the fact that the full coupling calculation produces resonances which are discernible to higher laser intensities.

4.7.3 Couplings to $J > 3$ levels

Although couplings to levels which do not satisfy the selection rules $|J-1| < J' < |J+1|$ have not been investigated previously due to the application of the dipole approximation to the calculations, the complete coupling (4.31) allows the laser to couple channels of any value of J to one another. Specifically, the metastable levels in the s-wave collisional state (with $J = 0$ or $J = 2$) can be coupled to excited levels with $J > 3$. These couplings occur through higher values of p in the summation of the complete coupling. However, a coupling between the levels does not necessarily mean there will be any visible resonance peaks. The major obstacle to the formation of resonances is the suppression of the coupling at small interatomic distances due to the relation $j_p(kR) \approx 0$ for $kR \ll p$ which severely limits the coupling strength for $p > 0$.

To investigate these couplings, the same Hund's case (c) 0_u^+ configuration that asymptotes to $j = 0$, used previously in this chapter, is employed. The state with the smallest value of J for which the dipole approximation allows no coupling from a metastable state to occur is the 0_u^+, $J = 5$ state. The binding energies of the three bound levels probed in this potential have been calculated with a single-channel approximation as described in chapter 3 and are -854.94 MHz, -286.85 MHz and -54.38 MHz. The method of calculation of the photoassociation profiles proceeds identically to that described in section 4.7, except that the excited molecular state $|e_0\rangle$ in state $|7\rangle$ of (4.86) is replaced by the 0_u^+, $J = 5$ state. In order to calculate all terms of the complete coupling (4.31), the p-summation must be extended to $p = 8$.

The photoassociation profiles $\sigma^{\text{nondipole}}$ are presented in figure 4.22 and show no visible resonances. Hence, it is concluded that the complete coupling cannot be responsible for any additional resonances that break the dipole selection rules.

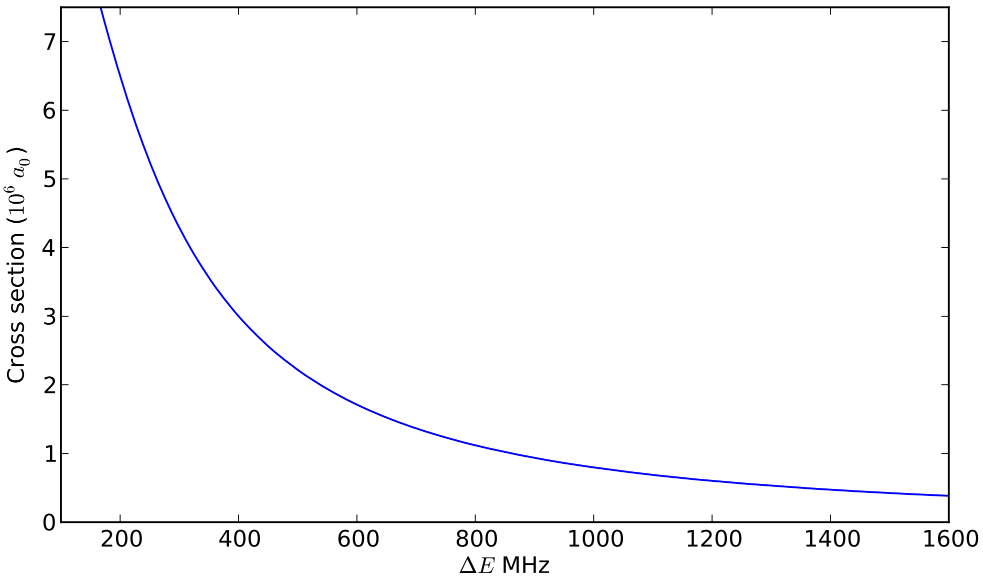

Figure 4.22: Photoassociation profiles based on the complete laser coupling between the metastable states and vibrational states in the 0_u^+, $J = 5$ potential asymptoting to $j = 0$. The couplings do not satisfy the selection rules of the dipole approximation. No visible resonances are present in the profile due to the Bessel functions $j_p(kR/2)$ present in the complete coupling term that are approximately zero for $kR \ll p$ and $p \neq 0$.

4.8 SUMMARY

In this chapter the line shifts and widths of photoassociation resonances to the lowest three vibrational states of 0_u^+, $J = 1$ potentials asymptoting to $j = 0$ were calculated using several different methods. Initially, perturbative calculations were used to determine the line shift in the low intensity limit and it was found that the shift depends linearly upon the laser intensity. The photoassociation process was then modelled using a full multichannel calculation which included the metastable basis states and the excited state. When the dipole approximation was used for the laser coupling, the coupled differential equations were not asymptotically decoupled, and extraction of the $\boldsymbol{S}$-matrix elements needed to calculate the photoassociation profiles required the introduction of one of two alternative methods. The first method was the dressed-state formalism that involves a transformation to a basis in which the equations are asymptotically decoupled whereas the second method introduced a modified radiation coupling that was dampened at large interatomic separations and artificially decoupled the equations. With either method, significant backgrounds were observed in the spontaneous emission photon cross section profiles due to the weakly bound nature of the excited state levels. When photon emission from the excited state was not included in the model, the profiles calculated from the elastic and total cross sections were found to be satisfactory only in the dressed-state formalism.

Finally, inclusion of the complete laser coupling, in which the commonly used dipole approximation is not made, allowed the differential equations to be solved without any need for dressed states or a modified laser coupling. Although the complete coupling allows for breaking of the dipole selection rules, no resonances were observed in those cases. The complete coupling also significantly improved the contrast between the background of the photon cross section profiles and the resonances, suggesting that models of ultracold photoassociation should make use of the complete coupling, especially for weakly bound levels. In all cases, the line shape parameters of line shift and width were found to agree well within numerical accuracy.

Chapter 5

Conclusions and future work

5.1 CONCLUSIONS

5.1.1 Calculations performed

This thesis reports an investigation of the process of photoassociation in ultracold metastable helium and the molecular properties that are involved. In chapter 2 the formalism framework for the molecular system of a pair of helium-4 atoms was outlined and the interactions between the atoms and with the laser radiation field were described. Several bases were formulated that allowed the matrix elements of one or more terms of the Hamiltonian to be written in their simplest form. From these, the hybrid jj basis (representing a Hund's case (c) basis) was chosen as being most suited to calculations within the framework of the helium system. Matrix elements of the Hamiltonian were then derived for the jj basis, with careful consideration given to the symmetries of the system.

Chapter 3 then utilised the jj basis to analyse the bound levels that exist in the $2s\,{}^3S_1 + 2p\,{}^3P_j$, $j = 0, 1, 2$ metastable helium configurations by using comprehensive multichannel calculations. Although approximate single-channel calculations of levels in this manifold already existed, no exact calculations had previously been performed and the effects of the neglected non-adiabatic and Coriolis couplings had not been investigated.

The multichannel calculations undertaken in the present study have been made possible due to the recently recent development of *ab initio* short-range potentials by Deguilhem *et al* [86]. In this thesis, results from approximate calculations were compared with the accurate multichannel results and some significant differences were observed, especially when Coriolis couplings were introduced. These differences are large enough to be noticeable in experiment and so indicate the necessity for using multichannel calculations, particularly for short-range bound levels. By using the exact results, assignments of theoretical levels were made to the experimental observations. The assignments were based on the formulation of several observability criteria that indicated the likelihood that the level would undergo ionisation and that the level would undergo a transition from a colliding metastable pair as used in an experimental setup. These criteria proved to be very successful as an almost unique set of assignments between experiment and theory were made. However, a consistent 3-5% difference existed between the experimental and theoretical binding energies in these assignments and a short-range correction to the ungerade input potentials was applied. This correction significantly improved the agreement between theory and experiment, as well as allowing additional levels to be assigned. The criteria were used to predict the existence of observable bound levels and resonances in ranges of detuning that have not yet been probed by experiment. It is anticipated that these predictions will be tested by future experiments.

In chapter 4, the photoassociation dynamics of a particular set of bound levels in the purely long-range 0_u^+, $J = 1$ potential that asymptotes to the $2s\,^3S_1 + 2p\,^3P_0$ limit was investigated. The line shifts of the levels were first calculated using an approximate perturbative technique and these results agreed well with previous perturbative calculations [88]. The PA process was then modelled using a precise multichannel calculation including the channels of the metastable and $2s2p$ manifolds. Accurate PA profiles were determined from the scattering matrix which was calculated from the solutions of the multichannel calculations.

Two classes of profile were generated to analyse the PA signal. The first class of PA profile used the mechanism of spontaneous emission from the excited state as the PA signal and required different treatments if the dipole approximation of the laser coupling was employed. These treatments in the dipole approximation used either a dressed state formalism or the application of a R-dependent dampening of the laser coupling. Both methods generated photoassociation profiles that exhibited a significant background that originated from the shallow nature of the long-range potential well. The complete laser coupling, without the dipole approximation, did not require the use of the dressed formalism or R-dependent dampening, and it produced noticeably less background in the profiles. This suggests that photoassociation calculations involving weakly bound dimers should not make use the dipole approximation as it can obscure the resonances under investigation. The second class of profile was calculated without inclusion of spontaneous emission in the system and analysed the PA signal via the elastic and total cross sections. For these profiles, only the dressed state formalism allowed the line parameters to be determined because the other methods produced an oscillatory background that dominated the profiles and obscured the resonances. All the different multichannel calculations, with and without loss, yielded the line shape parameters of line position and width for the extracted PA resonances which were the same to within numerical error.

5.1.2 Critical Appraisal

Although every effort was made to describe the system as accurately as possible, occasionally terms were ignored in the calculations because there were strong indicators that their effect was negligible. Determining the extent of their influence explicitly would require a significant amount of time and effort which was deemed unnecessary. The major assumptions are listed below, along with comments on their validity.

For the derivation of the matrix elements present in the differential equations, the electronic and rotational basis states were assumed to not vary with interatomic distance R and hence that the atomic quantum numbers L_α, S_α and j_α (the orbital, spin and total angular momenta respectively for atom α) remain well defined for all R. This is reasonable as the electronic wave functions of the separated atoms do not overlap for the ranges considered in this thesis. The molecular configuration of the electronic wave function can hence be approximately considered a combination of two separate atomic configurations that are only slightly perturbed from their atomic states.

Penning ionisation, a dominant process in metastable helium experiments, was not directly included in the molecular Hamiltonian, although an ionisation rate was estimated from the short-range form of the calculated wave functions in chapter 3. The ionisation can be neglected in the molecular Hamiltonian as it occurs with nearly 100% probability if the colliding atoms approach one another at close interatomic distances unless the spins of the colliding atoms are aligned in which case the ionisation is heavily suppressed. This allows a quick analysis of the wave function to retrospectively determine if and how much loss has occurred. The exclusion of the ionisation process in the differential equations of chapter 4 is not important as only line shifts of purely long-range excited levels were considered. These long-range levels cannot reach the short interatomic distances that are required for Penning ionisation to occur. To properly include ionisation into the system, an optical potential method similar to [79] could be used. Alternatively a separate channel representing the He_2^+ state can be introduced into the multichannel calculations to accurately model the ionisation process.

The Born-Oppenheimer (BO) approximation was used to calculate the electronic matrix elements. Its validity relies on the large mass ratio of the nucleus to the electron. Although this ratio is of four orders of magnitude, the helium nucleus is relatively light in comparison to other atomic species which have been photoassociated. To address this issue is not a trivial process however, as the BO approximation significantly reduces the complexity of the differential equations that must be solved. The reduction in nuclear motion due to the ultracold temperatures of the system also provides justification for the use of the BO approximation.

In chapter 4, the purely long-range excited levels were approximated using a single-channel potential. Although this appears to be in violation of the nature of the precise non-perturbative multichannel calculations, these purely long-range states have been shown, in chapter 3 of this thesis and previously [90], to experience very little influence from the non-adiabatic and Coriolis couplings of a full multichannel calculation. In chapter 4 it was also assumed that the photoassociation profiles observed in experiment result from only the *s*-, *p*- and *d*-wave colliding channels of a pair of metastable atoms. This is clearly justifiable due to the very small kinetic energies of the ultracold gas.

The formalism presented in chapter 2 and section 4.2 is complete for the helium-4 system but it lacks the inclusion of nuclear spin which is required for other systems such as helium-

3. The incorporation of nuclear spin and consequently hyperfine structure, however, is not likely to be a difficult process.

Finally, although a very successful improvement to the short-range electronic potentials was introduced in chapter 3, the choice of correction was not based on physical grounds and it is hoped that the successful predictions of the current investigation will motivate those with experience in calculating molecular potentials to consider and possibly improve the form of correction that has been presented here.

5.2 FUTURE WORK

The calculations presented in this thesis have accurately modelled photoassociation of the helium-4 system to the $2s2p$ excited state, and this will provide the foundation for many future studies. Investigation of bound levels of the helium system may be extended further by performing calculations with fermionic helium-3. Apart from the inclusion of nuclear spin and the corresponding hyperfine structure, the formalism is identical for helium-3 and helium-4. Although the hyperfine structure of helium-3 spans a range of energies comparable to the fine-structure of helium-4, helium-3 contains approximately double the number of asymptotic states and hence introduces a more complicated behaviour to the coupled equations. This complexity may enhance the likelihood for photoassociation to occur and give rise to more purely long-range states, including those suggested by existing approximate calculations [136].

The existing measurements in helium-4 photoassociation also provide a useful starting point for determining observability criteria for the helium-3 system. The application of these criteria for the coupling strength and ionisation rate will allow predictions for observable levels in the absence of any experimental measurements. A similar process can be applied to the mixed helium-3/helium-4 system, where the symmetries of the coupling scheme simplify. The possibility of using the $2s3p$ excited state, which is accessible in experiment from metastable helium using 389 nm lasers, is also available for helium-3, helium-4 and the mixed combination. Although initial investigations have not found any purely long-range resonances in the $2s3p$ level of helium-4, a thorough investigation must be performed. To this end it would be invaluable to have access to accurate short-range electronic potentials for this system.

In chapter 3, predictions for the existence of resonances up to 2000 MHz of detuning from the $j = 1$ asymptote were made and these are listed in table E.4. Many resonances overlap significantly and almost all possess observability properties that permit them to be seen in experiments using an ion detection mechanism. However, it is uncertain whether the resonances possess enough short-range proportion to produce a measurable ion signal. It would be very useful to perform calculations similar to those of chapter 4, so that the detail of the line shapes over this range of detuning can be analysed. The analysis may also expose interesting behaviour due to the overlapping resonances.

The effects of including the full laser coupling must also be investigated more thoroughly in systems other than helium so that the validity of the dipole approximation may be better evaluated for ultracold systems. The presence of the backgrounds to the loss profiles, which are believed to result from the weakly-bound nature of the levels, is unusual and has not been observed in other theoretical investigations known to the author. If similar shallow potential wells can be observed in other atomic species it would be most interesting to compare the behaviour of photoassociation in these species with calculations using either the dressed state formalism or the R-dependent dampening.

Trapping conditions of the ultracold gases should also play an interesting role in the photoassociation process. Previous investigations of trapping conditions in metastable helium gases [100, 79, 98] can be extended to include the photoassociation process. Different types of trapping potentials, such as those provided by optical dipole traps or optical lattices, may enhance the PA resonances or allow for multi-transition couplings between states of the system. The laser coupling to excited states also allows for the enhancement or suppression of collisions between atoms.

Finally, the calculations performed in this thesis may also be extended to other metastable rare gas systems such as neon or xenon. However, more detailed and accurate potentials are needed for these systems so, although the adaption of the formalism to these systems may not be too difficult to implement, the usefulness of results calculated from insufficiently accurate potentials is dubious. Although these atomic species have not been successfully condensed into a Bose-Einstein condensate, this does not impact on the potential applications of their interactions in the ultracold gaseous phase.

In conclusion, there are many untouched areas of ultracold quantum physics that may be investigated using the techniques established in this thesis. Although the photoassociation process is well known for a few transitions of a few atomic species, it will be many years or decades until the useful applications of photoassociation of ultracold gases are fully understood.

Publications and Conference Contributions

PUBLICATIONS

Cocks D G and Whittingham I B (2009) 'Laser-intensity dependence of photoassociation in ultracold metastable helium'. *Physical Review A.* **80** 023417.
Selected for publication in the September issue of *Virtual Journal of Atomic Quantum Fluids.*
`http://link.aps.org/abstract/PRA/v80/e023417`

Cocks D G and Whittingham I B (2009) 'Theoretical studies of photoassociation in ultracold metastable helium'. *Journal of Physics: Conference Series.* **185** 012004.
`http://www.iop.org/EJ/abstract/1742-6596/185/1/012004`

Cocks D G and Whittingham I B (2010) 'Photoassociation spectra and the validity of the dipole approximation for weakly bound dimers'. *Physical Review A.* **81** 033406.
`http://link.aps.org/doi/10.1103/PhysRevA.81.033406`

Cocks D G, Whittingham I B and Peach G (2010) 'Effects of non-adiabatic and Coriolis couplings on the bound states of He(2 ^{3}S)+He(2 ^{3}P)'. *Journal of Physics B.* **43** 135102
`http://stacks.iop.org/0953-4075/43/i=13/a=135102`

CONFERENCE CONTRIBUTIONS

Cocks D G and Whittingham I B (2008) 'Theoretical studies of photoassociation in ultracold metastable helium'. *8th Asian International Seminar on Atomic and Molecular Physics* (AISAMP8) Perth, Australia 2008.

Cocks D, Whittingham I B and Peach G (2009) 'Bound states of He(2 ^{3}S) + He(2 ^{3}P)'. *XXVI International Conference on Photonic, Electronic and Atomic Collisions* (XXVIth ICPEAC) Kalamazoo, Michigan 2009.

Cocks D, Whittingham I B, Peach G and Dickinson A (2010) 'Exact multichannel calculations of 2s2p bound levels in bosonic and fermionic ultracold helium dimers.' *22nd International Conference on Atomic Physics* (ICAP 2010) Cairns, Australia 2010.

Bibliography

[1] J. Weiner, V. S. Bagnato, S. Zilio, and P. S. Julienne. 1999. Experiments and theory in cold and ultracold collisions. *Rev. Mod. Phys.*, **71** 1–85.

[2] W. Ketterle and N. V. Druten. 1996. Evaporative cooling of trapped atoms. *Advances In Atomic, Molecular, and Optical Physics*, **37** 181 – 236.

[3] J. Dalibard and C. Cohen-Tannoudji. 1989. Laser cooling below the Doppler limit by polarization gradients: simple theoretical models. *J. Opt. Soc. Am. B*, **6** 2023–2045.

[4] T. Köhler, K. Góral, and P. S. Julienne. 2006. Production of cold molecules via magnetically tunable Feshbach resonances. *Rev. Mod. Phys.*, **78** 1311.

[5] M. Theis, G. Thalhammer, K. Winkler, M. Hellwig, G. Ruff, R. Grimm, and J. H. Denschlag. 2004. Tuning the scattering length with an optically induced Feshbach resonance. *Phys. Rev. Lett.*, **93** 123001.

[6] C. Chin, R. Grimm, P. Julienne, and E. Tiesinga. 2010. Feshbach resonances in ultracold gases. *Rev. Mod. Phys.*, **82** 1225–1286.

[7] T. Weber, J. Herbig, M. Mark, H.-C. Nagerl, and R. Grimm. 2003. Bose-Einstein condensation of cesium. *Science*, **299** 232–235.

[8] S. L. Cornish, N. R. Claussen, J. L. Roberts, E. A. Cornell, and C. E. Wieman. 2000. Stable ^{85}Rb Bose-Einstein condensates with widely tunable interactions. *Phys. Rev. Lett.*, **85** 1795–1798.

[9] G. Roati, M. Zaccanti, C. D'Errico, J. Catani, M. Modugno, A. Simoni, M. Inguscio, and G. Modugno. 2007. ^{39}K Bose-Einstein condensate with tunable interactions. *Phys. Rev. Lett.*, **99** 010403.

[10] R. Yamazaki, S. Taie, S. Sugawa, and Y. Takahashi. 2010. Submicron spatial modulation of an interatomic interaction in a Bose-Einstein condensate. *Phys. Rev. Lett.*, **105** 050405.

[11] P. S. Julienne. Ultracold collisions of atoms and molecules. In P. Sabatier and E. R. Pike, editors, *Scattering*, chapter 2.6.3. Academic Press, London, 2002.

[12] N. S. Ginsberg, S. R. Garner, and L. V. Hau. 2007. Coherent control of optical information with matter wave dynamics. *Nature*, **445** 623–626.

[13] M.-O. Mewes, M. R. Andrews, D. M. Kurn, D. S. Durfee, C. G. Townsend, and W. Ketterle. 1997. Output coupler for Bose-Einstein condensed atoms. *Phys. Rev. Lett.*, **78** 582–585.

[14] I. Bloch. 2005. Ultracold quantum gases in optical lattices. *Nat Phys*, **1** 23–30.

[15] M. Greiner and S. Folling. 2008. Condensed-matter physics: Optical lattices. *Nature*, **453** 736–738.

[16] M. Greiner, O. Mandel, T. Esslinger, T. W. Hansch, and I. Bloch. 2002. Quantum phase transition from a superfluid to a Mott insulator in a gas of ultracold atoms. *Nature*, **415** 39–44.

[17] D. Clément, A. F. Varón, J. A. Retter, L. Sanchez-Palencia, A. Aspect, and P. Bouyer. 2006. Experimental study of the transport of coherent interacting matter-waves in a 1D random potential induced by laser speckle. *New Journal of Physics*, **8** 165.

[18] T. Schwartz, G. Bartal, S. Fishman, and M. Segev. 2007. Transport and anderson localization in disordered two-dimensional photonic lattices. *Nature*, **446** 52–55.

[19] C. Weitenberg, M. Endres, J. F. Sherson, M. Cheneau, P. Schausz, T. Fukuhara, I. Bloch, and S. Kuhr. 2011. Single-spin addressing in an atomic mott insulator. *Nature*, **471** 319–324.

[20] B. Zimmermann, T. Müller, J. Meineke, T. Esslinger, and H. Moritz. 2011. High-resolution imaging of ultracold fermions in microscopically tailored optical potentials. *New Journal of Physics*, **13** 043007.

[21] F. Gerbier and J. Dalibard. 2010. Gauge fields for ultracold atoms in optical superlattices. *New Journal of Physics*, **12** 033007.

[22] I. B. Spielman. 2009. Raman processes and effective gauge potentials. *Phys. Rev. A*, **79** 063613.

[23] M. Z. Hasan and C. L. Kane. 2010. Colloquium: Topological insulators. *Rev. Mod. Phys.*, **82** 3045–3067.

[24] I. Bloch, J. Dalibard, and W. Zwerger. 2008. Many-body physics with ultracold gases. *Rev. Mod. Phys.*, **80** 885–964.

[25] M. Greiner, C. A. Regal, and D. S. Jin. 2003. Emergence of a molecular bose-einstein condensate from a fermi gas. *Nature*, **426** 537–540.

[26] I. Titvinidze, M. Snoek, and W. Hofstetter. 2008. Supersolid bose-fermi mixtures in optical lattices. *Phys. Rev. Lett.*, **100** 100401.

[27] M. H. Anderson, J. R. Ensher, M. R. Matthews, C. E. Wieman, and E. A. Cornell. 1995. Observation of Bose-Einstein condensation in a dilute atomic vapor. *Science*, **269** 198–201.

[28] C. C. Bradley, C. A. Sackett, J. J. Tollett, and R. G. Hulet. 1995. Evidence of Bose-Einstein condensation in an atomic gas with attractive interactions. *Phys. Rev. Lett.*, **75** 1687–1690.

[29] K. B. Davis, M. O. Mewes, M. R. Andrews, N. J. van Druten, D. S. Durfee, D. M. Kurn, and W. Ketterle. 1995. Bose-Einstein condensation in a gas of sodium atoms. *Phys. Rev. Lett.*, **75** 3969–3973.

[30] G. Modugno, G. Ferrari, G. Roati, R. J. Brecha, A. Simoni, and M. Inguscio. 2001. Bose-Einstein condensation of potassium atoms by sympathetic cooling. *Science*, **294** 1320–1322.

[31] D. G. Fried, T. C. Killian, L. Willmann, D. Landhuis, S. C. Moss, D. Kleppner, and T. J. Greytak. 1998. Bose-Einstein condensation of atomic hydrogen. *Phys. Rev. Lett.*, **81** 3811–3814.

[32] S. Kraft, F. Vogt, O. Appel, F. Riehle, and U. Sterr. 2009. Bose-Einstein condensation of alkaline earth atoms: ^{40}Ca. *Phys. Rev. Lett.*, **103** 130401.

[33] S. Stellmer, M. K. Tey, B. Huang, R. Grimm, and F. Schreck. 2009. Bose-Einstein condensation of strontium. *Phys. Rev. Lett.*, **103** 200401.

[34] Y. Takasu, K. Maki, K. Komori, T. Takano, K. Honda, M. Kumakura, T. Yabuzaki, and Y. Takahashi. 2003. Spin-singlet Bose-Einstein condensation of two-electron atoms. *Phys. Rev. Lett.*, **91** 040404.

[35] A. Griesmaier, J. Werner, S. Hensler, J. Stuhler, and T. Pfau. 2005. Bose-Einstein condensation of chromium. *Phys. Rev. Lett.*, **94** 160401.

[36] A. Robert, O. Sirjean, A. Browaeys, J. Poupard, S. Nowak, D. Boiron, C. I. Westbrook, and A. Aspect. 2001. A Bose-Einstein condensate of metastable atoms. *Science*, **292** 461–464.

[37] F. Pereira Dos Santos, J. Léonard, J. Wang, C. J. Barrelet, F. Perales, E. Rasel, C. S. Unnikrishnan, M. Leduc, and C. Cohen-Tannoudji. 2001. Bose-Einstein condensation of metastable helium. *Phys. Rev. Lett.*, **86** 3459–3462.

[38] H. R. Thorsheim, J. Weiner, and P. S. Julienne. 1987. Laser-induced photoassociation of ultracold sodium atoms. *Phys. Rev. Lett.*, **58** 2420–2423.

[39] P. L. Gould, P. D. Lett, P. S. Julienne, W. D. Phillips, H. R. Thorsheim, and J. Weiner. 1988. Observation of associative ionization of ultracold laser-trapped sodium atoms. *Phys. Rev. Lett.*, **60** 788–791.

[40] W. C. Stwalley, Y.-H. Uang, and G. Pichler. 1978. Pure long-range molecules. *Phys. Rev. Lett.*, **41** 1164–1167.

[41] K. M. Jones, E. Tiesinga, P. D. Lett, and P. S. Julienne. 2006. Ultracold photoassociation spectroscopy: Long-range molecules and atomic scattering. *Rev. Mod. Phys.*, **78** 483.

[42] O. Dulieu and C. Gabbanini. 2009. The formation and interactions of cold and ultracold molecules: new challenges for interdisciplinary physics. *Rep. Prog. Phys.*, **72** 086401.

[43] B. Bussery-Honvault, J.-M. Launay, and R. Moszynski. 2005. Photoassociation of cold calcium atoms through the A $^1\Sigma_u^+$ $(1\ ^1D + 1\ ^1S)$, c $^3\Pi_u(1\ ^3P + 1\ ^1S)$, and a $^3\Sigma_u^+(1\ ^3P + 1\ ^1S)$ states: An ab initio nonadiabatic treatment. *Phys. Rev. A*, **72** 012702.

[44] R. Ciurylo, E. Tiesinga, S. Kotochigova, and P. S. Julienne. 2004. Photoassociation spectroscopy of cold alkaline-earth-metal atoms near the intercombination line. *Phys. Rev. A*, **70** 062710.

[45] J. M. Sage, S. Sainis, T. Bergeman, and D. DeMille. 2005. Optical production of ultracold polar molecules. *Phys. Rev. Lett.*, **94** 203001.

[46] N. Bouloufa, A. Crubellier, and O. Dulieu. 2009. Photoassociative molecular spectroscopy for atomic radiative lifetimes. *Physica Scripta*, **T134** 014014 (13pp).

[47] U. Poschinger, W. Salzmann, R. Wester, M. Weidemüller, C. P. Koch, and R. Kosloff. 2006. Theoretical model for ultracold molecule formation via adaptive feedback control. *J. Phys. B: At. Mol. Opt. Phys.*, **39** S1001.

[48] F. Weise, S. Birkner, A. Merli, S. M. Weber, F. Sauer, L. Wöste, A. Lindinger, W. Salzmann, T. G. Mullins, J. Eng, M. Albert, R. Wester, and M. Weidemüller. 2007. Optimal control of multiphoton ionization of Rb_2 molecules in a magneto-optical trap. *Phys. Rev. A*, **76** 063404.

[49] P. Rivière, C. Ruiz, and J.-M. Rost. 2008. Attosecond light-pulse-induced photoassociation. *Phys. Rev. A*, **77** 033421.

[50] K. M. Jones, S. Maleki, L. P. Ratliff, and P. D. Lett. 1997. Two-colour photoassociation spectroscopy of ultracold sodium. *J. Phys. B: At. Mol. Opt. Phys.*, **30** 289.

[51] M. Kitagawa, K. Enomoto, K. Kasa, Y. Takahashi, R. C. o, P. Naidon, and P. S. Julienne. 2008. Two-color photoassociation spectroscopy of ytterbium atoms and the precise determinations of s-wave scattering lengths. *Phys. Rev. A*, **77** 012719.

[52] J. L. Bohn and P. S. Julienne. 1999. Semianalytic theory of laser-assisted resonant cold collisions. *Phys. Rev. A*, **60** 414–425.

[53] A. Simoni, P. S. Julienne, E. Tiesinga, and C. J. Williams. 2002. Intensity effects in ultracold photoassociation line shapes. *Phys. Rev. A*, **66** 063406.

[54] R. Napolitano. 1998. Non-hermitian multichannel theory of ultracold collisions modified by intense light fields tuned to the red of the trapping transition. *Phys. Rev. A*, **57** 1164–1175.

[55] R. W. Montalvão and R. d. J. Napolitano. 2001. Line shapes of singlet-state photoassociation spectra of trapped strontium atoms near the photon-recoil temperature. *Phys. Rev. A*, **64** 011403.

[56] T. Gasenzer. 2004. Photoassociation dynamics in a Bose-Einstein condensate. *Phys. Rev. A*, **70** 043618.

[57] M. K. Olsen and L. I. Plimak. 2003. Role of quantum statistics in the photoassociation of Bose-Einstein condensates. *Phys. Rev. A*, **68** 031603.

[58] B. Deb and L. You. 2003. Model study on the photoassociation of a pair of trapped atoms into an ultralong-range molecule. *Phys. Rev. A*, **68** 033408.

[59] S. Grishkevich and A. Saenz. 2007. Influence of a tight isotropic harmonic trap on photoassociation in ultracold homonuclear alkali-metal gases. *Phys. Rev. A*, **76** 022704.

[60] R. Gonzalez-Ferez, M. Weidemuller, and P. Schmelcher. 2007. Photoassociation of cold heteronuclear dimers in static electric fields. *Phys. Rev. A*, **76** 023402.

[61] P. S. Julienne. 2009. Ultracold molecules from ultracold atoms: a case study with the KRb molecule. *Faraday Discuss.*, **142** 361–388.

[62] S. S. Hodgman, R. G. Dall, L. J. Byron, K. G. H. Baldwin, S. J. Buckman, and A. G. Truscott. 2009. Metastable helium: A new determination of the longest atomic excited-state lifetime. *Phys. Rev. Lett.*, **103** 053002.

[63] K. G. H. Baldwin. 2005. Metastable helium: atom optics with nano-grenades. *Contemporary Physics*, **46** 105–120.

[64] G. V. Shlyapnikov, J. T. M. Walraven, U. M. Rahmanov, and M. W. Reynolds. 1994. Decay kinetics and Bose condensation in a gas of spin-polarized triplet helium. *Phys. Rev. Lett.*, **73** 3247–3250.

[65] P. J. J. Tol. *Trapping and evaporative cooling of metastable helium.* PhD thesis, Free University of Amsterdam, 2005.

[66] M. van Rijnbach. *Dynamical Spectroscopy of Transient He_2 Molecules.* PhD thesis, University of Utrecht, 2004.

[67] J. Kim, U. D. Rapol, S. Moal, J. Léonard, M. Walhout, and M. Leduc. 2004. Photoassociation experiments with ultracold metastable helium. *Eur. Phys. J. D*, **31** 227–237.

[68] N. Herschbach, P. J. J. Tol, W. Vassen, W. Hogervorst, G. Woestenenk, J. W. Thomsen, P. van der Straten, and A. Niehaus. 2000. Photoassociation spectroscopy of cold He(2^3S) atoms. *Phys. Rev. Lett.*, **84** 1874–1877.

[69] B. J. Verhaar, E. G. M. van Kempen, and S. J. J. M. F. Kokkelmans. 2009. Predicting scattering properties of ultracold atoms: Adiabatic accumulated phase method and mass scaling. *Phys. Rev. A*, **79** 032711.

[70] J. Kim, S. Moal, M. Portier, J. Dugué, M. Leduc, and C. Cohen-Tannoudji. 2005. Frequency shifts of photoassociative spectra of ultracold metastable helium atoms: A new measurement of the s-wave scattering length. *Eur. Phys. Lett.*, **72** 548–554.

[71] S. Seidelin, J. V. Gomes, R. Hoppeler, O. Sirjean, D. Boiron, A. Aspect, and C. I. Westbrook. 2004. Getting the elastic scattering length by observing inelastic collisions in ultracold metastable helium atoms. *Phys. Rev. Lett.*, **93** 090409.

[72] P. J. J. Tol, W. Hogervorst, and W. Vassen. 2004. Theory of evaporative cooling with energy-dependent elastic scattering cross section and application to metastable helium. *Phys. Rev. A*, **70** 013404.

[73] S. Moal, M. Portier, J. Kim, J. Dugue, U. D. Rapol, M. Leduc, and C. Cohen-Tannoudji. 2006. Accurate determination of the scattering length of metastable helium atoms using dark resonances between atoms and exotic molecules. *Phys. Rev. Lett.*, **96** 023203.

[74] R. G. Dall, K. G. H. Baldwin, L. J. Byron, and A. G. Truscott. 2008. Experimental determination of the helium 2 $^3P_1$–1 $^1S_0$ transition rate. *Phys. Rev. Lett.*, **100** 023001.

[75] S. S. Hodgman, R. G. Dall, K. G. H. Baldwin, and A. G. Truscott. 2009. Complete ground-state transition rates for the helium 2 ^3P manifold. *Phys. Rev. A*, **80** 044501.

[76] R. J. W. Stas, J. M. McNamara, W. Hogervorst, and W. Vassen. 2006. Homonuclear ionizing collisions of laser-cooled metastable helium atoms. *Phys. Rev. A*, **73** 032713.

[77] J. C. J. Koelemeij, A. S. Tychkov, T. Jeltes, W. Hogervorst, and W. Vassen. 2004. High densities and optical collisions in a two-colour magneto-optical trap for metastable helium. *J. Phys. B: At. Mol. Opt. Phys.*, **37** 3501–3520.

[78] S. Moal, M. Portier, N. Zahzam, and M. Leduc. 2007. Lifetime of weakly bound dimers of ultracold metastable helium studied by photoassociation. *Phys. Rev. A*, **75** 033415.

[79] T. J. Beams, G. Peach, and I. B. Whittingham. 2006. Spin-dipole-induced lifetime of the least-bound $^5\Sigma_g^+$ state of He(2 $^3S_1$) + He(2 $^3S_1$). *Phys. Rev. A*, **74** 014702.

[80] O. Sirjean, S. Seidelin, J. V. Gomes, D. Boiron, C. I. Westbrook, A. Aspect, and G. V. Shlyapnikov. 2002. Ionization rates in a Bose-Einstein condensate of metastable helium. *Phys. Rev. Lett.*, **89** 220406.

[81] J. M. McNamara, T. Jeltes, A. S. Tychkov, W. Hogervorst, and W. Vassen. 2006. Degenerate Bose-Fermi mixture of metastable atoms. *Phys. Rev. Lett.*, **97** 080404.

[82] J. M. McNamara, R. J. W. Stas, W. Hogervorst, and W. Vassen. 2007. Heteronuclear ionizing collisions between laser-cooled metastable helium atoms. *Phys. Rev. A*, **75** 062715.

[83] M. R. Goosen, T. G. Tiecke, W. Vassen, and S. J. J. M. F. Kokkelmans. 2010. Feshbach resonances in ^{3}He*-^{4}He* mixtures. *ArXiv e-prints*, art. 1008.1141.

[84] T. Jeltes, J. M. McNamara, W. Hogervorst, W. Vassen, V. Krachmalnicoff, M. Schellekens, A. Perrin, H. Chang, D. Boiron, A. Aspect, and C. I. Westbrook. 2007. Comparison of the Hanbury Brown-Twiss effect for bosons and fermions. *Nature*, **445** 402–405.

[85] A. S. Dickinson, F. X. Gadéa, and T. Leininger. 2005. Photoassociation of metastable helium. *Eur. Phys. Lett.*, **70** 320–326.

[86] B. Deguilhem, T. Leininger, F. X. Gadéa, and A. S. Dickinson. 2009. Photoassociation of He_2 revisited. *J. Phys. B: At. Mol. Opt. Phys.*, **42** 015102.

[87] J. Leonard, A. P. Mosk, M. Walhout, P. van der Straten, M. Leduc, and C. Cohen-Tannoudji. 2004. Analysis of photoassociation spectra for giant helium dimers. *Phys. Rev. A*, **69** 032702.

[88] M. Portier, S. Moal, J. Kim, M. Leduc, C. Cohen-Tannoudji, and O. Dulieu. 2006. Analysis of light-induced frequency shifts in the photoassociation of ultracold metastable helium atoms. *J. Phys. B: At. Mol. Opt. Phys.*, **39** S881–S904.

[89] J. Koelemeij and M. Leduc. 2004. Prospects for measurement and control of the scattering length of metastable helium using photoassociation techniques. *Eur. Phys. J. D*, **31** 263–27.

[90] V. Venturi, P. J. Leo, E. Tiesinga, C. J. Williams, and I. B. Whittingham. 2003. Purely-long-range bound states of $\mathrm{He}(2s\,^3S) + \mathrm{He}(2p\,^3P)$. *Phys. Rev. A*, **68** 022706.

[91] E. van der Zwan, D. van Oosten, D. Nehari, P. van der Straten, and H. T. C. Stoof. 2006. On the role of Penning ionization in photoassociation spectroscopy. *J. Phys. B: At. Mol. Opt. Phys.*, **39** S825–S847.

[92] M. W. Müller, A. Merz, M. W. Ruf, H. Hotop, M. W., and M. Movre. 1991. Experimental and theoretical studies of the bi-excited collision systems He*(2^3S) + He*(2^3S, 2^1S) at thermal and subthermal kinetic energies. *Z. Phys. D*, **21** 89–112.

[93] M. Przybytek and B. Jeziorski. 2005. Bounds for the scattering length of spin-polarized helium from high-accuracy electronic structure calculations. *J. Chem. Phys.*, **123** 134315.

[94] F. X. Gadea, T. Leininger, and A. S. Dickinson. 2002. Calculated scattering length for spin-polarized metastable helium. *J. Chem. Phys.*, **117** 7122–7127.

[95] A. S. Dickinson, F. X. Gadéa, and T. Leininger. 2004. Scattering lengths for spin-polarized metastable helium-3 and helium-4. *J. Phys. B: At. Mol. Opt. Phys.*, **37** 587–593.

[96] P. O. Fedichev, M. W. Reynolds, U. M. Rahmanov, and G. V. Shlyapnikov. 1996. Inelastic decay processes in a gas of spin-polarized triplet helium. *Phys. Rev. A*, **53** 1447–1453.

[97] V. Venturi and I. B. Whittingham. 2000. Close-coupled calculation of field-free collisions of cold metastable helium atoms. *Phys. Rev. A*, **61** 060703.

[98] V. Venturi, I. B. Whittingham, P. J. Leo, and G. Peach. 1999. Close-coupled calculation of collisions of magnetostatically trapped metastable helium atoms. *Phys. Rev. A*, **60** 4635–4646.

[99] T. J. Beams, I. B. Whittingham, and G. Peach. 2007. Autoionization of spin-polarized metastable helium in tight anisotropic harmonic traps. *Phys. Rev. A*, **76** 062707.

[100] T. J. Beams, G. Peach, and I. B. Whittingham. 2004. Ultracold atomic collisions in tight harmonic traps: perturbation theory, ionization losses and application to metastable helium atoms. *J. Phys. B: At. Mol. Opt. Phys.*, **37** 4561–4570.

[101] G. Peach, I. B. Whittingham, and T. J. Beams. 2004. Ultracold atomic collisions in tight harmonic traps: Quantum-defect model and application to metastable helium atoms. *Phys. Rev. A*, **70** 032713.

[102] A. S. Dickinson. 2007. Quantum reflection model for ionization rate coefficients in cold metastable helium collisions. *J. Phys. B: At. Mol. Opt. Phys.*, **40** F237–F240.

[103] P. J. Leo, V. Venturi, I. B. Whittingham, and J. F. Babb. 2001. Ultracold collisions of metastable helium atoms. *Phys. Rev. A*, **64** 042710.

[104] G. B. Partridge, J.-C. Jaskula, M. Bonneau, D. Boiron, and C. I. Westbrook. 2010. Bose-Einstein condensation and spin mixtures of optically trapped metastable helium. *Phys. Rev. A*, **81** 053631.

[105] R. G. Dall, L. J. Byron, A. G. Truscott, G. R. Dennis, M. T. Johnsson, and J. J. Hope. 2009. Paired-atom laser beams created via four-wave mixing. *Phys. Rev. A*, **79** 011601.

[106] H. Lefebvre-Brion and R. W. Field. *The Spectra and Dynamics of Diatomic Molecules.* Elsevier, Amsterdam, revised and enlarged edition edition, 2004.

[107] J.-Y. Zhang, Z.-C. Yan, D. Vrinceanu, J. F. Babb, and H. R. Sadeghpour. 2006. Long-range interactions between a He(2 ^{3}S) atom and a He(2 ^{3}P) atom for like isotopes. *Phys. Rev. A*, **73** 022710.

[108] W. J. Meath. 1968. Retarded interaction energies between like atoms in different energy states. *J. Chem. Phys.*, **48** 227–235.

[109] Y. Ralchenko, F.-C. Jou, D. Kelleher, A. Kramida, A. Musgrove, J. Reader, W. Wiese, and K. Olsen. *NIST Atomic Spectra Database (version 3.1.5).* Online, 2008. URL `http://physics.nist.gov/asd3`.

[110] M. Marinescu. Private communciation, 2009.

[111] G. Peach. private communciation, 2009.

[112] W. A. Bingel. 1959. United atom treatment of the behavior of potential energy curves of diatomic molecules for small R. *J. Chem. Phys.*, **30** 1250–1253.

[113] D. M. Brink and G. R. Satchler. *Angular Momentum.* Clarendon Press, Oxford, third edition, 1968.

[114] B. Gao. 1996. Theory of slow-atom collisions. *Phys. Rev. A*, **54** 2022–2039.

[115] E. E. Nikitin and S. Y. Umanskii. *Theory of Slow Atomic Collisions.* Springer-Verlag, Berlin, 1984.

[116] J. H. Van Vleck. 1951. The coupling of angular momentum vectors in molecules. *Rev. Mod. Phys.*, **23** 213–227.

[117] G. W. F. Drake. *Atomic, Molecular and Optical Physics Handbook.* AIP, Melville, New York, 1996.

[118] A. J. Moerdijk, W. C. Stwalley, R. G. Hulet, and B. J. Verhaar. 1994. Negative scattering length of ultracold ^{7}Li gas. *Phys. Rev. Lett.*, **72** 40–43.

[119] M. Movre and G. Pichler. 1977. Resonance interaction and self-broadening of alkali resonance lines. I. Adiabatic potential curves. *J. Phys. B: At. Mol. Opt. Phys.*, **10** 2631–2638.

[120] D. G. Cocks, I. B. Whittingham, and G. Peach. 2010. Effects of non-adiabatic and coriolis couplings on the bound states of He(2 ^{3}S)+He(2 ^{3}P). *J. Phys. B: At. Mol. Opt. Phys.*, **43** 135102.

[121] B. R. Johnson. 1978. The renormalized Numerov method applied to calculating bound states of the coupled-channel Schroedinger equation. *J. Chem. Phys.*, **69** 4678–4688.

[122] J. Léonard, A. P. Mosk, M. Walhout, M. Leduc, M. van Rijnbach, D. Nehari, and P. van der Straten. 2005. Rotationally induced Penning ionization of ultracold photoassociated helium dimers. *Europhys. Lett.*, **70** 190–196.

[123] J. Léonard. private communciation, 2009.

[124] A. S. Dickinson and F. X. Gadéa. private communication, 2009.

[125] B. Buijsse, W. J. van der Zande, A. T. J. B. Eppink, D. H. Parker, B. R. Lewis, and S. T. Gibson. 1998. Angular distributions for photodissociation of O_2 in the herzberg continuum. *J. Chem. Phys.*, **108** 7229–7243.

[126] B. R. Lewis, S. T. Gibson, W. Zhang, H. Lefebvre-Brion, and J.-M. Robbe. 2005. Predissociation mechanism for the lowest $^1\pi_u$ states of N_2. *J. Chem. Phys.*, **122** 144302.

[127] R. González-Férez and P. Schmelcher. 2009. Impact of electric fields on highly excited rovibrational states of polar dimers. *New J. Phys.*, **11** 055013.

[128] C. McKenzie, J. Hecker Denschlag, H. Häffner, A. Browaeys, L. E. E. de Araujo, F. K. Fatemi, K. M. Jones, J. E. Simsarian, D. Cho, A. Simoni, E. Tiesinga, P. S. Julienne, K. Helmerson, P. D. Lett, S. L. Rolston, and W. D. Phillips. 2002. Photoassociation of sodium in a Bose-Einstein condensate. *Phys. Rev. Lett.*, **88** 120403.

[129] T. Gasenzer. 2004. High-light-intensity photoassociation in a Bose-Einstein condensate. *Phys. Rev. A*, **70** 021603.

[130] J. Burke. *Theoretical investigations of cold alkali atom collisions.* PhD thesis, University of Colorado, 1999.

[131] A. Dalgarno and J. T. Lewis. 1955. The exact calculation of long-range forces between atoms by perturbation theory. *Proc. Roy. Soc. A*, **233** 70–74.

[132] F. H. Mies. 1980. A scattering theory of diatomic molecules: General formalism using the channel state representation. *Molec. Phys.*, **14** 953–972.

[133] W. H. Press, S. Teukolsky, W. Vetterling, and B. Flannery. *Numerical Recipes. The Art of Scientific Computing.* Cambridge University Press, Cambridge, 2nd edition, 1992.

[134] U. Fano. 1961. Effects of configuration interaction on intensities and phase shifts. *Phys. Rev.*, **124** 1866–1878.

[135] U. Fano and J. W. Cooper. 1965. Line profiles in the far-uv absorption spectra of the rare gases. *Phys. Rev.*, **137** A1364–A1379.

[136] A. Dickinson. 2006. Ultra-long-range states in excited $^3He_2$. *Eur. Phys. J. D*, **37** 435–439.

[137] P. J. Mohr, B. N. Taylor, and D. B. Newell. *2006 CODATA recommended values.* Online, 2007. URL `http://physics.nist.gov/constants.`

[138] J. L. M. Q. Gonzalez and D. Thompson. 1997. Getting started with Numerov's method. *Computers in Physics*, **11** 514–515.

[139] K. Willner, O. Dulieu, and F. Masnou-Seeuws. 2004. Mapped grid methods for long-range molecules and cold collisions. *J. Chem. Phys.*, **120** 548–561.

[140] H. Karabulut and E. L. S. III. 1997. Trigonometric discrete variable representations. *J. Phys. B: At. Mol. Opt. Phys.*, **30** L513–L516.

Appendix A

Notation and Physical Constants

A.1 NOTATION

$\boldsymbol{r}_i$: Coordinates of electron i.

$\boldsymbol{r}_k^N$: Coordinates of nucleus k.

$\boldsymbol{R} = (R, \theta, \phi)$: Relative nuclear separation. $R = |\boldsymbol{R}|$ is the interatomic separation and (θ, ϕ) are the angles of rotation of the molecule-fixed OZ axis from the space-fixed Oz axis.

$\hat{H}_{\text{mol}}$, $\hat{H}_{\text{el}}$, $\hat{H}_{\text{fs}}$: Molecular, electronic and relativistic correction Hamiltonians.

$\hat{T}_n$, $\hat{T}_R$: Kinetic energy operator of the nuclei and its radial component.

$C^{j_1 j_2 j}_{m_{j_1} m_{j_2} m_j}$: Clebsch-Gordan coefficient given by $\langle j_1 m_{j_1} j_2 m_{j_2} | j_1 j_2 j m_j \rangle$.

$k = A, B$: Label for the nuclei.

$\alpha = 1, 2$: Subscript on quantum numbers to denote an atomic state.

L_α, S_α, j_α: Orbital, spin and total angular momenta quantum numbers, respectively, of atom α.

L, S, j: Total orbital, total spin, and total electronic angular momenta quantum numbers, respectively, of the dimer.

l: Relative rotational angular momentum quantum number of the dimer.

J: Total angular momentum quantum number of the dimer.

m_x: Projection of quantity x along the laboratory, space-fixed Oz axis.

Ω_x: Projection of quantity x along the intermolecular OZ axis.

$\Lambda = |\Omega_L|$: The absolute projection of total orbital angular momentum along the intermolecular OZ axis and represented by the notation $\Lambda = \Sigma, \Pi, \Delta, ...$ for $|\Omega_L| = 0, 1, 2, ...$

$\Omega = |\Omega_j|$: The absolute projection of total electronic angular momentum along the intermolecular OZ axis.

γ_α: Represents the quantities $\{\overline{\gamma}_\alpha, L_\alpha, S_\alpha\}$ where $\overline{\gamma}_\alpha$ denotes the quantities implicitly specified in the basis that are required to designate the atomic state of atom α.

w: Quantum number given to the symmetry of the operator $\hat{i}$ which inverts the total electronic wave function through the centre of charge. $w = 0, 1$ for g, u symmetry.

σ: Quantum number given to the symmetry of the operator $\hat{\sigma}_e$ which reflects the wave function through a plane containing the intermolecular axis. When used in the Hund's case (a) basis (and the Born-Oppenheimer potentials) $\hat{\sigma}_e$ only reflects the spatial part of the electronic wave function. When used in the Hund's case (c) basis $\hat{\sigma}_e$ reflects the total electronic wave function.

${}^{2S+1}\Lambda_w^\sigma$: Hund's case (a) notation where $\Lambda = |\Omega_L|$.

${}^{2S+1}\Lambda_w^\sigma(R)$: Born-Oppenheimer potential.

Ω_w^σ: Hund's case (c) notation where $\Omega = |\Omega_j| = |\Omega_J|$.

$G_a(R)$: Radial wave function associated with basis state $|a\rangle$.

$D_{mm'}^j(\alpha, \beta, \gamma)$: Wigner rotation matrix where (α, β, γ) are Euler angles in the Z-Y-Z convention. The angles represent the rotation of the axes as is the convention of Brink and Satchler [113].

A.2 PHYSICAL CONSTANTS

The values used for the physical constants, taken from the 2006 CODATA recommended values [137], are:

Hartree energy: $E_h = 4.35974394 \times 10^{-18}$ J.

Reduced Planck's constant: $\hbar = h/2 = 1.054571628 \times 10^{-34}$ J.s.

Bohr radius: $a_0 = 5.291772108 \times 10^{-11}$ m.

Atomic mass of helium-4: $m = 4.002603$ u.

Atomic mass unit: $\mathrm{u} = 1.660538782 \times 10^{-27}$ kg.

Appendix B

Coupling Schemes and Symmetrisation

B.1 jj SYMMETRISATION

The hybrid jj basis, $|\gamma j_1 j_2 j \Omega_j J m_J\rangle$, must obey several symmetries of the molecular Hamiltonian to be properly classified as a basis of the molecular system. Bo Gao [114] has presented a comprehensive formulation of several different sets of basis states relevant to ultracold collisions that includes a careful consideration of nuclear statistics and molecular symmetries. Unfortunately, Bo Gao's states do not include the molecular projection Ω_j and so the derivation presented in [114] does not directly apply to the symmetry of the hybrid jj basis considered here.

The first symmetry that must be addressed is that of antisymmetry under electron permutation. Because the inner $1s$ electrons of the atomic states do not influence the matrix elements of the system, these will be ignored and only the labels of the outer $2s$ or $2p$ electrons will be considered. The unsymmetrised states (2.27) must be redefined so that they are properly antisymmetric under permutation of the two outer electrons without affecting the coupling scheme. This redefinition is

$$|\gamma j_1 j_2 j \Omega_j J m_J\rangle \equiv \frac{1}{\sqrt{2}} \left[|\gamma j_1 j_2 j \Omega_j J m_J; \boldsymbol{r}_1, \boldsymbol{r}_2\rangle - |\gamma j_1 j_2 j \Omega_j J m_J; \boldsymbol{r}_2, \boldsymbol{r}_1\rangle \right] \tag{B.1}$$

where $\boldsymbol{r}_1$ and $\boldsymbol{r}_2$ are the position vectors of the two electrons. The antisymmetrisation does not affect the matrix elements with the exception of those of the complete laser coupling when the dipole approximation is not assumed.

The next symmetry that must be analysed is the electronic inversion represented by the operator $\hat{\imath}$. This operator inverts the electronic wave function through the centre of charge of the system. Its action is equivalent to swapping the states of each atom and then inverting these states about their atomic centres, which is denoted by the operator $\hat{\imath}_\alpha$, $\alpha = \{1, 2\}$. The atomic inversion of a spherical harmonic is well known: $\hat{\imath}_\alpha |L_\alpha \Omega_{L_\alpha}\rangle = Y_{L_\alpha \Omega_{L_\alpha}}(\pi - \theta, \phi + \pi) = (-1)^{L_\alpha} Y_{L_\alpha \Omega_{L_\alpha}}(\theta, \phi) = (-1)^{L_\alpha} |L_\alpha \Omega_{L_\alpha}\rangle$ and the atomic inversion of the spin states has no effect. Hence the action of $\hat{\imath}$ is determined from the atomic state representation by using the molecule-fixed frame version of equations (2.19) and (2.20):

$$\begin{aligned}
\hat{i}|(\gamma_1 j_1)_A(\gamma_2 j_2)_B j\Omega_j J m_J\rangle &= \hat{i} \sum_{\substack{\Omega_{j_1}\Omega_{L_1}\Omega_{S_1}\\ \Omega_{j_2}\Omega_{L_2}\Omega_{S_2}}} C^{j_1 j_2 j}_{\Omega_{j_1}\Omega_{j_2}\Omega_j} C^{L_1 S_1 j_1}_{\Omega_{L_1}\Omega_{S_1}\Omega_{j_1}} \\
&\quad \times C^{L_2 S_2 j_2}_{\Omega_{L_2}\Omega_{S_2}\Omega_{j_2}} |\bar{\gamma}_1 L_1 \Omega_{L_1} S_1 \Omega_{S_1}\rangle_A |\bar{\gamma}_2 L_2 \Omega_{L_2} S_2 \Omega_{S_2}\rangle_B N^J_{m_J\Omega_j} \\
&= (-1)^{L_1+L_2} \sum_{\substack{\Omega_{j_1}\Omega_{L_1}\Omega_{S_1}\\ \Omega_{j_2}\Omega_{L_2}\Omega_{S_2}}} C^{j_1 j_2 j}_{\Omega_{j_1}\Omega_{j_2}\Omega_j} C^{L_1 S_1 j_1}_{\Omega_{L_1}\Omega_{S_1}\Omega_{j_1}} \\
&\quad \times C^{L_2 S_2 j_2}_{\Omega_{L_2}\Omega_{S_2}\Omega_{j_2}} |\bar{\gamma}_1 L_1 \Omega_{L_1} S_1 \Omega_{S_1}\rangle_B |\bar{\gamma}_2 L_2 \Omega_{L_2} S_2 \Omega_{S_2}\rangle_A N^J_{m_J\Omega_j} \\
&= (-1)^{L_1+L_2+j_1+j_2-j} \sum_{\substack{\Omega_{j_1}\Omega_{L_1}\Omega_{S_1}\\ \Omega_{j_2}\Omega_{L_2}\Omega_{S_2}}} C^{j_2 j_1 j}_{\Omega_{j_2}\Omega_{j_1}\Omega_j} C^{L_1 S_1 j_1}_{\Omega_{L_1}\Omega_{S_1}\Omega_{j_1}} \\
&\quad \times C^{L_2 S_2 j_2}_{\Omega_{L_2}\Omega_{S_2}\Omega_{j_2}} |\bar{\gamma}_1 L_1 \Omega_{L_1} S_1 \Omega_{S_1}\rangle_B |\bar{\gamma}_2 L_2 \Omega_{L_2} S_2 \Omega_{S_2}\rangle_A N^J_{m_J\Omega_j} \\
&= (-1)^{L_1+L_2+j_1+j_2-j} |(\gamma_2 j_2)_A(\gamma_1 j_1)_B j\Omega_j J m_J\rangle \qquad \text{(B.2)}
\end{aligned}$$

The factor of $(-1)^{j_1+j_2-j}$ arises from the symmetry of the Clebsch-Gordan coefficient [113]. The eigenstates of the operator $\hat{i}$ corresponding to the eigenvalue $(-1)^w$ must therefore have the form

$$\begin{aligned}
|\gamma j_1 j_2 j\Omega_j w J m_J\rangle \equiv N_{jj,w} \Bigg[& |(\gamma_1 j_1)_A(\gamma_2 j_2)_B j\Omega_j J m_J\rangle \\
& + (-1)^{w+L_1+L_2+j_1+j_2-j} |(\gamma_2 j_2)_A(\gamma_1 j_1)_B j\Omega_j J m_J\rangle \Bigg] \qquad \text{(B.3)}
\end{aligned}$$

where $N_{jj,w} = 1/2$ for $\gamma_1 j_1 = \gamma_2 j_2$ and $N_{jj,w} = 1/\sqrt{2}$ otherwise. For metastable states with $\gamma_1 j_1 = \gamma_2 j_2$, a selection rule $(-1)^{w-j} = 1$ is obtained.

The states must also be symmetrised with respect to the nuclear permutation, $\hat{X}_n$. This operator is nontrivial to analyse as swapping the nuclei also reverses the orientation of the interatomic axis. The nuclear parity operator can be considered instead of this permutation operator (as there is no nuclear spin or other structure to distinguish between the action of the parity and permutation operators). The action of $\hat{X}_n$ then simply inverts the Euler angles that rotate the space-fixed Oz axis onto the molecule-fixed OZ axis, $(\phi, \theta, 0) \to (\phi + \pi, \pi - \theta, 0)$. Along with the observation that $\hat{X}_n$ does not affect space-fixed atomic states, $|jm_j\rangle$, the action of $\hat{X}_n$ on a molecular-fixed atomic state can then be derived:

$$\begin{aligned}
\hat{X}_n |j\Omega_j\rangle &= \hat{X}_n \sum_{m_j} D^j_{m_j\Omega_j}(\phi, \theta, 0)|jm_j\rangle \\
&= \sum_{m_j} D^j_{m_j\Omega_j}(\phi + \pi, \pi - \theta, 0)|jm_j\rangle \\
&= \sum_{m_j} (-1)^j D^j_{m_j,-\Omega_j}(\phi, \theta, 0)|jm_j\rangle \\
&= (-1)^j |j, -\Omega_j\rangle. \qquad \text{(B.4)}
\end{aligned}$$

The symmetry of the rotation matrix arises because

$$\begin{aligned} D^{j}_{m_j\Omega_j}(\phi+\pi,\pi-\theta,0) &= e^{-im_j(\phi+\pi)}d^{j}_{m_j\Omega_j}(\pi-\theta) \\ &= (-1)^{-m_j}e^{-im_j\phi}(-1)^{j-m_j}d^{j}_{m_j,-\Omega_j}(\theta) \\ &= (-1)^{j}D^{j}_{m_j,-\Omega_j}(\phi,\theta,0) \end{aligned} \tag{B.5}$$

where $d^{j}_{m_j\Omega_j}(\theta)$ is the reduced rotation matrix [113]. Relation (B.5) also gives

$$\hat{X}_n N^{J}_{m_J\Omega_j}(\theta,\phi) = (-1)^{J}N^{J}_{m_J,-\Omega_j}. \tag{B.6}$$

From these relations, the action of $\hat{X}_n$ upon the states (B.2) is

$$\begin{aligned} &\hat{X}_n|(\gamma_1 j_1)_A(\gamma_2 j_2)_B j\Omega_j Jm_J\rangle \\ &\quad= \hat{X}_n|(\gamma_1 j_1)_A(\gamma_2 j_2)_B j\Omega_j\rangle N^{J}_{m_J\Omega_j}(\theta,\phi) \\ &\quad= \hat{X}_n\sum_{\Omega_{j_1}\Omega_{j_2}} C^{j_1j_2j}_{\Omega_{j_1}\Omega_{j_2}\Omega_j}|\gamma_1 j_1\Omega_{j_1}\rangle_A|\gamma_2 j_2\Omega_{j_2}\rangle_B N^{J}_{m_J\Omega_j} \\ &\quad= (-1)^{j_1+j_2+J}\sum_{\Omega_{j_1}\Omega_{j_2}} C^{j_1j_2j}_{\Omega_{j_1}\Omega_{j_2}\Omega_j}|\gamma_1 j_1,-\Omega_{j_1}\rangle_B|\gamma_2 j_2,-\Omega_{j_2}\rangle_A N^{J}_{m_J,-\Omega_j} \\ &\quad= (-1)^{j_1+j_2+J}\sum_{\Omega_{j_1}\Omega_{j_2}} (-1)^{2j_1+2j_1-2j}C^{j_2j_1j}_{-\Omega_{j_2}-\Omega_{j_1}-\Omega_j} \\ &\qquad\qquad \times|\gamma_1 j_1,-\Omega_{j_1}\rangle_B|\gamma_2 j_2,-\Omega_{j_2}\rangle_A N^{J}_{m_J,-\Omega_j} \\ &\quad= (-1)^{j_1+j_2+J}|(\gamma_2 j_2)_B(\gamma_1 j_1)_A j,-\Omega_j,Jm_J\rangle. \end{aligned} \tag{B.7}$$

Therefore, the states that are symmetric under the action of $\hat{X}_n$ and $\hat{\imath}$ must be

$$|\gamma j_1 j_2 jJm_J;\Omega w\rangle = N_{jj,\Omega}\left[|\gamma j_1 j_2 j\Omega wJm_J\rangle + (-1)^{w+L_1+L_2-j+J}|\gamma j_1 j_2 j,-\Omega,wJm_J\rangle\right], \tag{B.8}$$

where $N_{jj,\Omega} = 1/2$ for $\Omega = 0$ and $N_{jj,\Omega} = 1/\sqrt{2}$ otherwise. For $\Omega = 0$, a selection rule $(-1)^{w+L_1+L_2-j+J} = 1$ is obtained.

When $\Omega = 0$, these states also possess a reflection symmetry under the action of $\hat{\sigma}_e$ which performs a reflection through the XZ plane on the electronic wave function. Consider the action of $\hat{\sigma}_e$ on an atomic state: it is equivalent to an inversion of the atomic state ($\hat{\imath}_\alpha$) with a π rotation around the OY axis with the origin at the atomic centre ($\hat{C}_{Y\pi}$). The action of $\hat{\imath}_\alpha$ has been discussed previously. The rotation around the Y axis performed by $\hat{C}_{Y\pi}$ is equivalent to a set of Euler angles $(0,\pi,0)$ that generate a rotation matrix $D^{j}_{\Omega_j\Omega'_j}(0,\pi,0) = (-1)^{j+\Omega_j}\delta_{\Omega_j,-\Omega_j}$, which implies that $\hat{C}_{Y\pi}|j\Omega_j\rangle = (-1)^{j+\Omega_j}|j,-\Omega_j\rangle$. Therefore, the action of $\hat{\sigma}_e$ on the unsymmetrised states $|\gamma j_1 j_2 j\Omega_j Jm_J\rangle$ with $\Omega_j = 0$ is

$$\begin{aligned} \hat{\sigma}_e|\gamma j_1 j_2 j0Jm_J\rangle = \hat{\imath}\hat{C}_{\pi Y}&\sum_{\substack{\Omega_{j_1}\Omega_{L_1}\Omega_{S_1}\\ \Omega_{j_2}\Omega_{L_2}\Omega_{S_2}}} C^{j_1j_2j}_{\Omega_{j_1}\Omega_{j_2}0}C^{L_1S_1j_1}_{\Omega_{L_1}\Omega_{S_1}\Omega_{j_1}} \\ &\times C^{L_2S_2j_2}_{\Omega_{L_2}\Omega_{S_2}\Omega_{j_2}}|\bar{\gamma}_1 L_1\Omega_{L_1}S_1\Omega_{S_1}\rangle|\bar{\gamma}_2 L_2\Omega_{L_2}S_2\Omega_{S_2}\rangle N^{J}_{m_J0} \end{aligned}$$

$$
\begin{aligned}
&= (-1)^{2L_1+2L_2+S_1+S_2} \sum_{\substack{\Omega_{j_1}\Omega_{L_1}\Omega_{S_1}\\ \Omega_{j_2}\Omega_{L_2}\Omega_{S_2}}} C^{j_1 j_2 j}_{\Omega_{j_1}\Omega_{j_2}0} C^{L_1 S_1 j_1}_{\Omega_{L_1}\Omega_{S_1}\Omega_{j_1}} \\
&\quad \times C^{L_2 S_2 j_2}_{\Omega_{L_2}\Omega_{S_2}\Omega_{j_2}} |\bar{\gamma}_1 L_1, -\Omega_{L_1} S_1, -\Omega_{S_1}\rangle |\bar{\gamma}_2 L_2, -\Omega_{L_2} S_2, -\Omega_{S_2}\rangle N^J_{m_J 0} \\
&= (-1)^{L_1+L_2+2S_1+2S_2-j} \sum_{\substack{\Omega_{j_1}\Omega_{L_1}\Omega_{S_1}\\ \Omega_{j_2}\Omega_{L_2}\Omega_{S_2}}} C^{j_1 j_2 j}_{-\Omega_{j_1},-\Omega_{j_2}0} C^{L_1 S_1 j_1}_{-\Omega_{L_1},-\Omega_{S_1},-\Omega_{j_1}} \\
&\quad \times C^{L_2 S_2 j_2}_{-\Omega_{L_2},-\Omega_{S_2},-\Omega_{j_2}} |\bar{\gamma}_1 L_1, -\Omega_{L_1} S_1, -\Omega_{S_1}\rangle |\bar{\gamma}_2 L_2, -\Omega_{L_2} S_2, -\Omega_{S_2}\rangle N^J_{m_J 0} \\
&= (-1)^{L_1+L_2-j} |\gamma j_1 j_2 j 0 J m_J\rangle. \qquad \text{(B.9)}
\end{aligned}
$$

When this is applied to the complete symmetric state (B.8) with $\Omega = 0$, no additional complications arise and the result

$$\hat{\sigma}_e |\gamma j_1 j_2 j J m_J; 0w\rangle = (-1)^{L_1+L_2-j} |\gamma j_1 j_2 j J m_J; 0w\rangle \qquad \text{(B.10)}$$

is obtained. From this it can be seen that the symmetry requirement $(-1)^{w+L_1+L_2-j+J} = 1$ for $\Omega = 0$ in (B.8) can be rewritten as $(-1)^{w+\sigma+J} = 1$. Therefore a selection rule is obtained for states with $\Omega = 0$: Hund's case (c) sets 0_g^+ and 0_u^- only allow for even values of J and sets 0_g^- and 0_u^+ only allow for odd values of J.

B.2 LS COUPLING

The LS basis couples each atom's orbital angular momenta and each atom's spin angular momenta separately to form $\boldsymbol{L} = \boldsymbol{L}_1 + \boldsymbol{L}_2$ and $\boldsymbol{S} = \boldsymbol{S}_1 + \boldsymbol{S}_2$:

$$|\gamma L S m_L m_S\rangle = \sum_{\substack{m_{L_1} m_{L_2}\\ m_{S_1} m_{S_2}}} C^{L_1 L_2 L}_{m_{L_1} m_{L_2} m_L} C^{S_1 S_2 S}_{m_{S_1} m_{S_2} m_S} |\bar{\gamma}_1 L_1 m_{L_1} S_1 m_{S_1}\rangle |\bar{\gamma}_2 L_2 m_{L_2} S_2 m_{S_2}\rangle. \qquad \text{(B.11)}$$

The LS basis can also be represented in the molecule-fixed frame by replacing all quantities m_x with Ω_x. The transformation between these two frames of reference is

$$|\gamma L S \Omega_L \Omega_S\rangle = \sum_{m_L m_S} D^L_{m_L \Omega_L}(\phi, \theta, 0) D^S_{m_S \Omega_S}(\phi, \theta, 0) |\gamma L S m_L m_S\rangle. \qquad \text{(B.12)}$$

The total electronic states of the dimer are

$$|\gamma L S j m_j\rangle = \sum_{m_L m_S} C^{LSj}_{m_L m_S m_j} |\gamma L S m_L m_S\rangle \qquad \text{(B.13)}$$

and inclusion of the nuclear rotation, $|l m_l\rangle$, is analogous to that for the jj basis:

$$|\gamma L S j l J m_J\rangle = \sum_{m_L m_S m_j m_l} C^{LSj}_{m_L m_S m_j} C^{jlJ}_{m_j m_l m_J} |\gamma L S m_L m_S\rangle |l m_l\rangle. \qquad \text{(B.14)}$$

In a similar manner as for the hybrid jj basis states (2.25), the LS basis can be written in a mixed molecular-fixed and space-fixed frame representation as

$$|\gamma LSjlJm_J\rangle = \sum_{\Omega_L\Omega_S\Omega_j} (-1)^{j-\Omega_j} C^{LSj}_{\Omega_L\Omega_S\Omega_j} C^{jJl}_{\Omega_j,-\Omega_j,0} N^J_{m_J\Omega_j}(\theta,\phi)|\gamma LS\Omega_L\Omega_S\rangle \tag{B.15}$$

which demonstrates a coupling of $\boldsymbol{j} = \boldsymbol{L} + \boldsymbol{S}$ and $\boldsymbol{J}$ to form $\boldsymbol{l}$. Hence, the hybrid LS basis states are defined as

$$|\gamma LS\Omega_L\Omega_S Jm_J\rangle \equiv N^J_{m_J,\Omega_L+\Omega_S}(\theta,\phi)|\gamma LS\Omega_L\Omega_S\rangle. \tag{B.16}$$

The electronic Hamiltonian term, $\hat{H}_{\mathrm{el}}$, is diagonal in this basis.

The implementation of symmetry requirements for the hybrid LS basis is very similar to that for the jj basis and will not be shown here. However, one important difference between the LS and jj bases must be discussed. For the jj basis, the projection of the total electronic angular momentum Ω_j is no longer a good quantum number and only the modulus $\Omega = |\Omega_j|$ may be retained in the basis labels. Similarly, in the LS basis the total orbital and spin angular momentum Ω_L and Ω_S are no longer good quantum numbers, due to the requirement that nuclear permutation must be symmetric, and only their moduli, $\Lambda = |\Omega_L|$ and $\Sigma = |\Omega_S|$, can be retained. However, writing down the basis using only the labels $|\gamma LS\Lambda\Sigma\rangle$ means that the value of Ω is not well defined, as $\Omega = |\Omega_L + \Omega_S|$ which could be either $\Omega = \Lambda \pm \Sigma$. This ambiguity can be resolved by including Ω with the basis labels, i.e. $|\gamma LS\Lambda\Sigma\Omega\rangle$, as in [106]. Alternatively, the relative projection of L against S, $\mathrm{sgn}(\Omega_L\Omega_S)$, may be specified to uniquely determine the state. This thesis defines the quantity $\tilde{\Omega}_S$, which represents the magnitude Σ as well as the orientation of S relative to L. Explicitly $\tilde{\Omega}_S = \mathrm{sgn}(\Omega_L\Omega_S)|\Omega_S|$ and the states are $|\gamma LS\Lambda\tilde{\Omega}_S\rangle$.

The LS states that possess the correct symmetry under the action of $\hat{\imath}$ are

$$\begin{aligned}|\gamma LS\Omega_L\Omega_S wJm_J\rangle \equiv N_{LS,w}\Big[&|(\gamma_1)_A(\gamma_2)_B LS\Omega_L\Omega_S Jm_J\rangle \\ &+ (-1)^{w-L+S_1+S_2-S}|(\gamma_2)_A(\gamma_1)_B LS\Omega_L\Omega_S Jm_J\rangle\Big]\end{aligned} \tag{B.17}$$

where $N_{LS,w} = 1/2$ if $\gamma_1 = \gamma_2$ and $N_{LS,w} = 1/\sqrt{2}$ otherwise. For the metastable configuration, $\gamma_1 = \gamma_2$ and the selection rule $(-1)^{w-S}$ is obtained. The states that are also symmetric under permutation of the nuclei, $\hat{X}_n$, are

$$\begin{aligned}|\gamma LSJm_J;\Lambda\tilde{\Omega}_S w\rangle = N_{LS,\Lambda}\Big[&|\gamma LS\Lambda\tilde{\Omega}_S wJm_J\rangle \\ &+ (-1)^{w+L_1+L_2-L-S+J}|\gamma LS,-\Lambda,-\tilde{\Omega}_S,wJm_J\rangle\Big]\end{aligned} \tag{B.18}$$

where $|\Omega_L| = \Lambda > 0$, however $\tilde{\Omega}_S$ may be negative. The normalisation constant is $N_{LS,\Lambda} =$

$1/2$ if $\Lambda = \tilde{\Omega}_S = 0$ and $N_{LS,\Lambda} = 1/\sqrt{2}$ otherwise.

The states (B.18) are also symmetrised with respect to the reflection operator $\hat{\sigma}_e$ for $\Lambda + \tilde{\Omega}_S = \Omega = 0$ since

$$\hat{\sigma}_e|\gamma LSJm_J;\Lambda,-\Lambda,w\rangle = (-1)^{w+J}|\gamma LSJm_J;\Lambda,-\Lambda,w\rangle. \tag{B.19}$$

B.3 TRANSFORMATION BETWEEN LS AND jj BASES

Of the the hybrid jj and hybrid LS bases, each is best suited to regions of interatomic distance where its respective diagonal term of the Hamiltonian (either $\hat{H}_{\text{fs}}$ or $\hat{H}_{\text{el}}$) dominates. The jj basis is hence best used for large interatomic distances, where the fine-structure splitting is much larger than the electronic splittings and, similarly, the LS basis is most suited to small interatomic separations where the electronic splittings dominate. Although the jj basis has been chosen for this thesis, the LS state is still required to find the matrix elements of the electronic Hamiltonian and therefore the transformation between the two bases is needed.

The transformation between the unsymmetrised bases $|\gamma j_1 j_2 j\Omega_j Jm_J\rangle$ and $|\gamma LS\Omega_L\Omega_S Jm_J\rangle$ is found by inverting (B.11) in the molecular frame,

$$|\gamma_1\Omega_{L_1}\Omega_{S_1}\rangle|\gamma_2\Omega_{L_2}\Omega_{S_2}\rangle = \sum_{LS\Omega_L\Omega_S} C^{L_1L_2L}_{\Omega_{L_1}\Omega_{L_2}\Omega_L} C^{S_1S_2S}_{\Omega_{S_1}\Omega_{S_2}\Omega_S}|\gamma LS\Omega_L\Omega_S\rangle \tag{B.20}$$

and then using (2.20) and (2.19), also in the molecular frame, to find

$$\begin{aligned}|\gamma j_1 j_2 j\Omega_j\rangle &= \sum_{\substack{LS\\ \Omega_L\Omega_S}} \sum_{\substack{\Omega_{j_1}\Omega_{L_1}\Omega_{S_1}\\ \Omega_{j_2}\Omega_{L_2}\Omega_{S_2}}} C^{L_1L_2L}_{\Omega_{L_1}\Omega_{L_2}\Omega_L} C^{S_1S_2S}_{\Omega_{S_1}\Omega_{S_2}\Omega_S} \\ &\quad\times C^{j_1j_2j}_{\Omega_{j_1}\Omega_{j_2}\Omega_j} C^{L_1S_1j_1}_{\Omega_{L_1}\Omega_{S_1}\Omega_{j_1}} C^{L_2S_2j_2}_{\Omega_{L_2}\Omega_{S_2}\Omega_{j_2}}|\gamma LS\Omega_L\Omega_S\rangle \\ &= \sum_{L\Omega_L S\Omega_S} F^{j_1j_2j\Omega_j}_{LS\Omega_L\Omega_S}|\gamma LS\Omega_L\Omega_S\rangle \end{aligned} \tag{B.21}$$

where $F^{j_1j_2j\Omega_j}_{LS\Omega_L\Omega_S}$ is given by

$$F^{j_1j_2j\Omega_j}_{LS\Omega_L\Omega_S} = \sqrt{(2S+1)(2L+1)(2j_1+1)(2j_2+1)} \begin{Bmatrix} L_1 & L_2 & L \\ S_1 & S_2 & S \\ j_1 & j_2 & j \end{Bmatrix} C^{LSj}_{\Omega_L\Omega_S\Omega_j}, \tag{B.22}$$

which results from the contraction [113] of the five Clebsch-Gordan coefficients in equation (B.21). The term $\{\cdots\}$ is a Wigner 9-j symbol and the implicit set of quantum numbers $\{\gamma_1,\gamma_2\}$ has been suppressed in the labelling of $F^{j_1j_2j\Omega_j}_{LS\Omega_L\Omega_S}$. Two properties of the coefficient are required:

$$F^{j_2j_1j\Omega_j}_{LS\Omega_L\Omega_S} = (-1)^{L_1+L_2+L+S_1+S_2+S+j_1+j_2+j} F^{j_1j_2j\Omega_j}_{LS\Omega_L\Omega_S} \tag{B.23}$$

and

$$F^{j_1j_2j,-\Omega_j}_{LS,-\Omega_L,-\Omega_S} = (-1)^{L+S-j} F^{j_1j_2j\Omega_j}_{LS\Omega_L\Omega_S}. \tag{B.24}$$

The transformation from the $\hat{\imath}$-symmetrised jj (B.3) and LS (B.17) bases is straightforward after using (B.23):

$$\begin{aligned}
|\gamma j_1 j_2 j \Omega_j w J m_J\rangle &= N_{jj,w} \sum_{LS\Omega_L\Omega_S} F^{j_1j_2j\Omega_j}_{LS\Omega_L\Omega_S} |(\gamma_1)_A(\gamma_2)_B LS\Omega_L\Omega_S J m_J\rangle \\
&\quad + (-1)^{w+L_1+L_2+j_1+j_2-j} F^{j_2j_1j\Omega_j}_{LS\Omega_L\Omega_S} |(\gamma_1)_B(\gamma_2)_A LS\Omega_L\Omega_S J m_J\rangle \\
&= N_{jj,w} \sum_{LS\Omega_L\Omega_S} F^{j_1j_2j\Omega_j}_{LS\Omega_L\Omega_S} \Big[|(\gamma_1)_A(\gamma_2)_B LS\Omega_L\Omega_S J m_J\rangle \\
&\quad + (-1)^{w-L+S_1+S_2-S} F^{j_2j_1j\Omega_j}_{LS\Omega_L\Omega_S} |(\gamma_1)_B(\gamma_2)_A LS\Omega_L\Omega_S J m_J\rangle \Big] \\
&= \frac{N_{jj,w}}{N_{LS,w}} \sum_{LS\Omega_L\Omega_S} F^{j_1j_2j\Omega_j}_{LS\Omega_L\Omega_S} |\gamma LS\Omega_L\Omega_S w J m_J\rangle.
\end{aligned} \tag{B.25}$$

Because only $2s2s$ and $2s2p$ levels are considered here, either $\gamma_1 = \gamma_2$ and $j_1 = j_2$, or $\gamma_1 \neq \gamma_2$ and $j_1 \neq j_2$, making the fraction $N_{jj,w}/N_{LS,w} = 1$.

The transformation between the fully symmetrised jj and LS bases is not as concisely described. Using (B.8) and (B.25), the transformation becomes

$$\begin{aligned}
|\gamma j_1 j_2 j J m_J; \Omega w\rangle = N_{jj,\Omega} \sum_{LS\Omega_L\Omega_S} & F^{j_1j_2j\Omega}_{LS\Omega_L\Omega_S} |\gamma LS\Omega_L\Omega_S w J m_J\rangle \\
&+ (-1)^{w+L_1+L_2-j+J} F^{j_1j_2j,-\Omega}_{LS,-\Omega_L,-\Omega_S} |\gamma LS,-\Omega_L,-\Omega_S w J m_J\rangle.
\end{aligned} \tag{B.26}$$

To convert the RHS into a representation of symmetrised LS states (B.18), the coefficient symmetry (B.24) is required, as well as the separation of the $\Omega_L > 0$, $\Omega_L = 0$ and $\Omega_L < 0$ parts of the summation over Ω_L:

$$\begin{aligned}
|\gamma j_1 j_2 j J m_J; \Omega w\rangle = N_{jj,\Omega} \sum_{LS} \Bigg(& \sum_{\Omega_L>0,\Omega_S} \Big[F^{j_1j_2j\Omega}_{LS\Omega_L\Omega_S} |\gamma LS\Omega_L\Omega_S w J m_J\rangle \\
&\qquad + (-1)^{w+L_1+L_2-L-S+J} F^{j_1j_2j,\Omega}_{LS\Omega_L\Omega_S} |\gamma LS,-\Omega_L,-\Omega_S w J m_J\rangle \Big] \\
&+ \sum_{\Omega_L<0,\Omega_S} \Big[F^{j_1j_2j\Omega}_{LS\Omega_L\Omega_S} |\gamma LS\Omega_L\Omega_S w J m_J\rangle \\
&\qquad + (-1)^{w+L_1+L_2-L-S+J} F^{j_1j_2j,\Omega}_{LS,\Omega_L,\Omega_S} |\gamma LS,-\Omega_L,-\Omega_S w J m_J\rangle \Big] \\
&+ \sum_{\Omega_S} \Big[F^{j_1j_2j\Omega}_{LS0\Omega_S} |\gamma LS0\Omega_S w J m_J\rangle \\
&\qquad + (-1)^{w+L_1+L_2-L-S+J} F^{j_1j_2j,\Omega}_{LS0\Omega_S} |\gamma LS0,-\Omega_S w J m_J\rangle \Big] \Bigg).
\end{aligned} \tag{B.27}$$

In the first summation Ω_L can be relabelled Λ and the second summation can be converted to a sum over positive Λ by the substitutions $-\Omega_L \to \Lambda$ and $-\Omega_S \to \tilde{\Omega}_S$. Finally, the first and last summations can also be relabelled with $\Omega_S \to \tilde{\Omega}_S$. This gives

$$\begin{aligned}|\gamma j_1 j_2 j J m_J; \Omega w\rangle = N_{jj,\Omega} \sum_{LS} \Bigg[\sum_{\Lambda>0,\tilde{\Omega}_S} F^{j_1 j_2 j \Omega}_{LS\Lambda\tilde{\Omega}_S} \Big[&|\gamma LS\Lambda\tilde{\Omega}_S w J m_J\rangle \\ &+ (-1)^{w+L_1+L_2-L-S+J} |\gamma LS, -\Lambda, -\tilde{\Omega}_S w J m_J\rangle \Big] \\ + \sum_{\Lambda>0,\tilde{\Omega}_S} F^{j_1 j_2 j \Omega}_{LS,-\Lambda,-\tilde{\Omega}_S} \Big[&|\gamma LS, -\Lambda, -\tilde{\Omega}_S w J m_J\rangle \\ &+ (-1)^{w+L_1+L_2-L-S+J} |\gamma LS, \Lambda, \tilde{\Omega}_S, w J m_J\rangle \Big] \\ + \sum_{\tilde{\Omega}_S} F^{j_1 j_2 j \Omega}_{LS0\tilde{\Omega}_S} \Big[&|\gamma LS0\tilde{\Omega}_S w J m_J\rangle \\ &+ (-1)^{w+L_1+L_2-L-S+J} |\gamma LS0, -\tilde{\Omega}_S w J m_J\rangle \Big] \Bigg]. \end{aligned} \tag{B.28}$$

By taking out a phase factor from the second summation, the first two summations can be combined to give the final result

$$\begin{aligned} &|\gamma j_1 j_2 j J m_J; \Omega w\rangle \\ &= N_{jj,\Omega} \sum_{LS\tilde{\Omega}_S} \Bigg[\sqrt{2} \sum_{\Lambda>0} \left[F^{j_1 j_2 j \Omega}_{LS\Lambda\tilde{\Omega}_S} + (-1)^{w+L_1+L_2-L-S+J} F^{j_1 j_2 j \Omega}_{LS,-\Lambda,-\tilde{\Omega}_S} \right] |\gamma LS J m_J; \Lambda\tilde{\Omega}_S w\rangle \\ &\quad + \sqrt{2 + 2\delta_{\tilde{\Omega}_S,0}} F^{j_1 j_2 j \Omega}_{LS0\tilde{\Omega}_S} |\gamma LS J m_J; 0\tilde{\Omega}_S w\rangle \Bigg], \end{aligned} \tag{B.29}$$

where $1/N_{LS,\Lambda} = 2$ for $\Lambda = \tilde{\Omega}_S = 0$ and $1/N_{LS,\Lambda} = \sqrt{2}$ otherwise, has been used.

B.4 ELECTRONIC MATRIX ELEMENT

As described in section 2.1.1, the electronic Hamiltonian in the Born-Oppenheimer approximation satisfies the eigenvalue equation

$$\hat{H}_{\mathrm{el}} |\Lambda^\sigma S w\rangle = \left[E^\infty_\gamma + {}^{2S+1}\Lambda^\sigma_w(R) \right] |\Lambda^\sigma S w\rangle \tag{B.30}$$

where σ is required only for $\Lambda = 0$ and is the symmetry under reflection of the spatial part of the electronic wave function only through a plane containing the interatomic axis. Equation (B.30) implies that the matrix elements of $\hat{H}_{\mathrm{el}}$ are diagonal in the LS basis (B.18). Therefore, the states for the matrix elements of $\hat{H}_{\mathrm{el}}$ in the jj basis (B.8) must be transformed to the LS basis. That is, if $|a\rangle \equiv |\gamma j_1 j_2 j J m_J; \Omega w\rangle$ then, from (B.29), the matrix elements are

$$
\begin{aligned}
\langle a'|\hat{H}_{\mathrm{el}}|a\rangle = E_a^{\infty}\delta_{a'a} + \delta_{\eta'\eta}N_{jj,\Omega'}N_{jj,\Omega}\sum_{LS\tilde{\Omega}_S}\Bigg(2\sum_{\Lambda>0}{}^{2S+1}\Lambda_w(R)\Big[&F^{j_1'j_2'j'\Omega}_{LS\Lambda\tilde{\Omega}_S}F^{j_1j_2j\Omega}_{LS\Lambda\tilde{\Omega}_S} \\
&+ 2(-1)^{w+L_1+L_2-L-S+J}F^{j_1'j_2'j'\Omega}_{LS\Lambda\tilde{\Omega}_S}F^{j_1j_2j\Omega}_{LS,-\Lambda,-\tilde{\Omega}_S} + F^{j_1'j_2'j'\Omega}_{LS,-\Lambda,-\tilde{\Omega}_S}F^{j_1j_2j\Omega}_{LS,-\Lambda,-\tilde{\Omega}_S}\Big] \\
&+ (2+2\delta_{\tilde{\Omega}_S,0})^{2S+1}\Sigma_w^+(R)F^{j_1j_2j\Omega}_{LS0\tilde{\Omega}_S}F^{j_1'j_2'j'\Omega}_{LS0\tilde{\Omega}_S}\Bigg),
\end{aligned}
\tag{B.31}
$$

where $\eta = \{w, \Omega, J, m_J, \gamma\}$.

If $\Omega = 0$, then $\tilde{\Omega}_S = -\Lambda$ and this expression reduces to

$$
\begin{aligned}
\langle a'|\hat{H}_{\mathrm{el}}|a\rangle &= E_a^{\infty}\delta_{a'a} + \delta_{\eta'\eta}\frac{1}{4}\sum_{LS}\Bigg(2\sum_{\Lambda>0}{}^{2S+1}\Lambda_w(R)\Big[F^{j_1'j_2'j'0}_{LS\Lambda,-\Lambda}F^{j_1j_2j0}_{LS\Lambda,-\Lambda} \\
&\quad + 2(-1)^{w+L_1+L_2-j+J}F^{j_1'j_2'j'0}_{LS\Lambda,-\Lambda}F^{j_1j_2j0}_{LS\Lambda,-\Lambda} + (-1)^{j'-j}F^{j_1'j_2'j'0}_{LS\Lambda,-\Lambda}F^{j_1j_2j0}_{LS\Lambda,-\Lambda}\Big] \\
&\quad + 4\times{}^{2S+1}\Sigma_w^+(R)F^{j_1j_2j\Omega}_{LS00}F^{j_1'j_2'j'0}_{LS00}\Bigg), \\
&= E_a^{\infty}\delta_{a'a} + \delta_{\eta'\eta}\sum_{LS}\Bigg(2\sum_{\Lambda>0}{}^{2S+1}\Lambda_w(R)F^{j_1'j_2'j'0}_{LS\Lambda,-\Lambda}F^{j_1j_2j0}_{LS\Lambda,-\Lambda} + {}^{2S+1}\Sigma_w^+(R)F^{j_1'j_2'j'0}_{LS00}F^{j_1j_2j0}_{LS00}\Bigg) \\
&= E_a^{\infty}\delta_{a'a} + \delta_{\eta'\eta}\sum_{LS}\sum_{\Omega_L}{}^{2S+1}\Lambda_w(R)F^{j_1'j_2'j'0}_{LS\Omega_L,-\Omega_L}F^{j_1j_2j0}_{LS\Omega_L,-\Omega_L}
\end{aligned}
\tag{B.32}
$$

where $\Omega = 0$ implies that $(-1)^{w+L_1+L_2-j+J} = 1$ for the states (B.8) to be non-zero and $(-1)^{j'-j} = 1$ because of the $\hat{\sigma}_e$ symmetry (B.10).

If $\Omega > 0$ then expression (B.31) becomes

$$
\begin{aligned}
\langle a'|\hat{H}_{\mathrm{el}}|a\rangle &= E_a^{\infty}\delta_{a'a} + \delta_{\eta'\eta}\frac{1}{2}\sum_{LS\tilde{\Omega}_S}\Bigg(2\sum_{\Lambda>0}{}^{2S+1}\Lambda_w(R)\left[F^{j_1'j_2'j'\Omega}_{LS\Lambda\tilde{\Omega}_S}F^{j_1j_2j\Omega}_{LS\Lambda\tilde{\Omega}_S} + F^{j_1'j_2'j'\Omega}_{LS,-\Lambda,-\tilde{\Omega}_S}F^{j_1j_2j\Omega}_{LS,-\Lambda,-\tilde{\Omega}_S}\right] \\
&\quad + 2^{2S+1}\Sigma_w^+(R)F^{j_1j_2j\Omega}_{LS0\tilde{\Omega}_S}F^{j_1'j_2'j'\Omega}_{LS0\tilde{\Omega}_S}\Bigg), \\
&= E_a^{\infty}\delta_{a'a} + \delta_{\eta'\eta}\sum_{LS\tilde{\Omega}_S}\Bigg(\sum_{\Lambda>0}{}^{2S+1}\Lambda_w(R)\left[F^{j_1'j_2'j'\Omega}_{LS\Lambda\tilde{\Omega}_S}F^{j_1j_2j\Omega}_{LS\Lambda\tilde{\Omega}_S} + F^{j_1'j_2'j'\Omega}_{LS,-\Lambda,-\tilde{\Omega}_S}F^{j_1j_2j\Omega}_{LS,-\Lambda,-\tilde{\Omega}_S}\right] \\
&\quad + {}^{2S+1}\Sigma_w^+(R)F^{j_1j_2j\Omega}_{LS0\tilde{\Omega}_S}F^{j_1'j_2'j'\Omega}_{LS0\tilde{\Omega}_S}\Bigg) \\
&= E_a^{\infty}\delta_{a'a} + \delta_{\eta'\eta}\sum_{LS\tilde{\Omega}_S\Omega_L}{}^{2S+1}\Lambda_w(R)F^{j_1'j_2'j'\Omega}_{LS\Omega_L\tilde{\Omega}_S}F^{j_1j_2j\Omega}_{LS\Omega_L\tilde{\Omega}_S}
\end{aligned}
\tag{B.33}
$$

where the term $F^{j_1'j_2'j'\Omega}_{LS\Lambda\tilde{\Omega}_S}F^{j_1j_2j\Omega}_{LS,-\Lambda,-\tilde{\Omega}_S}$ in (B.31) is proportional to $C^{LSj'}_{\Lambda\tilde{\Omega}_S\Omega}C^{LSj}_{-\Lambda,-\tilde{\Omega}_S,\Omega}$ and must be zero for $\Omega \neq 0$.

Because the result (B.32) can also be retrieved from the form of (B.33) then this final result may be used in general.

B.5 EXPERIMENTALLY RELEVANT BASIS STATES

It is often more relevant to identify initial colliding metastable states in an experiment using the basis $|Sm_S, lm_l\rangle$, especially for a gas of spin-polarised metastable atoms. This basis is defined by

$$|Sm_S, lm_l\rangle \equiv |\gamma L S m_L m_S w\rangle |lm_l\rangle \tag{B.34}$$

where it is assumed that $L = m_L = 0$ and $(-1)^{w-S} = 1$ due to selection rules for metastable levels, as explained below equation (B.17). The transformation to the hybrid jj basis is derived by noting that $\boldsymbol{L_1} = \boldsymbol{L_2} = 0$ and hence $\boldsymbol{S_\alpha} = \boldsymbol{j_\alpha}$, so that the coupling scheme

$$|\gamma LSjlJm_Jw\rangle = \sum_{m_l m_S m_L} C^{jlJ}_{m_L+m_S, m_l, m_J} C^{LSj}_{m_L m_S m_L+m_S} |\gamma L S m_L m_S w\rangle |lm_l\rangle \tag{B.35}$$

becomes

$$|\gamma 0 SjlJm_Jw\rangle = \delta_{S,j} \sum_{m_l m_S} C^{SlJ}_{m_S m_l m_J} |Sm_S, lm_l\rangle. \tag{B.36}$$

This can be inverted to give

$$|Sm_S, lm_l\rangle = \sum_{Jm_J} C^{SlJ}_{m_S m_l m_J} |\gamma 0 SSlJm_Jw\rangle \tag{B.37}$$

which, when combined with equation (2.25), gives the desired transformation:

$$|Sm_S, lm_l\rangle = \sum_{Jm_J\Omega} (-1)^{S-\Omega} C^{SJl}_{\Omega -\Omega 0} C^{SlJ}_{m_S m_l m_J} |\gamma S_1 S_2 S J m_J; \Omega w\rangle. \tag{B.38}$$

Appendix C

Renormalised Numerov method

C.1 BOUND STATES

The Numerov method was devised to solve differential equations of the form

$$\left[\frac{d^2}{dx^2} + \boldsymbol{Q}(x)\right] \boldsymbol{\Psi}(x) = 0 \tag{C.1}$$

where $\boldsymbol{Q}$ is a $n \times n$ matrix and $\boldsymbol{\Psi}$ a matrix of vectors representing n-linearly independent solutions to the equation. The Numerov method is defined by the three term recurrence relationship [121]

$$(1 - \boldsymbol{T}_{n+1})\boldsymbol{\Psi}_{n+1} - (2 + 10\boldsymbol{T}_n)\boldsymbol{\Psi}_n + (1 - \boldsymbol{T}_{n-1})\boldsymbol{\Psi}_{n-1} = 0 \tag{C.2}$$

where $\boldsymbol{\Psi}_n = \boldsymbol{\Psi}(x_n)$,

$$\boldsymbol{T}_n = -\frac{h^2}{12}\boldsymbol{Q}(x_n), \tag{C.3}$$

h is the stepsize and and $x_n = nh$. The local error of the method is $O(h^6)$ at each step with a global error of $O(h^5)$. This recurrence relation can be written in a different manner by making a transformation $\boldsymbol{F}_n = (1 - \boldsymbol{T}_n)\boldsymbol{\Psi}_n$, that converts (C.2) to

$$\boldsymbol{F}_{n+1} - \boldsymbol{U}_n\boldsymbol{F}_n + \boldsymbol{F}_{n-1} = 0 \tag{C.4}$$

where $\boldsymbol{U}_n = 12(1 - \boldsymbol{T}_n)^{-1} - 10\boldsymbol{I}$. In this form, it is possible to define a ratio matrix

$$\boldsymbol{R}_n = \boldsymbol{F}_{n+1}\boldsymbol{F}_n^{-1} \tag{C.5}$$

that converts the three term recurrence relation to a two term recurrence relation [121]

$$\boldsymbol{R}_n = \boldsymbol{U}_n - \boldsymbol{R}_{n-1}^{-1}. \tag{C.6}$$

This recurrence relationship requires two matrix inversions in its evaluation, but it possesses some important advantages. Firstly, there is no likelihood of overflow errors in the calculations which is of great importance for wave function calculation in classically forbidden regions. Secondly, the transformation does not require an approximate determination of the first non-boundary point $\boldsymbol{\Psi}_1$ to maintain $O(h^5)$ global accuracy [138] if the initial value for $\boldsymbol{R}_0^{-1}$ is known from the boundary conditions. For zero valued boundary conditions, as is usually the case for calculation of wave functions, then $\boldsymbol{R}_0^{-1} = \boldsymbol{F}_0\boldsymbol{F}_1^{-1} = \mathbf{0}$.

In order to find the energies of bound levels, a scan over energy E is performed and equation (C.6) is used to integrate outwards to some maximum point x_N for each value of E. As the energy is scanned, nodes in the wave function appear at locations x_n, and are detected by the condition $|\boldsymbol{R}_n| < 0$ at these points. The only exception occurs for multiple nodes that exist at the same grid point. To detect these, the LU decomposition of $\boldsymbol{R}_n$ must be performed and the presence of negatives on the diagonal of U indicates the existence of nodes. Although this technique to count multiple nodes is unproven to work in all cases [121], no problems were observed for the calculations in this thesis. The exact binding energies of the bound levels are isolated by observing when the total node count is incremented as the energy is scanned. A bisection method is used to place upper and lower bounds on the binding energy to the accuracy required.

To calculate the wave function for a bound level or a scattering solution, repeated application of $\boldsymbol{R}_n^{-1}$ from equation (C.5) may be used to 'rewind' the wave function from a known value at a point x_N. This gives

$$\boldsymbol{\Psi}_n = (1 - \boldsymbol{T}_n)^{-1}\boldsymbol{F}_n = (1 - \boldsymbol{T}_n)^{-1}\left(\prod_{i=n}^{N}\boldsymbol{R}_i^{-1}\right)(1 - \boldsymbol{T}_N)\boldsymbol{\Psi}_N. \tag{C.7}$$

However, the outwards integration of (C.6) cannot be used alone to calculate bound wave functions because as it is difficult to accurately match to the decreasing exponential solutions at the outer boundary. Instead, one must integrate outwards from the inner boundary and inwards from the outer boundary to a matching point, x_m, at which the integrations can be appropriately joined. The inwards integration is similar in form to (C.6):

$$\bar{\boldsymbol{R}}_n = \boldsymbol{U}_n - \bar{\boldsymbol{R}}_{n+1}^{-1} \tag{C.8}$$

where $\bar{\boldsymbol{R}}_n = \boldsymbol{F}_{n-1}\boldsymbol{F}_n^{-1}$. The outer boundary condition for bound levels is $\bar{\boldsymbol{R}}_N^{-1} = \mathbf{0}$ which is analogous to the inner boundary condition. To match the inwards and outwards solutions, it is sufficient that the solutions must equal one another at two adjacent grid points. This can be shown [121] to require

$$(\boldsymbol{R}_m - \bar{\boldsymbol{R}}_{m+1}^{-1})\boldsymbol{f}(x_m) = 0 \tag{C.9}$$

where $\boldsymbol{f}(x_m) = (1 - \boldsymbol{T}_n)\boldsymbol{\psi}(x_m)$ and $\boldsymbol{\psi}(x_m)$ is the solution vector at the matching point. The desired solution is the eigenvector of the matrix $\boldsymbol{R}_m - \bar{\boldsymbol{R}}_{m+1}^{-1}$ that corresponds to an eigenvalue of zero. The goodness of match may be judged by calculating a few additional outward steps of the integration beyond the match point, so that the derivative $\boldsymbol{\psi}'(x_{m+1/2})$ may be calculated from both the inward and outward integrations. The agreement between the derivatives then gives a clear indication of the accuracy of the matching. Once the solution vector at the matching point, $\boldsymbol{\psi}(x_m)$, has been calculated from C.9, the entire solution may be generated via repeated application of the inverse ratio matrix in a similar fashion to (C.7): $\boldsymbol{F}_n = \boldsymbol{R}_n^{-1}\boldsymbol{R}_{n+1}^{-1}\ldots\boldsymbol{R}_{m-1}^{-1}\boldsymbol{F}_m$ for $n < m$ and $\boldsymbol{F}_n = \bar{\boldsymbol{R}}_n^{-1}\bar{\boldsymbol{R}}_{n-1}^{-1}\ldots\bar{\boldsymbol{R}}_{m+1}^{-1}\boldsymbol{F}_m$ for $n > m$.

C.2 RESONANCES

When searching for resonances in the coupled differential equations (C.1), open channels that represent the predissociation channels must possess proper outgoing boundary conditions. To determine the boundary condition upon the ratio matrix $\bar{\boldsymbol{R}}_N^{-1} = \boldsymbol{F}_N\boldsymbol{F}_{N-1}^{-1}$, the channels are assumed to be decoupled and hence the solution matrix $\boldsymbol{\Psi}(x \to \infty)$ may be written as a diagonal matrix $\Psi_{ij}(x) = \Psi_i(x)\delta_{ij}$. In this form it is simple to apply the appropriate boundary conditions by imposing conditions

$$\begin{aligned}\Psi_i(x_N) &= 0\\ \Psi_i(x_{N-1}) &= 1\end{aligned}$$

for closed channels, and conditions

$$\begin{aligned}\Psi_i(x_N) &= e^{ik_i x_N}\\ \Psi_i(x_{N-1}) &= e^{ik_i x_{N-1}}\end{aligned}$$

for open channels, where $k_i = \sqrt{Q_{ii}(x \to \infty)}$. These conditions mean that

$$(\boldsymbol{R}_N^{-1})_{ij} = \delta_{ij}\begin{cases} e^{ik_i h} & \text{for open channels}\\ 0 & \text{for closed channels.}\end{cases} \tag{C.10}$$

The energies of resonances are complex, the imaginary part of which is the decay width of the resonance. The bisection method based on counting nodes that was used to isolate bound levels cannot be used for resonances as a two dimensional search in the complex plane is required. The resonances exist at energies that satisfy equation C.9 which gives the condition $D(E) = |\boldsymbol{R}_m - \bar{\boldsymbol{R}}_{m+1}^{-1}|$ is zero. A gradient descent method can be used in the complex plane to find the zeros of $D(E)$. The starting energy for the descent, E_0, must be carefully chosen as the method will only converge to one final minimum for each choice of E_0. To produce many starting points to scan the complex plane, the equations were initially solved for artificial box states. The box states are the bound levels that result from treating all channels as closed, effectively discretising the continuum. The energies of these box states were trialled as starting energies for the descent method in the true system, however the results were not satisfactory as many known resonances were not identified.

An alternative procedure to search for the resonances was formulated that is similar to the bisection method of the node counting procedure for bound levels. The procedure first isolates regions that are known to contain an allowed solution, by using Cauchy's argument principle, which states a contour integral of $f'(z)/f(z)$, where $f(z)$ is a meromorphic function, will give

$$\frac{1}{2\pi i}\oint_C \frac{f'(z)}{f(z)}dz = N - P \tag{C.11}$$

where N is the number of zeros and P is the number of poles in the region bounded by the contour C, each zero or pole being counted as many times as its multiplicity. If the function $D(E)$ is assumed to be meromorphic and the contours chosen so that only a single zero or pole lies within each, then the contours place bounds upon the location of resonances. By using box shaped contours, with sides that have either a constant real or imaginary component, convergence to the exact location of the zeros may be obtained by repeated bisection of the dimensions of the box. Because the number of function evaluations of $D(E)$ required in this approach is very large, and each evaluation requires the complete outwards and inwards integration of the differential equations, it is best to use the argument principle only to isolate the local region of each resonance and then narrow the search with the gradient descent method to calculate the exact energy of the resonance.

C.3 APPLICATION TO REGIONS OF DIFFERENT STEP SIZE

Because the Numerov method uses a fixed size grid and the differential equations vary more rapidly for different ranges of interatomic distance, a multi-region procedure was developed that allows for different grid step sizes within each region. Each region is integrated using the appropriate equation (C.6) or (C.8), however only the innermost and outermost regions have a well defined value of $\boldsymbol{R}_0^{-1}$ or $\bar{\boldsymbol{R}}_N^{-1}$. At the connection between two adjacent regions, the ratio matrix $\boldsymbol{R}_c^{-1}$ exists for both regions but it has *different* values in each region because each region has a different value of h. The value of $\boldsymbol{R}_c^{-1}$ that must be found at the start of a new region can be calculated from the derivative term $\boldsymbol{\Psi}'(x_c)$ by predicting $\boldsymbol{\Psi}(x_{c+1})$ using the accurate $O(h^5)$ formula of Gonzalez and Thompson [138], adapted to multichannel calculations

$$\begin{aligned}\boldsymbol{\Psi}(x_{c+1}) = {} & \left[\boldsymbol{I} - 3\boldsymbol{T}_{c+1} + 8\boldsymbol{T}_{c+2}\boldsymbol{T}_{c+1}\right]^{-1} \\ & \times \left[\left(\boldsymbol{I} - \frac{1}{2}\boldsymbol{T}_{c+2}\right)\boldsymbol{\Psi}(x_c) + h\left(\boldsymbol{I} - \boldsymbol{T}_{c+2}\right)\boldsymbol{\Psi}'(x_c) + (\frac{7}{2}\boldsymbol{I} - 4\boldsymbol{T}_{c+2})\boldsymbol{T}_c\boldsymbol{\Psi}(x_c)\right].\end{aligned} \tag{C.12}$$

This formula preserves the global $O(h^5)$ accuracy of the solution. With the derivative found, it is simple to calculate $\boldsymbol{R}_c^{-1}$ in the next region and proceed with the integration as usual. Problems may occur in the node counting procedure when a node is in the vicinity of the border between regions as the procedure of matching between the regions may cause a node to be missed. If this is the case, the numerical routine will back away from the connecting point by finding a value x_{c-n} for which there are no nodes in the nearby vicinity and then applies the matching as normal.

The greatest advantage of the renormalised Numerov method is that it may be used to integrate the differential equations to any accuracy required without memory constraints. This is possible because only the previous value $\boldsymbol{R}_n$ is required to calculate the next value $\boldsymbol{R}_{n+1}$. If only every kth value of n is required to analyse the solutions, the $\boldsymbol{R}_n$ matrices can be stored as the combined product $\boldsymbol{R}_{n+k-1} \dots \boldsymbol{R}_n$. This is permitted because the relationship between points $\boldsymbol{F}_n$ and $\boldsymbol{F}_{n+k}$ is simply $\boldsymbol{F}_{n+k} = \boldsymbol{R}_{n+k-1} \dots \boldsymbol{R}_{n+1}\boldsymbol{R}_n\boldsymbol{F}_n$. The $\boldsymbol{R}_n^{-1}$ matrices may also be stored in a similar manner. These stored matrices produce the accuracy of a calculation at a stepsize of h, but on a coarse grid of hk.

Appendix D

Discrete Variable Representation (DVR) method

D.1 INTRODUCTION

The DVR method is a matrix method for solution of coupled ordinary differential equations that allows a solution to be expanded in terms of a functional basis upon a set of discrete grid points. Numerous DVR bases can be employed to enforce a variety of boundary conditions and each basis represents the solution in a different form. Any functional basis may be used, provided it satisfies the constraints described in this section. For atomic and molecular physics, two useful bases are the Fourier sine and cosine bases as these can be used to represent solutions of wave functions to a high degree of accuracy. Because the method creates a set of matrix equations, the numerical implementation is relatively straightforward. The only disadvantage of the DVR method is the large memory usage required. Because the DVR consists of large non-sparse matrices, it cannot be broken into smaller subproblems that may be more easily calculated within the constraints of the physical computer system.

An alternative mapped grid method developed by Willner *et al* [139] that is suited to near-dissociation calculations was brought to the author's attention after implementation of the DVR method. The mapped grid method uses a sophisticated technique to distribute grid points based on the local values of the de Broglie wavelength. Use of these grids allow a much smaller set of points to be used and hence permit calculations to a higher degree of accuracy. The accuracy of the DVR method, however, is more than sufficient for the calculations performed in this thesis.

In the DVR description, a set of Lagrange functions $\{f_i\}$ and a set of N discrete grid points $\{x_n\}$ over the range $a \leq x \leq b$ are used to express a set of coupled differential equations of the form

$$\sum_{\alpha} \left[\frac{d^2}{dx^2}\delta_{\beta\alpha} - E\delta_{\beta\alpha} + V_{\beta\alpha}(x) \right] \psi_{\alpha}(x) = h_{\beta}(x), \tag{D.1}$$

where $h(x)$ represents an optional inhomogeneity and α, β enumerate the channels of the problem, as the matrix form

$$\sum_j A_{ij}\Psi_j = H_i. \tag{D.2}$$

The Lagrange functions must satisfy two conditions:

$$f_i(x_j) = \delta_{ij} \tag{D.3}$$

and

$$\int_a^b f_i^*(x) f_j(x) dx = \lambda_i \delta_{ij}, \tag{D.4}$$

where λ_i is a real valued constant. Condition (D.3) allows any wave function $\Psi(x)$ to be expanded in these Lagrange functions and be exact upon the N discrete points x_i:

$$\Psi(x) = \sum_{i=1}^{N} \Psi(x_i) f_i(x). \tag{D.5}$$

The constants λ_i are chosen to represent the weights of a Gaussian quadrature on the points x_i, such that, for any function $F(x)$,

$$\int_a^b F(x) dx \approx \sum_{i=1}^{N} \lambda_i F(x_i). \tag{D.6}$$

This choice is well suited to calculating scalar products of wave functions expanded in the form (D.5). For example,

$$\begin{aligned} \int_a^b \Phi^*(x)\Psi(x) dx &= \sum_{ij} \Phi^*(x_i)\Psi(x_j) \int_a^b f_i^*(x) f_j(x) dx \\ &= \sum_i \Phi^*(x_i)\Psi(x_i)\lambda_i. \end{aligned} \tag{D.7}$$

The choice of Lagrange functions to most accurately approximate the solutions is an important one. The Lagrange functions can be related to a set of N orthonormal basis functions $\{\phi_k\}$ that satisfy the discrete orthonormality condition

$$\int_a^b \phi_k^*(x)\phi_l(x) dx = \delta_{kl} = \sum_i \lambda_i \phi_k^*(x_i)\phi_l(x_i) \tag{D.8}$$

by forming the linear combinations

$$f_i(x) = \sum_{k=1}^{N} c_{ki}\phi_k(x). \tag{D.9}$$

Inverting (D.9) using (D.8) gives

$$\phi_k(x) = \sum_i \frac{1}{\lambda_i} c_{ki}^* f_i(x). \tag{D.10}$$

Comparison of equation (D.10) with equation (D.5) shows that $c_{ki} = \lambda_i \phi_k^*(x_i)$. Furthermore, the functions (D.9) can only satisfy equation (D.4) if $\boldsymbol{\Lambda}^0 = \boldsymbol{C}^*\boldsymbol{C}$ where the matrix $\boldsymbol{C}$ has elements c_{ki} and $\boldsymbol{\Lambda}^0_{ki} = \delta_{ki}\lambda_i$. This relationship defines λ_i via the discrete closure relationship:

$$\lambda_i^{-1}\delta_{ij} = \sum_{k=1}^{N} \phi_k^*(x_i)\phi_k(x_j). \tag{D.11}$$

The quadrature points of x_i for polynomial bases ϕ_k are given by the zeros of first truncated basis function. That is, if $k = 1, \ldots, N$ for the truncated orthonormal basis set, then the N zeros of $\phi_{N+1}(x)$ are the quadrature points x_i.

D.2 CONVERSION OF DIFFERENTIAL EQUATIONS TO MATRIX EQUATIONS

Once a basis has been chosen, the differential equations (D.1) may be converted into a matrix equation by expanding the wave functions and the inhomogeneity, if present, in the form (D.5):

$$\sum_{i=1}^{N}\sum_{\alpha}\left[\frac{d^2}{dx^2}\delta_{\beta\alpha} - E\delta_{\beta\alpha} + V_{\beta\alpha}(x)\right] f_i(x)\psi_\alpha(x_i) = \sum_{j=1}^{N} h_\beta(x_j) f_j(x). \tag{D.12}$$

Forming an inner product with $f_{i'}(x)$ gives

$$\int_a^b f_{i'}^*(x)\sum_{i=1}^{N}\sum_{\alpha}\left[\frac{d^2}{dx^2}\delta_{\beta\alpha} - E\delta_{\beta\alpha} + V_{\beta\alpha}(x)\right] f_i(x)\psi_\alpha(x_i) = \int_a^b \sum_{j=1}^{N} h_\beta(x_j) f_{i'}^*(x) f_j(x), \tag{D.13}$$

and making use of (D.4) gives:

$$\sum_{i=1}^{N}\sum_{a'}\left[\int_a^b f_{i'}^*(x)\frac{d^2}{dx^2} f_i(x)\delta_{\beta\alpha} - E\lambda_{i'}\delta_{ii'}\delta_{\beta\alpha} + \int_a^b V_{\beta\alpha}(x) f_{i'}^*(x) f_i(x)\right]\psi_\alpha(x_i) = \lambda_{i'} h_\beta(x_{i'}). \tag{D.14}$$

If the term involving the potential $V_{a'a}(x)$ is assumed to be well described by a linear expansion of the basis functions ϕ_k then Gaussian quadrature may be used to simplify the integral

$$\begin{aligned}\int_a^b V_{\beta\alpha}(x) f_{i'}^*(x) f_i(x) &\approx \sum_n \lambda_n V_{\beta\alpha}(x_n) f_{i'}^*(x_n) f_i(x_n)\\ &= \lambda_{i'} V_{\beta\alpha}(x_i)\delta_{ii'}\end{aligned} \tag{D.15}$$

where $f_i(x_n) = \delta_{in}$ has been used. Additionally, the derivative term can be written

$$\begin{aligned} T_{i'i} &= \frac{1}{\lambda_{i'}} \int_a^b f_{i'}^*(x) \frac{d^2}{dx^2} f_i(x) dx \\ &= \frac{1}{\lambda_{i'}} \sum_n \lambda_n f_{i'}^*(x_n) \frac{d^2 f_i}{dx^2}(x_n) \\ &= \frac{d^2 f_i}{dx^2}(x_{i'}) \end{aligned} \tag{D.16}$$

This is exact for polynomial bases as $d^2 f_i/dx^2$ can be represented by a linear combination of the set of $f_i(x)$ functions. By using (D.15) and (D.16), equation (D.14) may be rewritten as

$$\sum_{i=1}^{N} \sum_{\alpha} \left[T_{i'i}\delta_{\beta\alpha} - E\delta_{ii'}\delta_{\beta\alpha} + V_{\beta\alpha}(x_i)\delta_{ii'} \right] \psi_\alpha(x_i) = h_\beta(x_{i'}) \tag{D.17}$$

which can also be expressed in matrix form

$$\left(\boldsymbol{T} - \boldsymbol{E}^0 + \boldsymbol{V}^B \right) \boldsymbol{\Psi} = \boldsymbol{H} \tag{D.18}$$

where the matrices are in a block structure with indices, $\gamma = \alpha N + i$ and $\gamma' = \beta N + i'$

$$\boldsymbol{T}_{\gamma'\gamma} = T_{i'i}\, \delta_{\beta\alpha}, \tag{D.19}$$

$$\boldsymbol{E}^0_{\gamma'\gamma} = E\delta_{ii'}\, \delta_{\beta\alpha}, \tag{D.20}$$

$$\boldsymbol{V}^B_{\gamma'\gamma} = \delta_{ii'}\, V_{\beta\alpha}(x_i), \tag{D.21}$$

$$\boldsymbol{\Psi}_\gamma = \psi_\alpha(x_i) \tag{D.22}$$

and

$$\boldsymbol{H}_{\gamma'} = h_\beta(x_{i'}). \tag{D.23}$$

The only unevaluated portion of this matrix equation is the differential term, $\boldsymbol{T}$, which can be calculated analytically in most cases without prior knowledge of the potential or inhomogeneity. If no inhomogeneity is present, then (D.18) represents an eigenvalue problem, which may be solved with any standard numerical package to determine the allowed energies of the system. If the inhomogeneity is present, then the system may be solved in a standard fashion to determine the solutions $\psi_\alpha(x)$.

D.3 FOURIER SINE DVR BASIS

The choice of basis $\phi_k(x)$ determines the boundary conditions that are placed upon the differential equations. The Fourier sine basis that is orthogonal on the range $a \le x \le b$ has zero value boundary conditions and is defined by

$$\phi_k(x) = \sqrt{\frac{2}{b-a}} \sin \frac{k\pi(x-a)}{(b-a)} \tag{D.24}$$

where $k = \{1, \ldots, N\}$. The basis is associated with a set of N quadrature weights λ_i and N equidistant quadrature grid points $x_i = a + i\Delta x$ where $\Delta x = (b-a)/(N+1)$. From equation (D.11) the quadrature weights may be calculated as follows

$$\begin{aligned}\lambda_i^{-1} &= \frac{2}{b-a}\sum_{k=1}^{N}\sin^2\frac{k\pi(x_i-a)}{(b-a)} \\ &= \frac{2}{b-a}\sum_{k=1}^{N}\sin^2\frac{k\pi i}{N+1} \\ &= \frac{1}{b-a}\sum_{k=1}^{N}\left[1-\cos\frac{2i\pi k}{N+1}\right].\end{aligned} \tag{D.25}$$

The sum over the cosine terms may be replaced by the real part of a summation over the complex variable $z^k = \cos k\theta + i\sin k\theta$. Because,

$$\begin{aligned}\sum_{k=1}^{N} z^k &= \frac{z-z^{N+1}}{1-z} \\ &= \frac{(z-z^{N+1})(1-z^*)}{(1-z)(1-z^*)} \\ &= \frac{z-1-z^{N+1}+z^{N+1}z^*}{2(1-\cos k\theta)},\end{aligned} \tag{D.26}$$

then the real part, after substitution of $\theta = n\pi/(N+1)$, becomes

$$\cos\frac{kn\pi}{N+1} = \mathfrak{Re}\{\sum_{k=1}^{N} z^k\} = \frac{\cos\frac{n\pi}{N+1} - 1 - \cos n\pi + \cos\frac{n\pi}{N+1}\cos n\pi + \sin\frac{n\pi}{N+1}\sin n\pi}{2(1-\cos\frac{n\pi}{N+1})} \tag{D.27}$$

$$\begin{aligned} &= \frac{-(1-\cos\frac{n\pi}{N+1})(1+\cos n\pi)}{2(1-\cos\frac{n\pi}{N+1})} \\ &= -\frac{[1+(-1)^n]}{2} \\ &= \begin{cases} -1 & n \text{ even} \\ 0 & n \text{ odd} \end{cases}.\end{aligned} \tag{D.28}$$

Substituting this result back into (D.25), where $n = 2i$, gives the result

$$\lambda_i = \frac{b-a}{N+1}. \tag{D.29}$$

Using these weights, the discrete orthonormality condition (D.8) is satisfied for the Fourier sine basis. To see this, consider

$$\begin{aligned}\int_a^b \phi_k^*(x)\phi_l(x)dx &= \sum_{i=1}^N \lambda_i \phi_k^*(x_i)\phi_l(x_i)\\ &= \frac{2}{N+1}\sum_{i=1}^N \sin\frac{k\pi(x_i-a)}{b-a}\sin\frac{l\pi(x_i-a)}{b-a}\\ &= \frac{2}{N+1}\sum_{i=1}^N \sin\frac{k\pi i}{N+1}\sin\frac{l\pi i}{N+1}\\ &= \frac{1}{N+1}\sum_{i=1}^N \cos\frac{(k-l)\pi i}{N+1} - \cos\frac{(k+l)\pi i}{N+1}. \qquad \text{(D.30)}\end{aligned}$$

Since $k-l$ and $k+l$ possess the same odd/even parity, equation (D.28) shows that each term of the summation is zero for $k \neq l$. In the case of $k = l$,

$$\sum_{i=1}^N \lambda_i \phi_k^*(x_i)\phi_k(x_i) = \frac{1}{N+1}\left[\left(\sum_{i=1}^N 1\right) - (-1)^{2k}\right] = 1 \qquad \text{(D.31)}$$

which leads to the desired result:

$$\int_a^b \phi_k^*(x)\phi_l^*(x)dx = \sum_{i=1}^N \lambda_i \phi_k^*(x_i)\phi_l(x_i) = \delta_{kl}. \qquad \text{(D.32)}$$

For the basis to produce the correct Lagrange functions that satisfy conditions (D.3) and (D.4), the functions must also satisfy the discrete closure condition (D.11):

$$\begin{aligned}\sum_{k=1}^N \phi_k^*(x_i)\phi_k(x_j) &= \frac{2}{b-a}\sum_{k=1}^N \sin\frac{k\pi(x_i-a)}{(b-a)}\sin\frac{k\pi(x_j-a)}{(b-a)}\\ &= \frac{2}{b-a}\sum_{k=1}^N \sin\frac{k\pi i}{N+1}\sin\frac{k\pi j}{N+1}\\ &= \frac{1}{b-a}\sum_{k=1}^N \left[\cos\frac{(i-j)k\pi}{N+1} - \cos\frac{(i+j)k\pi}{N+1}\right]. \qquad \text{(D.33)}\end{aligned}$$

This simplifies upon using (D.28) in an analogous manner to (D.30), to give the desired result

$$\begin{aligned}\sum_{k=0}^{N-1} \phi_k^*(x_i)\phi_k(x_j) &= \frac{N+1}{b-a}\delta_{ij}\\ &= \lambda_{ij}^{-1}\delta_{ij}. \qquad \text{(D.34)}\end{aligned}$$

Having proved that the Fourier sine basis successfully implements a DVR basis, the derivative matrix $\boldsymbol{T}$ given by (D.16) must be determined. Noting that

$$\frac{d^2}{dx^2}\phi_l(x) = -\frac{l^2\pi^2}{(b-a)^2}\phi_l(x) \tag{D.35}$$

then

$$\begin{aligned} T_{ji} &= \frac{b-a}{N+1}\int_a^b \sum_{kl}\phi_k(x_j)\phi_k^*(x)\frac{d^2}{dx^2}\phi_l^*(x_i)\phi_l(x)dx \\ &= -\frac{\pi^2}{(N+1)(b-a)^2}\sum_{kl} l^2\phi_k(x_j)\phi_l^*(x_i)\int_a^b \phi_k^*(x)\phi_l(x)dx \\ &= -\frac{\pi^2}{(N+1)(b-a)^2}\sum_{k=1}^{N} k^2\left[\cos\frac{(i-j)\pi k}{N+1} - \cos\frac{(i+j)\pi k}{N+1}\right]. \end{aligned} \tag{D.36}$$

The summations can be rewritten by considering the real part of another summation

$$\begin{aligned} \sum_{k=1}^{N} k^2\cos\frac{n\pi k}{N+1} &= -\frac{(N+1)^2}{\pi^2}\frac{d^2}{dn^2}\mathfrak{Re}\{\sum_{k=1}^{N}\exp i\frac{k\pi n}{(N+1)}\} \\ &= -\frac{(N+1)^2}{\pi^2}\frac{d^2}{dn^2}\mathfrak{Re}\{\sum_{k=1}^{N} z^k\}, \end{aligned} \tag{D.37}$$

where $n = i \pm j$. After differentiating (D.27), this gives

$$\sum_{k=1}^{N} k^2\cos\frac{n\pi k}{N+1} = -\frac{(N+1)(-1)^n}{2}\left[(N+1) - \csc^2\frac{n\pi}{2(N+1)}\right]. \tag{D.38}$$

If $i \neq j$ then the complete term is

$$T_{ji} = -\frac{\pi^2(-1)^{i+j}}{2(b-a)^2}\left[\csc^2\frac{(i-j)\pi}{2(N+1)} - \csc^2\frac{(i+j)\pi}{2(N+1)}\right]. \tag{D.39}$$

On the other hand, if $i = j$ then the first cosine term of (D.36) becomes a sum of squares and gives

$$\begin{aligned} T_{ii} &= -\frac{\pi^2}{(N+1)(b-a)^2}\left[\frac{1}{6}N(N+1)(2N+1) + \frac{1}{2}(N+1)^2 - \frac{1}{2}(N+1)\csc^2\frac{i\pi}{N+1}\right] \\ &= -\frac{\pi^2}{2(b-a)^2}\left[\frac{1}{3}(2(N+1)^2+1) - \csc^2\frac{i\pi}{N+1}\right]. \end{aligned} \tag{D.40}$$

Consequently the complete matrix can be written as

$$T_{ji} = -\frac{\pi^2(-1)^{i+j}}{2(b-a)^2}\begin{cases} \frac{1}{3}(2(N+1)^2+1) - \csc^2\frac{i\pi}{N+1} & \text{if } i = j \\ \csc^2\frac{(i-j)\pi}{2(N+1)} - \csc^2\frac{(i+j)\pi}{2(N+1)} & \text{if } i \neq j. \end{cases} \tag{D.41}$$

D.4 FOURIER COSINE DVR BASIS

The Fourier cosine DVR basis, first investigated by Karabulut and Sibert [140], has the form

$$\phi_k(x) = \begin{cases} \frac{1}{\sqrt{b-a}} & \text{for } k=0 \\ \sqrt{\frac{2}{b-a}} \cos \frac{k\pi(x-a)}{(b-a)} & \text{otherwise} \end{cases} \tag{D.42}$$

where $k = \{0, \ldots, N-1\}$. The boundary conditions enforced by this basis are of zero derivative and the N equidistant quadrature grid points associated with the basis are $x_i = a + (i - \frac{1}{2})\Delta x$ where $\Delta x = (b-a)/N$. The quadrature weights, calculated from (D.11), are

$$\begin{aligned} \lambda_i^{-1} &= \frac{1}{b-a} + \frac{2}{b-a} \sum_{k=1}^{N-1} \cos^2 \frac{k\pi(x_i - a)}{(b-a)} \\ &= \frac{1}{b-a} + \frac{2}{b-a} \sum_{k=1}^{N-1} \cos^2 \frac{k\pi(i-\frac{1}{2})}{N} \\ &= \frac{1}{b-a} \left(1 + \sum_{k=1}^{N-1} \left[1 - \cos \frac{(2i-1)\pi k}{N} \right] \right). \end{aligned} \tag{D.43}$$

Using equation (D.28), this simplifies to

$$\lambda_i^{-1} = \frac{1}{b-a} N. \tag{D.44}$$

These weights allow the the Fourier cosine basis to satisfy the discrete orthonormality condition (D.8). Consider

$$\begin{aligned} \int_a^b \phi_k^*(x)\phi_l(x) dx &= \sum_{i=1}^{N} \lambda_i \phi_k^*(x_i)\phi_l(x_i) \\ &= \frac{2}{N} \sum_{i=1}^{N} \cos \frac{k\pi(x_i - a)}{b-a} \cos \frac{l\pi(x_i-a)}{b-a} \\ &= \frac{1}{N} \sum_{i=1}^{N} \cos \frac{(k-l)\pi(i-\frac{1}{2})}{N} + \cos \frac{(k+l)\pi(i-\frac{1}{2})}{N}. \end{aligned} \tag{D.45}$$

The summation over half integer cosines may be evaluated in a similar manner to (D.27) by considering a complex variable $z = \exp(i\theta)$, where $\theta = n\pi/2N$, and the series

$$\begin{aligned} \sum_{i=1}^{N} z^{2i-1} &= \frac{z - z^{2N+1}}{1-z^2} \\ &= \frac{z - z^* - z^{2N}(z - z^*)}{2 - z^2 - (z^*)^2} \\ &= \frac{z - \bar{z} - z^{2N}(z - z^*)}{2(1 - \cos^2\theta + \sin^2\theta)}. \end{aligned} \tag{D.46}$$

Taking the real part of the series gives

$$\begin{aligned}\mathfrak{Re}\{\sum_{i=1}^{N} z^{2i-1}\} &= \frac{\sin 2N\theta \sin\theta}{2(1-\cos^2\theta+\sin^2\theta)} \\ &= \frac{\sin n\pi \sin\frac{n\pi}{2N}}{2(1-\cos^2\theta+\sin^2\theta)} \\ &= 0. \end{aligned} \tag{D.47}$$

This means that equation (D.45) is zero for $k \neq l$. For $k = l$ only the first term contributes and gives the desired result:

$$\sum_{i=1}^{N} \lambda_i \phi_k^*(x_i)\phi_l(x_i) = \delta_{kl}. \tag{D.48}$$

To satisfy conditions (D.3) and (D.4) the discrete closure relationship (D.11) must be satisfied:

$$\begin{aligned}\sum_{k=0}^{N-1} \lambda_i \phi_k^*(x_i)\phi_k(x_j) &= \frac{1}{N} + \frac{2}{N}\sum_{k=1}^{N-1} \cos\frac{k\pi(x_i-a)}{b-a}\cos\frac{k\pi(x_j-a)}{b-a} \\ &= \frac{1}{N}\left[1 + \sum_{k=1}^{N-1} \cos\frac{k\pi(i-j)}{N} + \cos\frac{k\pi(i+j-1)}{N}\right]. \end{aligned} \tag{D.49}$$

Making use of (D.28) in the $i \neq j$ case, allows the reduction of the RHS of (D.49) to

$$\frac{1}{N}\left[1 + -1\right] = 0 \tag{D.50}$$

as either $i-j$ or $i+j-1$ will be even but not both. For $i = j$ the second term has $i+j-1$ odd and so

$$\sum_{k=0}^{N-1} \lambda_i \phi_k^*(x_i)\phi_k(x_j) = \delta_{ij} \tag{D.51}$$

as desired.

To calculate the derivative term in the cosine basis the relationship

$$\frac{d^2}{dR^2}\phi_l(x) = -\frac{l^2\pi^2}{(b-a)^2}\phi_l(x)(1-\delta_{l0}) \tag{D.52}$$

is used to solve for the derivative matrix:

$$\begin{aligned} T_{ji} &= \frac{b-a}{N}\int_a^b \sum_{k=0}^{N-1}\sum_{l=0}^{N-1} \phi_k(x_j)\phi_k^*(x)\frac{d^2}{dR^2}\phi_l^*(x_i)\phi_l(x)dx \\ &= -\frac{2\pi^2}{N(b-a)^2}\sum_{k=1}^{N-1} k^2 \cos\frac{k\pi(j-\frac{1}{2})}{N}\cos\frac{k\pi(i-\frac{1}{2})}{N} \\ &= -\frac{\pi^2}{N(b-a)^2}\sum_{k=1}^{N-1} k^2\left[\cos\frac{k\pi(i-j)}{N} + \cos\frac{k\pi(i+j-1)}{N}\right]. \end{aligned} \tag{D.53}$$

Using equation (D.38) this can be reduced for $i \neq j$ to

$$T_{ji} = -\frac{\pi^2(-1)^{i+j}}{2(b-a)^2}\left[\csc^2\frac{(i-j)\pi}{2N} - \csc^2\frac{(i+j-1)\pi}{2N}\right] \tag{D.54}$$

whereas for $i = j$, it reduces to

$$\begin{aligned} T_{ii} &= -\frac{\pi^2}{N(b-a)^2}\left[\frac{1}{6}(N-1)N(2N-1) + \frac{N^2}{2} - \frac{N}{2}\csc^2\frac{(2i-1)\pi}{2N}\right] \\ &= -\frac{\pi^2}{2(b-a)^2}\left[\frac{1}{3}(2N^2+1) - \csc^2\frac{(2i-1)\pi}{2N}\right]. \end{aligned} \tag{D.55}$$

The complete matrix is therefore

$$T_{ji} = \frac{\pi^2(-1)^{i+j}}{2(b-a)^2}\begin{cases} \frac{1}{3}(2N^2+1) - \csc^2\frac{(2i-1)\pi}{2N} & \text{for } i = j \\ \csc^2\frac{(i-j)\pi}{2N} - \csc^2\frac{(i+j-1)\pi}{2N} & \text{for } i \neq j \end{cases}. \tag{D.56}$$

D.5 SCALED GRID

The Fourier sine and cosine DVR bases are associated with a linearly spaced grid. For the helium system under investigation it is preferable to place many grid points at short interatomic distances. Unfortunately, attempting this with a linearly spaced grid will also require many unnecessary points at large interatomic distances. To handle this issue in a more elegant manner, a scaling may be applied to the variable x such that the DVR grid is mapped onto a non-linear mesh grid [100]. The scaling must be treated correctly however, so that the boundary conditions are not affected.

If the scaling is defined by $x = \chi(t)$ where $t_{\min} < t < t_{\max}$ such that $a = \chi(t_{\min})$ and $b = \chi(t_{\max})$ then the change of variable in the derivative term is

$$\begin{aligned} \frac{d^2}{dx^2} &= g^2\frac{d}{dt}g^2\frac{d}{dt} \\ &= g^3(2\frac{dg}{dt}\frac{d}{dt} + g\frac{d^2}{dt^2}) \\ &= g^3(\frac{d^2}{dt^2}g - \frac{d^2g}{dt^2}) \end{aligned} \tag{D.57}$$

where $g = \sqrt{1/\chi'(t)}$ where $\chi'(t) = d\chi/dt$. Using this result in the expansion of the differential equation (D.1) gives

$$\sum_{\alpha}\Big(g^3(t)\frac{d^2}{dt^2}g(t)\delta_{\alpha'\alpha} - E\delta_{\alpha'\alpha} + \tilde{V}_{\alpha'\alpha}(t)\Big)\psi_\alpha(\chi(t)) = h_{\alpha'}(\chi(t))$$

where $\tilde{V}_{a'a}(t) = V_{a'a}(\chi(t)) + \delta_{a'a}g^3(t)g''(t)$. The required expansion in terms of the Lagrange functions occurs in a slightly different manner to (D.12) as the product $g(t)\psi_a(\chi(t))$ of the derivative term is expanded in terms of the Lagrange basis separately to the potential term:

$$\sum_{\alpha}\left[\left(\sum_{i} g^3(t)\frac{d^2}{dt^2}f_i(t)g(t_i)\psi_\alpha(x_i)\delta_{\alpha'\alpha}\right)+\left(\sum_{k}\left[-E\delta_{\alpha'\alpha}+\tilde{V}_{\alpha'\alpha}(t)\right]f_k(t)\psi_\alpha(x_k)\right)\right] = \sum_j h_{\alpha'}(x_j)f_j(x) \quad \text{(D.58)}$$

where $x_i = \chi(t_i)$. Like terms of $\psi_\alpha(x_i)$ can be collected between the two expansions so that the expression becomes

$$\sum_{i=1}^{N}\sum_{\alpha}\left[g^3(t)\frac{d^2}{dt^2}f_i(t)g(t_i)\delta_{\alpha'\alpha}+\left(-E\delta_{\alpha'\alpha}+\tilde{V}_{\alpha'\alpha}(t)\right)f_i(t)\right]\psi_\alpha(x_i) = \sum_j h_{\alpha'}(x_j)f_j(x) \quad \text{(D.59)}$$

and, after forming the inner product with $f_{i'}(t)$ as in equation (D.13), the result is

$$\sum_{i=1}^{N}\sum_{\alpha}\left(g^3(t_{i'})T_{i'i}g(t_i)\delta_{\alpha'\alpha}-E\delta_{\alpha'\alpha}+\tilde{V}_{\alpha'\alpha}(t_i)\delta_{ii'}\right)\psi_\alpha(\chi(t_i)) = h_{\alpha'}(\chi(t_i)). \quad \text{(D.60)}$$

In matrix form this is

$$\left(\tilde{\boldsymbol{T}}-\boldsymbol{E}^0+\tilde{\boldsymbol{V}}^B\right)\boldsymbol{\Psi} = \boldsymbol{H}, \quad \text{(D.61)}$$

where $(\tilde{\boldsymbol{T}})_{\gamma'\gamma} = g^3(t_{i'})T_{i'i}g(t_i)\delta_{\alpha'\alpha}$.

Because in (D.58) the product $g(t)\psi_\alpha(\chi(t))$ is expanded in the DVR basis, one must be careful that the boundary conditions on $\psi_\alpha(x)$ remain the same. If the sine Fourier basis is used, with zero value boundary conditions, then the desired conditions $\psi_\alpha(a) = \psi_\alpha(b) = 0$ can only be satisfied for $g(t_{\min})\psi_\alpha(a) = 0$ and $g(t_{\max})\psi_\alpha(b) = 0$ if $g(t) \neq 0$. This is always satisfied due to the definition of $g(t)$ and hence there are no problems with introducing a scaling to the sine Fourier basis. On the other hand, in the cosine Fourier basis the scaled boundary conditions give

$$\frac{d}{dt}\left[g(t)\psi_\alpha(\chi(t))\right]\Big|_{t_{\min}} = \frac{dg}{dt}(t_{\min})\psi_\alpha(a)+g(t_{\min})\frac{d\chi}{dt}(t_{\min})\frac{d\psi_\alpha}{dx}(a) = 0 \quad \text{(D.62)}$$

and similarly for $t_{\max}$. To satisfy the desired boundary conditions $d\psi_\alpha/dx = 0$ at $x = a, b$ requires the constraints $dg/dt = 0$ and $d\chi/dt \neq 0$ at the boundaries. The first constraint is satisfied if $d^2\chi/dt^2 = 0$ and so a monotonically increasing quartic was tried:

$$\chi(t) = c_4t^4 + c_3t^3 + c_2t^2 + c_1t + c_0 \quad \text{(D.63)}$$

where $t_{\min} = 0$ and $t_{\max} = 1$, and the constants are $c_0 = a$, $c_2 = 0$, $c_3 = 2(b - a - c_1)$, and $c_4 = -\frac{1}{2}c_3$. The value of c_1 can be any arbitrary positive value (c_1 cannot be zero because of the constraint $d\chi/dt \neq 0$) and influences the linearity of the scaling. A value of $c_1 = 10$ was chosen that places 53% of points within the first quartile, 22% within the second quartile and gave reasonable results for the integration. This use of the scaling reduces the required number of grid points by an order of magnitude.

Appendix E

Tabulation of results

This appendix presents more detailed tabulations of results obtained for the bound states and resonances of the $2s2p$ helium system. Listed below are the sections of the thesis relevant to each table:

Table E.1: Comparison between the single-channel results of Deguilhem *et al* [86] and the single-channel results calculated in section 3.2 for levels near the $j = 2$ asymptote.

Table E.2: Complete list of resonances near the $j = 1$ asymptote. This table lists the resonances found in section 3.3.4 and shown in table 3.8. The table here includes the calculated observability criteria that are defined in section 3.4.2.

Table E.3: As for table E.2 but for resonances near the $j = 0$ asymptote that are shown in table 3.9.

Table E.4: List of resonances, that are up to 2 GHz of detuning from the $j = 1$ asymptote and are predicted to be observable in an experiment using an ion detection mechanism. The resonances are found by the calculations presented in section 3.3.4 and satisfy the observability criteria that are defined in section 3.4.2.

Table E.1: Deguilhem *et al* [86] results compared with this work's single-channel results using potentials smoothly matched using equation (3.7). The large differences in the 0_u^+ series are commented upon in chapter 3. All values are in GHz detuning from the $j = 2$ asymptote.

$1_u, J = 1$		$1_u, J = 2$		$1_u, J = 3$		$2_u, J = 2$		$2_u, J = 4$		$3_g, J = 3$	
This work	[86]	This work	[86]	This work	[86]	This work	[86]	This work	[86]	This work	[86]
11.319	11.301	11.006	10.989	10.544	10.527	13.666	13.647	12.513	12.494	10.253	10.243
7.167	7.154	6.930	6.918	6.582	6.569	9.020	9.006	8.127	8.113	6.086	6.080
4.316	4.307	4.141	4.132	3.885	3.877	5.703	5.692	5.027	5.017	3.432	3.428
2.432	2.426	2.307	2.301	2.126	2.120	3.414	3.407	2.920	2.913	1.816	1.813
1.250	1.246	1.166	1.162	1.044	1.041	1.913	1.908	1.569	1.564	0.887	0.886
0.566	0.564	0.513	0.511	0.438	0.436	0.996	0.992	0.770	0.767		
0.216	0.215	0.187	0.186	0.146	0.145	0.478	0.476	0.339	0.338		
						0.208	0.207				
						0.079	0.079				
						0.025	0.025				

$0_u^+, J = 1$		$0_u^+, J = 3$		$0_g^+, J = 0$							
This work	[86]	This work	[86]	This work	[86]	This work	[86]	This work	[86]	This work	[86]
14.583	13.658	13.723	12.832	328865	329019	146839	146963	29134.0	29195.5	1306.02	1303.84
9.699	9.029	9.030	8.389	316676	316830	137864	137985	25152.1	25207.4	1036.99	1035.43
6.205	5.735	5.698	5.252	304672	304823	129100	129663	21574.4	21623.2	816.338	814.929
3.796	3.481	3.425	3.130	292852	293002	120553	120669	18397.9	18440.1	635.999	634.969
2.215	2.015	1.954	1.770	281216	281364	112229	112343	15610.6	15646.2	489.948	489.201
1.229	1.108	1.052	0.942	269763	269909	104136	104248	13190.8	13219.9	372.634	372.093
0.642	0.572	0.527	0.465	258493	258637	96283.6	96392.0	11108.3	11131.3	279.319	278.898
0.311	0.273	0.240	0.208	247406	247548	88679.2	88784.7	9327.25	9344.62	205.851	205.531
0.136	0.117	0.096	0.080	236503	236643	81334.3	80735.3	7810.11	7822.30	148.662	148.423
0.052	0.044	0.031	0.025	225783	225922	74260.3	74359.3	6520.57	6528.04	104.738	104.559
				215249	215385	67469.9	67565.1	5425.98	5429.21	71.5190	71.3779
				204900	205035	60976.7	61068.3	4498.05	4497.67	46.8564	46.7391
				194739	194872	54796.0	54883.3	3712.72	3709.75	28.9585	28.8703
				184768	184899	48943.2	49026.3	3049.57	3045.65	16.3890	16.3330
				174989	175119	43434.7	43512.8	2491.18	2487.39	8.01767	7.98018
				165406	165534	38287.1	38359.9	2022.71	2019.43	2.92504	2.90289
				156021	156147	33515.6	33583.1	1631.39	1628.59	0.33791	0.327973

Table E.2: Resonances that are present in the helium $2s\,^3S_1 + 2p\,^3P_j$ dimer within 600 MHz of detuning from the $j = 1$ asymptote. The detuning and predissociation width Γ_v^{pre} have been given in MHz. These resonances have been calculated without any modification of the short-range potentials. The columns 5–8 list the properties of the levels that may be used as observability criteria. $\mathcal{A}_v$ is the coupling strength of the level in E_h photoassociated from either a spin-polarised (spin) or unpolarised (unpolar) collision of metastable states. $f_{5,v}$ is the proportion of quintet character at short range ($R < 20\,a_0$) and $f_{R<20}$ is the proportion of the wave function at short range.

$j = 1$ asymptote							
J, w	Detuning	Γ_v^{pre}	Case (c)	$\mathcal{A}_v$spin	$\mathcal{A}_v$unpolar	$f_{5,v}$(%)	$f_{R<20}$
$J = 1,\ g$	-282.545	6.510	0_g^-	0.0	1.827	99.6	1×10^{-4}
	-164.426	0.259	1_g	0.0	2.615	78.3	6×10^{-5}
	-116.695	3.281	0_g^-	0.0	2.418	99.2	6×10^{-5}
	-62.573	1.156	1_g	0.0	1.172	78.8	2×10^{-4}
	-40.463	1.309	0_g^-	0.0	3.273	99.5	3×10^{-5}
	-27.739	0.057	1_g	0.0	3.358	78.4	1×10^{-5}
	-15.900	0.677	1_g	0.0	2.989	79.1	1×10^{-4}
	-9.978	0.471	0_g^-	0.0	3.786	97.6	1×10^{-5}
$J = 2,\ g$	-130.220	0.357	1_g	0.0	2.674	77.5	7×10^{-6}
	-30.227	0.374	1_g	0.0	2.083	78.25	9×10^{-6}
	-19.068	0.037	1_g	0.0	2.507	76.7	1×10^{-6}
$J = 3,\ g$	-427.213	70.193	0_g^-	0.0	1.331	98.9	2×10^{-5}
	-181.796	35.987	0_g^-	0.0	1.708	98.7	5×10^{-5}
	-87.659	0.217	1_g	0.0	3.317	75.1	1×10^{-6}
	-64.683	16.147	0_g^-	0.0	2.154	98.8	5×10^{-5}
	-17.337	5.851	0_g^-	0.0	3.170	98.9	3×10^{-5}
	-11.694	0.045	1_g	0.0	0.739	78.1	5×10^{-7}
	-5.659	0.033	1_g	0.0	3.167	75.5	4×10^{-7}
$J = 0,\ u$	-18.276	0.002	0_u^-	0.0	0.0	0.0	1×10^{-9}
$J = 1,\ u$	-418.241	0.419	0_u^+	3.096	2.448	0.0	1×10^{-4}
	-204.732	0.282	0_u^+	2.778	2.278	0.0	8×10^{-5}
	-82.005	0.147	0_u^+	3.976	3.269	0.0	4×10^{-5}
	-25.649	0.059	0_u^+	5.160	4.277	0.0	2×10^{-5}
$J = 2,\ u$	-191.499	0.020	2_u	4.826	4.202	2.1	4×10^{-8}
	-72.254	0.017	2_u	3.742	3.259	2.4	4×10^{-8}
	-21.434	0.008	2_u	6.336	5.517	2.5	2×10^{-8}
$J = 3,\ u$	-478.137	5.301	0_u^+	1.967	1.398	0.0	3×10^{-4}
	-282.480	3.213	0_u^+	0.573	0.408	0.0	2×10^{-4}
	-166.782	0.063	2_u	2.023	1.438	2.0	4×10^{-8}
	-121.640	1.610	0_u^+	0.291	0.207	0.0	8×10^{-5}
	-57.555	0.044	2_u	0.427	0.304	2.2	3×10^{-8}
	-38.405	0.665	0_u^+	0.162	0.115	0.0	3×10^{-5}
	-14.288	0.019	2_u	0.523	0.372	2.3	1×10^{-8}
	-7.024	0.222	0_u^+	0.027	0.019	0.0	2×10^{-5}

Table E.3: Resonances that are present in the helium $2s\,^3S_1 + 2p\,^3P_j$ dimer within 1500 MHz of detuning from the $j = 0$ asymptote. The detuning and predissociation width Γ_v^{pre} have been given in MHz. These resonances have been calculated without any modification of the short-range potentials. The columns 5–8 list the properties of the levels that may be used as observability criteria. $\mathcal{A}_v$ is the coupling strength in E_h of the level photoassociated from either a spin-polarised (spin) or unpolarised (unpolar) collision of metastable states. $f_{5,v}$ is the proportion of quintet character at short range ($R < 20\,a_0$) and $f_{R<20}$ is the proportion of the wave function at short range.

$j = 0$ asymptote							
J, w	Detuning	Γ_v^{pre}	Case (c)	$\mathcal{A}_v$spin	$\mathcal{A}_v$unpolar	$f_{5,v}(\%)$	$f_{R<20}$
$J = 1,\ g$	−207.681	0.002	1_g	0.0	2.211	25.7	4×10^{-13}
	−43.804	0.002	1_g	0.0	2.234	77.7	1×10^{-13}
$J = 2,\ g$	−170.933	0.002	1_g	0.0	1.858	68.6	1×10^{-10}
	−28.523	0.002	1_g	0.0	2.008	69.6	7×10^{-11}
$J = 3,\ g$	−115.744	0.000	1_g	0.0	0.195	60.3	3×10^{-11}
	−7.964	0.002	1_g	0.0	0.030	71.4	4×10^{-14}
$J = 1,\ u$	−1418.047	0.008	0_u^+	3.472	2.458	45.4	1×10^{-9}
	−648.486	0.008	0_u^+	2.095	1.554	9.5	3×10^{-10}
	−253.120	0.008	0_u^+	3.812	2.766	3.5	1×10^{-11}
	−79.653	0.002	0_u^+	4.399	3.236	2.3	6×10^{-11}
	−18.286	0.002	0_u^+	6.858	5.021	2.1	2×10^{-11}
$J = 3,\ u$	−1212.671	0.045	0_u^+	0.595	0.423	26.0	9×10^{-10}
	−513.066	0.045	0_u^+	0.111	0.079	48.7	4×10^{-10}
	−174.558	0.026	0_u^+	0.190	0.135	0.0	3×10^{-9}
	−41.635	0.008	0_u^+	0.058	0.041	82.7	2×10^{-9}

Table E.4: Resonances near the $j = 1$ asymptote that may be observable in experiments using an ion detection mechanism. The observability criteria for $\mathcal{A}_v$, $f_{5,v}$ and Γ_v^{pre} have been applied in a similar manner to table 3.14 as described in the text. An additional criterion, $f_{R<20}$, is present which indicates whether or not the resonance has a purely long-range nature. Many of the resonances overlap with one another.

J, w	Theor	Γ_v^{pre}(MHz)	$\mathcal{A}_v$ (E_h)	$f_{5,v}$	$f_{R<20}$	Case (c)
$J = 1$, g	-1178.7	20.5	0.934	99.7	1×10^{-4}	0_g^-
	-603.9	11.9	1.336	99.7	1×10^{-4}	0_g^-
$J = 2$, g	-1996.5	54.5	2.454	89.3	1×10^{-6}	1_g
	-1963.7	56.5	1.418	91.5	7×10^{-8}	$1_g, 2_g$
	-1952.5	59.4	1.231	95.8	6×10^{-7}	1_g
	-1899.6	63.3	3.108	90.8	7×10^{-8}	$1_g, 2_g$
	-1889.2	66.9	0.843	95.7	5×10^{-7}	1_g
	-1867.1	59.4	0.948	97.2	2×10^{-7}	1_g
	-1861.5	70.1	2.221	96.9	1×10^{-6}	$1_g, 2_g$
	-1821.2	73.6	0.749	93.4	5×10^{-7}	1_g
	-1804.3	60.3	2.122	98.2	5×10^{-7}	1_g
	-1742.7	64.0	0.724	97.9	7×10^{-7}	1_g
	-1704.0	85.3	1.814	98.9	8×10^{-7}	$1_g, 2_g$
	-1684.2	75.5	0.828	99.4	6×10^{-7}	1_g
	-1676.2	83.8	1.698	89.6	2×10^{-7}	1_g
	-1617.4	93.3	1.973	98.7	7×10^{-7}	$1_g, 2_g$
	-1613.3	83.1	1.385	93.6	7×10^{-7}	1_g
	-1591.7	91.2	2.958	92.9	1×10^{-7}	1_g
	-1581.5	90.0	0.972	91.1	7×10^{-7}	1_g
	-1502.1	98.5	1.754	93.4	1×10^{-7}	1_g
	-1490.9	97.3	1.197	91.8	9×10^{-7}	1_g
$J = 3$, g	-1998.3	59.7	0.950	95.0	5×10^{-7}	0_g^-
	-1985.2	53.0	1.820	90.0	7×10^{-7}	0_g^-
	-1973.4	56.6	0.760	91.4	7×10^{-7}	0_g^-
	-1956.2	56.5	1.041	96.8	3×10^{-7}	0_g^-
	-1937.2	68.2	1.014	88.7	5×10^{-7}	0_g^-
	-1912.0	61.0	1.165	92.4	1×10^{-6}	0_g^-
	-1842.3	68.5	1.629	96.9	1×10^{-6}	0_g^-
	-1822.5	69.4	1.366	89.3	5×10^{-7}	0_g^-
	-1691.3	69.8	1.553	89.6	3×10^{-6}	0_g^-
	-1541.2	82.3	1.718	94.3	2×10^{-6}	0_g^-
	-1456.5	90.3	1.982	91.0	2×10^{-6}	0_g^-
	-1365.1	97.2	1.720	90.8	1×10^{-6}	0_g^-